Simulation d'interactions vagues-structure par un couplage bidirectionnel entre un codepotentiel complètement non-linéaire et un code Navier-Stokes

Paul Landesman

École des Ponts ParisTech

THÈSE DE DOCTORAT

de l'École des Ponts ParisTech

Simulation of wave-structure interaction by a two-way coupling between a fully nonlinear potential flow model and a Navier-Stokes solver

École doctorale N°531, Sciences, Ingénierie et Environnement (SIE)

Mécanique des fluides

Thèse préparée au **Laboratoire d'Hydraulique Saint-Venant**

Thèse soutenue publiquement le 06/04/2022, par

Paul LANDESMAN

Composition du jury:

David LE TOUZÉ Professeur des Universités, Ecole Centrale Nantes	*Rapporteur*
Frédéric GOLAY Maître de Conférences, Université de Toulon	*Rapporteur*
Marilena GRECO Professeure, Norwegian University of Science and Technology	*Examinateur*
Stéphan GRILLI Professeur, University of Rhode Island	*Examinateur*
Sylvain GUILLOU Professeur des Universités, Université de Caen Normandie	*Examinateur*
Jeffrey HARRIS Chargé de recherche, HDR, École des Ponts ParisTech	*Directeur de thèse*
Michel BENOIT Professeur des Universités, Ecole Centrale Marseille (jusqu'au 31/08/2020) - Chercheur senior, HDR, EDF R&D, LNHE	*Co-directeur de thèse*
Christophe PEYRARD Ingénieur, chercheur expert, EDF R&D, LNHE	*Invité*

Thèse effectuée au sein du **Laboratoire d'Hydraulique Saint-Venant**

de l'Ecole des Ponts ParisTech et d'EDF R&D

6, quai Watier

BP 49

78401 Chatou cedex

France

Convention CIFRE EDF 2018/0235

Abstract

This thesis deals with the development and application of a two-way coupling procedure between a fully nonlinear potential flow model and a Navier-Stokes solver to study wave-structure interaction applied to offshore wind turbines.

The coupling strategy relies on a domain decomposition method, in which the wave field close to the structure of interest is simulated with the Navier-Stokes solver *Code_Saturne*, an open-source Finite Volume code capturing the free surface with a Volume of Fluid method. Away from the structure, where viscous and turbulent effects may be neglected, the potential code, solving the Laplace equation for the velocity potential with a boundary integral formulation, is applied to model the large scale wave field.

Generation and absorption of waves in this three-dimensional hybrid numerical wave tank take place in the outer potential domain. The potential and Navier-Stokes codes exchange data in the region around their common boundaries. The coupling may thus be referred to as "two-way", enabling one to propagate waves in and out of the viscous subdomain, and making the hybrid algorithm suitable to study wave diffraction on fixed offshore wind turbines, while keeping the viscous subdomain as small as possible. Each code uses its own mesh and time step. Subdomains are overlapping, therefore a velocity continuity condition and a free surface continuity condition have to be verified on two distinct coupling surfaces at any time.

Parallel implementation of the coupling strategy with communications between the models relying on the Message Passing Interface (MPI) library allows calculations to be run on large spatial and temporal scales on distributed memory clusters. The coupling algorithm is tested for various incident wave conditions, including solitary waves and regular nonlinear waves. It is then applied to the simulation of wave loads exerted on a vertical monopile and numerical results are compared with experimental measurements performed in a wave flume considering various values of the period and steepness of incident waves. Attention is paid to the analysis of high-order components of the nonlinear horizontal force.

Keywords:

Wave-structure interaction; offshore wind turbines; fully nonlinear potential flow; computational fluid dynamics; two-way coupling

Simulation d'interactions vagues-structure par un couplage bidirectionnel entre un code potentiel complètement non-linéaire et un code Navier-Stokes

Résumé

Cette thèse traite de la conception, du développement et de l'application d'une stratégie de couplage entre un code de vagues potentiel complètement non-linéaire et un modèle résolvant les équations de Navier-Stokes, dans le but d'étudier les interactions vagues-structure à l'oeuvre sur les fondations d'éoliennes en mer.

La stratégie de couplage suppose une décomposition du domaine de calcul suivant laquelle le champ de vagues proche de la structure étudiée est simulé à l'aide du solveur Navier-Stokes *Code_Saturne*, code open source à Volumes Finis mettant en oeuvre une méthode de capture de la surface libre de type Volume Of Fluid (VOF). A l'écart de la structure, là où les effets visqueux et turbulents peuvent être négligés, le code potentiel résout l'équation de Laplace pour le potentiel des vitesses, par le biais d'une formulation intégrale aux frontières et permet ainsi la simulation du champ de vagues lointain.

La génération et l'absorption de vagues sont effectuées dans le sous-domaine potentiel extérieur de ce canal à houle numérique hybride en trois dimensions. Les codes visqueux et potentiel échangent des informations liées au calcul couplé à proximité de leurs frontières communes. La procédure de couplage peut donc être qualifiée de bidirectionnelle, en ce qu'elle autorise la propagation de vagues du sous-domaine potentiel au sous-domaine visqueux, et réciproquement. Il devient ainsi possible d'étudier la diffraction de houles sur des fondations fixes d'éoliennes en mer, tout en réduisant au minimum l'étendue du sous-domaine visqueux, de même que les coûts de calcul associés. Chacun des codes utilise un pas de temps qui lui est propre. Le recouvrement partiel des sous-domaines impose de s'assurer que des conditions de continuité de la vitesse et de la position de surface libre sont vérifiées à tout instant sur les deux frontières couplées distinctes.

Cette méthodologie de calcul hybride, et les communications entre codes qu'elle implique, sont rendues parallèles par le recours à la bibliothèque Message Passing Interface (MPI). De ce fait, des simulations à de grandes échelles spatiales et temporelles sont permises par l'emploi d'une grappe de serveurs à mémoire distribuée.

La méthodologie de couplage est expérimentée pour divers types de vagues incidentes, incluant des ondes solitaires et des houles régulières non-linéaires. Elle est par la suite appliquée à la simulation des efforts s'exerçant sur un monopieu. Les résultats, dans le cas de la houle régulière, sont comparés à des données expérimentales obtenues dans un canal à houle. Différentes périodes et cambrures de vagues sont étudiées. Une attention particulière est portée aux composantes d'ordre élevés de la force horizontale non-linéaire.

Mots-clé:

Interactions vague-structure; éolien *offshore*; écoulement potentiel complètement non-linéaire; dynamique des fluides numérique; couplage bidirectionnel

Remerciements

Je tiens à remercier ici tous ceux qui ont rendu ce travail de thèse possible. Merci à Frédéric Golay et David Le Touzé d'avoir accepté d'être les rapporteurs de mon manuscrit de thèse. Leurs nombreuses remarques m'offrent la possibilité de prendre davantage de recul sur mon travail. Je tiens également à remercier Marilena Greco, Stéfan Grilli et Sylvain Guillou pour avoir accepté d'examiner ce travail de doctorat, et d'en avoir animé la soutenance par leurs questions. Je me dois aussi de remercier une nouvelle fois Frédéric Golay et Sylvain Guillou pour leur participation à mes Comités de Suivi Individuel de Thèse, qui ont donné lieu à des discussions d'un grand intérêt pour mon travail.

Merci évidemment à Jeffrey C. Harris, Michel Benoit et Christophe Peyrard, respectivement directeur, co-directeur et encadrant de thèse, pour m'avoir accordé leur confiance et guidé tout au long de ce doctorat, ainsi que pour leurs remarques, conseils, encouragements et relectures. J'adresse également mes remerciements à l'équipe de développement de *Code_Saturne*, et notamment à Yvan Fournier pour le temps qu'il a consacré à répondre à mes questions.

Je garderai un très bon souvenir des équipes d'EDF et de l'IRPHE qui m'ont accueilli, à Chatou et à Marseille. Merci aux permanents, ainsi qu'aux nombreux stagiaires, doctorants et post-doctorants rencontrés : Daniel, Teddy, Thomas, Hannah, Rem Sophia, Roberto, Florent, Florian, Athanasios, Konstantin, Lydia, Rajae, Elie, Sarah, Suzanne, Jie, Paul, Romain,... et toutes mes excuses à ceux dont j'aurais oublié le prénom. Merci à Fabien, qui m'a plus d'une fois montré la voie, et pas seulement au pied des falaises. Un grand merci à Antoine et Rémi : pour les discussions riches et animées et les aventures nautiques, notamment mais pas uniquement. Merci enfin à mes proches, pour leur soutien et leurs encouragements.

Contents

1 Introduction **21**

1.1 General introduction and industrial context 22

1.2 Review of coupled approaches to free surface problems 26

1.2.1 General considerations justifying the use of a hybrid approach . . . 26

1.2.2 3D wave models suited for far field simulation 26

1.2.3 Highly-accurate 3D models allowing to describe complex flow features close to a structure in waves 29

1.2.4 A review of coupling methods 31

1.3 Objectives of the present work 37

1.4 Structure of the PhD report 37

2 Description of BEM-VOF coupling strategy **39**

2.1 Description of the fully-nonlinear potential flow solver *seine3d* 40

2.1.1 Governing equations and boundary integral formulation 40

2.1.2 Time integration scheme 41

2.2 Description of the NS solver *Code_Saturne* 44

2.2.1 The Navier-Stokes model 44

2.2.2 VOF model description 44

2.2.3 Time stepping scheme 46

2.3 General strategy for a two-way coupling based on overlapping subdomains . 48

2.3.1 General considerations 48

2.3.2 Selected type of two-way coupling 48

2.3.3 Overlapping subdomains 49

2.4 Velocity matching at coupled boundaries 50

2.4.1 Wave generation in the VOF model through boundary conditions . . 50

2.4.2 Processing of velocity extracted from the interior of the NWT domain 52

2.4.3 Velocity extraction in *CS* domain 54
2.5 Free surface matching in the overlapping region 57
2.5.1 A need for matching free surfaces in $\Omega_{overlap}$ 57
2.5.2 Capturing free surface in *CS* 58
2.5.3 Free surface relaxation in *seine3d* 59
2.6 Advancing coupled simulations in time 62
2.6.1 Using different time step sizes for each code 62
2.6.2 Interpolation of *CS* coupling boundary conditions between *seine3d* time steps 62
2.6.3 Detailed description of the time stepping procedure 64
2.6.4 Calculation of ϕ_{rlx} 65
2.7 Parallelization of coupled simulations 67
2.7.1 Building a MPI communicator where coupling takes place 67
2.7.2 Sequential or parallel coupling communications 67
2.8 Coupling several instances of each code 69

3 Coupled simulation of the propagation of a solitary wave over a constant depth 71
3.1 Solitary wave of moderate relative height over constant depth 72
3.1.1 Description of the case 72
3.1.2 Description of reference case and first results 74
3.1.3 Relevance of free surface potential relaxation 81
3.1.4 Time evolution of errors on wave shape and wave celerity 83
3.1.5 Influence of the principal coupling parameters 87
3.2 Solitary wave of high relative height over constant depth 92
3.3 Conclusion 96

4 2DV regular waves simulations in the hybrid model 97
4.1 General considerations about 2DV regular waves coupled simulations 98
4.2 Global simulation setup 98
4.2.1 Design waves from WAS-XL campaign 98
4.2.2 Numerical domains 99
4.3 Choosing the right parameters and discretization levels in *seine3d* 100
4.3.1 Wave damping in *seine3d* 101

4.3.2 Choosing appropriate parameters for *seine3d* simulations 105
4.4 Improving *CS* simulation results 109
4.4.1 Simulation setup for tests in *CS* 109
4.4.2 Analysis of free surface elevation signal 112
4.4.3 Assessment of wave kinematics 113
4.4.4 Influence of certain numerical parameters on the velocity field 120
4.5 Coupled simulation of regular wave propagation in 2D 124
4.5.1 Coupling parameters 124
4.5.2 Simulation results 125
4.5.3 Testing coupled model limits in terms of wave steepness 130
4.6 Conclusions 133

5 Coupled simulation of the diffraction of a solitary wave on a vertical cylinder 135
5.1 General considerations 136
5.2 Case description 136
5.3 First 3D results and limitations 139
5.4 Overcoming stability limitations 141
5.5 Conclusions 145

6 Coupled simulations of the diffraction of regular nonlinear waves on a vertical cylinder 147
6.1 Case presentation and numerical settings 148
6.1.1 Numerical settings 148
6.1.2 Spectral analysis of the horizontal force exerted on the monopile . . 150
6.2 Coupled results for the smallest wave steepness 152
6.2.1 15 s wave period 152
6.2.2 Amplitude of harmonics of normalized horizontal force 158
6.3 12 s wave period 161
6.3.1 Free surface time signals 161
6.3.2 First order wave amplitude 161
6.3.3 Amplitude of harmonics of normalized horizontal force 163
6.4 9 s wave period 165
6.4.1 Free surface time signals 165

6.4.2 First order wave amplitude 166
6.4.3 Amplitude of harmonics of normalized horizontal force 166
6.4.4 *CS*-only simulation of the same problem with 9 s wave period 169
6.4.5 Amplitude of harmonics of normalized horizontal force 171
6.5 A coupled simulation featuring waves with higher nonlinearity 173
6.5.1 Free surface shape close to the cylinder 173
6.5.2 Free surface time signals 175
6.5.3 First order wave amplitude 176
6.5.4 Inline force time signal 176
6.5.5 Amplitude of harmonics of normalized horizontal force 177
6.6 Conclusions 179

7 Conclusions and future work **181**
7.1 Summary of main outcomes and discussion 182
7.2 Research and application perspectives 183

A Calculation of linear reflection coefficient **187**

Bibliography **201**

List of Figures

1 Introduction **21**

1.1 Wind Power Density (WPD) close to hub-height, *i.e.* 100m above ground and sea levels (a) and bathymetry (b) in Europe. WPD obtained from 10 years (2009 - 2018) mesoscale simulations with the Weather & Research Forecasting (WRF) model in the context of the New European Wind Atlas project (NEWA, Hahmann et al. (2020)). Bathymetry data from European Marine Observation and Data Network (EMODnet) Digital Terrain Model (Schmitt et al., 2019). Note that color scale for bathymetry is not linear. Figures from online mapping tools available at `https://map.neweuropeanwindatlas.eu/` and `https://www.emodnet-bathymetry.eu/data-products`, respectively. 23

1.2 Five different OWT fixed foundation concepts (Oh et al., 2018) 24

2 Description of BEM-VOF coupling strategy **39**

2.1 Coupled domains and related boundaries. Blue *CS* cells are cells filled with water, while red cells are full of air. Pale blue and pale red cells contain a mix of the two phases. 49

2.2 Dirichlet velocity boundary condition on the *CS* side of the overlapping area. Crosses mark the centers of the boundary faces belonging to $\Gamma^{\mathrm{D}}_{\mathrm{C,CS}}$. Yellow arrows represent the vertical profile of horizontal velocity $\mathbf{u}_{seine3d}$. . 51

2.3 Calculation of horizontal internal velocity close to free surface in *seine3d* domain. Crosses mark the centers of boundary faces belonging to $\Gamma^{\mathrm{D}}_{\mathrm{C,CS}}$ where *CS* velocity is sought. Red arrows with full lines represent the partially unphysical vertical velocity profile of $u_{seine3d}$ while dashed ones illustrate the corrected velocity profile (by local extrapolation). 53

2.4 Neumann boundary condition on the velocity potential on *seine3d* side of the overlapping region. Crosses mark the centers of *CS* cells in the vicinity of a given *seine3d* node. *CS* cells too close to free surface to yield a correct velocity value bear red crosses. Rectangle stands for the selection box centered on the *seine3d* node. Yellow arrows represent the vertical profile of normal velocity $\mathbf{u}_{seine3d} \cdot \mathbf{n}$. 54

2.5 Non-physical void fraction jump on *CS* side of overlapping area caused by non-matching free surfaces. Δ_η stands for difference in vertical position of free surfaces in both models. Vertical velocity profile is drawn in yellow, only its horizontal component is represented. 57

2.6 Consequences of a mismatch in free surfaces on *seine3d* side of the overlapping region. Δ_η stands for difference in vertical position of free surfaces in both models. Aberrant vertical profile of normal velocity is drawn in yellow. 58

2.7 Free surface relaxation in *seine3d*. The yellow line represents the position of *seine3d* free surface after correction. 60

2.8 Plots of different free surface blending functions 61

2.9 Main steps and information fluxes of coupling time stepping scheme. Red lines illustrate time stepping operations while blue ones show MPI communications between coupled programs. Top axis stands for *seine3d* while bottom axis represents operations conducted in *CS*. 64

2.10 MPI communicators and communications realized at each synchronized (*seine3d*) time step. Red boxes stand for *seine3d* processes while blue ones stand for *CS* processes. Hatched boxes represent root processes. Only processes with MPI ranks ranging from 1 to 3 are directly involved in the coupling. MPI communications at initialization are not shown for the sake of clarity. 68

3 Coupled simulation of the propagation of a solitary wave over a constant depth 71

3.1 Coupled domains and related boundaries. Blue *CS* cells are cells filled with water, while red cells are full of air. Pale blue and pale red cells contain a mix of the two phases. 73

3.2 Close-up view of the meshes around the left coupling region at $t = 6$. Void fraction field $\alpha(\mathbf{x})$ in *CS* domain is shown with corresponding colorbar. *seine3d* mesh is displayed in orange. 74

3.3 Time history of free surface profiles for the reference case of a solitary wave with $H = 0.3$. Dashed lines represent *seine3d* free surface nodes. 76

3.4 Close-up view of free surface profiles comprising overlapping regions at time instants $t = 18$ (a) and $t = 33$ (b) where spurious peaks and wiggles are observed. 77

3.5 *CS* and *seine3d* velocity fields in $\Omega_{overlap}$ for each coupling in the reference case of solitary wave propagation with $H = 0.3$. Due to overlapping results, red and yellow vectors are not always visible. 78

3.6 Velocity components in the leftmost potential domain (*seine3d* 1) at the time $t = 10$ when free surface instability is detected. It appears that velocity continuity is not realized at edges and corners related to the face receiving coupling Neumann condition from *CS* 1. 79

3.7 Scalar fields of the velocity potential ϕ (a) and its normal derivative ϕ_n (b) in the same *seine3d* domain at $t = 10$. 80

3.8 *seine3d* free surface geometry and free surface velocity potential in the left overlapping region in the reference case where computed free surface potential ϕ is not relaxed towards reconstructed solution ϕ_{rlx}. Left column : comparison of ϕ and ϕ_{rlx}. Right column : comparison of free surface position η computed in *seine3d*, before free surface relaxation and *CS* solution η_{CS}. 81

3.9 *seine3d* free surface geometry and free surface velocity potential in the left overlapping region up to the failure of the simulation when velocity potential relaxation is used, and comparison with and η_{CS} and ϕ_{rlx}, respectively. . . . 82

3.10 Time evolution of errors on wave height, crest position and width at half wave height for the solitary wave with $H = 0.3$. Time instants when wave crest passes in the middle of a coupling region are marked with vertical colored lines. 86

3.11 Influence of time step ratio $N_{\Delta t}$ on the characteristics of a solitary wave with $H = 0.3$ propagating over a constant depth. Only results from stable simulations are shown. 88

3.12 Computational speed, expressed as the ratio of physical time over computing time, for different values of $N_{\Delta t}$. 90

3.13 Influence of the width of overlapping regions on characteristics of a solitary wave with $H = 0.3$. Only results from stable simulations are shown. 91

3.14 Close-up view of the meshes in the left coupling region at $t = 8.9$ just before the solitary wave simulation with $H = 0.5$ fails. The void fraction field $\alpha(\mathbf{x})$ in the *CS* domain is shown with corresponding colorbar. Note x-axis is inverted. *seine3d* mesh is displayed in orange. 92

3.15 Time history of free surface profiles for a solitary wave with $H = 0.5$. 94

3.16 Time evolution of errors on wave height, crest position, and width at half wave height for the solitary wave with $H = 0.5$. Time instants when wave crest passes in the middle of a coupling region are marked with vertical colored lines. 95

4 2DV regular waves simulations in the hybrid model 97

4.1 Coupled domains for periodic waves simulations. Blue *CS* cells are cells filled with water, while red cells are full of air. Pale blue and pale red cells contain a mix of the two phases. *CS* mesh and *seine3d* boundary elements are drawn for illustrative purposes only. Horizontal proportions are realistic and correspond to the case of $T = 15$ s. The area in shaded grey represents the damping region in $\Omega_{seine3d,2}$, long of one wavelength (reported in table 4.1). 100

4.2 Comparison of the streamfunction and computed free surface signals at upstream wave gauge ($x_1 = 3\lambda$) used for the calculation of reflection coefficient. 102

4.3 Influence of damping intensity on reflection coefficient measured upstream of the damping region. 103

4.4 Phase shift (b) and relative error on wave height (a) at $x = 0$ m for *seine3d* alone. Longitudinal dimension of *seine3d* boundary elements is set to $\Delta x = \frac{\lambda}{16}$. 106

4.5 Vertical profiles of *seine3d* velocity at the virtual abscissa of the monopile ($x = 0.0$ m) during the 50^{th} wave period for several values of Δt and N_z. Δx is set to $\frac{\lambda}{16}$. 108

4.6 Streamfunction and computed free surface time history at $x = 2\lambda$, in a test simulation involving only *CS*. 112

4.7 Phase shift (b) and relative error on wave height (a) at $x = 2\lambda$. Simulation using only *CS*. 113

4.8 Comparison of the streamfunction and computed free surface profiles at time instants $t = 5T$ and $t = 50T$ in a test simulation involving only *CS*. . . 114

4.9 Scalar fields of horizontal (a) and vertical (b) velocity components at $t = 5T$. Black line represents the streamfunctionl free surface profile. 115

4.10 Scalar fields of horizontal (a) and vertical (b) velocity components at $t = 50T$. Black line represents the streamfunction free surface profile. 116

4.11 Vertical profiles of horizontal velocity beneath the wave crest at $x = 2\lambda$. . . 117

4.12 Normalized error on vertical velocity over one wavelength, at time instants $t = 5T$ (a) and $t = 50T$ (b). Domain ranges from $x = 1.25\lambda$ to $x = 2.25\lambda$. . 118

4.13 Vertical profile of time average of horizontal velocity over one wave period, at $x = 2\lambda$ at various time instants in the *CS* domain. Time average is calculated between t_0 and $t_0 + T$. Mean Eulerian horizontal velocity, as computed by the streamfunction wave algorithm, is shown for comparison. . 119

4.14 Horizontal (a) and vertical (b) velocity fields at $t = 50T$. Close-up view around the interface. Black lines illustrate the position of the free surface. . 119

4.15 Comparison of streamfunction and computed vertical profiles of velocity components at $t = 5T$. Simulations using only *CS* with the same setup as before. (a) simulation with varying cell aspect ratio, other parameters are set to $\Delta z = \frac{H}{20}$ and $\Delta_t = \frac{T}{1500}$. (b) simulation with varying time step, other parameters are set to $AR = 1$ and $\Delta z = \frac{H}{20}$. (c) simulation with varying cell height, other parameters are set to $AR = 1$, $\Delta t = \frac{T}{1500}$. 121

4.16 Vertical profiles of velocity at $x = 2\lambda$ during one wave period just before $t = 5T$, $t = 50T$ and $t = 100T$. Simulation using *CS* only. 123

4.17 Instantaneous free surface profiles from coupled models instances at $t = 50T$. Circles mark the position of *seine3d* free surface nodes. 125

4.18 Comparison of the streamfunction and computed free surface signals at the virtual position of the monopile ($x = 0$ m). 126

4.19 Phase shift (b) and relative error on wave height (a) at the virtual location of the monopile in the case of a coupled simulation. The first 20 wave periods are not displayed. 127

4.20 *CS* and *seine3d* velocity fields in $\Omega_{overlap}$ and for each coupling during the 50^{th} simulated wave period. Velocity is extracted at the location of *seine3d* boundary nodes. 128

4.21 Vertical profiles of *CS* velocity in a coupled simulation, compared to the reference streamfunction solution, just before $t = 20T$, $t = 50T$ and $t = 100T$. 129

4.22 Comparison of the streamfunction and computed free surface signals at the virtual position of the monopile ($x = 0$ m) in the case of a wave steepness of $\frac{1}{22}$. 131

4.23 Relative error on wave height (a) and phase shift (b) at the virtual location of the monopile in the case of a coupled simulation with $\epsilon = \frac{1}{40}$. The first 20 wave periods are not displayed. 132

5 Coupled simulation of the diffraction of a solitary wave on a vertical cylinder 135

5.1 Computational domains used in the successful simulation of the diffraction of a solitary wave with $H = 0.3$, see section 5.4. 137

5.2 Detail of *CS* mesh near the monopile. 138

5.3 Detail corner instability occuring at the downstream boundary of the *seine3d* 2 domain, $t = 32.4$. 139

5.4 Snapshots of free surface elevation contours during the propagation and interaction with a vertical surface piercing cylinder of a solitary wave with $H = 0.2$. Dashed lines indicate limits of potential domains. 140

5.5 Snapshots of free surface elevation contours during the propagation and interaction with a vertical surface piercing cylinder of a solitary wave with $H = 0.3$. Dashed lines indicate limits of potential domains. 142

5.6 Detailed free surface elevation contours at different time instants in the case of $H = 0.3$. Dashed line indicates coupled boundary of *seine3d* 1 instance. Square patterns are visualization artifacts related to the interpolation of values between *seine3d* boundary nodes. 143

5.7 Snapshots of free surface shape near the monopile at various time instants. Incident wave comes from the left. 144

6 Coupled simulation of the diffraction of regular nonlinear waves on a vertical cylinder 147

6.1 Experimental domain layout. Reproduced from Dadmarzi et al. (2019). . . 148

6.2 Close-up view of the *CS* mesh in the vicinity of the monopile in the case of $T = 15$ s and $\epsilon = \frac{1}{40}$. 149

6.3 View of the computational domains in the case of $T = 15$ s and $\epsilon = \frac{1}{40}$. . . . 150

6.4 Comparison of streamfunction and computed free surface signals at the wave gauge next to the monopile, of coordinates ($x = 0$ m, $y = 31.25$ m). . 153

6.5 Relative error on wave height (a) and Phase shift (b) recorded by a wave gauge located at $x = 0$ m, $y = 31.25$ m. The first $20T$ are excluded from the analysis. 154

6.6 Snapshots of the free surface in the *CS* domain near the monopile, as a wave crest passes. Incident waves are coming from the left. 156

6.7 First order wave amplitude in the coupled simulation for $T = 15$ s. The spectral analysis of the numerical results is realized over one wave period (red nodes). A dashed red line illustrates the average amplitude over the whole displayed time interval. The free surface signal is recorded by the same wave gauge as in figure 6.4, while the first $20T$ are excluded from the analysis and therefore not shown. 157

6.8 Normalized horizontal force time signal between $t = 40T$ and $t = 45T$ for $T = 15$ s and $\epsilon = \frac{1}{40}$. 158

6.9 Amplitudes of the first three harmonics of horizontal force applying on the monopile, obtained from the WAS-XL experimental campaign and the coupled simulation for $T = 15$ s and wave steepness $\epsilon = \frac{1}{40}$. Spectral analysis of numerical results is realized over one sliding wave period (red nodes). Time-averaged values are illustrated by dashed red lines. The first $22T$ are excluded from the analysis. 160

6.10 Comparison of streamfunction and computed free surface signals at the wave gauge closest to the monopile for $T = 12$ s and $\epsilon = \frac{1}{40}$. 162

6.11 First order wave amplitude signal obtained from coupled simulation for $T = 12$ s and $\epsilon = \frac{1}{40}$. The first $12T$ are excluded from the analysis and therefore not shown. 162

6.12 Amplitudes of the first three harmonics of horizontal force applying on the monopile, obtained from the WAS-XL experimental campaign and the coupled simulation for $T = 12$ s. Gray areas illustrate the time window excluded from the computation of harmonics mean values starting at $t = 33T$, due to non-convergent behavior of $\frac{F_x^{(2\omega)}}{\rho g a^2 A_1}$, and $\frac{F_x^{(3\omega)}}{\rho g a^2 A_1}$ to a lesser extent. The first $12T$ are excluded from the analysis and therefore not shown. . . . 164

6.13 Comparison of streamfunction and computed free surface signals at the wave gauge closest to the monopile for $T = 9$ s and $\epsilon = \frac{1}{40}$. 165

6.14 First harmonic amplitude of the free surface elevation signal in the coupled simulation for $T = 9$ s and $\epsilon = \frac{1}{40}$. The first $21T$ are excluded from the analysis and therefore not shown. 166

6.15 Amplitudes of the first three harmonics of horizontal force applying on the monopile, obtained from the WAS-XL experimental campaign and the coupled simulation for $T = 9$ s and $\epsilon = \frac{1}{40}$. The first $23T$ are excluded from the analysis and therefore not shown. 168

6.16 Comparison of streamfunction and computed free surface signals at the wave gauge closest to the monopile for a *CS*-only computation with $T = 9$ s. 170

6.17 First harmonic amplitude of the free surface elevation signal from the *CS*-only simulation for $T = 9$ s and $\epsilon = \frac{1}{40}$. Spectral analysis of numerical results is realized over one sliding wave period (red nodes). The first $24T$ are excluded from the analysis and therefore not shown. Coupled results are drawn in yellow for comparison. 170

6.18 Amplitudes of the first three harmonics of horizontal force applying on the monopile, obtained from the WAS-XL experimental campaign and the *CS*-only simulation for $T = 9$ s and $\epsilon = \frac{1}{40}$. The first $23T$ are excluded from the analysis and therefore not shown. Coupled results are drawn in yellow for comparison. 172

6.19 Snapshots of the free surface in the CS domain near the monopile, as a wave crest passes, with $T = 15$ s and $\epsilon = \frac{1}{22}$. Incident waves come from the left. . 174

6.20 Comparison of the streamfunction and computed free surface signals at the wave gauge closest to the monopile for a coupled computation with $T = 15$ s and $\epsilon = \frac{1}{22}$. 175

6.21 First harmonic amplitude of the free surface elevation signal obtained from the coupled simulation for $T = 15$ s for $\epsilon = \frac{1}{22}$. The first $22T$ are excluded from the analysis and therefore not shown. 176

6.22 Normalized horizontal force time signal between $t = 40T$ and $t = 45T$ for $T = 15$ s and $\epsilon = \frac{1}{22}$. 176

6.23 Amplitudes of the first three harmonics of horizontal force applying on the monopile, obtained from the WAS-XL experimental campaign and the coupled simulation for $T = 15$ s and $\epsilon = \frac{1}{22}$. The first $20T$ are excluded from the analysis. 178

A Calculation of linear reflection coefficient **187**

List of Tables

1 Introduction **21**

2 Description of BEM-VOF coupling strategy **39**

3 Coupled simulation of the propagation of a solitary wave over a constant depth **71**

3.1 $N_{\Delta t}$ and associated *seine3d* time and space discretizations. 89

4 2DV regular waves simulations in the hybrid model **97**

4.1 Characteristics of simulated waves with steepness $\epsilon = \frac{1}{40}$ and $h = 27$ m. . . 99

5 Coupled simulation of the diffraction of a solitary wave on a vertical cylinder **135**

6 Coupled simulation of the diffraction of regular nonlinear waves on a vertical cylinder **147**

6.1 Normalized amplitude of the first three harmonics of the depth-integrated inline force on the cylinder, in the case of $T = 15$ s and $\epsilon = \frac{1}{40}$. 159

6.2 Normalized amplitude of the first three harmonics of the depth-integrated inline force on the cylinder, in the case of $T = 12$ s and $\epsilon = \frac{1}{40}$. Computation of the mean values is realized over a restricted time window $(12T - 33T)$. . 163

6.3 Normalized amplitude of the first three harmonics of the depth-integrated inline force on the cylinder, in the case of $T = 9$ s and $\epsilon = \frac{1}{40}$ 167

6.4 Normalized amplitude of the first three harmonics of the depth-integrated inline force on the cylinder, in the case of $T = 9$ s and $\epsilon = \frac{1}{40}$ for a simulation involving only *CS*. Algebraic error levels obtained with the corresponding coupled simulation are recalled in parentheses. 171

6.5 Normalized amplitude of the first three harmonics of the depth-integrated inline force on the cylinder, in the case of $T = 15$ s and $\epsilon = \frac{1}{22}$. 177

A Calculation of linear reflection coefficient **187**

Chapter 1

Introduction

Dans ce premier chapitre, on présente de manière globale le contexte industriel de la thèse : la génération d'électricité par extraction et conversion de l'énergie cinétique du vent, permise par le recours à des éoliennes en mer. Les principaux défis techniques, solutions et outils d'ingénierie disponibles sont brièvement abordés. Dans un second temps, une revue de la littérature scientifique consacrée à l'hydrodynamique numérique à surface libre est réalisée. Différents types de modèles mathématiques et codes de calculs associés sont évoqués, leur principales caractéristiques rappelées. On distingue également diverses stratégies de couplage combinant certains de ces codes. En particulier, les travaux antérieurs portant sur des méthodes de couplage bidirectionnel potentiel/visqueux reposant sur une approche par décomposition de domaine sont passés en revue et analysés. Enfin, on présente les objectifs de ce travail de thèse, et la structure retenue pour la suite du manuscrit.

1.1 General introduction and industrial context

To meet the requirements of the United Nations's Paris Agreement (United Nations, 2015) on mitigating global warming to 2° and possibly 1.5° above pre-industrial levels, the European Union (EU) has pledged to decrease the global greenhouse gas emissions of its member states by 55% by 2030 and to reach carbon neutrality by 2050 (European Commission, 2019). To that end, lowering the mean carbon dioxide equivalent (CO_{2eq}) content of the European electricity production is necessary, with low-carbon facilities expected to take over power plants relying on the combustion of fossil fuels. Among these decarbonized power sources, long-established hydro power and nuclear power facilities are being supplemented by rapidly growing solar power and wind power. Focusing on the latter, it appears that it accounts for 194GW of installed capacity as of 2020, among which 25GW (12.9%) come from Offshore Wind Turbines (OWT) (Wind Europe, 2021). Due to the intrinsic qualities of offshore wind technology, and to the rising opposition encountered to new onshore wind farms, the EU Commission plans the massive development of the former, with total capacities reaching 60GW in 2030, and 300GW in 2050 (European Commission, 2020).

Deploying wind farms in the coastal area rather than onshore indeed has numerous advantages. The wind resource to be harvested is on average more powerful and stable, with reduced turbulence levels, due to lower surface roughness and a more stable atmospheric boundary layer over the sea. For illustration purposes, the upper panel of figure 1.1 shows the mean Wind Power Density (WPD) levels over Europe, including the whole Baltic and North Seas, as well as in areas extending up to 100km offshore from any coastline. WPD represents the mean energy flux available at a given altitude, here taken to be 100m over ground or sea levels, to match hub-heights attained by new large wind turbines. It can be noticed that wind resource density in most coastal areas is nearly twice as high as compared to land. Such discrepancies in wind resource should definitely rule in favor of offshore wind farms. As generated power is proportional to the square of the turbine diameter, increasingly larger machines are installed both on land and at sea, making social acceptance even more difficult, and further pushing for OWTs. It should nevertheless be noted that offshore wind turbines, as well as onshore ones, might represent a threat for certain bird species. At the same time, fish sheltering capacities are expected to improve from OWT parks (Lindeboom et al., 2011).

Major limiting factors reside in the technical difficulties related to operating wind turbines at sea. Very harsh environmental conditions are indeed experienced, and the design of OWTs benefits from the fact that ships and oil & gas production platforms provide decades of records and engineering knowledge related to surviving extreme storms and sea states, as well as dealing with rapid marine corrosion and bio-fouling growth, among others. Besides this, installation, maintenance and decommission challenges should be dealt with, alongside with the electrical grid connection. For safety and production reasons, it is then necessary to ensure that the foundation of an offshore wind turbine delivers sufficient

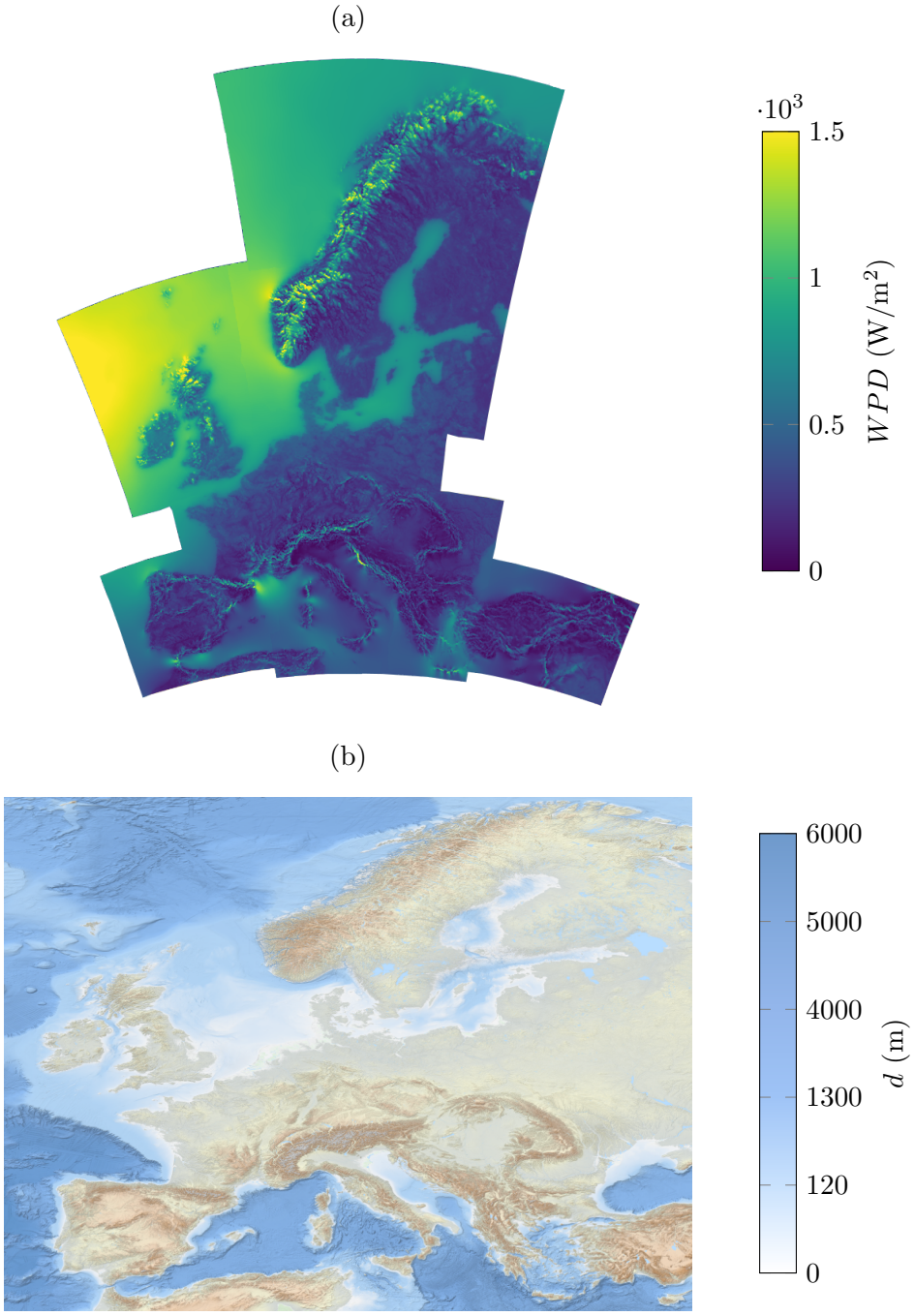

Figure 1.1: Wind Power Density (WPD) close to hub-height, *i.e.* 100m above ground and sea levels (a) and bathymetry (b) in Europe. WPD obtained from 10 years (2009 - 2018) mesoscale simulations with the Weather & Research Forecasting (WRF) model in the context of the New European Wind Atlas project (NEWA, Hahmann et al. (2020)). Bathymetry data from European Marine Observation and Data Network (EMODnet) Digital Terrain Model (Schmitt et al., 2019). Note that color scale for bathymetry is not linear. Figures from online mapping tools available at `https://map.neweuropeanwindatlas.eu/` and `https://www.emodnet-bathymetry.eu/data-products`, respectively.

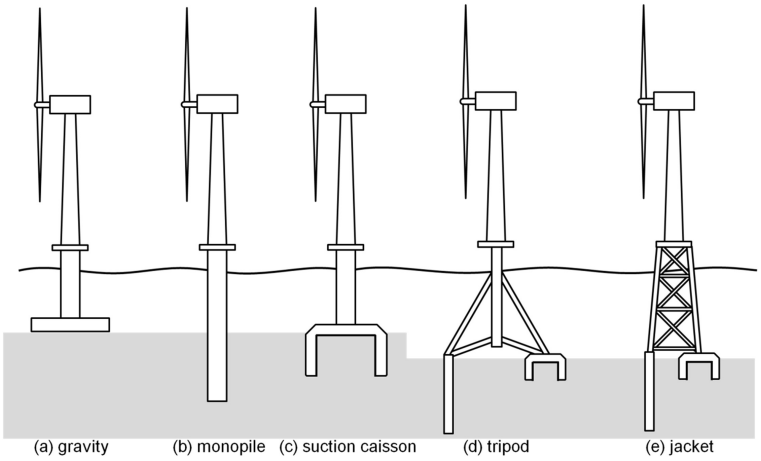

Figure 1.2: Five different OWT fixed foundation concepts (Oh et al., 2018)

restoring forces and moments to oppose aerodynamic and hydrodynamic loads.

To that end, the most straightforward solution resides in the use of bottom-fixed foundations, either stuck in or laid on the ground, as displayed in figure 1.2. These are however limited to water depths around 60m (Musial et al., 2007). From the lower panel of figure 1.1, it thus appears that the North Sea does not only features great wind resources, but due to shallow areas extending far offshore, it is also quite convenient for OWT deployment. However, in other windy places, such as in the Gulf of Lion in the Mediterranean Sea, with the Mistral and Tramontane strong wind regimes, high water depths require floating solution. These imply additional technical challenges related to stability or mooring. Although the development of floating OWTs is increasing very rapidly in recent years (Global Wind Energy Council (GWEC), 2021), the present work is dedicated to the hydrodynamics of bottom-fixed foundations and does not discuss moving body in waves. It is applied to the most common bottom-fixed foundations type used in Europe : the monopile. Whatever the retained solution, OWT structures should withstand various mechanical loads, originating from wind, waves or ocean currents, in production or in worst case (storm) scenarios. In the latter case, due to the strong winds, the OWTs is parked, and the hydrodynamic loads dominate. Among these, the wave loads are the most prominent ones. For that purpose, analytical, experimental and numerical investigations are conducted in the design phase of OWT units. Due to the diversity and complexity of the physical phenomena related to wave-structure interaction, analytical, or semi-analytical approaches such as the Morison equation (Morison et al., 1950), albeit widely used in the industry, are limited to small wave steepness.

Model-scale experiments, on the other hand, account for the full physics and remain an important point for the validation of numerical models used in the design process, in particular for floating foundations or in case of specific nonlinear wave loads, like breaking loads. They are however time-consuming and costly, and do not always allow for an accurate assessment of certain wave-induced flow properties, such as complex three dimensional

(3D) velocity fields or hydrodynamic pressure levels on a structure. Furthermore, scale effects might deteriorate the quality of results, in particular regarding damping.

Numerical methods of OWT design provide access to any variable of interest in the whole computational domain at prototype scale, and are less expensive than experimental campaigns. However, as the most widely used engineering tools rely on the Morison equation for the hydrodynamic part, which only takes incident wave kinematics into account, not all physical phenomena can be simulated and various approximations are made. This way, low computational costs are obtained. Indeed, the drag force exerted on the structure is estimated from a drag coefficient, the wave diffraction is modeled by a single coefficient, and the wetted area is approximated. One should ensure that such numerical results are relevant and capture the main physical processes, like drag and inertia forces for hydrodynamics, thrust and wake description for aerodynamics.

This might make necessary the development and use of higher fidelity models, able to account for almost all the physical processes, in order to identify the domain of validity of design models. As very different time and space scales are involved, this might call for the use of very fine time and space discretizations, and lead to unrealistic computational costs. Numerical methods allowing for a reduced computational burden are then sought that also keep a sufficient accuracy.

Hence, coupling a potential model accurately describing large scale wave propagation in the absence of a structure, and a viscous solver simulating the main physical phenomena related to wave-structure interaction at the local scale is an interesting option. This is the major motivation of this work. In the following section, a literature review is thus presented that deals with numerical methods applied to the simulation of wave-induced flows and emphasizes the main aspects of potential/viscous hybrid strategies.

1.2 Review of coupled approaches to free surface problems

1.2.1 General considerations justifying the use of a hybrid approach

Here, we focus our attention to hybrid numerical methods previously applied to the simulation of free surface problems, that combine heterogeneous physical models solving different sets of equations. Fields of applications of these methods span from the simulation of wave propagation over constant or uneven water depths, to the description of wave flows around fixed or moving structures, possibly piercing the free surface. All of them intend to take advantage of the discrepancies in terms of free surface shape and wave kinematics observed between the close vicinity of a structure or a region of rapidly changing bathymetry and an outer, often larger, region where the wave field is less complex. Indeed, rotational, viscous and turbulent effects, as well as wave breaking and subsequent air entrapment, are limited to the former (local) area. This distinction between near-field and far-field free surface flows calls for the use of different physical hypotheses and mathematical models in their simulation.

1.2.2 3D wave models suited for far field simulation

Wave propagation, wave-wave interactions, or wave transformation on a slowly varying bottom over large distances in finite depth, among other problems, are efficiently handled by mathematical models devoted to the description of incompressible and irrotational (hence kinematically inviscid) flows, namely potential free surface models. In these models, a Laplace equation on the velocity potential for mass conservation is solved in a domain in which free surface position is not known *a priori*. Indeed, nonlinear kinematic and dynamic boundary conditions govern the time-evolution of the free surface shape and potential at the free surface. Other linear conditions complete the set of boundary equations to yield a Boundary Value Problem (BVP) to be resolved at every considered time instant. Certain numerical strategies consider linearized versions of these free surface boundary conditions, in which nonlinear terms are neglected. Combined for example with a Boundary Element Method (BEM) formalism, fast computations are made possible in the frequency domain, such as with the codes AQUAPLUS (Delhommeau, 1993), WAMIT (Lee, 1995) or NEMOH (Fàbregas Flavià et al., 2016) aiming at the resolution of diffraction-radiation problems. However, only waves with small steepness can be rigorously handled with these methods.

Another solution is to expand the free surface boundary equations from the still water level following a perturbation approach. A Taylor expansion is used in which different orders of a small parameter appear, namely the wave steepness. Such weakly nonlinear resolution method was applied by Belibassakis and Athanassoulis (2002) to simulate regular second-order Stokes waves in a nonperiodic domain with rapidly varying bathymetry. Leroy et al. (2021) make use of the weak-scatterer (WS) perturbation approach introduced by Pawlowski (1992) to solve an hydroelastic coupling problem on a flexible monopile-supported OWT, submitted to regular nonlinear waves. In the hydrodynamic problem,

the velocity potential and the free surface elevation are decomposed into incident and perturbed (scattered by the structure) fields, where it is assumed that the latter is small as compared to the former. This way the free surface boundary conditions are linearized around the incident free surface elevation. Zhang and Teng (2021) investigated high-frequency wave loads on a fixed vertical cylinder, as well as the rigid body motion of a bottom-hinged pitching monopile, both in regular nonlinear waves, with a WS model.

1.2.2.1 3D volume field methods

To fully overcome the limitation in wave steepness and deal with highly nonlinear waves, it is necessary to account for the complete nonlinear terms in the free surface boundary conditions. This makes the resolution of the Laplace problem far more complex and computationally demanding. Several strategies have been considered to deal with fully-nonlinear 3D free surface flows. Some of them rely on the resolution of the flow kinematics in the whole volume field. This is the case of the Finite Difference Method (FDM), which has been used, for example, by Engsig-Karup et al. (2009) in the code OceanWave3D. Finite Element Method (FEM), implemented by Ma and Yan (2006) in the QALE-FEM, also solves Laplace equation in a 3D domain. Finite Volume Method (FVM) might also be used for this purpose, as done in Mehmood et al. (2015) in 2D. The Harmonic Polynomial Cell (HPC) method, (Shao and Faltinsen (2014), Robaux and Benoit (2021)), is yet another method of this type. These numerical strategies share in common the need to build large sparse matrices to solve free surface problems, for which efficient inversion algorithms are available. They have also been successfully applied to the simulation of wave-structure interactions, to describe nonlinear flows close to fixed or moving bodies.

1.2.2.2 Reduced dimensionality approaches

Apart from the field solvers, other families of models exist in which the straightforward resolution of the 3D Laplace equation on the velocity potential is replaced by the knowledge of relevant physical quantities over certain domain boundaries. A preliminary step prior to applying reduced dimensionality approaches might be to write the free surface boundary conditions following the formalism of Zakharov (1968). The free surface boundary conditions are expressed at the vertical position of the free surface and involve free surface position, free surface velocity potential and vertical velocity at the free surface. Therefore the knowledge of these three variables suffices to describe the wave flow.

Spectral methods make use of such formalism to reduce the dimensionality of the problem by one. A spectral method's crux lies in the determination of the vertical velocity at the free surface, also referred to as "Dirichlet-to-Neumann" (DtN) problem. The High-Order Spectral (HOS) method, used by West et al. (1987) and Dommermuth and Yue (1987) or Ducrozet et al. (2012), is one of them. It relies on a perturbation description of the velocity potential in a power series expansion based on wave steepness. This perturbation

series is truncated at an arbitrary approximation order, namely the HOS order. Another approximation level lies in the fact that the potential is further expressed as a Taylor series expansion of the vertical coordinate around the resting free surface level. This is an accurate and computationally efficient method, however there exists constraints on the basis functions used to account for the domain geometry, and wave-structure interactions can not be dealt with. Also, only single-valued free surfaces are handled, thus this technique can not be used to simulate the development of overturning waves. Another approach was developed by Tian and Sato (2008), Raoult et al. (2016) and Zhang and Benoit (2021). In these works, the velocity potential is approximated from a linear combination of vertical base functions built from Chebyshev polynomials. Varying bottoms are considered in nonlinear and dispersive wave propagation simulations. This model was compared to a Finite Difference one close to that developed by Engsig-Karup et al. (2009) in Yates and Benoit (2015). In Belibassakis and Athanassoulis (2011) and Papoutsellis et al. (2018), the system of equations established by Zakharov (1968) is solved in a non-perturbative way through the Hamiltonian Coupled Mode Theory (HCMT) to simulate nonlinear free surface waves, again over non-uniform bathymetry.

Another way to reduce the dimensionality of the problem, and therefore the number of unknowns, is to make use of Green's second identity to express the velocity potential anywhere inside the water volume as a function of the potential and its normal derivative on the fluid domain boundaries, in the form of Boundary Integral Equations (BIE). Physical assumptions made to characterize the flow on every domain boundary translate into Dirichlet and Neumann conditions on the velocity potential, and possibly on its time derivative. The above-mentioned fully-nonlinear kinematic and dynamic free surface boundary conditions yield, through a time-stepping procedure, a Dirichlet condition for the potential (and its time derivative), whereas Neumann conditions are imposed on all other boundaries. A BEM approach is used to solve this set of integral equations at each time-step, in which boundaries are discretized into elements over which variables are interpolated. BEM methods have been implemented with various interpolation orders, the lowest one reducing to the constant panel method.

Grilli et al. (2001) proposed one such high-order method (HOBEM) for 3D computations, relying on cubic Mid-Interval Interpolation (MII) elements built from a structured grid. It was successfully applied to the modeling of a solitary wave shoaling and overturning on a sloping ridge, to the study of landslide-generated tsunamis or to investigate the occurrence of freak waves. Simulation of overturning waves was made possible by the fact that free surface does not rely on a single-valued description. Fully nonlinear wave-structure interaction problems were investigated using HOBEM Numerical Wave Tanks (NWT) having wave generation and absorption capabilities, extending the seminal work of Grilli et al. (2002). Guerber et al. (2012) indeed enabled the physical description of 2D fixed or moving submerged structures, in the context of Wave Energy Converter (WEC) simulation. Dombre et al. (2015) enabled the 3D simulation of floating rigid bodies of complex shapes, enabled by the use of unstructured grids. The original 3D HOBEM

NWT of Grilli et al. (2002) was also recently enriched with the possibility to employ cubic B-spline elements on structured meshes to describe fluid domain boundaries, as reported in Harris et al. (2017). It allowed to reach even higher accuracy level than those obtained with MII. A number of other high-order BEM models were proposed to treat various 3D free surface wave problems, as the ones of Romate (1990), Fochesato and Dias (2006), Bai and Eatock Taylor (2006) or Maestre et al. (2016).

3D BEM applications suffer from the inherently high computational complexity of the method. Indeed, the influence matrix accounting for the contribution of all boundary nodes in the calculation of the potential at each point is dense. Its cost, in terms of storage memory requirements, amounts to $O(N^2)$ with N the number of boundary nodes. Inverting it with direct methods like the Gaussian elimination or Lower-Upper (LU) decomposition leads to a computing complexity greater than $O(N^2)$, making the resolution of large 3D problems very computationally demanding. Iterative solvers might as well be used, like the Gauss-Seidel method or the GMRES method (Generalized Minimal Residual) that decrease the number of operations, and thus the computational time needed, to follow a $O(N^2)$ rule. Further progress have been made towards a $O(N)$ complexity with the use of the Fast Multipole Method, introduced by Greengard and Rokhlin (1987). A parallel version of such method was implemented in a HOBEM model derived from that of Grilli et al. (2002), as described in Harris et al. (2022).

However, even with fully-nonlinear models, the potential flow assumption inherently prevents from describing rotational, viscous, and turbulent effects experienced near the structures of interest. It should be noticed at last that although all the previously mentioned potential methods only handle the deformation of a body of water with time, it is possible to solve potential problems involving two phases separated by a moving interface, such as air and water, as done in Colicchio et al. (2006). This is made possible by assuming a high density ratio between phases, and no influence of the light phase on the heavy one.

1.2.3 Highly-accurate 3D models allowing to describe complex flow features close to a structure in waves

As already stated, a precise description of wave-induced flows in the neighborhood of a fixed or moving structure requires to solve the full Navier-Stokes (NS) equations to account for rotational, viscous, and possible turbulent effects. Relying on NS equations to model free surface flows opens a wider scope of possibilities, through Computational Fluid Dynamics (CFD) computations, at the cost of dealing with more unknowns than in the potential case. However, the description of such problems relies on sparse matrices, enabling lower resolution time for a given problem size, as compared to the above-mentioned models featuring full matrices. Two-phase simulations might be conducted, representing air and water in our case, as well as ones featuring only the liquid phase. As finding an approximate solution to NS equations requires establishing and solving a BVP, the number of handled phases is in close relation with the choice of boundary conditions.

1.2.3.1 Front-capturing methods

Considering two-phase incompressible flows solved in an Eulerian manner, a numerical domain of constant shape is used in which mass conservation should be ensured for each phase. Boundary conditions, possibly heterogeneous, are applied to predetermined sets of boundary cells and faces belonging to a fixed mesh. Time evolution of interface geometry might be obtained by front-capturing methods, such as the Level-Set (LS) method employed by Yue et al. (2003), Colicchio et al. (2005) and Bihs et al. (2016) or the Volume Of Fluid (VOF) method (Abadie et al. (2010), Xie (2012), Higuera et al. (2013)) following the pioneering work of Hirt and Nichols (1981). In these approaches, the extent of each phase is computed by integrating the transport equation of a discrete variable accounting for the local distribution of phases in a cell (VOF) or a continuous signed distance to the air-water interface (LS). Free surface shapes of high complexity might be simulated, including free surface large deformation, breaking and merging. Level-set methods have also been extensively been applied to one-phase simulations (Di Mascio et al., 2007; Reliquet et al., 2013).

1.2.3.2 Front-tracking techniques

Among front-tracking approaches, Lagrangian methods occupy a special place as they do not necessarily require the use of any computational mesh. Fluid particles are followed in their trajectory and discretize the fluid continuum. The Smoothed Particle Hydrodynamic (SPH) method (Gingold and Monaghan, 1977) is one of them. It allows for the computation of highly complex free surface flows, for a high computational cost however, as done by Dalrymple et al. (2011) and Altomare et al. (2020). Again, one-phase and two-phase versions of the method exist.

Certain interface tracking methodologies, on the opposite, require a fixed grid, like the Marker-and-Cell (MAC) method of Harlow and Welch (1965), in which a Lagrangian description of the free surface is used. It was applied for example by Wang et al. (2007) for the computation of 3D waves. The related Particle-in-Cell (PIC) method should also be mentioned, that differs from MAC in the treatment of advection terms (Chen et al., 2018).

Other free surface tracking techniques make use of the Arbitrary Lagrangian-Eulerian (ALE) formalism. Contrary to previous approaches, a moving mesh is used that follows the movement of the interface. An implementation of the ALE method in the CFD code Code_Saturne (CS) is described in Ferrand and Harris (2021), and 2D and 3D applications including a vertical cylinder in regular waves are considered.

The use of these high-fidelity CFD models to simulate free surface flows over large temporal and spatial scales is limited, as already stated, by the large associated computational costs. These methods also suffer from possibly excessive numerical diffusion levels, hence they are not as accurate as the potential models to simulate wave propagation over large distances.

This explains why hybrid or coupled methods, either based on functional decomposition or domain decomposition, have been used to solve large scale wave-induced flows.

1.2.4 A review of coupling methods

1.2.4.1 Taxonomy of hybrid techniques

Among hybrid techniques previously applied to water waves propagation and wave-structure interaction simulation, that rely on the near-field/far-field distinction, different global approaches can be distinguished.

Physical assumptions made in both near-field and far-field models may differ: although in the majority of far-field models a potential flow is considered, in certain cases Euler equations are solved instead, allowing to represent rotational effects (Di Paolo et al., 2021). The scope of the current review is limited to studies involving the resolution of NS equations in near-field domain, although investigations have been reported that use potential methods of uneven accuracy levels and CPU costs to describe flows in both regions (Ferrant (1998), Bai and Eatock Taylor (2007)). When it comes to solving the near-field wave problem then, the diversity of NS numerical methods described above is reproduced in hybrid approaches.

Discrepancies are also related to the extent of numerical domains where the respective sets of equations are solved. Indeed, the use of a domain-decomposition (DD) method, as its name suggests, involves that in most of the global simulation domain the description of the flow is provided by only one model. Solvers thus exchange information at their coupled boundaries. On the other hand, in functional decomposition (FD) approaches, where variables of interest (namely velocity, pressure, free surface position or phase function) are decomposed into a part related to the incident (as well as, possibly, diffracted) wave field, and a complementary one taking into account the remaining wave-structure interaction phenomena, potential and NS equations are solved over fully overlapped domains. Nested domain-decomposition techniques are singular in that the small CFD domain of limited extent is enclosed in a wider far-field domain, thus it implies that the corresponding part of the far-field domain is not taken into account in the simulation. If near-field to far-field feedback is made possible, near-field variables should be imposed to the outer solver in the interior of its numerical domain.

A last criteria enabling to sort coupling strategies is whether simulation data are only transmitted from the far-field to the near-field model (one-way coupling), or if the opposite is also true (two-way coupling). A one-way coupling methodology enables a preliminary computation of the outer wave field, as near-field feedback is not provided during the simulation. In two-way coupling techniques, reflected, diffracted or radiated waves might be dealt with in the far-field model. Therefore it formally allows for a reduction of the near-field domain's size, as compared to one-way hybrid methods where wave scattered by a structure can only be simulated in the inner region. This also comes at the cost of extra

implementation choices and challenges, and possible stability issues. In the following, a literature review is conducted on the basis of this classification.

1.2.4.2 Functional decomposition based couplings

FD methods have been successfully applied to a number of wave-body interaction cases. The Spectral Wave Explicit Navier Stokes Equation (SWENSE) is one of the most prominent FD, also called perturbation, approach. Among numerous other works, it enabled the simulation of a bottom-mounted circular cylinder in regular nonlinear waves (Gentaz et al., 2004) as well as that of a captive buoy with a heaving skirt subject to plane regular and irregular multidirectional waves (Monroy et al., 2010). It consists of a combination of a fully nonlinear potential spectral model with a one-phase or two-phase (Li et al., 2021; Vukčević, 2016) Reynolds Averaged Navier-Stokes Equations (RANSE) solver (several models have been used). It should be noted that the far-field model only accounts for the incident wave field, due to the spectral formalism, in which only symmetrical or periodic domains can be represented. Hence, far-field potential calculation can be run prior to the viscous near-field one.

General considerations about FD methods, as well as an implementation with OceanWave3D as the comprehensive model to treat wave-body interactions are reported in Ducrozet et al. (2014). It should be mentioned that this technique permits all physical phenomena related to wave-body interactions, as well as nonlinear wave-wave and wave-bottom interactions. Therefore, it belongs to the class of "strong" couplings that can simulate large scattered wave fields away from the body. Nonlinear interactions between waves and uneven bottom, if not accounted for by the far-field solver, as well as nonlinear interactions between incident and scattered waves, are indeed described by the viscous CFD model without any restrictive hypothesis. In the SWENSE formalism, this means that the refined part of the RANSE mesh, in which the latter effects operate, should have its size adapted to their expected spatial extent. It is therefore very well adapted, in the context of wave-structure interaction, to the description of problems involving small bodies, in which incident flow is not disturbed much and viscous effects are predominant, while occurrence of diffraction and radiation phenomena are limited to the body's vicinity. Small body problems are characterized by large Keulegan-Carpenter numbers ($\mathrm{KC} = \frac{2\pi A}{D}$, where A is the incident wave amplitude and D the characteristic size of the structure). The larger the structure, the smaller the KC, and the larger the diffraction/radiation effects. To deal with this latter case in the SWENSE framework or with related methods, it is necessary to increase the size of the refined part of the RANSE grid to allow for physically accurate computations. This leads to growing mesh sizes and CPU time requirements, minimizing the gains brought about by the coupling. If the refined part of the RANSE grid is too small, waves are damped in an unphysical manner while traveling on coarser parts of the mesh. It would be interesting to compare the relative performances of FD methods and two-way DD ones on such cases, as in the latter nonlinear wave-wave

interactions are dealt with in the computationally less demanding far-field model.

A perturbation approach is used in Harris and Grilli (2012) to simulate wave-induced boundary layer flows, where a 2D FNPF-BEM solver is coupled to a 3D NS-LS model. Recently, Robaux (2020) and Robaux and Benoit (2022-submitted, in revision) proposed a FD model coupling a 2D in-house HPC potential model with a RANSE VOF solver of OpenFoam. The HPC formalism represents interactions of waves with possibly moving and surface-piercing structures in the potential flow model. In the mentioned work, only cases involving fixed 2D fully-submerged bodies were investigated. Therefore, it enables simulating incident, as well as the fully-nonlinear potential diffracted wave field. Thus, larger values of KC might be considered without an excessive penalty on computational cost, as long as viscous and turbulent effects on the scattered wave field are restricted to the vicinity of the body.

1.2.4.3 One-way coupling domain decomposition approaches

One-way DD coupling techniques, as they only require transfer of information from the far-field to the near-field model, are a lot easier to implement than two-way DD methods. For this reason, a large number of authors have applied them to wave-induced flows occurring in ocean or coastal engineering. Therefore, we do not intend to be exhaustive here, and only a few works related to wave-body interactions are presented.

Guignard et al. (1999) computed the shoaling of solitary waves on a mild slope through a BEM/VOF hybrid one-way 2D approach. Hildebrandt and Sriram (2014) studied pressure distribution on and vortex shedding behind a bottom-mounted vertical circular cylinder impacted by steep focused waves combining a FEM potential model and a commercial RANSE solver. Numerical results were compared to experimental ones. Similarly, Paulsen et al. (2014) used OceanWave3D and a VOF solver from OpenFoam to study wave loads on a surface-piercing cylinder standing for an offshore wind turbine foundation, under different wave conditions and bottom configurations. Using the same tool, Veic and Sulisz (2018) investigated pressure distribution from irregular breaking waves on a monopile with the same setup. A 3-hour storm was simulated in the potential model and the impact of the highest breaking wave was then numerically reproduced.

Note also that Robaux (2020) and Robaux and Benoit (2022-submitted, in revision) implemented both FD and one-way DD methods, and compared them on the case of waves diffracted by a submerged fixed body.

1.2.4.4 Two-way coupled methods

As not so many two-way coupled models have been reported so far, in this section the scope of considered applications is widened beyond wave-body interactions in finite water depth. Some of the earliest two-way hybrid approaches were reported for steady free surface problems. Campana et al. (1995) and Chen and Lee (1999) studied the flow past a

ship advancing at a constant speed using overlapping domain decomposition methods, with linear and nonlinear assumptions for the free surface boundary conditions, respectively. Guillerm and Alessandrini (2003) used a similar approach in the same context.

Iafrati and Campana (2003) computed wave-breaking 2D flows with a two-way coupled method, in which free surface is enclosed in the viscous top domain, while a Laplace equation on the potential is solved in a region underneath the latter. In this paper, a further distinction is established among two-way coupling methods, that we endorse and employ to describe and sort other two-way hybrid studies. For the sake of simplicity, we restrict the description to the case a single coupling region. Iafrati and Campana (2003) state that, depending on whether near-field and far-field numerical domains are overlapped or not, different sets of coupling transmission conditions should be specified on their common boundary(ies). In both situations, continuity of the velocity should be ensured on the near-field or common matching surface, therefore all components of the potential far-field velocity vector are sent to the near-field NS model to be used as Dirichlet boundary condition on the viscous velocity. If both domains overlap, a kinematic condition imposing the continuity of the normal velocity on the far-field boundary should be set. This amounts to a heterogeneous Neumann boundary condition on the velocity potential, thus the overlapping domain decomposition coupling is called "Neumann type" (NT) coupling. If, alternatively, a common coupling boundary is used, the velocity continuity condition already mentioned is complemented by a normal stress continuity condition, through which pressure from the RANSE solver is imposed to the outer potential model. By integrating Bernoulli's equation, a Dirichlet condition on the velocity potential is obtained on the unique coupling boundary ("Dirichlet type" coupling (DT)). Note that nothing is said about the free surface, as it is totally enclosed in the viscous domain. Whatever the coupling type, an iterative time-stepping procedure is followed in Iafrati and Campana (2003) to enforce the continuity requirements.

Lachaume et al. (2003) briefly discuss two-way coupled simulations of a solitary wave shoaling over a plane slope, in which the free surface is described in both models. The BEM model of Grilli et al. (2001) is combined with a VOF instance, but very few results are displayed, and for the considered case a one-way coupling approach seems to be sufficient. Greco et al. (2002) applied a DT coupling between BEM and VOF models to dam-breaking and water loading on deck structure 2D problems involving complex free surface geometries. Again, and as for all the remaining studies addressed in this section, free surface is split between near-field and far-field wave models. Alongside with experimental results, a comparison of DT and NT coupling VOF-based techniques is realized in Greco (2002) in the same context. The NT coupling, albeit less computationally efficient than the DT coupling, is found to successfully simulate a wave-induced flow oriented towards the outer region, whereas the DT coupling fails. A NT strategy is thus retained and described in detail in Colicchio et al. (2006), involving two-phase BEM and NS-LS models. Further explanations are given as to the advantages of the NT technique over the DT one, in terms of allowed flexibility of spatial discretizations in each model. It should be noted

that the NT coupling procedure differs from the one presented in Iafrati and Campana (2003) as information on free surface position and orientation, but also pressure values are exchanged between coupled models. This way a Neumann boundary condition on the time derivative of the potential in the BEM model is available. An intrinsic algorithm is used for time integration, in which time stepping schemes of BEM and NS-LS models are linked. At several instants per time step, both sub-domains successively exchange coupling variables. This is made possible by the fact that they share the same time-step size. Siddiqui et al. (2018), from the same research group, used a HPC-VOF DT coupling method to simulate the 2D behavior of a damaged ship section in forced heave motion. Coupled models still share the same time step size, but time marching is done separately and coupling information is exchanged only once per time step through the matching boundary. Following the work of Colicchio et al. (2006), a NT coupling involving HPC and single phase NS-LS models is presented in Hanssen (2019) and applied to the 2D propagation of regular waves.

A 2D BEM-VOF NT hybrid model is presented in Kim et al. (2010), and successfully applied to nonlinear regular and irregular wave propagation problems. It features several noteworthy characteristics. Indeed, both models use different spatial and temporal resolutions, such that the BEM time step equals an integer multiple N of the NS-VOF one. Hence, exchange of coupling data at both ends of the overlapping region occurs once every N VOF time steps, and the coupling procedure is not iterative. Moreover, the BEM free surface in the latter part of the domain is relaxed towards the VOF solution to ensure continuity. Changes made to the velocity potential at the free surface account for this modification of the free surface shape. Hybrid simulation results are compared to those of VOF-only computations and equivalent accuracy levels are observed, for a fraction of the computational time.

Another 2D BEM-VOF model similar to that of Kim et al. (2010) is proposed by Guo et al. (2012). As in Kim et al. (2010), a low-order in space fully nonlinear potential model is coupled with a NS-VOF solver. Verification of the coupled model is done with regular wave propagation and full reflection cases, prior to its application to the simulation of regular nonlinear wave impacts on a fixed horizontal plate. A non-overlapping DT coupling is implemented by Zhang et al. (2013) and tested on 2D dam-break and solitary wave propagation over constant depth cases. Lu et al. (2017) is one of the few reported 3D two-way couplings. It is of Neumann type, combines potential and viscous solvers both based on Finite Volume formalism and relies heavily on the OpenFoam toolbox. 2D cases of solitary wave propagation, regular waves forces on a fixed partly-submerged barge, regular shallow-water waves shoaling and breaking on a slope are investigated, whose results are compared to theoretical and experimental references. At last, a qualitative study of the motion and subsequent radiated wave field of a freely falling 3D object is presented. This last article might well be the one with which the present study is the most closely related. Choi (2019) implemented a version of the SWENSE method in which the scattered wave field is simulated using a domain-decomposition method, to study diffraction-radiation

problems.

Two-way hybrid models involving shallow-water models and more comprehensive RANS models have been developed and successfully applied to 2D shallow-water wave flows by Sitanggang and Lynett (2010) and Pringle et al. (2016). Mintgen and Manhart (2018) used a Shallow-Water Equations (SWE) 2D solver combined with a VOF module for surface capturing in 3D in OpenFoam to simulate wave propagation and wave-structure interactions. It should be noted that in this work, the direction of the transfer of coupling information depends on the instantaneous nature of the flow.

Several authors have investigated hybrid methods combining a potential model and a meshless Lagrangian NS solver. Sueyoshi et al. (2007) simulated 2D wave-body interactions with a BEM model and a Moving Particle Semi-Implicit (MPS) method, with a top-bottom domain decomposition approach inspired from that of Iafrati and Campana (2003). A novel moving overlapping zone is implemented in Sriram et al. (2014) to build a NT hybrid method between a FEM potential model and an Improved Meshless Local Petrov Galerkin method with Rankine source solution (IMLPG_R) to simulate propagation and breaking of 2D waves. Similarly, Yan and Ma (2017) simulate 2D non-breaking focused waves. Verbrugghe et al. (2018) built a two-way coupling strategy in which the numerical domain of OceanWave3D, the large scale fully-nonlinear potential model, encloses a small SPH (DualSPHysics) domain. Horizontal velocity is transmitted to SPH boundaries. The two-way coupling is however not complete, as only free surface position is transmitted to the potential model from the SPH instance. The method is verified with regular wave propagation cases, then applied in 2D to the simulation of a fixed oscillating water column and a floating box in waves. 3D simulations of a heaving cylinder in waves presented in Verbrugghe et al. (2019) are realized with a one-way coupling approach only.

Hamilton and Yeung (2011) simulated diffraction of linear plane waves by a vertical cylinder with a singular two-way coupling method that could be considered of Dirichlet type. Shell functions in a polar coordinate system are used to characterize a linear outer wave-induced potential flow coupled with an inner one-phase viscous solution, through a vertical cylinder matching boundary. It should be noticed that the NS solver also makes use of linearized free surface boundary conditions. Kemper et al. (2019) developed a DD method in which a small OpenFoam NS-VOF domain is nested in a larger FDM OceanWave3D domain. It was applied to 2D wave propagation over a submerged bar. Recently, a somewhat different 2D-3D coupling strategy involving OpenFoam instances was reported by Di Paolo et al. (2021). Plane wave generation and propagation is done in a NS-VOF two-dimensional vertical (2DV) domain while interaction with structures is dealt with using the same solver, but accounting for 3D effects.

1.3 Objectives of the present work

From the literature review, it appears that although 3D one-way DD methods and FD methods combining potential and NS solvers have been successfully applied to a number of different wave-body interaction problems, the same can not be said of two-way DD techniques. The vast majority of investigations indeed involve 2DV domains, and to the author's knowledge, the only 3D case reported - the sinking semi-submersible platform in the study of Lu et al. (2017) - was not compared to reference results. Hence, there seems to be room for improvements and validated applications to 3D cases.

In the current work, a 3D two-way coupled model is developed, with the goal of applying it to wave-interaction problems of large spatial and temporal scales involving fixed structures. To that end, attention is paid to flexibility of the designed hybrid strategy and suitability for the simulation of various wave-induced flows. Accuracy and stability properties of the simulated cases are investigated in detail, as well as several related numerical challenges. Parallelisation of the hybrid procedure is ensured, so that the method can be applied to 3D cases of potential interest for the engineer. Complex model layouts are considered, involving more than one instance of each code.

1.4 Structure of the PhD report

The remaining of this PhD report is organized as follows:

- In chapter 2, the coupling procedure developed during the PhD is presented, which combines the fully-nonlinear potential flow solver *seine3d* with the all-purpose CFD code *CS*. Short summaries of the main characteristics of these codes are provided. The hybrid method itself is then described in detail, and different possible implementations are distinguished on certain of its aspects. The main coupling parameters are listed.

- In chapter 3, a verification study dealing with the propagation of a plane 2D solitary wave through several coupled code instances is reported. It allows a first investigation of the hybrid model's behavior, and also enables to arbitrate, for part, the previously-mentioned implementation choices. The solitary wave simulations are assessed in terms of conservation of the wave properties. Two relative wave heights are considered.

- In chapter 4, results of regular nonlinear waves 2DV simulations with the hybrid method are presented and compared to computations involving one model at a time. Performances of each model, in terms of accuracy, are assessed and a partial sensitivity analysis is realized to select values for certain numerical parameters of the coupled simulations. Two values of the wave steepness are investigated, and the challenges related to highly nonlinear waves are highlighted.

- A first 3D wave-structure interaction application is described in chapter 5, where the diffraction by a vertical bottom-mounted cylinder of an initially plane solitary wave of moderate relative height is investigated. Possible issues exclusively related to 3D simulations are discussed.

- Finally, in chapter 6, diffraction of nonlinear regular waves by a vertical cylinder is studied. Results are compared, in terms of spectral analysis of the free surface elevation and the normalized horizontal force on the cylinder, to those of an experimental measurement campaign, the Wave loads and soil support for extra large monopiles (WAS-XL, Dadmarzi et al. (2019)).

- Concluding remarks and perspectives are reported in chapter 7.

Chapter 2

Description of BEM-VOF coupling strategy

Après une brève description de chacun des deux codes de calcul, ce chapitre met en œuvre une description détaillée de la stratégie retenue pour le couplage du solveur potentiel complètement non-linéaire seine3d *avec* CS*, qui résout les équations de Navier-Stokes. L'extraction de variables physiques d'intérêt - vitesse, position de la surface libre - dans chacun des deux types de domaines numériques est présentée, de même que le traitement des champs de données extraits et leur utilisation dans le modèle auquel ils sont destinés. Dans chacun des codes en effet, la connaissance du champ de vitesse à proximité de la surface libre requiert certaines précautions. De plus, l'approche de capture de la surface libre mise en œuvre dans le module Volume of Fluid utilisé dans* CS *ne permet qu'un accès indirect à la position de la surface libre, suivant une méthode décrite dans ce chapitre. Les différences existant entre modèles en termes de phases fluides simulées, de discrétisation spatiale mais aussi temporelle contraignent par ailleurs les choix opérés pour le couplage. Deux valeurs de pas de temps sont en effet utilisées dans le couplage, ce qui implique une nécessaire interpolation des conditions limites transmises par* seine3d *à* CS *entre deux instants simulés dans* seine3d*. La coïncidence des surfaces libres dans la zone de recouvrement des domaines numériques, qui conditionne la stabilité des calculs, est également abordée. Enfin, des notions relatives à la parallélisation des calculs sont introduites.*

2.1 Description of the fully-nonlinear potential flow solver *seine3d*

Here we intend to give a brief description of the main physical, mathematical, and numerical features of the fully-nonlinear potential flow solver *seine3d*, whose name stands for *Simple Efficient Inviscid Numerical Environment*. It relies on the higher-order BEM resolution of a boundary integral problem. It serves as the far-field flow solver in the two-way hybrid strategy implemented in the current work. For a more in-depth presentation of this model, the reader is referred to the already mentioned articles of Grilli et al. (2001) and Harris et al. (2022), which this section heavily relies on.

2.1.1 Governing equations and boundary integral formulation

As stated above, we consider the irrotational flow of an icompressible and inviscid fluid as a physical model for wave-induced water flows. Mass conservation in the fluid domain Ω yields the following Laplace equation:

$$\nabla^2\phi = 0 \qquad \text{in } \Omega \tag{2.1}$$

$$\mathbf{u} = \nabla\phi \qquad \text{in } \Omega \tag{2.2}$$

with ϕ the velocity potential and $\mathbf{u}$ the flow velocity in Ω. From Green's second identity, it comes that equation 2.1 is changed into a Boundary Integral Equation (BIE) to be verified on the domain boundary Γ, at a collection of collocation points $\mathbf{x}_i$ $(i = 1, \ldots, N_\Gamma)$,

$$\alpha(\mathbf{x}_i)\phi(\mathbf{x}_i) = \int_\Gamma \left[\frac{\partial\phi}{\partial n}(\mathbf{x})G(\mathbf{x}-\mathbf{x}_i) - \phi(\mathbf{x})\frac{\partial G}{\partial n}(\mathbf{x}-\mathbf{x}_i)\right] \mathrm{d}\Gamma, \tag{2.3}$$

where α is the interior solid angle made by the boundary at $\mathbf{x}_i$, that equals 2π if the surface is smooth, $\mathbf{n}$ the outwards normal vector to the boundary at point $\mathbf{x}$ and G the 3D free space Green's function of Laplace's equation, based on the distance $r_i = \|\mathbf{x}-\mathbf{x}_i\|$ from point $\mathbf{x}_i$ to point $\mathbf{x}$ on the boundary. Green's function satisfies the following relations:

$$G(\mathbf{x}-\mathbf{x}_i) = \frac{1}{4\pi\, r_i} \tag{2.4}$$

$$\frac{\partial G}{\partial n}(\mathbf{x}-\mathbf{x}_i) = -\frac{(\mathbf{x}-\mathbf{x}_i)\cdot\mathbf{n}}{4\pi\, r_i^3} \tag{2.5}$$

Under the same set of assumptions, the integrated form of the momentum conservation equation reduces to the generalized unsteady Bernoulli equation, which reads, at all times:

$$\frac{\partial \phi}{\partial t} = -gz - \frac{1}{2}\nabla\phi \cdot \nabla\phi - \frac{p}{\rho} \qquad \text{in } \Omega \tag{2.6}$$

with g the gravitational acceleration, z the vertical coordinate, p the fluid pressure assumed to be constant on the free surface, and ρ the fluid density. Equation 2.6, yields the dynamic free surface boundary condition prescribed on the air-water interface, alongside with a kinematic free surface boundary condition expressing that free surface Γ_f is advected with the flow,

$$\frac{\delta \mathbf{r}}{\delta `t} = \frac{\partial \mathbf{r}}{\partial t} + \mathbf{u} \cdot \nabla \mathbf{r} = \mathbf{u} = \nabla\phi \qquad \text{on } \Gamma_f \tag{2.7}$$

where $\dfrac{\delta \mathbf{r}}{\delta t}$ is the material derivative of a point $\mathbf{r}$ located on and thus staying on the free surface.

The nonlinear equation 2.6, once integrated in time, yields a Dirichlet condition on ϕ on the free surface whose geometry is computed by integrating equation 2.7. Other boundary conditions include homogeneous Neumann conditions on ϕ on the vertical lateral faces and bottom region enclosing Ω, expressing the impermeability of these walls. In certain cases, these are complemented by a heterogeneous Neumann condition on a part of the domain dedicated to wave generation, either vertically fixed or moving. Wave kinematics from various waves theories might indeed be enforced on a vertical boundary, or alternately a realistic wavemaker motion might be reproduced. See Grilli and Horrillo (1997) for details about wave generation. As only far-field waves are investigated in *seine3d* in the current work, there is no need of representing submerged or surface-piercing, fixed or floating bodies in Ω, thus we have a complete set of boundary conditions available, ensuring the well-posedness of the problem. Given that suitable initial conditions are provided, as well as spatial discretization of the boundaries and a time-stepping strategy, simulation of potential wave flow through time is made possible.

2.1.2 Time integration scheme

The resolution of the BIE at any time instant t yields both ϕ and its normal derivative ϕ_n at every node $\mathbf{x_i}$ of the free surface. Time integration of free surface boundary conditions 2.6 and 2.7 is then needed to advance the solution (geometry alongside with boundary conditions) in time. This is done following a Mixed Eulerian-Lagrangian (MEL) method, originally introduced by Longuet-Higgins and Cokelet (1976). Here another hypothesis is made as to the nature of the flow and the geometry of the free surface. The latter is indeed assumed to be single-valued. Again as the most complex interface shapes are expected in the near-field domain treated with *CS*, this should have a negligible influence on the range of application of the hybrid method. Thus we opt for a semi-Lagrangian time updating

scheme for Γ, for which free surface nodes are only allowed to move vertically. This makes mesh handling easier. The material derivative then becomes:

$$\frac{\delta}{\delta t} = \delta_t = \frac{\partial}{\partial t} + \frac{\partial \eta}{\partial t}\frac{\partial}{\partial z} \tag{2.8}$$

where $\eta = \mathbf{r} \cdot \mathbf{k}$ denotes the vertical free surface elevation, $\mathbf{k}$ being the vertical unit vector. Making use of this formalism in equations 2.6 and 2.7 leads to:

$$\frac{\delta \eta}{\delta t} = \frac{\partial \phi}{\partial z} - \frac{\partial \phi}{\partial x}\frac{\partial \eta}{\partial x} - \frac{\partial \phi}{\partial y}\frac{\partial \eta}{\partial y} \qquad \text{at } z = \eta \tag{2.9}$$

$$\frac{\delta \phi}{\delta t} = -g\eta - \frac{1}{2}\nabla\phi \cdot \nabla\phi + \frac{\partial \eta}{\partial t}\frac{\partial \phi}{\partial z} \qquad \text{at } z = \eta \tag{2.10}$$

It should be noted that $(\partial\eta/\partial x, \partial\eta/\partial y)$ might be rewritten using components of the outward normal vector on Γ_f, $\mathbf{n} = (n_x, n_y, n_z)$, yielding $(-n_x/n_z, -n_y/n_z)$.

A third-order explicit Runge-Kutta scheme, inspired from that of Gottlieb (2005), is chosen to integrate equations 2.9 and 2.10 in time. With f standing for either η or ϕ, the following relations are established:

$$\begin{aligned} f^{(1)} &= f^{(n)} + \Delta t \left(\delta_t f^{(n)}\right) \\ f^{(2)} &= \frac{3}{4} f^{(n)} + \frac{1}{4}\left(f^{(1)} + \Delta t(\delta_t f^{(1)})\right) \\ f^{(n+1)} &= \frac{1}{3} f^{(n)} + \frac{2}{3}\left(f^{(2)} + \Delta t(\delta_t f^{(2)})\right) \end{aligned} \tag{2.11}$$

where Δt is the time step. Alongside with ϕ and ϕ_n, their respective time derivatives might also be needed if one wants to use another time-stepping scheme, such as an explicit Taylor series expansion (again, see Grilli et al. (2001) for example). Besides this, computation of forces and moments exerted on structures is realized through pressure integration on the body's surface (obtained from Bernoulli's equation), therefore wave-structure interaction studies also require the resolution of a second Laplace equation for ϕ_t. As only third-order Runge-Kutta scheme is considered in the present work, and no structure is considered in the potential region, this is not needed.

Additionally, it should be noted that a careful computation of the tangential derivatives of ϕ is needed on Γ_f to express certain terms of 2.9 and 2.10. For brevity reasons, the discretized equations are not presented here.

2.1.2.1 Discretization of boundaries and solver type

Spatial discretization of the numerical domain boundaries relies on B-spline elements, described in depth in Harris et al. (2022). As for the considered cases the number of grid

nodes N_Γ remains lower than 2000, the use of a direct LU solver was preferred for the resolution of the algebraic system of BIEs. In Grilli et al. (2001), it is indicated that this solver is more efficient than an iterative one like the Generalized Minimal Residual (GMRES) for such grid sizes, as a good part of the computational burden is related to the assembling of the system matrix.

2.2 Description of the NS solver *Code_Saturne*

In this section, we describe the main characteristics of the NS solver *Code_Saturne* used to describe complex near-field wave-induced flows in coupled problems. In the rest of this document, it will be referred to as *CS*. *CS* is an open-source, multi-purpose CFD code aimed at solving the full NS equations, for either incompressible or weakly compressible flows, through a Finite Volume approach with co-located variables. Equations are integrated in time according to a predictor/corrector method. The code deals with structured as well as unstructured meshes and was recently enriched with an algebraic VOF module for interface capturing purposes in multiphase simulations. Several turbulence models are available to be used with RANS or LES formalisms, although in this work, due to the high Reynolds number at stake, no turbulence model is used so that turbulence is neglected. Also, as will be detailed later, structured grids are used exclusively. The VOF module was recently added to *CS* alongside with the release of version *5.0.0* in 2017. All *CS*-based developments reported in this document rely on the stable version *6.0.0*.

2.2.1 The Navier-Stokes model

If the gravity is the only external force at work, the NS equations for continuity and momentum respectively write:

$$\frac{\partial \rho}{\partial t} + \nabla \cdot (\rho \mathbf{u}) = 0 \tag{2.12}$$

$$\frac{\partial \rho \mathbf{u}}{\partial t} + \nabla \cdot (\rho \mathbf{u} \otimes \mathbf{u}) = -\nabla p + \nabla \cdot \mathbb{T} + \rho \mathbf{g} \tag{2.13}$$

with ρ the fluid density, $\mathbf{u}$ the velocity, $\rho\mathbf{u}$ the volume momentum quantity, and $\mathbb{T}$ the deviatoric stress tensor while $\otimes$ is the tensor product. Note that surface tension is neglected. For simplicity, possible additional source terms are not taken into account. Assuming a Newtonian fluid, $\mathbb{T}$ can be written as follows:

$$\mathbb{T} = \mu \left[\nabla \mathbf{u} + \nabla \mathbf{u}^T \right] - \frac{2}{3} \mu \nabla \cdot \mathbf{u} \, \mathbb{1} \tag{2.14}$$

where μ is the dynamic viscosity and $\mathbb{1}$ the identity tensor.

2.2.2 VOF model description

The VOF method enables to simulate multiphase flows with a one-fluid formalism, by describing the phase content of any fluid region from volume fractions of the different phases. In the context of wave-induced free surface flows, only two immiscible phases are considered, namely air and water. Hence, α is defined as the volume fraction of air, or

void fraction.

$$\alpha = \frac{\text{air volume in a domain } \Omega}{\text{volume of the domain } \Omega} \tag{2.15}$$

Using equation 2.15, linear mixture properties laws are established so that ρ and μ are continuously defined throughout the fluid. Subscripts $_{water}$ and $_{air}$ designate respective phases.

$$\rho = \alpha\rho_{air} + (1-\alpha)\,\rho_{water} \tag{2.16}$$

$$\mu = \alpha\mu_{air} + (1-\alpha)\,\mu_{water} \tag{2.17}$$

Unless otherwise stated, the density values are set to $\rho_{water} = 1025\ \mathrm{kg\,m^{-3}}$ and $\rho_{air} = 1\ \mathrm{kg\,m^{-3}}$ for the whole study, while the dynamic viscosity values are $\mu_{water} = 1\times10^{-3}\ \mathrm{Pa\,s}$ and $\mu_{air} = 1\times10^{-5}\ \mathrm{Pa\,s}$. Assuming that both ρ_{water} and ρ_{air} are constant, equation 2.12 for mass conservation writes:

$$\begin{aligned} &\frac{\partial\big(\alpha\rho_{air} + (1-\alpha)\rho_{water}\big)}{\partial t} + \nabla\cdot\big(\,[\alpha\rho_{air} + (1-\alpha)\rho_{water}]\,\mathbf{u}\big) = 0 \\ &\text{thus}\quad \big(\rho_{air} - \rho_{water}\big)\left[\frac{\partial\alpha}{\partial t} + \nabla\cdot(\alpha\mathbf{u})\right] + \rho_{water}\nabla\cdot\mathbf{u} = 0 \end{aligned} \tag{2.18}$$

The incompressible flow constraint of $\nabla\cdot\mathbf{u} = 0$, once injected in equation 2.18, leads to the following system, which includes the transport equation of α:

$$\nabla\cdot\mathbf{u} = 0 \tag{2.19}$$

$$\frac{\partial\alpha}{\partial t} + \nabla\cdot(\alpha\mathbf{u}) = 0 \tag{2.20}$$

For an easier definition of boundary conditions, the relative pressure $p^* = p - \rho_{air}\mathbf{g}\cdot\mathbf{x} - p_0$ is introduced, where p_0 is the reference pressure at a fixed arbitrary location. However for the sake of clarity, $p*$ is denoted p hereafter.

Finally the VOF model comes down to the three following equations:

$$\frac{\partial\rho\mathbf{u}}{\partial t} + \nabla\cdot(\rho\mathbf{u}\otimes\mathbf{u}) = -\nabla p + \nabla\cdot(\mathbb{T}) + (\rho-\rho_{air})\mathbf{g} \tag{2.21a}$$

$$\nabla\cdot\mathbf{u} = 0 \tag{2.21b}$$

$$\frac{\partial\alpha}{\partial t} + \nabla\cdot(\alpha\mathbf{u}) = 0 \tag{2.21c}$$

Note that expanding the instationary term $\dfrac{\partial\rho\mathbf{u}}{\partial t}$ as well as the stress tensor $\mathbb{T}$ in equation 2.21a leads to:

$$\begin{aligned} \rho\frac{\partial\mathbf{u}}{\partial t} + \nabla\cdot(\rho\mathbf{u}\otimes\mathbf{u}) - \mathbf{u}\nabla\cdot(\rho\mathbf{u}) = &-\nabla p - (\rho-\rho_{air})\mathbf{g} \\ &+ \nabla\cdot\left(\mu\left[\nabla\mathbf{u} + \nabla\mathbf{u}^T\right] - \frac{2}{3}\mu\nabla\cdot\mathbf{u}\,\mathbb{1}\right) \end{aligned} \tag{2.22}$$

2.2.3 Time stepping scheme

Here a brief overview of the time-stepping method employed to advance the VOF solution in time is given. It is based on the fractional step scheme of Chorin (1968) and can be associated to the SIMPLEC scheme (Versteeg and Malalasekera, 2007). More details on this topic can be found in Archambeau et al. (2004). This last reference, alongside with *CS*'s theory guide (Code_Saturne development team, 2019), should also be used for an in-depth description of spatial discretization strategies, and the discretized equations are not recalled here for brevity.

2.2.3.1 Prediction step

A prediction step is conducted to integrate the momentum balance equation 2.22 with an explicit pressure gradient. Mass fluxes are also treated explicity, while an implicit form of the viscous diffusive term is used. This first step allows computing a predicted velocity field $\mathbf{u}^*$ for which mass conservation is not necessary realized, following:

$$\begin{aligned}
&\rho\frac{\mathbf{u}^* - \mathbf{u}^{(n)}}{\Delta t} - \nabla\cdot\left((\rho\mathbf{u})^{(n)}\otimes\mathbf{u}^*\right) - \mathbf{u}^*\nabla\cdot\left((\rho\mathbf{u})^{(n)}\right)\\
&= -\nabla p^{(n)} - (\rho-\rho_{air})\mathbf{g}\\
&+\nabla\cdot\left(\mu\left[\nabla\mathbf{u}^* + \nabla(\mathbf{u}^*)^T\right] - \frac{2}{3}\mu\nabla\cdot\mathbf{u}^*\,\mathbb{1}\right)
\end{aligned} \tag{2.23}$$

where Δt is the fixed or varying time step size, $^{()}$ stands for the considered time step, while $^{(n)}$ denotes the previous one. Note that ρ and μ are known at time (n) and will only be updated at the end of the time scheme loop, after the resolution of equation 2.21c.

2.2.3.2 Correction step

In this step, the pressure increment $\delta p = p^{(n+1)} - p^{(n)}$ is computed to enforce mass conservation and thus correct $\mathbf{u}^*$ to yield the final field $\mathbf{u}^{(n+1)}$. $^{(n+1)}$ represents the current computed time step. Considering a form of equation 2.22 in which non-pressure right hand-side terms are neglected, it becomes:

$$\frac{\mathbf{u}^{(n+1)} - \mathbf{u}^*}{\Delta t} = -\frac{1}{\rho}\nabla\delta p \tag{2.24}$$

$$\nabla\cdot\mathbf{u}^{(n+1)} = 0 \tag{2.25}$$

Taking the divergence of equation 2.25 leads to the following Poisson equation:

$$\nabla \cdot \mathbf{u}^* = \nabla \cdot \left(\frac{\Delta t}{\rho} \nabla \delta p \right) \tag{2.26}$$

from which $p^{(n+1)}$ then $\mathbf{u}^{(n+1)}$ are deduced.

2.2.3.3 Time integration of the scalar transport equation

The last step in the time-stepping procedure consists in the time integration of the scalar transport equation on α. To that end, an Implicit Euler scheme is selected.

$$\frac{\alpha^{(n+1)} - \alpha^{(n)}}{\Delta t} + \nabla \cdot (\alpha \mathbf{u})^{(n+1)} = 0 \tag{2.27}$$

With $\alpha^{(n+1)}$ available, it is then possible to get updated fluid properties $\rho^{(n+1)}$ and $\mu^{(n+1)}$ as well as mass fluxes $(\rho \mathbf{u})^{(n+1)}$ that are ready to be used in the next time step.

To compute the advection term of equation 2.27, various schemes might be selected in *CS*, namely the *Switching Technique for Advection and Capturing of Surfaces* (STACS, Darwish and Moukalled (2006)), the modified-*High Resolution Interface Capturing scheme* (M-HRIC, Muzaferija (1999)) and the modified-*Compressive Interface Capturing Scheme for Arbitrary Meshes* (M-CICSAM, Zhang et al. (2014)).

All of them rely on the principle of blending a very compressive scheme and a high-resolution diffusive scheme, on the basis of a weighting factor that is a function of the Courant number and other local conditions. The idea is to keep α from taking unphysical values outside of the range $[0; 1]$ while also limiting interface diffusion.

In the current study, a version of the M-CICSAM scheme of Zhang et al. (2014) is used. Boundary conditions needed to fulfill time integration are described in detail in Archambeau et al. (2004).

2.3 General strategy for a two-way coupling based on overlapping subdomains

2.3.1 General considerations

For the sake of clarity, we restrict the description of the coupling methodology to the simplest case of one instance of *seine3d* being associated with one instance of *CS*. Applications featuring several instances of one or either models, which are an available feature of the present coupling implementation, are treated in chapter 3 and beyond. For the same reason, figures illustrating the coupling procedure for two-dimensional (2D) situations will be preferred, keeping in mind that extension to three dimensions (3D) is most of the time straightforward.

Potential and viscous domains are coupled through the mutual exchange of computational variables at their coupled boundaries. Certain *CS* computational fields (void fraction and/or velocity) may also optionally be modified in the computational volume as well, through source terms added to the corresponding governing equations 2.21a, 2.21b, and 2.21c, based on values extracted in the interior of the *seine3d* domain. These optional source terms were nevertheless found not necessary to the accuracy and stability of hybrid computations, therefore they are not further mentioned in the description of the coupling strategy. However, as they are needed for wave generation and damping in *CS*-only simulations, a description is done is section 4.4.1 in this context. Velocity and free surface position are the exchanged physical variables, but it should be noted that the latter is not a direct outcome of a NS-VOF simulation, where a free surface capturing scheme is used. By contrast, free surface geometry is explicitly known in the potential code. Raw coupling information extracted from one model should thus be processed and adapted to the other model's requirements prior to being used in the coupling procedure, as both models employ different spatial and temporal discretizations, as well as different representations of the free surface.

2.3.2 Selected type of two-way coupling

As stated above, Iafrati and Campana (2003) make a distinction between two different types of two-way coupling: Dirichlet-type coupling and Neumann-type coupling, depending on whether viscous and potential domains partially overlap or not. Whereas in both methods velocity is specified on the coupled boundary of *CS* through a Dirichlet boundary condition on the water phase, coupling strategies differ in the type of coupling boundary condition used in *seine3d*, as their names suggest.

In this work we chose to implement a NT coupling, given that resolving the Bernoulli equation for the velocity potential on *seine3d*'s coupled boundary is not needed, hence making implementation easier at first sight. Besides, higher stability of the NT coupling as compared to DT was reported by Colicchio et al. (2006).

2.3.3 Overlapping subdomains

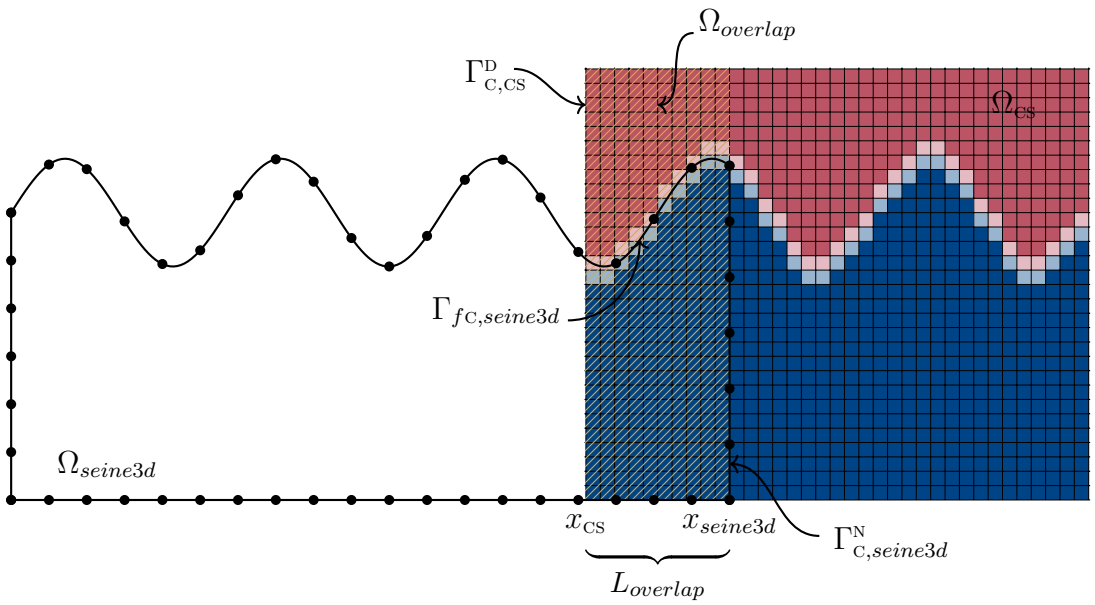

Figure 2.1: Coupled domains and related boundaries. Blue *CS* cells are cells filled with water, while red cells are full of air. Pale blue and pale red cells contain a mix of the two phases.

A coupling strategy requiring BEM and VOF domains to partially overlap is employed in this study, as illustrated in figure 2.1. The associated overlapping region $\Omega_{overlap}$ is bounded by coupling boundaries $\Gamma^{\mathrm{D}}_{\mathrm{C,CS}}$ and $\Gamma^{\mathrm{N}}_{\mathrm{C},seine3d}$ with D standing for a Dirichlet boundary condition on water velocity on *CS* side and N for a Neumann boundary condition on the velocity potential on *seine3d* side. $\Gamma_{f\mathrm{C},seine3d}$ is the part of $\Gamma_{f,seine3d}$ that receives a free surface position signal from *CS* during the coupling process. As stated above, void fraction and velocity fields may also be modified in *CS* in the volume of $\Omega_{overlap}$ through source terms. Coupling boundary conditions for this type of coupling are recalled in the following system and are described in detail in the next sections.

$$\begin{aligned} \mathbf{u}_{\mathrm{CS}} &= \mathbf{u}_{seine3d} && \text{at } x = x_{\mathrm{CS}} \\ \mathbf{u}_{\mathrm{CS}} \cdot \mathbf{n}_{seine3d} &= \frac{\partial \phi}{\partial n} && \text{at } x = x_{seine3d} \end{aligned} \tag{2.28}$$

x_{CS} and $x_{seine3d}$ designate the location of both ends of the overlapping region, as shown in figure 2.1. In this 2D representation, x axis stands for horizontal axis, z axis for the vertical one.

2.4 Velocity matching at coupled boundaries

2.4.1 Wave generation in the VOF model through boundary conditions

In the collocated Finite Volume formulation of *CS*, boundary conditions are needed at the centers of boundary faces. Let $\Gamma^{\mathrm{D}}_{\mathrm{C,CS}}$ represent the set of boundary faces involved in the coupling. *CS* mesh being fixed, boundary face center coordinates are extracted once at the beginning of a calculation and sent to the coupled *seine3d* instance. Elements involved in the construction of this boundary condition are recalled in figure 2.2. At each *CS* iteration, water velocity and void fraction boundary conditions on $\Gamma^{\mathrm{D}}_{\mathrm{C,CS}}$ are generated from the variables $\mathbf{u}_{seine3d}$ and $\eta_{seine3d}$ sent by *seine3d*. $\Gamma^{\mathrm{D}}_{\mathrm{C,CS}}$ boundary surface is then split in two parts, each one corresponding to a given phase of the fluid and receiving its own set of boundary conditions. A Dirichlet boundary condition on the void fraction is employed in both phases to set the free surface vertical position. A rather rough way of specifying the void fraction field for a given boundary face is to set the void fraction value to 0.0 if its center, or the center of the boundary cell to which it belongs, is located below $\eta_{seine3d}$, and to 1.0 otherwise. This leads to an artificially sharp free surface field for *CS* in $\Omega_{overlap}$ near $\Gamma^{\mathrm{D}}_{\mathrm{C,CS}}$, contrasting with its diffuse nature elsewhere in the numerical domain, and it induces a loss of accuracy in free surface definition. Therefore, void fraction Dirichlet condition is set with a basic geometrical free surface reconstruction strategy. Free surface in the cell is, to a first approximation, horizontal, hence the volume of water in the cell and thus the void fraction value can be deduced from the distance from the cell floor to $\eta_{seine3d}$ if the latter is above the cell center in the case of a cell mostly filled with air or from the ceiling if the cell is mostly filled with water. A Dirichlet boundary condition on all velocity components in the water phase is used to generate waves in this study, as in a number of other VOF models. Several options are available for velocity in the air phase that are described later. The boundary value problem would not be complete without a condition on pressure. A homogeneous Neumann boundary condition on pressure is used in either part of $\Gamma^{\mathrm{D}}_{\mathrm{C,CS}}$, *i.e.* a zero normal pressure gradient is imposed which is the default behavior for pressure as implemented in the *Inlet* and *Symmetry* boundary conditions of *CS*.

The process is summarized for coupled variables in the following algorithm, where i stands for the *CS* coupled boundary face of interest, for which $\eta_{seine3d,i}$ is the vertical position of the free surface. $z_{i,cen.}$ is the adjacent cell center's vertical coordinate.

The boundary condition for velocity in the part of $\Gamma^{\mathrm{D}}_{\mathrm{C,CS}}$ that lies in the air phase can be imposed in different ways. Among the standard boundary conditions implemented in *CS*, the aforementioned *Inlet* and *Symmetry* are suitable for this task. One may also assign an arbitrary vertical velocity profile as Dirichlet condition on a *Inlet* type boundary. As explained in section 2.1, influence of air phase on the water phase outside of the vicinity of the simulated structures can be modeled by a constant atmospheric pressure imposed on the free surface. This assumption holds in the overlapping area belonging to both *CS* and

Algorithm 1 Dirichlet velocity and void fraction boundary condition on $\Gamma^{\mathrm{D}}_{\mathrm{C,CS}}$

for $i = 1$ to $card\left(\Gamma^{\mathrm{D}}_{\mathrm{C,CS}}\right)$ **do**
  if $z_{i,cen.} \leq \eta_{seine3d}$ **then**
    if $z_{i,cen.} \geq \eta_{seine3d} - \frac{dz}{2}$ **then**
      $\alpha_i \leftarrow \frac{\eta_{z_{i,cen.}+\frac{dz}{2}-seine3d,i}}{dz}$
    else
      $\alpha_i \leftarrow 0.0$
    end if
    $\mathbf{u}_i \leftarrow \mathbf{u}_{seine3d}(z = z_{i,cen.})$
  else
    Set velocity and void fraction boundary conditions for air phase
  end if
end for

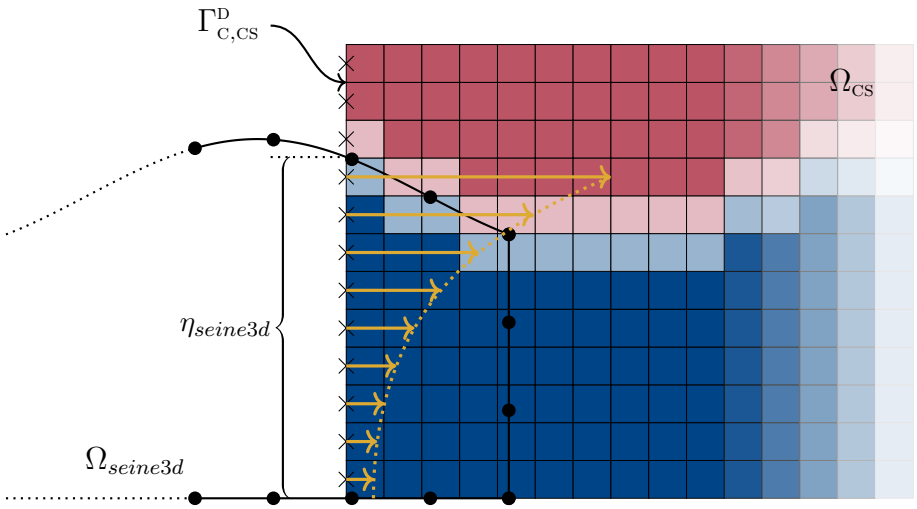

Figure 2.2: Dirichlet velocity boundary condition on the *CS* side of the overlapping area. Crosses mark the centers of the boundary faces belonging to $\Gamma^{\mathrm{D}}_{\mathrm{C,CS}}$. Yellow arrows represent the vertical profile of horizontal velocity $\mathbf{u}_{seine3d}$.

seine3d, if the latter is kept sufficiently far away from the bodies that may be placed in the water. Dynamic pressure effects and shear stresses applied by the air on the free surface may then be neglected as long as the velocity remains in a realistic range. The velocity field in the air phase is thus not of direct interest, at least in the outer region of the *CS* domain. It is therefore not mandatory to impose a lifelike vertical velocity profile at the edge of the domain but if this is to be done, we may think of an air velocity distribution verifying a no-slip condition on the free surface. Using a *Symmetry* boundary condition assigns a zero Dirichlet condition on the velocity component normal to the face and a homogeneous Neumann condition on its tangential components.

2.4.2 Processing of velocity extracted from the interior of the NWT domain

Velocity computation in the interior of the NWT domain is described in Fochesato et al. (2005). Such calculation can be prone to instabilities since singular integrals might have to be dealt with. If free surface boundary $\Gamma_{f,seine3d}$ comes too close to a *CS* boundary face center belonging to $\Gamma^D_{\mathrm{C,CS}}$ where *seine3d* interior velocity is sought, erroneous value is sent to *CS* as boundary condition in the current iteration of the coupling, and the simulation may diverge and fail. Future improvements based on the PART method of Hayami and Matsumoto (1994) could solve this problem. As *CS* boundary face centers are supposed to be aligned along vertical lines in a dense pattern - typically 20 cells or more per wave height - compared to the number of *seine3d* elements in a vertical, this situation happens frequently in the course of the simulation. It is then necessary to set a threshold value in *seine3d* for one or for all of the components of the internal velocity vector above which velocity is recalculated by an extrapolation from values at underlying *CS* face centers. A corrected velocity value is then sent to *CS*.

To extrapolate a value along the vertical, a polynomial is established for which the user can choose the order and the number of basis points. Using a least-squares estimation, a polynomial best fitted to the velocity values at underlying internal basis points is generated, that is latter used for extrapolation. Such extrapolation is done on all velocity components. *seine3d* vertical velocity profiles employed for coupling are stored in a log file so that it is possible to check their coherence and thus the validity of the extrapolation parameters while post processing the calculations results. It is to be noted that this one dimensional extrapolation strategy is valid only in the case of a *CS* mesh whose face centers are aligned along verticals. In the most general 3D case, such a mesh could be built from the (possibly non-uniform) vertical extrusion of an arbitrary conformal horizontal 2D mesh. *CS* meshes used for coupling should therefore comply with the latter rules. Figure 2.3 illustrates this upwards extrapolation process in the case of an horizontal internal velocity field featuring spurious values close to the free surface.

The same type of error occurs for a *CS* boundary face center from $\Gamma^D_{\mathrm{C,CS}}$ located too close to *seine3d* domain's bottom, in which case a similar but downwards extrapolation strategy is employed. If these precautions are sufficient for 2D vertical coupled simulations this is no longer true in 3D. Indeed, it appeared that in this latter case some coupled *CS* boundary face centers may lie too close to *seine3d* lateral vertical boundaries, leading to the same type of errors. It was then decided in this case to employ a simpler "nearest neighbor" extrapolation method for which the replacement velocity value is chosen from the closest interior point of *seine3d* with a velocity norm lower than the above mentioned threshold value.

Singularity errors related to velocity extraction in the interior of *seine3d* may also partially be treated from the tuning of some numerical parameters of *seine3d*. This model can indeed solve certain singularity problems thanks to subdivisions of boundary elements allowing

adaptive integration of the BIE kernel. The higher the number of subdivisions allowed to handle singularities, the closer to *seine3d* boundaries the coupled *CS* boundary face centers may lie without any divergence of the extracted coupling velocity values. This reduces the needed for the aforementioned extrapolation schemes, some of them having a low order convergence rate in space and therefore diminishes extrapolation errors. This comes at the cost of increased simulation times for *seine3d* and therefore for the coupled simulations as adaptive integration is time-consuming. A trade-off between accuracy and speed should then be sought so that subdivisions are used with parsimony.

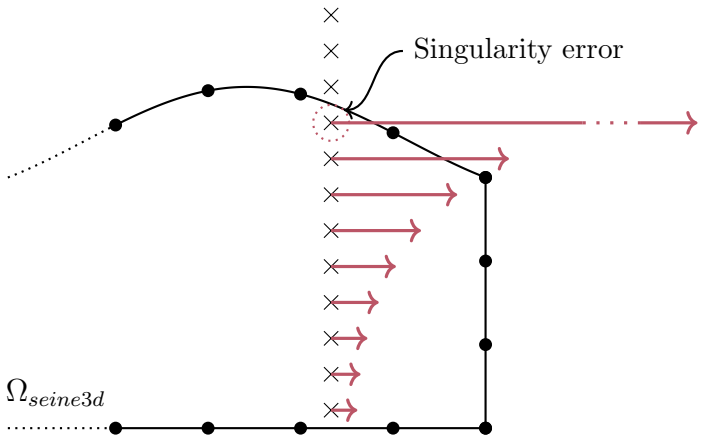

(a) Spurious horizontal internal velocity generated under free surface

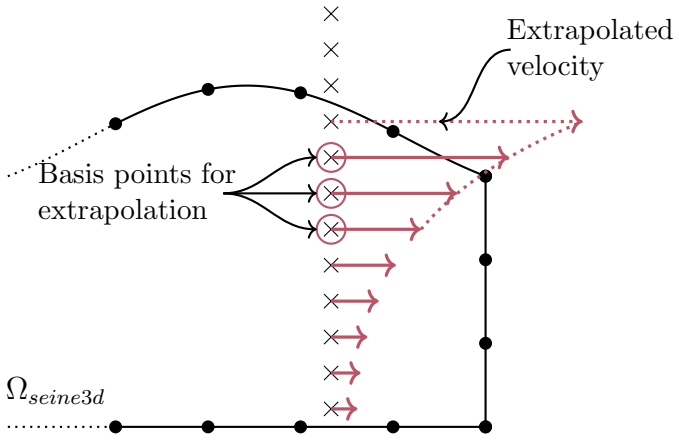

(b) Velocity correction through extrapolation

Figure 2.3: Calculation of horizontal internal velocity close to free surface in *seine3d* domain. Crosses mark the centers of boundary faces belonging to $\Gamma^{\mathrm{D}}_{\mathrm{C,CS}}$ where *CS* velocity is sought. Red arrows with full lines represent the partially unphysical vertical velocity profile of $u_{seine3d}$ while dashed ones illustrate the corrected velocity profile (by local extrapolation).

2.4.3 Velocity extraction in *CS* domain

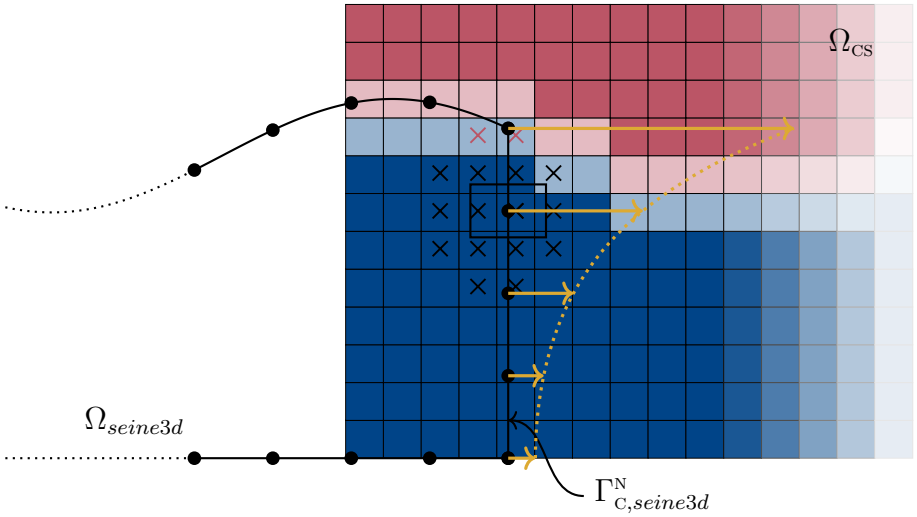

Figure 2.4: Neumann boundary condition on the velocity potential on *seine3d* side of the overlapping region. Crosses mark the centers of *CS* cells in the vicinity of a given *seine3d* node. *CS* cells too close to free surface to yield a correct velocity value bear red crosses. Rectangle stands for the selection box centered on the *seine3d* node. Yellow arrows represent the vertical profile of normal velocity $\mathbf{u}_{seine3d} \cdot \mathbf{n}$.

In this Neumann-type coupling methodology, *CS* produces a value for the normal derivative of the velocity potential $\frac{\partial \phi}{\partial n}$ on the lateral coupling boundary $\Gamma^{N}_{C,seine3d}$. As the physical assumptions made in *seine3d* are more stringent than those applying in *CS*, one should make sure that *seine3d* constraints of irrotational flow, negligible viscous effects and single-valued free surface are valid in the overlapping region. This predicament governs the location and horizontal extension of $\Omega_{overlap}$. Assuming these requirements are met, we can admit that *CS* velocity known at the location of a *seine3d* boundary node is that of a potential flow. Its projection along the normal direction to the local BEM panel produces a Neumann boundary condition on the potential.

seine3d's surface mesh moves with the fluid in a semi-Lagrangian fashion. Thus, contrary to *CS* boundary face centers belonging to $\Gamma^{N}_{C,CS}$ where *seine3d* velocity is calculated and whose position is fixed and known at the beginning of the simulation, velocity extraction in *CS* is done in locations varying with time. This poses serious efficiency issues to the coupling algorithm if not implemented adequately.

Thankfully, cell selection based on geometrical criteria is easily realized in *CS* and is described in figure 2.4. An array containing the coordinates of all the coupled *seine3d* nodes is sent to *CS* at every iteration of the coupling. A box of constant dimensions is built in *CS* domain around each *seine3d* node, the latter coinciding with the box's geometrical center. Cells whose center is included in the box are selected, and the associated velocity $\mathbf{u}_{CS}$ values, stored at cells centers, are saved, along with cell center coordinates. There may be several selected cells for each *seine3d* node, and multiple *seine3d* nodes associated

to the same *CS* cell in the case of 2D vertical simulations. Indeed, we shall place multiple nodes in the width of a *seine3d* domain even for two-dimensional calculations, whereas one cell occupying the entire width is sufficient for *CS* in that case.

Because of the absence of bijection between *seine3d* nodes and *CS* cells, and because *CS* cell extraction functions do not preserve cell order, arrays containing *CS* cell center coordinates and corresponding velocity values are sent back to *seine3d* in arbitrary order of the cells. It is to be noted that in the current state of the coupling methodology, no gradient calculation is conducted for coupled velocity extracted from *CS*. Then for every coupled *seine3d* node, the distance to every extracted *CS* cell center is computed, and $\mathbf{u}_{\mathrm{CS}}$ is taken as the value at the closest cell center. This sorting operation is realized in a single MPI process of *seine3d* (the one with root rank), so it is a blocking step for the simulation and its cost is therefore not negligible. Selecting the lowest possible number of *CS* cells using the smallest selection box is then of central interest. In practice, the choice of selection box size is left to the user, and it is straightforward in the case of a uniform Cartesian grid, for which the box should be slightly larger than a cell so that *CS* cells are always located.

VOF models are also known to suffer from the occurrence of spurious velocities close to the free surface. Therefore, if a coupled *seine3d* node lies in the area of mixed phases in *CS* domain, as illustrated by the red crosses on 2.4, the velocity extracted near its location may be unphysical. If it is the case, this will surely lead to the failure of the simulation. To avoid such issue, velocity is, by a way of precaution, not extracted in the region of mixed phases, but a large dummy value is rather sent to *seine3d*. The width of the region of mixed phases should be approximated by the user, in the form of an assumption on the vertical distance (or the number of cells) below the calculated free surface position within which the large dummy value is sent. This distance strongly depends on the selected void fraction advection scheme. In turn, when *seine3d* receives such dummy value, a vertical extrapolation procedure similar to that used for the internal velocity transmitted to *CS* is conducted. Basis points then needed for polynomial regression are *seine3d* nodes belonging to $\Gamma^{\mathrm{N}}_{\mathrm{C},seine3d}$ and located beneath the current node. Algorithm 2 summarizes the procedure. *threshold* value is only used to detect large dummy values requiring local extrapolation. Once $\mathbf{u}_{\mathrm{CS}}$ is known at all nodes located on $\Gamma^{\mathrm{N}}_{\mathrm{C},seine3d}$, it is projected on the local normal vector to generate a Neumann boundary condition on the potential.

Algorithm 2 Neumann boundary condition on $\Gamma^{\mathrm{N}}_{\mathrm{C},seine3d}$.

for $i = 1$ to $card\left(\Gamma^{\mathrm{N}}_{\mathrm{C},seine3d}\right)$ **do**
    Calculate distances from current node to every extracted CS cell center
    Get closest CS cell center and associated $\mathbf{u}_{CS,i}$
    if $\mathbf{u}_{CS,i} > threshold$ **then**
        Extrapolate velocity from underlying nodes
    end if
    $\left(\frac{\partial \phi}{\partial n}\right)_i \leftarrow \mathbf{u}_{\mathrm{CS},i} \cdot \mathbf{n}_i$
end for

2.5 Free surface matching in the overlapping region

2.5.1 A need for matching free surfaces in $\Omega_{overlap}$

The velocity exchange procedure described above does not guarantee the matching of free surfaces in $\Omega_{overlap}$. On the *CS* side of the overlapping region, free surface information on $\Gamma^{\mathrm{D}}_{\mathrm{C,CS}}$ is received from *seine3d* along with velocity data as the velocity profile imposed to the water phase on the boundary is of limited vertical extent. On the opposite, velocity extraction in *CS* cells located near $\Gamma^{\mathrm{N}}_{\mathrm{C},seine3d}$ nodes does not incorporate any free surface position information, and velocity values are sought in the *CS* domain without any restriction on the phase in which extraction is realized. An additional operation on the free surface of *seine3d* is then needed to ensure interface continuity between the viscous and potential domains, which was found to be a necessary condition for the accuracy and stability of coupled simulations.

If free surface positions $\eta_{\mathrm{CS}}(\mathbf{x}_{\mathrm{CS}})$ and $\eta_{seine3d}(\mathbf{x}_{\mathrm{CS}})$ differ on the *CS* side of $\Omega_{overlap}$, the *seine3d* vertical velocity profile specified on $\Gamma^{D}_{\mathrm{C,CS}}$ does not match with the geometry of the water phase in the interior of *CS* domain. As the imposition of this velocity profile comes along with that of a Dirichlet boundary condition on the void fraction on $\Gamma^{\mathrm{D}}_{\mathrm{C,CS}}$ as described in 2.4.1, free surface mismatching leads to an artificial jump in the void fraction field, either positive or negative, causing a spurious free surface flow. Such a void fraction jump and subsequent gravity-driven flow deteriorate the accuracy of simulations, but were found seldom problematic for their stability in preliminary tests.

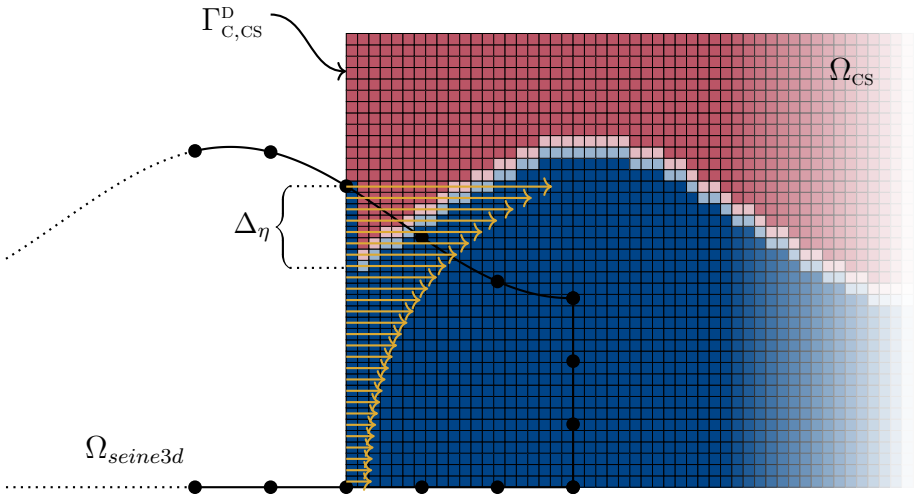

Figure 2.5: Non-physical void fraction jump on *CS* side of overlapping area caused by non-matching free surfaces. Δ_η stands for difference in vertical position of free surfaces in both models. Vertical velocity profile is drawn in yellow, only its horizontal component is represented.

Conversely, a free surface mismatch on *seine3d* side of the overlapping region quickly produces a growing instability in *seine3d*. Indeed, coupled nodes belonging to $\Gamma^{\mathrm{N}}_{\mathrm{C},seine3d}$

may happen to be located in the air phase of the viscous domain, or at least in the area of mixed phases. Because of the incompressible nature of the flow simulated with the VOF method, and due to the high density ratio between phases, the velocity in the air phase may be several orders of magnitude higher than in the dense phase. If a *seine3d* node where normal velocity is needed is located in the air phase, the velocity value it gets from *CS* can largely exceed velocity values in the rest of the potential domain, leading to a divergence in the resolution of the Laplace equation and consequently to the failure of the calculation in *seine3d*. If the same node lies in the region of mixed phases near the free surface, the velocity may still take spurious values - which are inherent to VOF simulations - triggering the same type of instability.

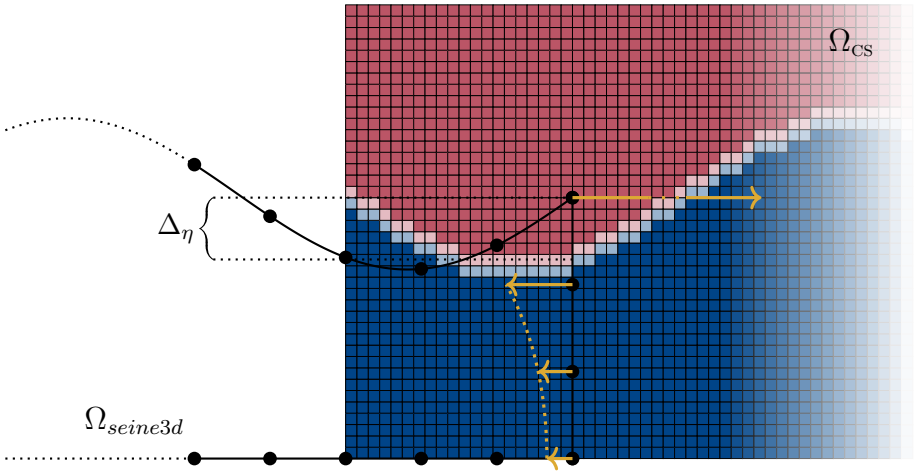

Figure 2.6: Consequences of a mismatch in free surfaces on *seine3d* side of the overlapping region. Δ_η stands for difference in vertical position of free surfaces in both models. Aberrant vertical profile of normal velocity is drawn in yellow.

One thus has to make sure that the free surface position in *seine3d* and the void fraction field in *CS* remain consistent in the overlapping region, with a special focus near the endpoint of each domain. It appears that no special treatment is necessary on the *CS* side of $\Omega_{overlap}$, and that the void fraction jump can be avoided with a cautious selection of the coupling parameters that will be presented in the coming sections. Interface position in *seine3d*, on the contrary, has to be relaxed towards the estimated location of the interface in *CS* over the whole extent of the overlapping region.

2.5.2 Capturing free surface in *CS*

As already written, free surface position is not explicitly known in simulations conducted with the algebraic VOF module of *CS*. Region of mixed phases around free surface is smeared over a few cells even though interface recompression methods are employed. Taking advantage of the fact that free surface topology in the overlapping area satisfies assumptions made in *seine3d*, in particular it has to be single-valued, a method to estimate the vertical position of the free surface in *CS* is devised.

To that end, for every coupled *seine3d* node where free surface vertical position is sought in *CS*, we consider the complete fluid column extending vertically from the position of the associated *CS* cell, whose center is the closest to the *seine3d* node of interest. Free surface vertical location $z_{fC,\mathrm{CS}}$ is approximated by the ratio of water volume in the column to the total volume of the column. Computing volumes with vertical integrations gives:

$$\eta_{\mathrm{CS}} = \frac{\int_{-h}^{h_c}(1-\alpha)d\Omega}{\int_{-h}^{h_c} d\Omega} \tag{2.29}$$

where α is the void fraction, h is the depth, h_c the height of *CS* domain above the resting free surface (up to the ceiling) and $d\Omega$ is an infinitesimal volume. As the meshes used for coupled simulations in *CS* are structured in the vertical direction, *i.e.* they can be obtained from the vertical extrusion of an arbitrary horizontal 2D conformal mesh, a column of cells is also a fluid column. Calculation of water volume and total column volume is then straightforward and equation 2.29 becomes:

$$\eta_{\mathrm{CS}} = \frac{\sum_{j\in C_i}(1-\alpha_j)|\Omega_j|}{\sum_{j\in C_i}|\Omega_j|} \tag{2.30}$$

for every cell j of volume $|\Omega_j|$ in the fluid column C_i centered on cell i. This way η_{CS} can take any value within the continuous range $[-h; h_c]$.

2.5.3 Free surface relaxation in *seine3d*

2.5.3.1 Principle of free surface relaxation

$\Gamma_{fC,seine3d}$ is modified to conform with the free surface solution η_{CS} in $\Omega_{overlap}$ built in *CS* as described in section 2.5.2 (see figure 2.1). Time stepping in *seine3d* follows a semi-Lagrangian rule, thus only the vertical coordinate of *seine3d* nodes belonging to $\Omega_{overlap}$ is modified, as it is the only direction along which they are free to translate. Relaxation refers to the fact that pure potential free surface solution which has just been computed in *seine3d* is combined with a free surface signal extracted from *CS* void fraction field at the same new time instant to produce a relaxed solution. This ensures free surface matching at *seine3d* side of the overlapping region at any time. Following the time stepping stage in *seine3d*, the vertical position of each node i belonging to $\Gamma_{fC,seine3d}$ is indeed replaced by the weighted sum of *seine3d* free surface position and *CS* free surface solution η_{CS}, following equation 2.31:

$$z \leftarrow (1-\omega)z + \omega\eta_{\mathrm{CS}} \qquad \text{on } \Gamma_{fC,seine3d} \tag{2.31}$$

z is the current vertical coordinate while ω is the relaxation weight, varying between 0 at $\mathbf{x}_{\mathrm{CS}}$ and 1 at $\mathbf{x}_{seine3d}$ over the length of $\Omega_{overlap}$. Different spatial functions may be used for ω to allow a smooth relaxation. Relaxation strategy is illustrated in figure 2.7, where

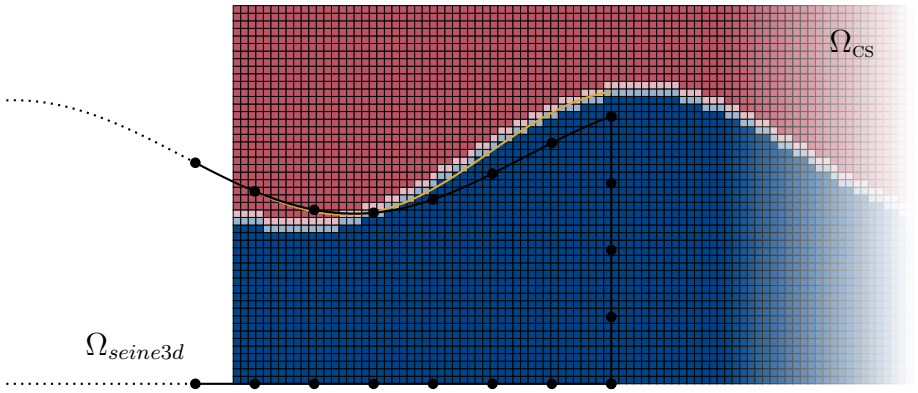

Figure 2.7: Free surface relaxation in *seine3d*. The yellow line represents the position of *seine3d* free surface after correction.

a yellow line marks the corrected position of the free surface.

Mass conservation is thus no longer ensured in the coupled *seine3d* domain, as an extra mass flux originates from the changes made to the interface geometry in $\Omega_{overlap}$. Its magnitude grows with the gap between the target value η_{CS} and the geometry of $\Gamma_{fc,seine3d}$ prior to relaxation. Hence, the kinematic free surface boundary condition (2.9) established for the potential flow, stating that no mass flux goes through the free surface, is no longer satisfied, as the free surface is not rigorously advected with the flow anymore. Such mass imbalance goes along with momentum imbalance in the dynamic free surface boundary condition (2.10). Through the time stepping procedure used in *seine3d* and the time integation of equations 2.9 and 2.10, these mass and momentum discrepancies yield erroneous free surface shape and velocity potential at subsequent time instants, thus calling for stronger free surface relaxation in return. The cumulated errors might lead to the failure of the coupled simulation. To avoid this and to make sure that free surface boundary conditions are still satisfied after the interface relaxation step, the velocity potential on $\Gamma_{fc,seine3d}$ should be modified accordingly, as described in sections 2.5.3.3 and 2.6.4.

2.5.3.2 Relaxation weight

Different spatially varying functions, or blending functions, can be used for ω in equation 2.31, such as linear, exponential or third order polynomial. The associated weights are given hereafter, setting $b = \frac{x - x_{\text{CS}}}{L_{overlap}}$ with x the current horizontal coordinate. Three functions were tested:

$$\omega_{lin.} = b \tag{2.32a}$$

$$\omega_{expo.} = \frac{e^{b^2} - 1}{e^1 - 1} \tag{2.32b}$$

$$\omega_{herm.} = b^2(3 - 2b) \tag{2.32c}$$

Figure 2.8 shows the graphs of these relaxation functions or weights. Relaxation weights

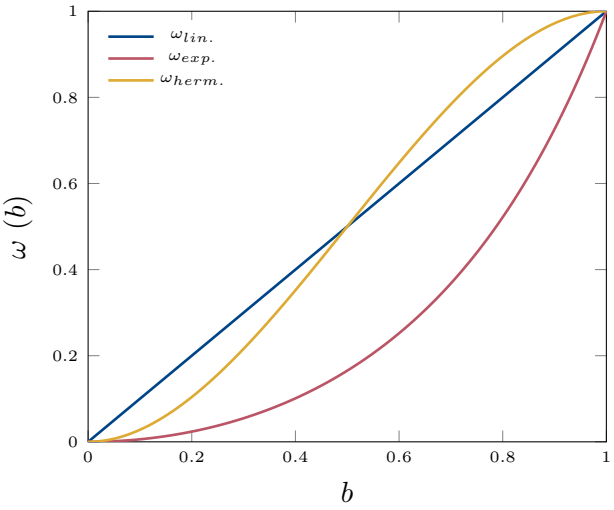

Figure 2.8: Plots of different free surface blending functions

based on the third order cubic polynomial and weights featuring exponential variation where both used in this work, and no significant impact on the simulation results was detected. Thorough comparison of the performance of blending functions was nevertheless not considered in this study.

2.5.3.3 Relaxation of velocity potential on the free surface

As already mentioned, as the position of free surface nodes is modified, so should be the value of the velocity potential ϕ at these nodes, as follows:

$$\phi \leftarrow (1-\omega)\phi + \omega\phi_{rlx} \qquad \text{on } \Gamma_{fC,seine3d} \tag{2.33}$$

The potential has no physical meaning in the NS simulation, thus its corrected value ϕ_{rlx} should be built from other *seine3d* and *CS* variables. Prior to explaining how ϕ_{rlx} is obtained, we should introduce the time stepping strategy used for coupled simulations. This is the subject of the next section, in which ϕ_{rlx} is eventually described.

2.6 Advancing coupled simulations in time

The extraction and processing of coupling variables as well as the imposition of coupling boundary conditions having been detailed in previous sections, we now explain how time stepping is done in coupled BEM-VOF simulations.

2.6.1 Using different time step sizes for each code

The time step size in each code is governed by physical and numerical considerations, for which the Courant-Friedrichs-Lewy (CFL) number offers a synthesis. It indeed quantifies the balance between temporal and spatial discretizations. Spatial discretization differs a lot between *CS* and *seine3d*. While in the former a target number of 20 cells along the vertical direction is employed to cover the height of the reference wave, the latter only requires a smaller number (typically 4 or slightly more) of boundary elements to occupy the whole water column under the wave. The need for limited aspect ratios of *CS* cells as well as *seine3d* boundary elements further sets constraints on the number of cells or boundary elements per reference wavelength in each code. Such differences in spatial discretization call for the use of different time step sizes, so that there is flexibility to set CFL number in each code independently. Using *CS* and *seine3d* with respective sets of parameters close to optimal values is indeed a necessary condition for the global efficiency of the coupling strategy. To that end, the *CS* time step size Δt_{CS} has to be kept smaller than its potential counterpart $\Delta t_{seine3d}$. We define the time step ratio $N_{\Delta t}$ as:

$$N_{\Delta t} = \frac{\Delta t_{seine3d}}{\Delta t_{\mathrm{CS}}} \tag{2.34}$$

Both models are synchronized when the coupled computation time reaches an integer multiple of $\Delta t_{seine3d}$, that is to say that physical variables of interest are exchanged through MPI communications every $\Delta t_{seine3d}$ seconds. *seine3d* is thus waiting for *CS* calculations over sub time steps (of size Δt_{CS}) to end during most of the computational time, as the coupling is done in serial mode.

2.6.2 Interpolation of *CS* coupling boundary conditions between *seine3d* time steps

CS boundary conditions are needed at time $t^{(n_{\mathrm{CS}})}$ to advance the NS solution up to $t^{(n_{\mathrm{CS}}+1)}$ where n_{CS} enumerates the *CS* time stepping sub-stages between successive synchronization time instants $t^{(n)}$ and $t^{(n+1)}$.

$$\begin{aligned} t^{(n_{\mathrm{CS}})} &= t^{(n)} + n_{\mathrm{CS}}\Delta t_{\mathrm{CS}} \quad \forall\ n_{\mathrm{CS}} \in \{0, N_{\Delta t} - 1\} \\ t^{(n_{\mathrm{CS}})} &= t^{(n+1)} \qquad \text{if } n_{\mathrm{CS}} = N_{\Delta t} \end{aligned} \tag{2.35}$$

Inlet Dirichlet boundary conditions on velocity and void fraction on $\Gamma^{\mathrm{D}}_{\mathrm{C,CS}}$ are obtained

from interpolations of $\mathbf{u}_{seine3d}$ and $\eta_{seine3d}$ between $t^{(n)}$ and $t^{(n+1)}$. $\mathbf{u}_{seine3d}^{(n_{\mathrm{CS}})}$ and $\eta_{seine3d}^{(n_{\mathrm{CS}})}$ stand for values interpolated at time $t^{(n_{\mathrm{CS}})}$. As described below, interpolation schemes of various orders may be employed, using values of $\eta_{seine3d}$ and $\mathbf{u}_{seine3d}$ at different *seine3d* time instants.

2.6.2.1 Linear time interpolation

Requiring values of $\eta_{seine3d}$ and $\mathbf{u}_{seine3d}$ only at current (n) and following $(n+1)$ time instants, one may build a linear interpolation scheme as follows, setting $\beta = \frac{n_{\mathrm{CS}}}{N_{\Delta t}}$ as a new variable. As n_{CS} belongs to $\{0, N_{\Delta t}\}$, β evolves in $[0,1]$.

$$\begin{aligned} \mathbf{u}_{seine3d}^{(n_{\mathrm{CS}})} &= (1-\beta)\mathbf{u}_{seine3d}^{(n)} + \beta\mathbf{u}_{seine3d}^{(n+1)} \\ \eta_{seine3d}^{(n_{\mathrm{CS}})} &= (1-\beta)\eta_{seine3d}^{(n)} + \beta\eta_{seine3d}^{(n+1)} \\ \forall\ \beta\ &\in [0,1] \end{aligned} \tag{2.36}$$

2.6.2.2 Higher order polynomial time interpolation

If values of $\eta_{seine3d}$ and $\mathbf{u}_{seine3d}$ are stored at additional time instants $(n-1)$ and $(n-2)$, a higher order interpolation procedure is established, permitting a better rendering of the nonlinear nature of the time evolution of wave kinematics. Such a scheme is more accurate than the linear one for a given time step size under certain assumptions, but it may lead to greater interpolation errors in the case of large time steps. It also uses a larger amount of computer memory as physical variables are saved at 4 time instants, as opposed to 2 in the linear case. As constant time steps sizes are used exclusively in the coupling procedure, the Lagrange polynomial of the 3^{rd} degree is retained that is easily implemented and expressed here in terms of the same variable β:

$$\begin{aligned} \mathbf{u}_{seine3d}^{(n_{\mathrm{CS}})} = & -\frac{1}{6}(\beta+1)\beta(\beta-1)\mathbf{u}_{seine3d}^{(n-2)} + \frac{1}{2}(\beta+2)\beta(\beta-1)\mathbf{u}_{seine3d}^{(n-1)} \\ & -\frac{1}{2}(\beta+2)(\beta+1)(\beta-1)\mathbf{u}_{seine3d}^{(n)} + \frac{1}{6}(\beta+2)(\beta+1)\beta\mathbf{u}_{seine3d}^{(n+1)} \\ \eta_{seine3d}^{(n_{\mathrm{CS}})} = & -\frac{1}{6}(\beta+1)\beta(\beta-1)\eta_{seine3d}^{(n-2)} + \frac{1}{2}(\beta+2)\beta(\beta-1)\eta_{seine3d}^{(n-2)} \\ & -\frac{1}{2}(\beta+2)(\beta+1)(\beta-1)\eta_{seine3d}^{(n)} + \frac{1}{6}(\beta+2)(\beta+1)\beta\eta_{seine3d}^{(n+1)} \\ \forall\ \beta\ &\in [0,1] \end{aligned} \tag{2.37}$$

The number of coupling *seine3d* nodes being limited to relatively small values, storing *seine3d* coupling velocity profile and free surface function at 4 time instants is not very memory-consuming. Besides, $\Delta t_{seine3d}$ values were found to remain in a range where high-order polynomial interpolation is more accurate than the linear one. It is to be noted that the choice of $N_{\Delta t}$ is the result of a balance between accuracy (limited interpolation errors) and efficiency (sufficiently high CFL number in *seine3d*), and as such is a crucial

parameter of the coupling strategy. Its influence on the coupled simulations is studied in chapters 3 and 4.

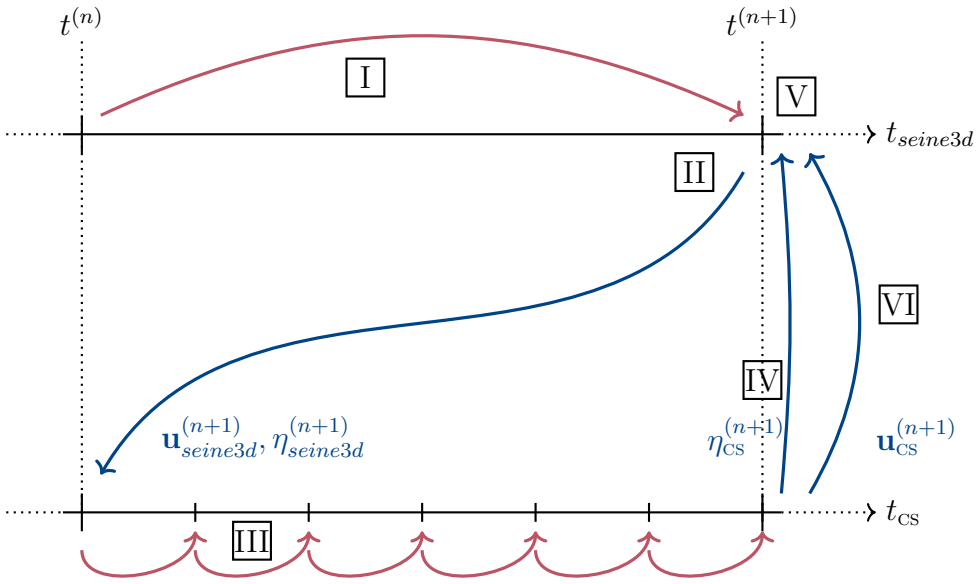

Figure 2.9: Main steps and information fluxes of coupling time stepping scheme. Red lines illustrate time stepping operations while blue ones show MPI communications between coupled programs. Top axis stands for *seine3d* while bottom axis represents operations conducted in *CS*.

2.6.3 Detailed description of the time stepping procedure

The time stepping procedure is summarized in figure 2.9, with roman figures enumerating the different stages.

I: *seine3d* free surface conditions are advanced in time from $t^{(n)}$ to $t^{(n+1)}$ following an explicit 3^{rd} order Runge-Kutta scheme. Geometry of *seine3d* domain is updated and so are $\Gamma_{\mathrm{C},seine3d}^{\mathrm{N},(n+1)}$ and $\Gamma_{f\mathrm{C},seine3d}^{(n+1)}$. The boundary integral problem is solved once boundary conditions are established. To that end, a Neumann boundary condition on the velocity potential on $\Gamma_{\mathrm{C},seine3d}^{\mathrm{N},(n+1)}$ is built from a *CS* vertical velocity profile extracted at current time step (n) as in equation 2.38. $\mathbf{u}_{\mathrm{CS}}^{(n)}$ is indeed obtained as an output of the previous coupling iteration.

$$\frac{\partial \phi}{\partial n}^{(n+1)} = \mathbf{u}_{\mathrm{CS}}^{(n)} \cdot \mathbf{n}_{seine3d} \qquad \text{on } \Gamma_{\mathrm{C},seine3d}^{\mathrm{N},(n+1)} \tag{2.38}$$

It should be noted that $\mathbf{u}_{\mathrm{CS}}^{(n)}$ velocity profile has been extracted and is therefore known at the previous location of coupled *seine3d* nodes, *i.e.* on $\Gamma_{\mathrm{C},seine3d}^{\mathrm{N},(n)}$. We assume that this holds on $\Gamma_{\mathrm{C},seine3d}^{\mathrm{N},(n+1)}$.

II: internal velocity $\mathbf{u}_{seine3d}^{(n+1)}$ is extracted in *seine3d* domain. Spurious velocity values are replaced with extrapolated ones as explained in section 2.4.2. $\mathbf{u}_{seine3d}^{(n+1)}$ and $\eta_{seine3d}^{(n+1)}$ are sent to *CS* in an MPI communication operation.

III: *CS* solution is advanced in time through $N_{\Delta t}$ sub time steps with the inlet boundary conditions described in equation 2.37.

IV: *CS* free surface data $\eta_{seine3d}^{(n+1)}$ at cells close to free surface nodes belonging to $\Gamma_{f\mathrm{C},seine3d}$ is sent to *seine3d*.

V: free surface position in *seine3d* is relaxed towards *CS* solution such that free surfaces matching is ensured at $x_{seine3d}$. $\Gamma_{\mathrm{C},seine3d}^{\mathrm{N},(n+1)}$ becomes $\Gamma_{\mathrm{C},seine3d}^{\mathrm{N},(n+1),rlx}$ and accordingly $\Gamma_{f\mathrm{C},seine3d}^{(n+1)}$ is now $\Gamma_{f\mathrm{C},seine3d}^{(n+1),rlx}$. Velocity potential can be relaxed accordingly. Relaxation procedure is explained in section 2.5.3.

VI: coordinates of *seine3d* boundary nodes on $\Gamma_{\mathrm{C},seine3d}^{\mathrm{N},(n+1),rlx}$ are sent to *CS* and velocity $\mathbf{u}_{\mathrm{CS}^{(n+1)}}$ close to those nodes is sent back to *seine3d* to generate Neumann condition at $t^{(n+1)}$ as follows:

$$\frac{\partial \phi^{(n+1)}}{\partial n} = \mathbf{u}_{\mathrm{CS}}^{(n+1)} \cdot \mathbf{n}_{seine3d} \qquad \text{on } \Gamma_{\mathrm{C},seine3d}^{\mathrm{N},(n+1),rlx} \tag{2.39}$$

VII: in *seine3d*, the boundary integral problem at time $t^{(n+1)}$ is solved for the second time.

This two-way coupling strategy is similar to the one described in Kim et al. (2010) and theoretically enables wave propagation in any direction.

2.6.4 Calculation of ϕ_{rlx}

The time stepping procedure has been described in detail and every notion needed to explain how the relaxation of free surface velocity potential may be done in *seine3d* has been introduced. With the newly introduced time stepping exponents, equation 2.31 writes:

$$z^{(n+1)} \leftarrow (1-\omega) z^{(n+1)} + \omega \eta_{\mathrm{CS}}^{(n+1)} \qquad \text{on } \Gamma_{f\mathrm{C},seine3d}^{(n+1)} \tag{2.40}$$

as $\Gamma_{f\mathrm{C},seine3d}^{(n+1)}$ is turned into $\Gamma_{f\mathrm{C},seine3d}^{(n+1),rlx}$.

As stated in section 2.5.3.3, potential relaxation through $\phi_{rlx}^{(n+1)}$ is needed so that free surface relaxation influence on potential distribution on *seine3d* boundaries can be applied. ϕ_{rlx} is sought at time $t^{(n+1)}$ and equation 2.33 becomes:

$$\phi^{(n+1)} \leftarrow (1-\omega) \phi^{(n+1)} + \omega \phi_{rlx}^{(n+1)} \qquad \text{on } \Gamma_{f\mathrm{C},seine3d}^{(n+1),rlx} \tag{2.41}$$

At stage V of the above coupling procedure, the dynamic free surface boundary condition

is integrated again, this time in a single step and following a centered scheme:

$$\frac{\delta\phi}{\delta t}^{(n)} = \frac{\phi_{rlx}^{(n+1)} - \phi^{(n-1)}}{2\Delta t} = -g\eta^{(n)} - \frac{1}{2}\left(\nabla\phi_{rlx}^{(n)}\right)^2 + \frac{\partial\eta}{\partial t}^{(n)}_{rlx}\frac{\partial\phi}{\partial z}^{(n)}_{rlx} \tag{2.42}$$

thus

$$\begin{aligned}\phi_{rlx}^{(n+1)} = \phi^{(n-1)} + 2\Delta t\left(-g\eta^{(n)} - \frac{1}{2}\left(\nabla\phi_{rlx}^{(n)}\right)^2 + \frac{\partial\eta}{\partial t}^{(n)}_{rlx}\frac{\partial\phi}{\partial z}^{(n)}_{rlx}\right)\\ \text{where } z = \eta\left(x, y, t^{(n)}\right)\end{aligned} \tag{2.43}$$

Free surface velocity is rewritten as follows:

$$\nabla\phi_{rlx}^{(n)} = \nabla_h\phi^{(n)} + \frac{\partial\phi}{\partial z}^{(n)}_{rlx}\mathbf{e_z} \tag{2.44}$$

where ∇_h stands for horizontal gradient and $\mathbf{e_z}$ is the vertical unit vector.

Every right hand side term in equation 2.43 is known explicitly except $\frac{\partial\eta}{\partial t}^{(n)}_{rlx}$ and $\frac{\partial\phi}{\partial z}^{(n)}_{rlx}$. Using another centered scheme to solve the kinematic free surface boundary condition and obtain $\frac{\partial\eta}{\partial t}^{(n)}_{rlx}$, it becomes:

$$\begin{aligned}\frac{\partial\eta}{\partial t}^{(n)}_{rlx} &= \frac{\delta\eta}{\delta t}^{(n)}_{rlx} = \frac{\eta_{\text{CS}}^{(n+1)} - \eta^{(n-1)}}{2\Delta t}\\ &= \frac{\partial\phi}{\partial z}^{(n)}_{rlx} - \frac{\partial\phi}{\partial x}^{(n)}\frac{\partial\eta}{\partial x}^{(n)} - \frac{\partial\phi}{\partial y}^{(n)}\frac{\partial\eta}{\partial y}^{(n)}\end{aligned} \tag{2.45}$$

from which the value of $\frac{\partial\phi}{\partial z}^{(n)}_{rlx}$ is also deduced.

This method is inspired from that described in Kim et al. (2010) to relax velocity potential on $\Gamma_{fC,seine3d}$. Other methods include not relaxing the free surface velocity potential, or using free surface velocity extracted in the viscous model to set the value of $\nabla\phi_{rlx}^{(n)}$, or that of its vertical component $\frac{\partial\phi}{\partial z}^{(n)}_{rlx}$ only, as in Kemper et al. (2019). In this latter work, in which the potential model relies on the formalism of Zakharov (1968), the vertical velocity close to interface extracted in the viscous code is used as vertical velocity at the free surface in the potential model. From time integration of the dynamic free surface boundary condition, a corrected value for free surface potential is obtained. Free surface horizontal velocity in the VOF calculation is however not transmitted to the potential calculation. It is to be noted that extracting valid values for vertical water velocity at free surface is not an easy task. It has been tested in the current coupled model but was found to be less accurate and stable than the above-described method.

2.7 Parallelization of coupled simulations

2.7.1 Building a MPI communicator where coupling takes place

Both potential and viscous numerical codes that are coupled in this work allow parallel simulations when used alone. They are adapted to high performance computing on large computers with distributed memory, and coupled simulations should exhibit the same behavior. Message Passing Interface (MPI) protocol is used with this goal in mind. Each application operates in a MPI communicator, or intracommunicator, allowing point-to-point and collective communications between processes owned by the application. As in the previous sections of this chapter, we will restrict the description of the coupling communications to the simplest case of a calculation coupling one instance of each code. Therefore, in this case, allowing the exchange of variables between *CS* and *seine3d* amounts to building a new global communicator or extra-communicator from the union of both application's communicators. This is done conveniently thanks to ad-hoc MPI functions from the Parallel Location and Exchange (PLE) library (Fournier, 2020) coming with *CS* that had to be adapted in *seine3d*. Exchanges of coupling variables are exclusively realized with point-to-point MPI communications in the newly built coupling (global) communicator. Such communications may be sequential, if only root processes are involved, or parallel. Communicators and communications are illustrated in figure 2.10.

2.7.2 Sequential or parallel coupling communications

The choice between sequential or parallel coupling communications mostly depends on the characteristics of *CS* and *seine3d* and on the location of the variables of interest in the applications.

2.7.2.1 *seine3d* → *CS* communications

In *CS*, a domain decomposition approach is used to split the computational domain between MPI processes. Each process owns a part of the field variables arrays. Besides that, as the *CS* grid is fixed, the location of cells centers on $\Gamma^{\mathrm{D}}_{\mathrm{C,CS}}$, where values of $\mathbf{u}_{seine3d}$ and $\eta_{seine3d}$ are sought, are known from the start of the simulation. Therefore, *CS* processes that will receive these values from *seine3d* are identified at the initialization stage of the coupled calculation. Point-to-point communications are established between those *CS* processes and selected *seine3d* processes. Indeed velocity at any internal point in $\Omega_{seine3d}$ and position of any boundary free surface node belonging to $\Gamma_{fC,seine3d}$ may be respectively accessed or computed from any *seine3d* process. Coordinates of the above-listed coupled *CS* cell centers are then gathered at *CS*'s root process once and sent to *seine3d*'s root process, from where they are equally scattered to an arbitrary selection of *seine3d* processes and stored as internal points or used to create free surface gauges, allowing point-to-point MPI communications in parallel.

2.7.2.2 *seine3d* ← *CS* communications

As *seine3d* grid is moving, it is not possible to send the location of nodes where $\mathbf{u}_{\mathrm{CS}}$ and η_{CS} should be extracted to *CS* only once at the beginning of the simulation, because it changes with time. This information is to be sent at every synchronization *seine3d* time step, after the free surface relaxation stage and before the second resolution of the boundary integral problem. *CS* cells extraction is explained in section 2.4.3. Coupled *seine3d* nodes' coordinates $\mathbf{x}_{\Gamma^{\mathrm{N}}_{\mathrm{C},seine3d}}$ and $\mathbf{x}_{\Gamma_{f\mathrm{C},seine3d}}$ are therefore gathered in *seine3d*'s root process and sent to *CS*'s root process, where they will be broadcast to every process. This is a sequential procedure, as only the root processes of coupled applications are involved in MPI communications.

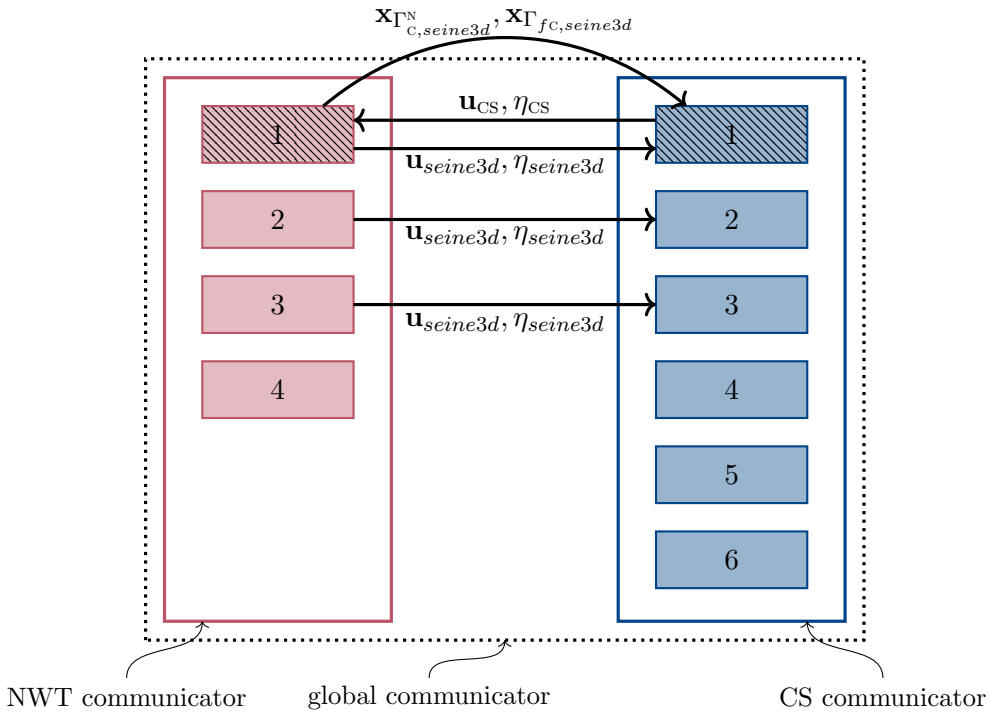

Figure 2.10: MPI communicators and communications realized at each synchronized (*seine3d*) time step. Red boxes stand for *seine3d* processes while blue ones stand for *CS* processes. Hatched boxes represent root processes. Only processes with MPI ranks ranging from 1 to 3 are directly involved in the coupling. MPI communications at initialization are not shown for the sake of clarity.

2.8 Coupling several instances of each code

So far, emphasis has been put on the most simple coupling case of one instance of *CS* and one instance of *seine3d*, in the context of 2D vertical applications. One of the goals of this study is to develop a flexible tool, adapted to a wide spectrum of wave simulation applications. To that end, it was decided to allow the coupling of several instances of the applications. One *CS* application may indeed exchange simulation variables with several instances of *seine3d*, and the other way around. Coupling interfaces $\Gamma^{\mathrm{D}}_{\mathrm{C,CS}}$ and $\Gamma^{\mathrm{N}}_{\mathrm{C},seine3d}$ as well as volumes $\Omega_{\mathrm{C,CS}}$ may be multiplied at will thus their topology could remain simple, avoiding the use of discontinuous objects, *i.e.* calculation surfaces and volumes made of several distinct parts. Currently accepted topologies include vertical lines, for 2D vertical couplings and vertical planes for 3D simulations. In future developments, possibly all surfaces described by a system of equations might be adapted for coupling, where an analytical function can be defined to calculate the distance from the center of a *CS* cell or a *seine3d* node to the vertical coupling boundaries. This is indeed needed to get the spatial blending functions from which relaxation weights are built.

Couplings are built as instances of C^{++} classes of *seine3d* and C structures of *CS*. It was intended to make the most of the object-oriented nature of *seine3d* to allow future improvements of the coupled model. In the following work and applications, we make extensive use of the coupling configuration *seine3d-CS-seine3d*, where the *CS* model is applied at a local scale around a marine structure.

Chapter 3

Coupled simulation of the propagation of a solitary wave over a constant depth

Dans ce chapitre, la stratégie de couplage précédemment décrite est appliquée au cas de la propagation d'une onde solitaire à la surface d'une étendue d'eau de profondeur uniforme. Deux hauteurs relatives de vagues sont successivement étudiées : 0.3 *et* 0.5*. Une formulation 2D verticale est retenue, dans laquelle deux instances de* seine3d *sont chacune couplées à une instance de* CS *par le biais de deux zones de recouvrement de leurs domaines de calcul. De cette manière, la transmission bidirectionnelle de vague peut être testée. L'onde solitaire se propage théoriquement à vitesse constante tout en conservant sa forme. Le profil ainsi que la position de la crête de la solution numérique sont donc comparés respectivement au cours du temps au profil de vague initial ainsi qu'à l'abscisse théorique de son sommet. Des artefacts numériques récurrents liés à la présence des couplages sont identifiés et décrits. Les limites de stabilité des calculs sont partiellement testées. On attend également de la résolution de ce problème physique fondamental des connaissances quant au comportement du couplage qui puissent être mises à profit dans de futures études. Ainsi, la pertinence de la relaxation du potentiel des vitesses à la surface libre, dans les zones de couplage, vers une solution tenant compte de la modification de la géométrie de surface libre dans* seine3d *est évaluée. Les conclusions tirées à cette occasion sont appliquées dans le reste de ce travail. On traite enfin plus brièvement de la propagation d'une onde solitaire de hauteur relative égale à* 0.5*.*

3.1 Solitary wave of moderate relative height over constant depth

3.1.1 Description of the case

As a first test case for the two-way coupling strategy, the propagation of a solitary wave over a constant depth is a good candidate. This is a two-dimensional vertical (2DV) problem for which a numerical approximation of a solitary wave solution of the irrotational Euler equations is computed thanks to the algorithm of Tanaka (1986). Conservation of wave shape, celerity, volume and energy is theoretically ensured during the propagation of any exact solitary wave over uniform water depth. Therefore, computing this propagation problem in our coupled model and tracking errors in the conservation of these wave parameters gives insight into the performances of this hybrid numerical method. These relatively light (in terms of computer resources requirements) coupled simulations test the relevance of the coupling strategy and assess the individual impact on the simulations of certain elements of this strategy. As an example, the benefits in accuracy and stability of the relaxation of *seine3d* free surface velocity potential in the overlapping region, as dealt with in section 2.6.4, are assessed in this chapter. These calculations also give an idea of the impact on stability, efficiency and accuracy of certain coupling parameters. In particular the sensitivity to time step ratio $N_{\Delta t}$ and overlapping length $L_{overlap}$ is studied.

It should be noted that the solitary wave solution is relevant in *seine3d* as potential flow equations admit a solitary wave solution. At the same time, no such solution exists for the NS equations due to the presence of the viscous diffusive term (remember that surface tension effects are not taken into account in the current study). In *CS*, where the flow is considered laminar and therefore viscosity is limited to molecular viscosity, it is assumed that physical diffusion due to viscosity is small compared to the numerical diffusion inherent to the solution procedure. Hence, even if NS equations do not admit a solitary wave solution, we can make the assumption that changes to any of the above-mentioned solitary wave invariants (wave shape, celerity, mass and energy) in the duration of the simulation are mostly related to numerical aspects of the coupled model and to the associated numerical errors. This amounts to neglecting dissipation of wave energy taking place in the bottom boundary layer and at the interface between both phases, as a free-slip boundary condition is assumed at the bottom.

For the conservation study to be relevant, the initial wave profile should be as close to the theoretical one as possible. The initialization of the solitary wave is done is a *seine3d* domain, through the imposition of the free surface geometry $\eta(x, t = 0)$, and the velocity potential $\phi(x, z = \eta, t = 0)$ as well as the normal velocity $\frac{\partial \phi}{\partial n}(x, z = \eta, t = 0)$ on the free surface. To that end, we use Tanaka's algorithm that is already available for use in *seine3d*. The solitary wave crest is initially located at the abscissa $x = 0$. The wave then propagates towards a *CS* domain through a first coupling region and later enters a second *seine3d* domain. As already stated, we make use of the capability to define several

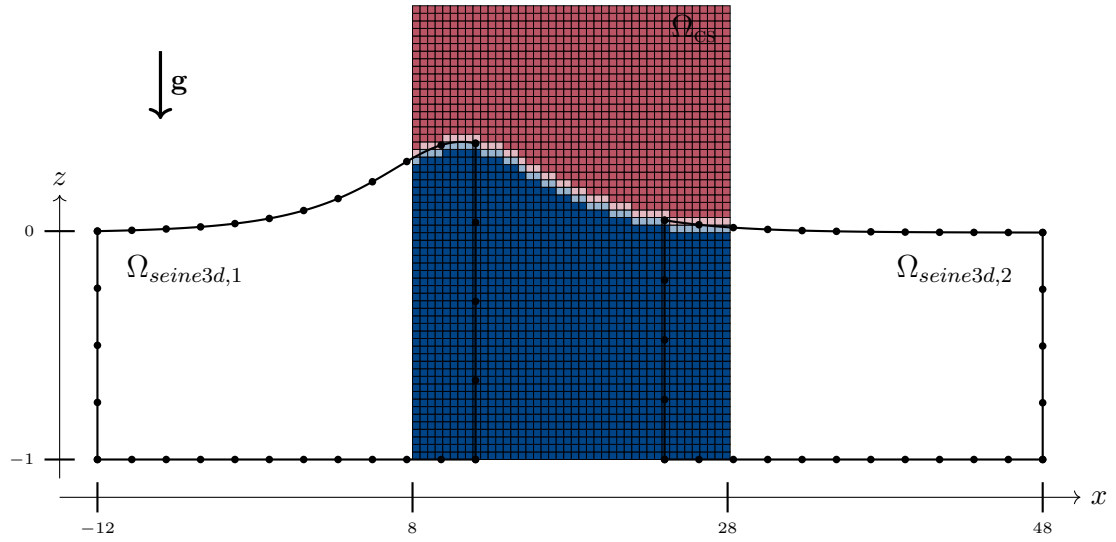

Figure 3.1: Coupled domains and related boundaries. Blue *CS* cells are cells filled with water, while red cells are full of air. Pale blue and pale red cells contain a mix of the two phases.

couplings comprising a *CS* instance and a *seine3d* instance in a single simulation of the current hybrid model. This way, it is possible to verify that the latter enables two-way wave transmission between the two models. Figure 3.1 illustrates the layout of the different computational domains.

In this chapter, the problem is solved in dimensionless form using Froude scaling. The uniform water depth at rest h is selected to make all distances dimensionless, e.g. $x' = \frac{x}{h}$. In particular, the non-dimensional water depth is then $h' = 1$. The time scale is chosen as $t_0 = \sqrt{\frac{h}{g}}$ to make time non-dimensional as $t' = \frac{t}{t_0} = t\sqrt{\frac{g}{h}}$. Other variables used in this chapter are then scaled by one of these characteristic quantities, or a combination of them. With this choice, the acceleration due to gravity becomes $g' = g\frac{t_0^2}{h} = 1$ in the dimensionless form of the equations of motion. For the sake of simplicity, primes are omitted hereafter for all non-dimensional variables.

The whole numerical domain thus extends from $x = -12$ to $x = 48$ and has a width of 1. As its name might suggest, *seine3d* is a 3D code, its domain should be discretized with several boundary elements in the transverse direction (at least 4). A moderate wave height of $H = 0.3$ is chosen for which stability of computations is ensured with a sufficient leeway on the values of the major coupling parameters. This way we are able to conduct a sensitivity analysis of the influence of these parameters.

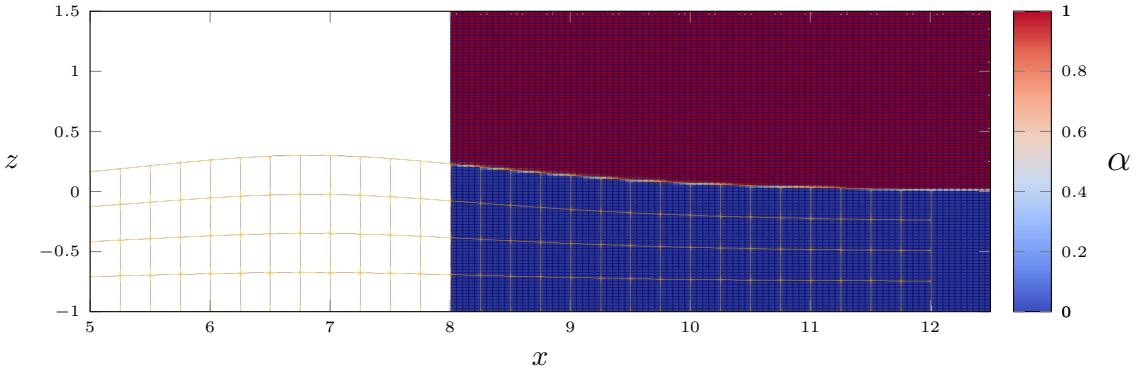

Figure 3.2: Close-up view of the meshes around the left coupling region at $t = 6$. Void fraction field $\alpha(\mathbf{x})$ in *CS* domain is shown with corresponding colorbar. *seine3d* mesh is displayed in orange.

3.1.2 Description of reference case and first results

3.1.2.1 Case setting

A reference case is built with arbitrary values of the coupling parameters. This serves as a basis for the sensitivity analysis to come. In both *seine3d* domains, boundary elements have an aspect ratio tending to one - whatever the face orientation - as the local free surface gets close to the resting position. The water column is discretized with 4 elements in its height. As a consequence of the aspect ratio, 4 elements are used in the width of the *seine3d* domains, as well as 96 elements in their length. Overlapping length $L_{overlap}$ is set to 4, with as many as 17 *seine3d* free surface nodes involved in each coupling. The *CS* domain, of constant shape, extends from $z = -1$ to $z = 1.5$. *CS* mesh is a uniform Cartesian grid with 400 cells occupying its length and 100 cells its height, amounting to 12 cells in the height of the solitary wave with an aspect ratio $\frac{\Delta x_{\text{CS}}}{\Delta z_{\text{CS}}}$ of 2. Hence, longitudinal cell sizes are $\Delta x_{\text{CS}} = 0.05$ and $\Delta x_{seine3d} = 0.25$. $N_{\Delta t}$ is set to 10 with $\Delta t_{seine3d} = 0.1$ and consequently $\Delta t_{\text{CS}} = 0.01$. In terms of theoretical longitudinal CFL numbers, one can roughly estimate them as:

$$\begin{aligned} CFL_{seine3d} &= \frac{\Delta t_{seine3d}\sqrt{gh}}{\Delta x_{seine3d}} = 0.4 \\ CFL_{\text{CS}} &= \frac{\Delta t_{\text{CS}}\sqrt{gh}}{\Delta x_{\text{CS}}} = 0.2 \end{aligned} \tag{3.1}$$

Meshes used in each model are presented in figure 3.2 at time $t = 6$ when the wave enters *CS* domain. It indeed shows meshes layout for the first (left) coupling region, given that both overlapping areas are discretized identically. Void fraction field in *CS* domain is also displayed, and it should be noted that free surface smearing due void fraction diffusion is small, as expected with the selected advection scheme. It is to be noted that relaxation of free surface potential is disabled in the reference case. Its influence on the simulation

results is assessed later. This case runs for around 60 time units in 2 hours on a single HPC node, with 8 cores allocated to each *seine3d* instance and 2 to *CS*.

3.1.2.2 Free surface profiles in the reference case

Solitary wave propagation through time and the different coupled domains is depicted for the reference case in figure 3.3. *seine3d* free surface profiles are based on raw geometry results as only the position of free surface boundary nodes is drawn. *CS* free surface signal is obtain after post-processing through the subsequent use of Paraview filters *Cell Data to Point Data* and *Contour*, defining a void fraction isosurface from points verifying $\alpha(\mathbf{x}) = 0.5$. Results look satisfactory: free surface signals are continuous, indicating that free surface matching is achieved and enabling sufficiently stable calculations. Besides, the wave profile globally seems to retain its shape through time. Small unexpected secondary peaks may be observed on the back of the wave, mostly after it leaves the *CS* domain, starting from $t = 33$. The same is seen when the water hump enters the *CS* domain, starting from $t = 18$. A close-up view at these two time instants is shown in figure 3.4, with an appropriate vertical scale. On this view again, it appears that free surfaces closely match. It also illustrates the fact that the wave is slightly distorted when transmitted from a model to another, thus the implemented couplings are not fully transparent. We can reasonably assume that this phenomenon is mostly numerical as the appearance of spurious small waves and wiggles is localized in time and space and corresponds to wave passing from one model to the other, whereas the wave profile seems constant during its propagation in the *CS* domain. As already said, the NS equations do not admit a solitary wave solution, therefore the solitary wave might also suffer from physical diffusion when travelling through the *CS* domain. A more detailed study of wave shape conservation is presented in section 3.1.4. It allows a estimate of undesired wave reflection and distortion inherent to the coupling method. It also finely keeps track of the evolution of wave characteristics, such as height or width. A simulation identical to the reference one with molecular viscosity set to zero was then run to assess the amount of physical diffusion. Detailed simulation results were found indistinguishable from the reference ones, indicating that the influence of physical diffusion is negligible. We might thus conclude that all spurious phenomena observed during the travel of the solitary wave through coupled domains and described above are purely numerical.

3.1.2.3 Overlapping area velocity fields in the reference case

As explained in chapter 1, the current two-way coupling strategy relies on the fulfillment of two velocity continuity conditions on both sides of every overlapping region.

To check that velocity continuity is ensured, we might look at the velocity fields in both models for each overlapping area, as shown in figure 3.5. In this figure, three time instants are used to describe the velocity under the crest of the solitary wave in each overlapping

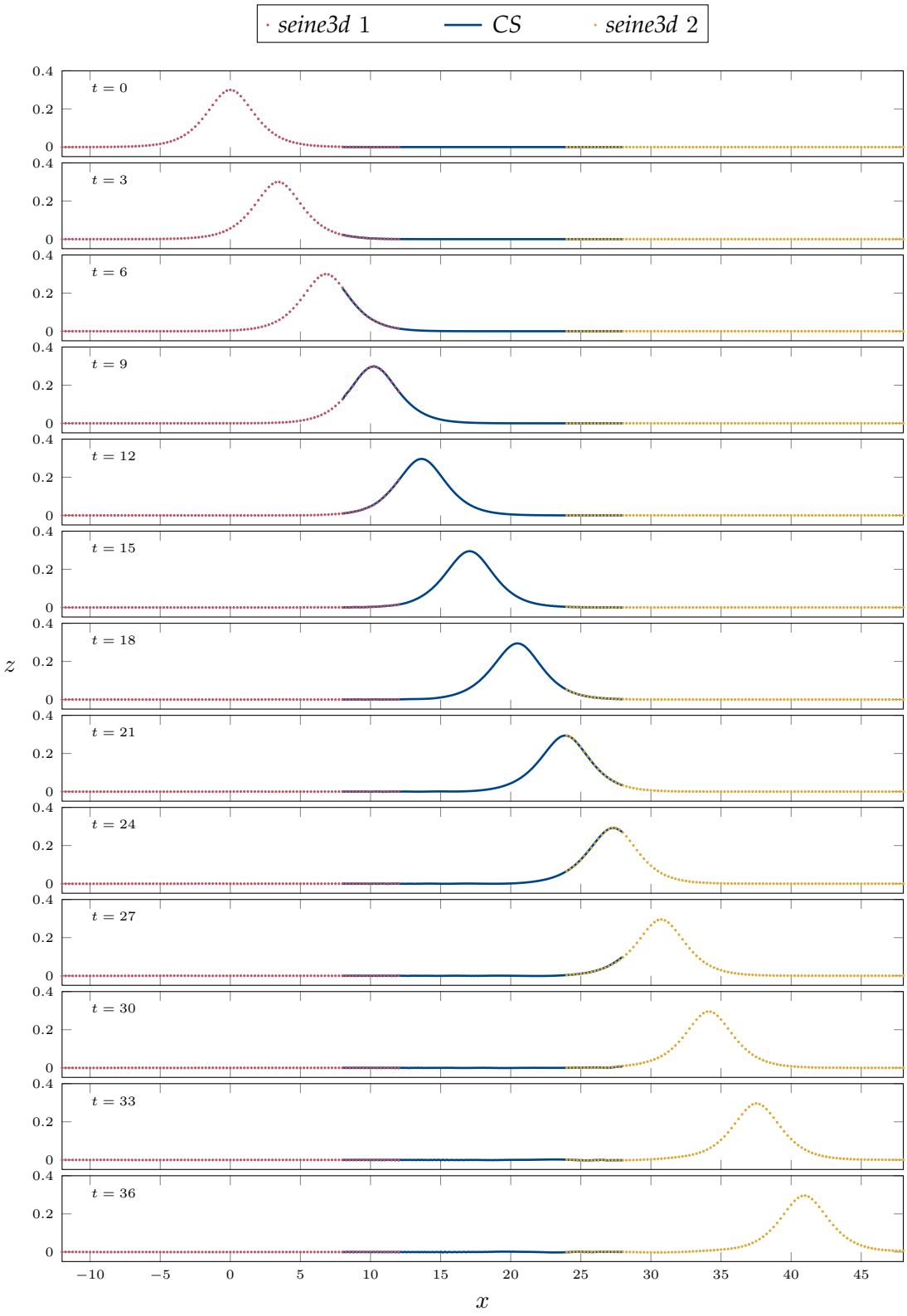

Figure 3.3: Time history of free surface profiles for the reference case of a solitary wave with $H = 0.3$. Dashed lines represent *seine3d* free surface nodes.

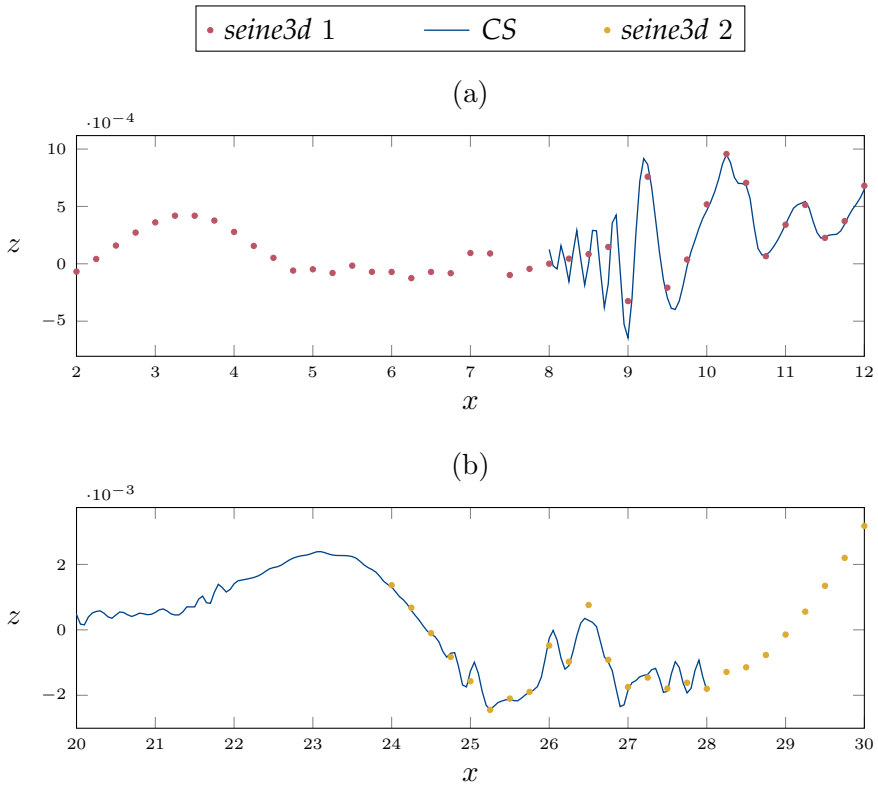

Figure 3.4: Close-up view of free surface profiles comprising overlapping regions at time instants $t = 18$ (a) and $t = 33$ (b) where spurious peaks and wiggles are observed.

region. For the sake of clarity, velocity vectors are drawn at every *seine3d* node located on one of the vertical lateral faces. *CS* velocity is then linearly interpolated at these locations, yielding superimposed velocity fields. These fields match well at most time instants, whatever the coupling region, with very few discrepancies excepted close to the free surface when the wave crest leaves the first *seine3d* domain. At $t = 10$ indeed, *seine3d* free surface velocity near the right side of the *seine3d* 1/*CS* 1 coupling region (left overlapping region in figure 3.1) exhibits a non-physical behaviour, with a diverging value on the top right corner node. Nevertheless, such instability in the potential domain does not affect the stability of the simulation too much, as the travel of the hump of water continues without any major shift: no significant impact is seen on the wave profile at the corresponding time instant.

To get a better insight into this velocity discrepancy, we can study the velocity component fields displayed in figure 3.6. If transverse invariance in longitudinal velocity (u_x) is almost respected with only a moderate non-symmetrical peak at one corner, it is not the case for lateral (u_y) and vertical (u_z) components. u_y is theoretically zero in the whole domain at any time, and this condition is not verified. u_y and u_z suffer from singularities at corners and edges between the coupled face of *seine3d* (*i.e.* the one receiving Neumann boundary condition on ϕ from *CS* 1) and the free surface, and between vertical walls and the free surface. Fortunately in this case it does not lead to the failure of the simulation and does

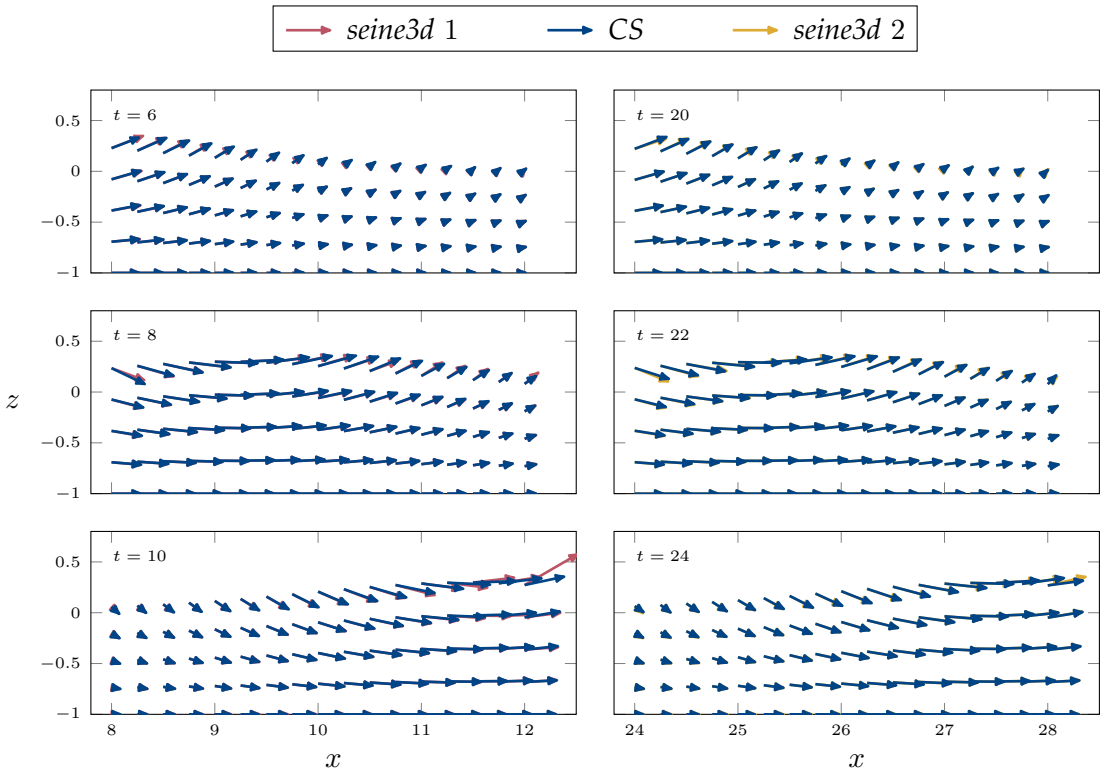

Figure 3.5: *CS* and *seine3d* velocity fields in $\Omega_{overlap}$ for each coupling in the reference case of solitary wave propagation with $H = 0.3$. Due to overlapping results, red and yellow vectors are not always visible.

not affect the accuracy of the results significantly.

Figure 3.7 shows the fields of the velocity potential and its normal derivative. No singularity on the potential is visible, whereas it is the case for free surface values of ϕ_n close to coupling face $\Gamma^{\mathrm{N}}_{\mathrm{C},seine3d}$.

All these aspects are similar to the edge/corner instability patterns frequently encountered on the free surface close to the wavemaker face in simulations with *seine3d* alone. Grilli and Svendsen (1990) proposed a nomenclature for such corner issues in fully nonlinear potential models. See also the PhD work of Mivehchi (2018) for improved treatment of the 3D corner compatibility conditions in the current potential flow model. *seine3d* coupling face is indeed quite close to a vertical wavemaking face in its design. A Neumann boundary condition on ϕ is enforced on $\Gamma^{\mathrm{N}}_{\mathrm{C},seine3d}$. In the meantime, the face vertical extent is specified through a prior *seine3d* free surface relaxation step. Therefore is it not surprising to notice the same instability issues as for the wavemaker side.

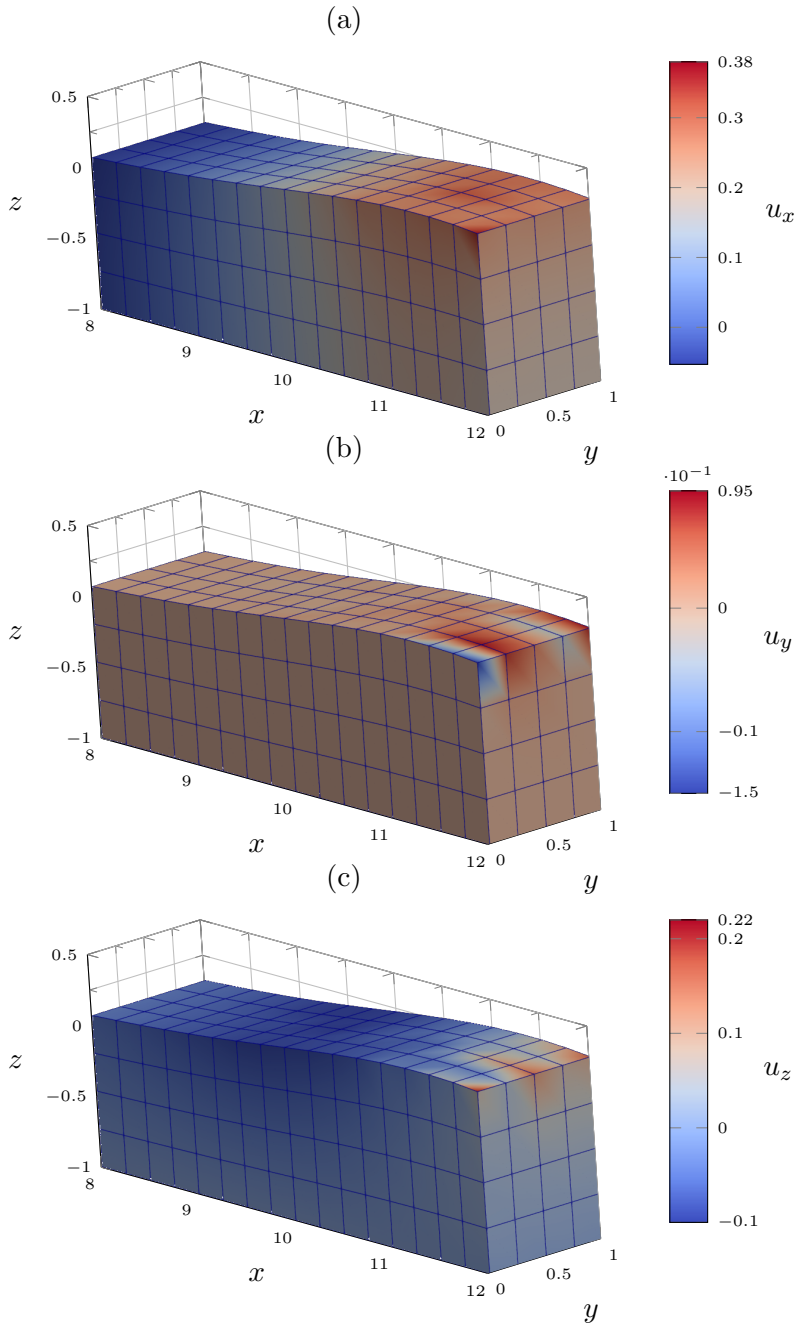

Figure 3.6: Velocity components in the leftmost potential domain (*seine3d* 1) at the time $t = 10$ when free surface instability is detected. It appears that velocity continuity is not realized at edges and corners related to the face receiving coupling Neumann condition from *CS* 1.

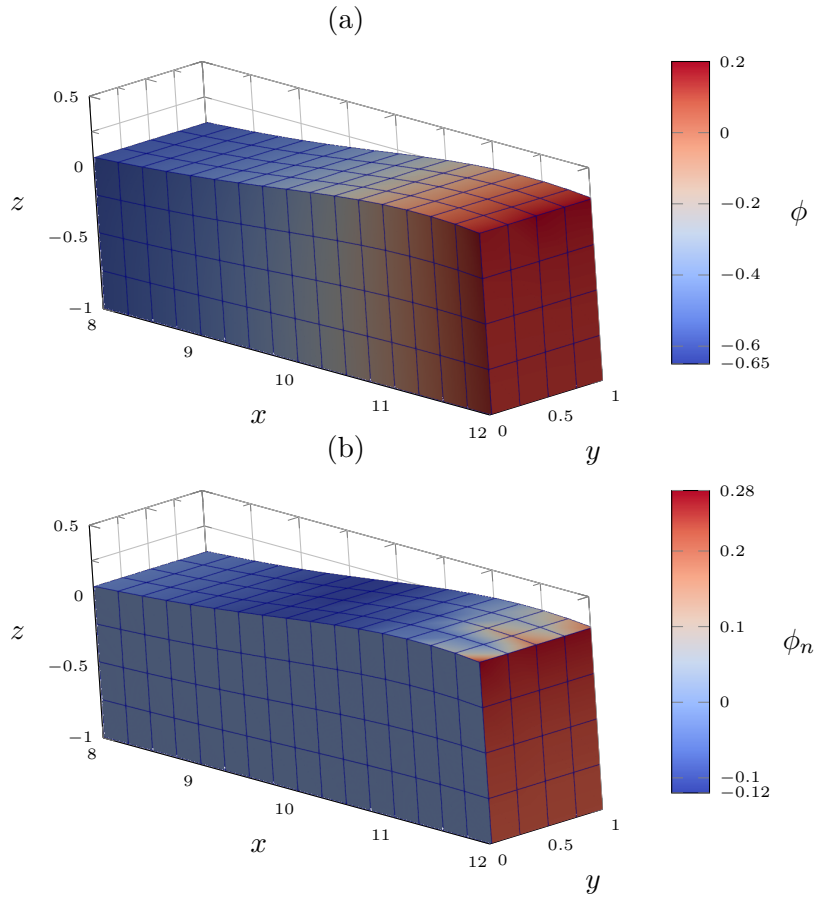

Figure 3.7: Scalar fields of the velocity potential ϕ (a) and its normal derivative ϕ_n (b) in the same *seine3d* domain at $t = 10$.

3.1.3 Relevance of free surface potential relaxation

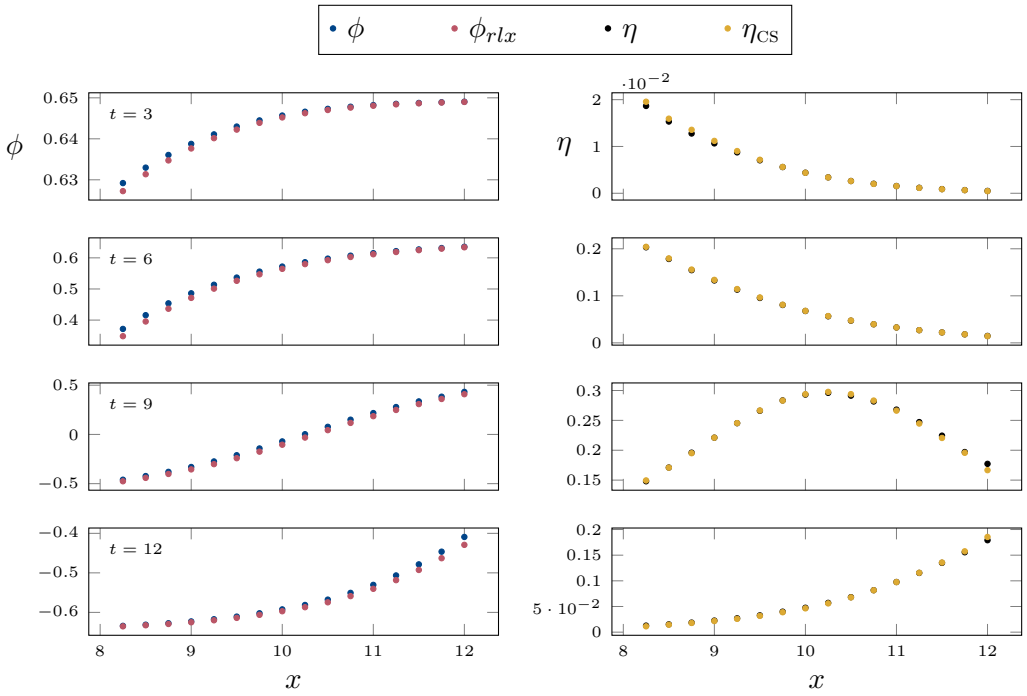

Figure 3.8: *seine3d* free surface geometry and free surface velocity potential in the left overlapping region in the reference case where computed free surface potential ϕ is not relaxed towards reconstructed solution ϕ_{rlx}. Left column : comparison of ϕ and ϕ_{rlx}. Right column : comparison of free surface position η computed in *seine3d*, before free surface relaxation and *CS* solution η_{CS}.

In section 2.6.4, a description is made of the velocity potential relaxation strategy at the free surface of overlapping regions. As written in section 3.1.2.1, potential relaxation is deactivated in the reference case. It was indeed found that to compute the propagation of a solitary wave through coupled domains, adapting the free surface potential to comply with *seine3d* free surface changes is not necessary nor beneficial to the simulation.

In this section, we present computational results that illustrate the effect of potential relaxation and justify this assertion. Nevertheless, it should be noted that in general, relaxation of *seine3d* free surface towards *CS* solution is necessary for both stability and accuracy in coupled simulations. Figure 3.8 shows free surface geometry and free surface potential at four time instants when the solitary wave crosses the left overlapping region common to *seine3d* 1 and *CS* 1. ϕ corresponds to the velocity potential in *seine3d* 1, as computed after the first resolution of the boundary value problem, prior to free surface relaxation. The reader can refer to section 2.6.3 for a reminder of the coupled time stepping procedure. ϕ_{rlx} is the potential solution built from *CS* η_{CS} free surface signal.

It might be seen in this figure that *seine3d* free surface signal η differs only slightly from η_{CS} over the length of the overlapping region. η_{CS} serves as a reference for free surface

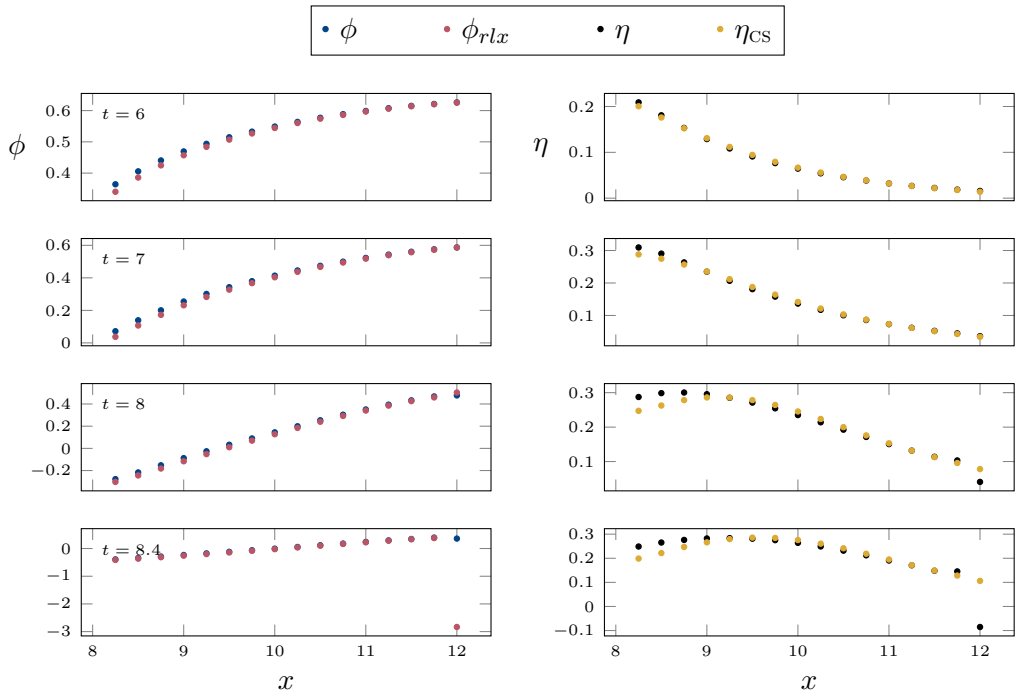

Figure 3.9: *seine3d* free surface geometry and free surface velocity potential in the left overlapping region up to the failure of the simulation when velocity potential relaxation is used, and comparison with and η_{CS} and ϕ_{rlx}, respectively.

relaxation. η is indeed forced towards η_{CS} thanks to a spatially-varying coefficient (see equation 2.31), so that both profiles exactly match at the right (*CS*) end of this coupling region. This explains why a small discrepancy exists between η and η_{CS} at the left side of the displayed area at $t = 3$, that vanishes afterwards. At $t = 6$, both profiles match over the full length of the domain, thus the need for and the effect of free surface relaxation are negligible.

Hence, it is interesting to compare values of ϕ and ϕ_{rlx} at the same time instant. As the relaxation of free surface is insignificant, ϕ_{rlx} that is based on η_{CS} should also be close to ϕ. It happens to be the case in most of the coupling area, therefore suggesting that the potential reconstruction procedure described in section 2.6.4 is relevant.

The same type of conclusions might be drawn from the next time instants, at which one should also note that free surface positions differ at the very right end of the coupling region. As only the *seine3d* corner node is concerned, we link this event to the above-mentioned corner instability .

Hence, from figure 3.8, the free surface potential reconstruction method seems valid but potential relaxation does not appear to be necessary to obtain accurate and sufficiently stable results. Let us now study the effect of the relaxation of ϕ towards ϕ_{rlx} on the same solitary wave in figure 3.9. In this figure, simulation results are displayed up to $t = 8.4$ when the computation fails. From $t = 6$ to $t = 8$, ϕ and ϕ_{rlx} are close to each other, in a

fashion similar to the reference case. During the same time interval however, free surface signals do not match as well as before, as the *CS* profile loses height on the left side of the coupling region. At $t = 8$, a strong discrepancy is seen at the corner node on the other end. This divergence in free surface position worsens up to $t = 8.4$, when the instability of *seine3d* 1 computation is manifest. Corner position error also leads to the computation of an erroneous value of ϕ_{rlx} at the same time instant.

It appears that the relaxation of free surface potential towards ϕ_{rlx} yields a divergence in free surface positions between *seine3d* and *CS* instances, with the *CS* profile deviating from the theoretical solution. The *CS* wave profile is indeed indirectly modified by the potential relaxation. A striking finding is that ϕ_{rlx} nevertheless remains close to ϕ, thus indicating that ϕ_{rlx} does not depend much on η_{CS}, at least in this case. A stronger corner instability than in the reference case in *seine3d* leads to the failure of the simulation anyway.

3.1.4 Time evolution of errors on wave shape and wave celerity

3.1.4.1 Building a common free surface signal

To compute errors relative to wave shape and wave celerity, it is necessary at first to build a global free surface signal from the geometry of potential domains *seine3d* 1 and *seine3d* 2 as well as from *CS* void fraction field. For the current 2DV application, results are saved for every instance of both models at each *seine3d* time instant, corresponding to a synchronization step in the coupling strategy. Hence, time interpolation is not needed to post process results.

As in *seine3d* results files contain information about domain geometry that is limited to boundary nodes coordinates and the associated connectivity list, the high-order nature of the boundary elements might be lost. Bi-cubic B-spline elements are indeed employed to discretize the boundaries of the potential domains in all the simulations presented in this thesis. Hence, boundary elements are rendered as planar facets in visualization tools such as Paraview (Ahrens et al., 2005), causing errors in the representation of the free surface geometry between nodes. To recover reliable free surface spatial profiles in potential domains when post-processing 2DV simulations, an interpolation method associating piece-wise cubic splines to *seine3d* free surface nodes at every time instant is implemented in a Python script.

As already stated, in the *CS* domain, the free surface geometry is not explicitly known but should be deduced from the void fraction field. The reconstruction of the free surface in the coupling region taking place during the coupling procedure, as described in section 2.5.2, is only valid to get a loosely discretized free surface signal near certain *seine3d* boundary nodes. Integrating void fraction field along the vertical in every *CS* water column, *i.e.* at every unique horizontal cell center position, as done in the coupling would thus prove computationally intensive and not as efficient as available post-processing tools. Paraview provides the appropriate *Contour* numerical filter based on linear interpolation

that allows to compute void fraction isosurfaces quickly enough for the considered post-processing task. This tool is used in a Python script, alongside with the above-mentioned cubic B-spline interpolation method for *seine3d* free surface, as it is possible to call Paraview functions in a Python shell thanks to the *Paraview Simple* library. Free surface is then defined in *CS* in the *Contour* filter as the set of points verifying $\alpha(\mathbf{x}) = 0.5$. Such cloud of points is in general sufficiently dense to provide a reliable free surface profile for visualization purposes.

Furthermore, the overlaying of numerical domains in the two coupling regions requires specifying how free surface profiles are calculated in these areas. The following and partly arbitrary choice was made: free surface signal in the overlapping areas reduces to *seine3d* free surface signal. This was motivated by the observation that the potential profile is in general smoother than its NS counterpart, due to the fact that is it explicitly known and its high-order nature.

From this post-processed global free surface signal comes the ability to compute the wave height H as the highest position reached by the free surface and the wave crest position x_c as the associated abscissa.

3.1.4.2 Computing errors

Following a rather qualitative description of the simulation results for the reference case of solitary wave propagation, a study quantifying conservation of wave characteristics is conducted. To that end, relative errors on wave height (ϵ_{H}), wave crest location ($\epsilon_{x_{\mathrm{c}}}$) and wave width at half height ($\epsilon_{\Delta x_{\frac{1}{2}}}$) are computed as functions of time:

$$\epsilon_{\mathrm{H}}(t) = \frac{H(t) - H_0}{H_0} \tag{3.2a}$$

$$\epsilon_{x_{\mathrm{c}}}(t) = \frac{x_c(t) - Ct}{h} \tag{3.2b}$$

$$\epsilon_{\Delta x_{\frac{1}{2}}}(t) = \frac{\Delta x_{\frac{1}{2}}(t) - \Delta x_{\frac{1}{2}0}}{\Delta x_{\frac{1}{2}0}} \tag{3.2c}$$

H_0 stands for the reference wave height, C for the reference wave velocity, and $\Delta x_{\frac{1}{2}}$ is the width at half wave height while $\Delta x_{\frac{1}{2}0}$ is its initial value.

3.1.4.3 Time history of conservation errors

Time history of errors on wave height, wave crest location and wave width are displayed in figure 3.10. Wave crest passing in the middle of successive coupling regions are shown under the form of colored vertical lines. These events match most major curve inflections quite well.

We see that wave height error is negligible for most of its travelling time in the initial

potential domain *seine3d* 1, corresponding to the first 5 time units when the influence of *CS* on wave propagation in the potential domain is still small. From approximately $t = 5$ to $t = 10$, wave crest crosses the leftmost coupling region. Approximations on height computation lead to a noisy height signal but a general trend is seen in which wave height decreases, with the associated relative error ϵ_{H} reaching -0.01. Starting from $t = 10$, *seine3d* 1 domain is close to recovering its resting position as the water hump travels in the *CS* domain while regularly losing height until around $t = 23$ when the wave crest crosses the middle of the second coupling zone. Then, in domain *seine3d* 2, wave height increases again and later stabilises around an error of -0.014. This graph clearly indicates the distinct behaviours of the solitary wave in the different domains. Resolution of the NS equations with VOF capture of the free surface is known to suffer from spurious numerical diffusion, and it seems that this phenomenon can be observed here. It should be noted that the fully nonlinear potential flow model has proved able to propagate waves over long time and distance with very good conservation properties. The height signal in the left overlapping region features many more disturbances and a higher global height variation than in the right one. The existence of couplings is globally detrimental to the simulation accuracy, even if such effect remains limited. The lowest wave height is not reached at the end of the simulation as wave grows while entering domain *seine3d* 2. This phenomenon is more annoying than excessive diffusion because it means that numerical errors lead to an increase in wave energy.

Crest location error plot shows higher error levels, with a strong peak exactly matching the passing of the wave crest in the middle of the first coupling region. The noise level of the signal is also globally higher than for the previous signal. Crest location stays close to the calculated theoretical value while the solitary wave propagates in *seine3d* 1 domain. The subsequent series of high amplitude wiggles around $t = 9$ during wave transmission from *seine3d* to *CS* could be caused by errors in the computation of wave crest position. $\epsilon_{x_{\mathrm{C}}}$ and therefore wave celerity in the *CS* domain gradually increases as simulated wave slightly overtakes its theoretical counterpart. This advance steeply grows around $t = 22$ as the crest enters *seine3d* 2, then wave slows down continuously, down to a celerity inferior to the theoretical value.

The last curve, showing the variations of wave width calculated at half wave height displays the most pronounced coupling artifacts. Similar to previous error measures, $\epsilon_{\Delta x_{\frac{1}{2}}}$ remains very close to its initial value up to the moment when wave crest passes in the *CS* domain. Starting from around $t = 9$, the wave widens up to $t = 23$, when wave width diminishes and stabilises with a relative error under 0.01.

Observations about solitary wave propagation through the different coupled domains might be summarized in the following way: at first, the solitary wave propagates while globally retaining its characteristics. As the wave crest enters the *CS* domain, the wave starts vertically shrinking and widening while it also accelerates. After its reentry in a potential domain, the solitary wave regains a part of the height it has lost, while its width slightly diminishes and it decelerates.

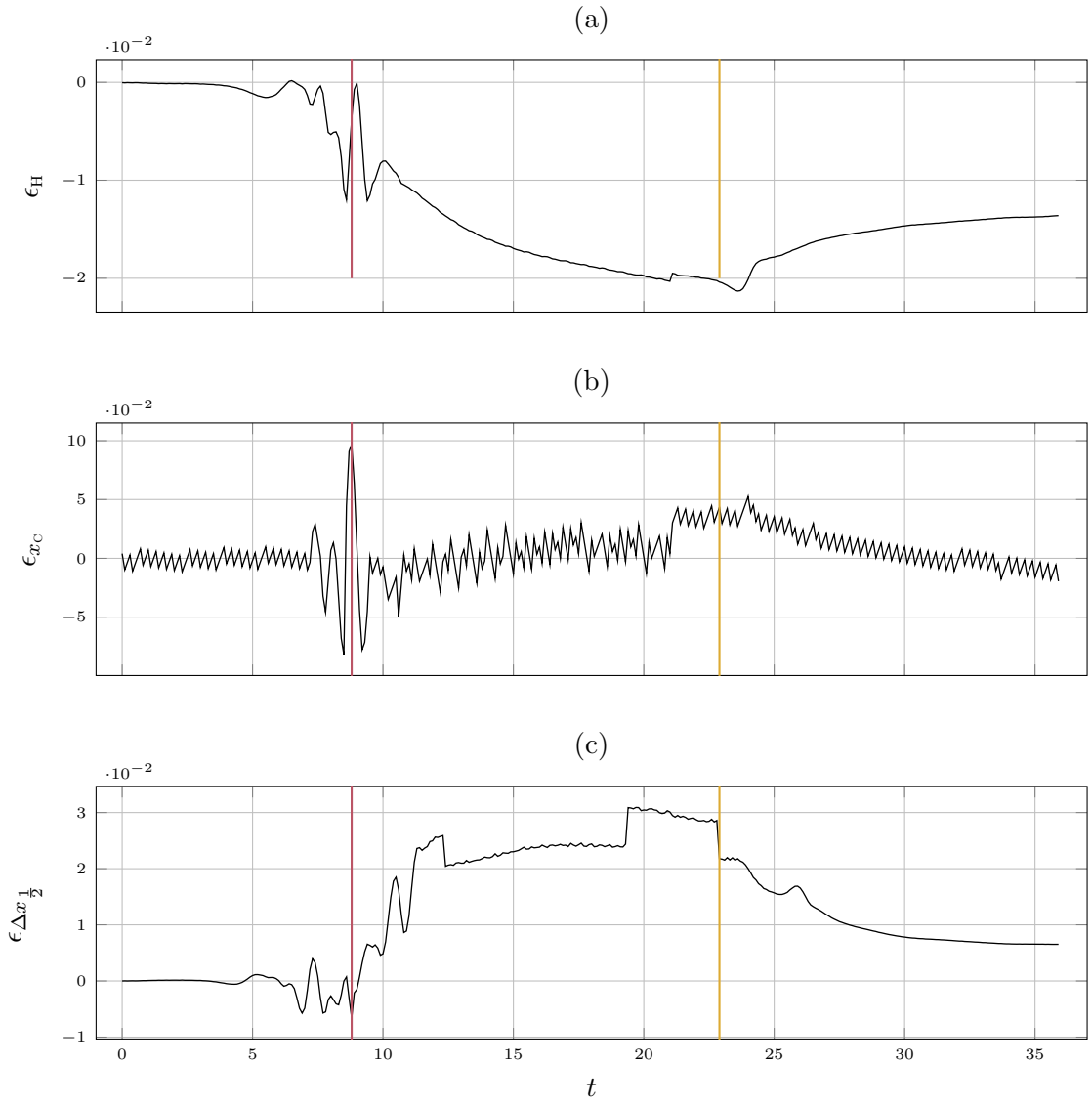

Figure 3.10: Time evolution of errors on wave height, crest position and width at half wave height for the solitary wave with $H = 0.3$. Time instants when wave crest passes in the middle of a coupling region are marked with vertical colored lines.

3.1.5 Influence of the principal coupling parameters

According to each code's behaviour when run alone, the quality of coupled simulations is strongly influenced by spatial and temporal discretizations in both models. An in-depth study of the sensitivity of coupling results to spatial and temporal discretization levels is nevertheless out of the scope of the current section. Hence, we focus on the influence of two major coupling parameters on the results. The need for the models to synchronize at certain time instants implies that temporal discretizations can not be established independently. Assessing the sensitivity of the results to time step values Δt_{CS} and $\Delta t_{seine3d}$ in each model thus implies that the influence of the time step ratio $N_{\Delta t} = \frac{\Delta t_{seine3d}}{\Delta t_{\mathrm{CS}}}$ is addressed. As $N_{\Delta t}$ increases and for given spatial and temporal *CS* discretizations, *seine3d* iterations and MPI coupling transmissions become less frequent, hence lowering the computational burden. $N_{\Delta t}$ is therefore a key parameter of the coupling strategy. The overlapping region length $L_{overlap}$ is of central interest too. Keeping it the smallest possible reduces the size of numerical domains and thus limits the computational cost associated to the execution of each model alone. Besides, as the overlapping region grows, and for a given size of *seine3d* boundary elements, the number of *seine3d* free surface nodes where *CS* free surface position is calculated gets larger. The computational costs of free surface extraction and consecutive free surface transmission to *seine3d* thus increase. However, diminishing $L_{overlap}$ also diminishes the length over which *seine3d* free surface geometry and potential are relaxed towards *CS* solution, potentially triggering instabilities.

It should then be possible to find trade-offs concerning the value of these two coupling parameters from the results presented below. Hence, we study the impact of variations of $N_{\Delta t}$ and $L_{overlap}$ on the coupled simulation of the propagation of a solitary wave with $H = 0.3$ over a uniform depth. As in the reference case, free surface potential relaxation is deactivated. *seine3d* instances are attributed 8 central processing unit cores (CPU cores) each while *CS* instance uses 2.

3.1.5.1 Influence of time step ratio

Fixed temporal and spatial discretization are used for *CS*, with $\Delta t_{\mathrm{CS}} = 0.01$ and $\Delta x_{\mathrm{CS}} = 2\Delta z_{\mathrm{CS}} = 0.05$. As a consequence, the CFL number for *CS* is set to:

$$CFL_{\mathrm{CS}} = \frac{\Delta t_{\mathrm{CS}}\sqrt{gh}}{\Delta x_{\mathrm{CS}}} = 0.2. \tag{3.3}$$

seine3d boundary elements are such that $\Delta x_{seine3d} = \frac{1}{4}$ and $\Delta x_{seine3d} = \Delta y_{seine3d}$. To modify $N_{\Delta t}$ while *CS* time step is fixed, $\Delta t_{seine3d}$ varies according to table 3.1.

It is to be noted that *seine3d* alone is able to simulate the propagation of the same solitary wave with these values of $\Delta t_{seine3d}$ and $CFL_{seine3d}$. Computations are considered stable, and their results are displayed in coming figures, if the wave reaches the right potential domain (*seine3d* 2) without major trouble. Otherwise, the results and associated errors on

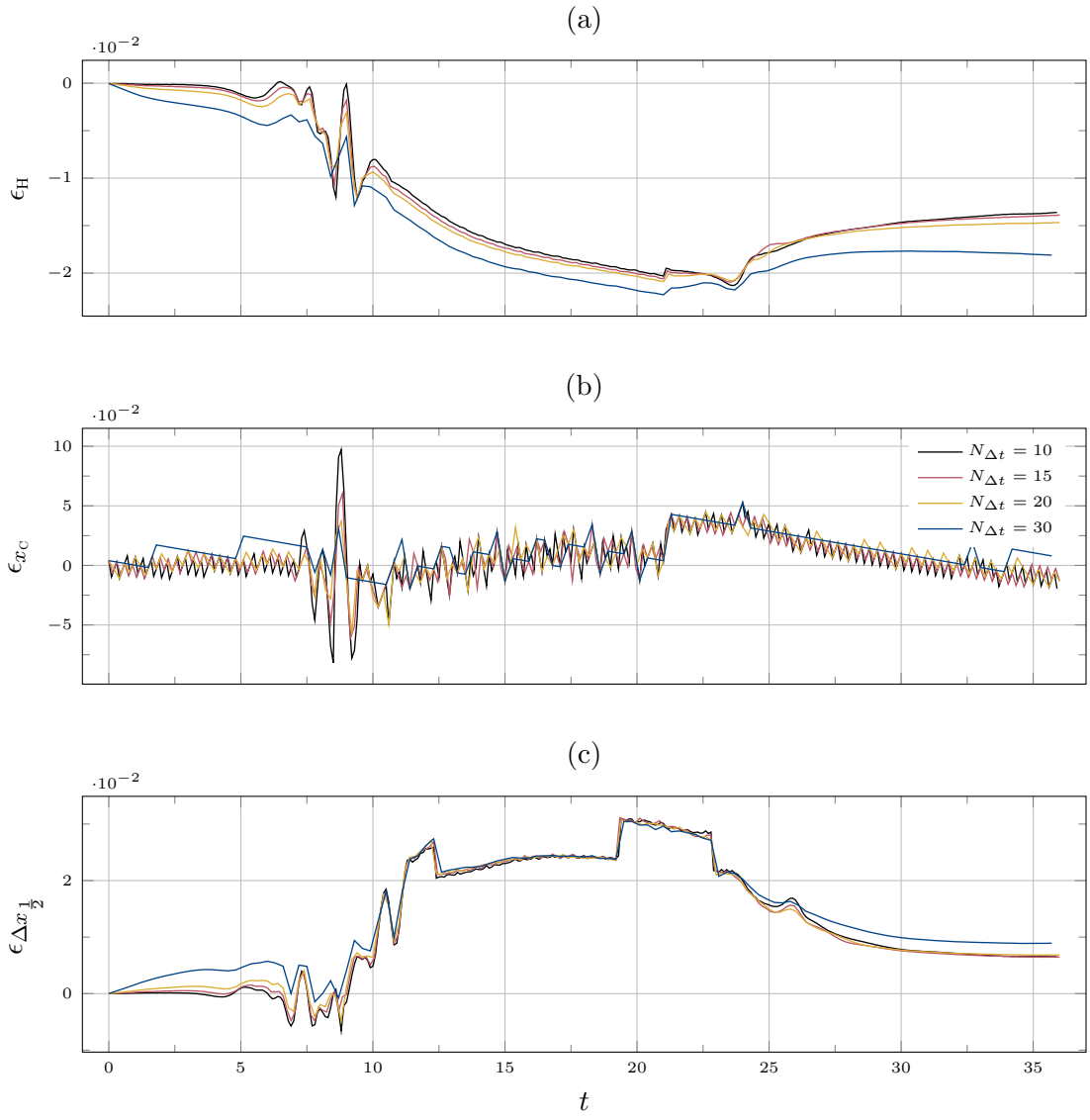

Figure 3.11: Influence of time step ratio $N_{\Delta t}$ on the characteristics of a solitary wave with $H = 0.3$ propagating over a constant depth. Only results from stable simulations are shown.

Table 3.1: $N_{\Delta t}$ and associated *seine3d* time and space discretizations.

$N_{\Delta t}$	$\Delta t_{seine3d}$	$CFL_{seine3d}$
1	0.01	0.04
5	0.05	0.2
10	0.1	0.4
15	0.15	0.6
20	0.2	0.8
30	0.3	1.2
50	0.5	2

wave height, crest position and width are not shown. Results are presented in figure 3.11, showing that computations with $N_{\Delta t}$ taking values of 1, 5 and 50 failed. In all these three cases, the hump of water did not manage to pass from *seine3d* 1 to *CS* 1, and simulations respectively stopped at time instants $t = 8.3$, $t = 11.4$ and $t = 11$ due to a failure in the execution of *seine3d* 1. Determining the exact phenomenon causing these failures exceeds the scope of the current section.

Errors on H, x_C, and $\Delta x_{\frac{1}{2}}$ with $N_{\Delta t} = 10$, corresponding to the above-mentioned reference case, are drawn in black. Looking at the whole network or curves, we note that only the case with $N_{\Delta t} = 30$ differs noticeably from the reference, nevertheless in this latter case absolute error levels remain reasonably low. The observations made in the analysis of the reference computational results globally hold for the four displayed cases. It seems therefore that the time interpolation method used to provide coupling boundary conditions to *CS* between *seine3d* time instants is accurate enough for time step ratio values ranging at least from 10 to 30.

As already written, the computational effort theoretically diminishes as $N_{\Delta t}$ increases. Computational resources employed are kept constant throughout the simulations, thus we can expect a speed-up in calculation time with growing time step ratio. Figure 3.12 gives an idea of the dependence of computational speed, defined as the ratio of physical time over computing time, on $N_{\Delta t}$. It is found to evolve linearly with a slope of around 0.0005. Besides, it should also be noted that computational speed can be considered constant throughout a given simulation. As an example, running a coupled simulation with $N_{\Delta t} = 20$, thus with 50% less *seine3d* iterations than in the reference case but the same number of *CS* time steps, is not twice as fast but approximately 66% faster. In other words, in the current 2DV solitary wave case, a computational bottleneck exists in *seine3d* instances, as global computing time can be greatly reduced without diminishing the number of computed *CS* instants. *seine3d* computational burden mostly divides into the computation of the potential Laplace problem on one side, and the extraction of internal velocity values aimed at *CS* on the other. As stated in section 2.7.2 and illustrated in figure 2.10, the same number of MPI processes is employed in *seine3d* and *CS* for a given

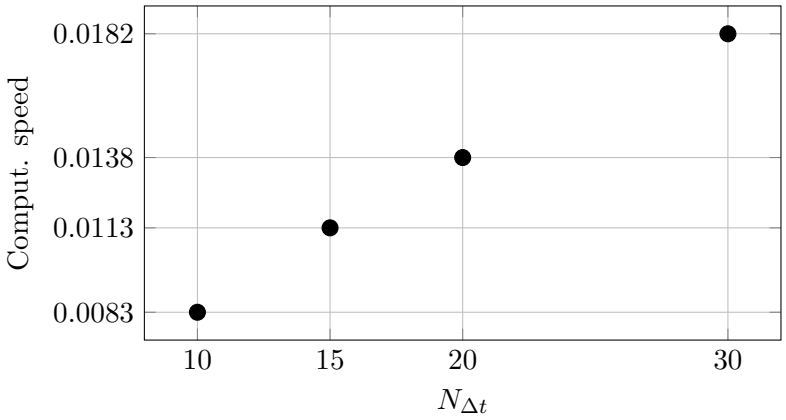

Figure 3.12: Computational speed, expressed as the ratio of physical time over computing time, for different values of $N_{\Delta t}$.

coupling, to deal with velocity extraction and exchange. *CS* 1 uses 2 MPI processes which run on 2 CPU cores, hence each established coupling ({*seine3d* 1, *CS* 1} and {*CS* 1, *seine3d* 2}) is associated with a single *CS* processor. If the boundary integral problem itself is the bottleneck of the coupled simulation, increasing the number of CPU cores for *seine3d* instances should speed-up the simulation. At the same time, if the limiting operation is the extraction of coupling velocity values, such increase will not accelerate the computation much.

Another simulation is then run for the reference solitary wave case ($N_{\Delta t} = 10$) with 16 processors per *seine3d* instance instead of 8. We measure a speed-up of around 53%. It is thus clear that the resolution of the Laplace problem in time is the limiting operation for the presented 2DV solitary wave cases. One may find surprising that potential computations end up needing that much computational resources as compared to the NS one, but it should be recalled that *CS* is 2D whereas *seine3d* is 3D with several boundary elements placed in the width of its domain.

3.1.5.2 Impact of overlapping region's length

The other parameter that emerges when *seine3d* and *CS* are coupled is the geometry of the overlapping region, thus its length $L_{overlap}$ in 2D. In the simulations whose results are displayed in figure 3.13, $L_{overlap}$ takes the values 4, 2 and 1 where 4 is used in the reference case. A case with $L_{overlap} = \frac{1}{2}$ was launched and failed. As $\Delta x_{\mathrm{CS}} = \frac{1}{4}$, such a short overlapping length only allows to place 3 *seine3d* nodes on the free surface of the coupling region. Obviously this value is too small, and should be taken as strict lower bound for further simulations.

Case with $L_{overlap} = 2$ behaves similarly to the reference, with globally acceptable error levels. However it locally features high absolute levels of $\epsilon_{x_{\mathrm{C}}}$ around $t = 8$ when the wave passes from *seine3d*1 to *CS* 1. Case with $L_{overlap} = 1$ shows a better time profile of $\epsilon_{x_{\mathrm{C}}}$ but

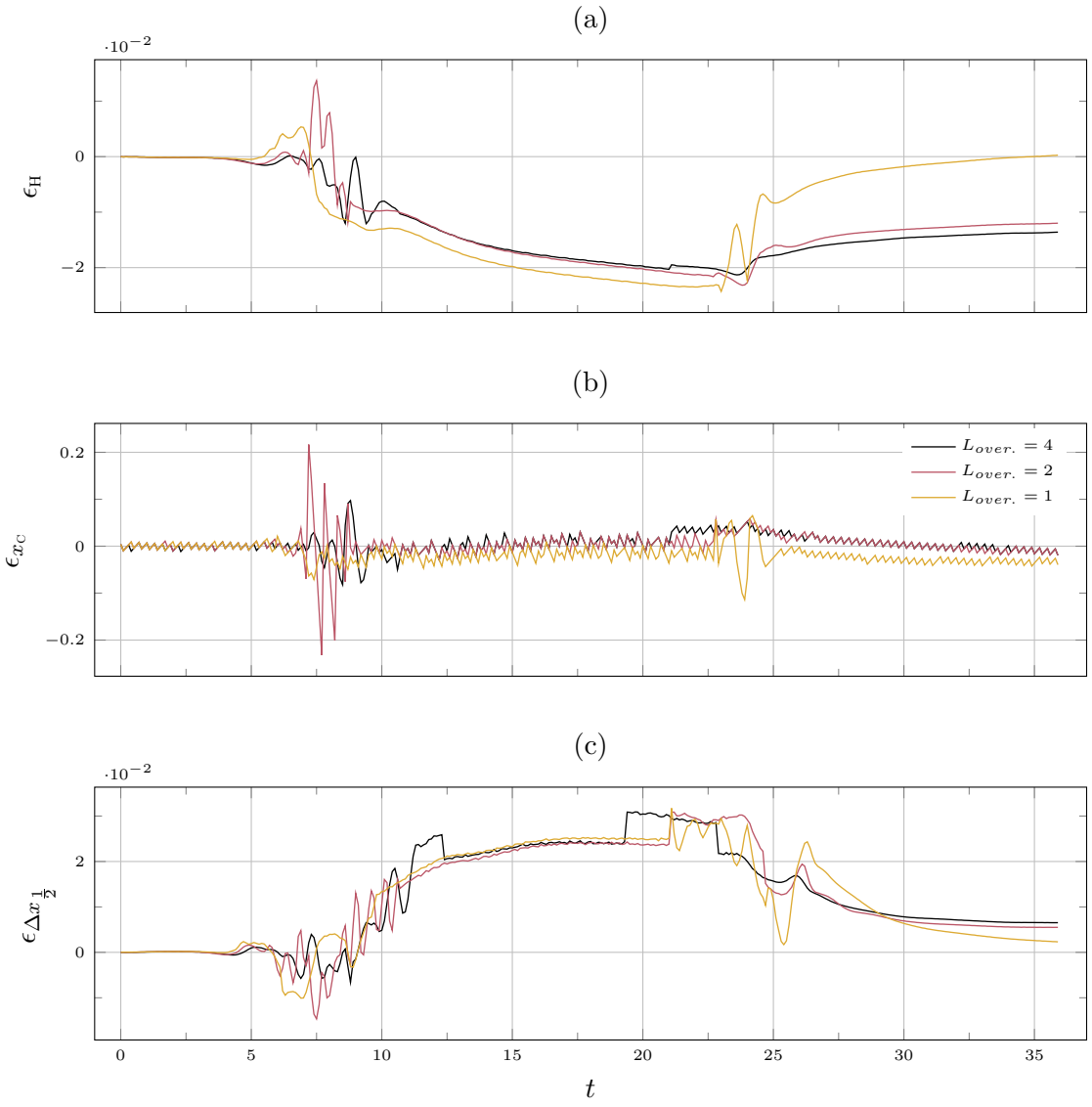

Figure 3.13: Influence of the width of overlapping regions on characteristics of a solitary wave with $H = 0.3$. Only results from stable simulations are shown.

also a concerning patterns when it comes to ϵ_{H}, with strongly re-increasing wave height when the crest arrives in *seine3d* 2.

A value of 4 then seems to be a correct trade-off for 2DV solitary wave simulations, as $L_{overlap}$ has little influence on the computational speed. Indeed as explained in the previous sub-section, the main computational bottleneck for this case is the boundary integral problem, therefore greater free surface position extraction and transmission cost in *CS* related to a longer overlapping region are negligible. Furthermore, reducing $L_{overlap}$ from 4 to 2 for example only slightly reduces the number of *seine3d* nodes, and thus the size of the potential problem's matrix.

3.2 Solitary wave of high relative height over constant depth

In this section, we present the results of simulations of solitary wave propagation with $H = 0.5$. A first try is made with the exact same setup as used in the reference case with smaller wave amplitude: $N_{\Delta t}$ is set to 10 and $L_{overlap}$ to 4. Meshes are kept identical. This combination of numerical parameters does not prevent the simulation from diverging around $t = 9$ when the wave crest leaves *seine3d* 1 domain to enter *CS* 1. Again, *seine3d* 1 is the failing model instance. A view of its mesh, along with *CS* 1 void fraction field, is shown in figure 3.14. Note that the x axis is reversed, as the free surface saw-tooth instability is at first limited to the side with equation $y = 1$. This time, no corner instability is detected, as opposed to what happens in the reference solitary wave case.

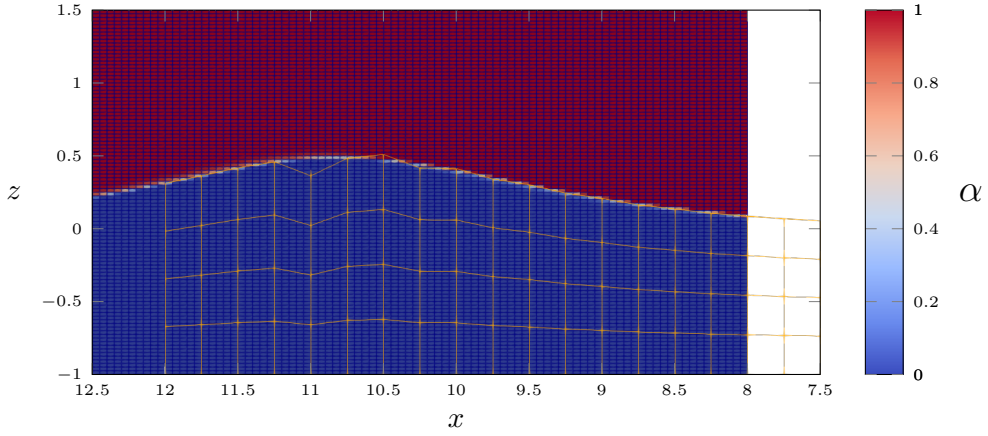

Figure 3.14: Close-up view of the meshes in the left coupling region at $t = 8.9$ just before the solitary wave simulation with $H = 0.5$ fails. The void fraction field $\alpha(\mathbf{x})$ in the *CS* domain is shown with corresponding colorbar. Note x-axis is inverted. *seine3d* mesh is displayed in orange.

Other trials were made with different values of $N_{\Delta t}$, $L_{overlap}$, as well as time and space discretization levels in *seine3d* and *CS*. None of these changes allowed satisfying simulations of the high amplitude solitary wave propagation, as most of them stopped at approximately

the same time instant.

In a rather counterintuitive but efficient manner, changing the length of *seine3d* 1 domain and leaving the overlapping region unmodified yielded substantial improvements. The left potential domain, spanning from $x = -12$ to $x = 12$ with $x = 0$ as the initial crest abscissa in all previous simulation setups, was shortened to $[-8; 12]$.

The associated free surface profiles are presented in figure 3.15. Wave propagation is satisfactory. Spurious small waves are seen on the back of the wave, illustrating again the fact that the two couplings are not fully transparent.

The time history of errors on wave height, wave crest position and wave width is shown in figure 3.16. The time profiles are clipped after $t = 30$ as the solitary wave starts interacting with the fully reflective vertical wall at the right end of the *seine3d* 2 domain afterwards. On average, error levels are higher than in the case with $H = 0.3$. Indeed, the solitary wave loses up to 4% of its height. As previously observed, it accelerates while passing from *seine3d* 1 to *CS* 1 and decelerates while entering *seine3d* 2 domain. This constant decrease in speed might be due for part to the existence of the wall, at the position of which the wave speed should drop to 0. Guillou et al. (2000), using an analytical solution formulated by Laitone (1960), established that the interaction of a solitary wave with a vertical wall might be neglected if the distance d from its crest to the wall verifies:

$$d \geq \frac{6.9}{2}\sqrt{\frac{1}{H}} \tag{3.4}$$

It should be recalled that d is normalized by the unitary water depth h, as is H. With $H = 0.5$, we find that d should be greater than 10, therefore x_C should stay below 38. A look at the free surface profiles tells us that $x_C = 38$ when $t = 31.3$. Therefore continuous wave slow-down seems quite independent from wave reflection at the wall. Besides, the moving hump of water tends to widen during its travel, as the evolution of $\epsilon_{\Delta x_{\frac{1}{2}}}$ tells.

While it is possible to recreate and propagate highly nonlinear waves in the present coupled model, it comes at the cost of constraining choices relating to the geometry of *seine3d* 1 domain. For that reason, this solitary wave study is not pushed further, as the coupled model has shown satisfactory behavior with moderately high solitary waves.

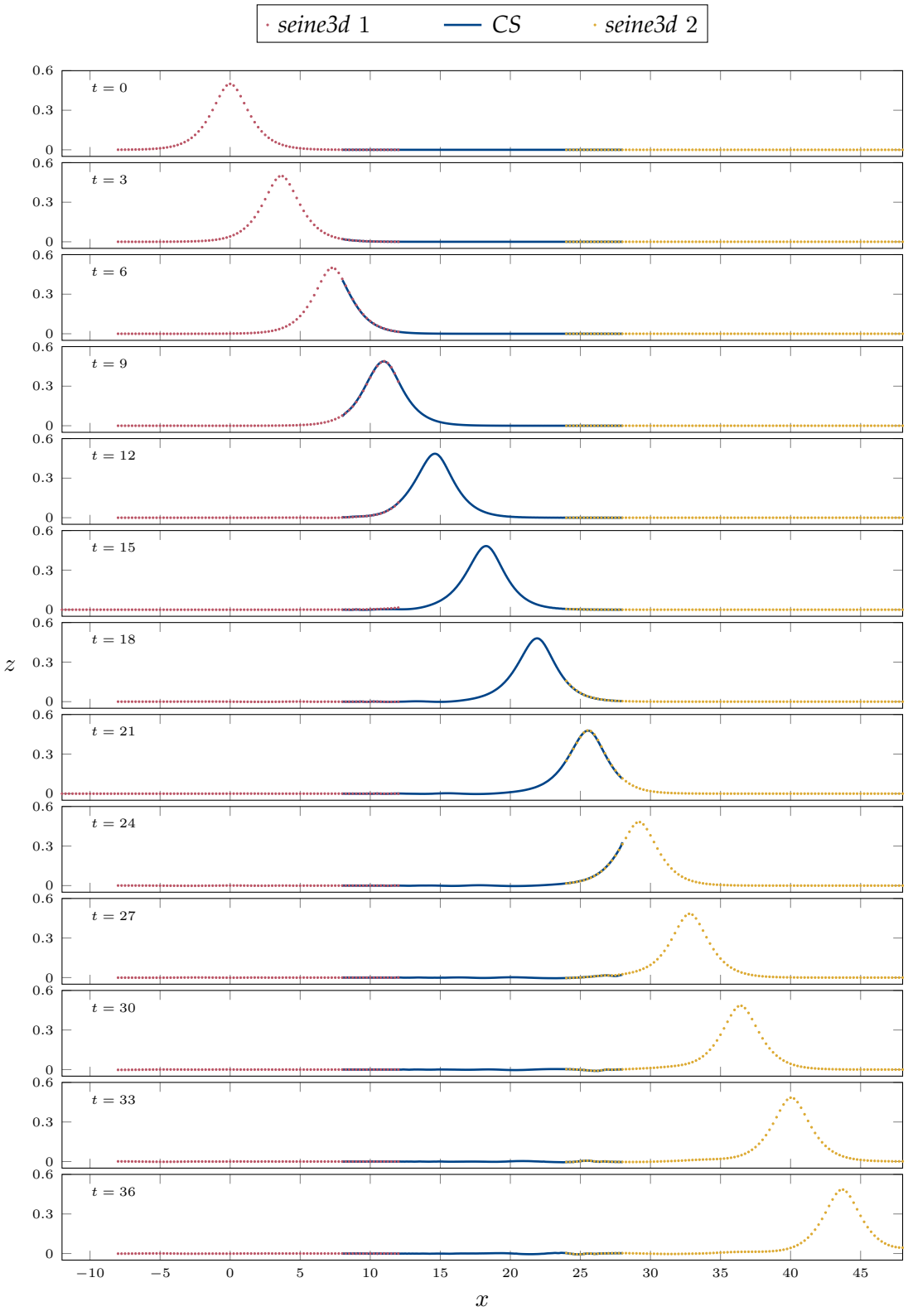

Figure 3.15: Time history of free surface profiles for a solitary wave with $H = 0.5$.

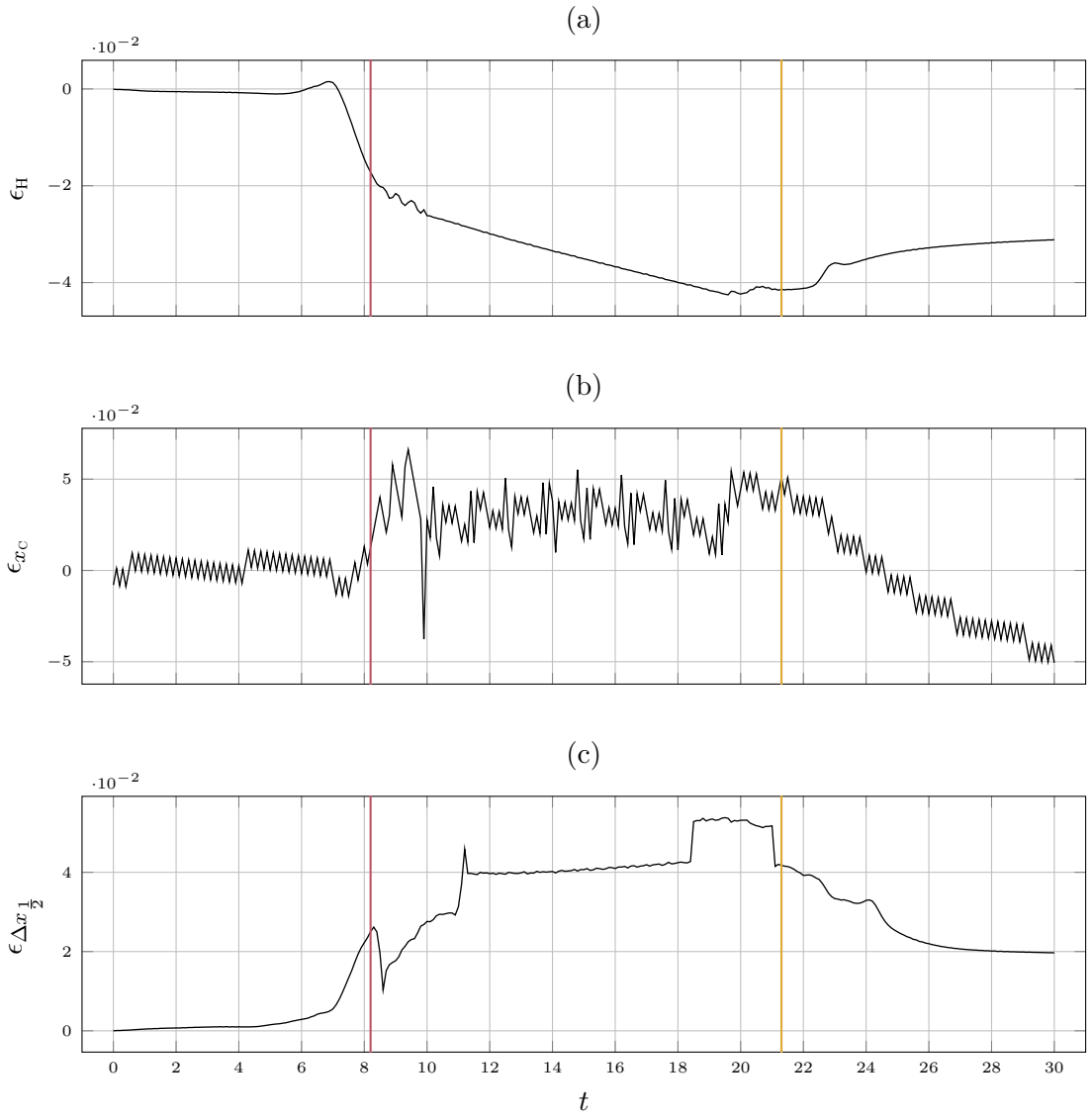

Figure 3.16: Time evolution of errors on wave height, crest position, and width at half wave height for the solitary wave with $H = 0.5$. Time instants when wave crest passes in the middle of a coupling region are marked with vertical colored lines.

3.3 Conclusion

In this chapter, it has been demonstrated that the hybrid strategy succeeds at simulating the propagation of a solitary wave over constant water depth through multiple coupled model instances. Indeed, the traveling solitary wave manages to cross successive and heterogeneous numerical domains and overlapping regions without excessive changes of its characteristics. Such observation, made for moderate as well as important relative wave heights, allows to verify that the implemented coupling procedure is bidirectional.

The developed model shows a relative flexibility, as various combinations of coupling parameters, as well as time and space discretizations, enable quite accurate computations. However, limits of the hybrid procedure were also highlighted, especially in terms of stability. Stability issues appear to systematically stem from a *seine3d* instance, and appear to be correlated to certain values of the major coupling parameters. General rules aiming at setting the values of the latter were thus stated. These should be confirmed or reversed by further studies.

Hence, the BEM-VOF coupling is not fully transparent and is a source for numerical instability and errors, but satisfactory simulation results were obtained without too much trial and error iterations in the search for working settings. This is an auspicious finding when it comes to simulating other 2DV and 3D wave problems. It should be noticed that a similar case of solitary wave propagation, but with a smaller relative wave height of $H = 0.20$ was investigated with an overlapping 3D two-way coupling model in the already mentioned article of Lu et al. (2017). In the reported simulation, the wave only travels from an initial potential domain to a viscous domain, hence a unique coupling region is considered. It appears that in this case, errors on wave height and velocity are greater than in the current study. Zhang et al. (2013) also report on a solitary wave propagation with relative height close to $H = 0.6$, to which results presented in section 3.2 could be related. Their non-overlapping domain decomposition strategy succeeds at propagating such a solitary wave through domains of both types. Discrepancies are noticed, as compared to some numerical reference results, in term of wave height and local higher order free surface elevation derivatives when the wave crest crosses the common boundary. The results presented in the current work for $H = 0.5$ in figure 3.16 (b) seem smoother and more accurate.

Investigations were also conducted about the relevance of relaxing the free surface velocity potential in *seine3d*, in overlapping regions, towards a value accounting for changes made to the free surface position. It seems that it is of no interest, and even detrimental, to either stability or accuracy of the coupled computations, at least in the way it is currently implemented. Therefore, potential relaxation is disabled in coming simulations. Again, this calls for further investigations, as relaxing the free surface potential could help increase the quality of hybrid results as well as it could widen the method's range of application.

Chapter 4

2DV regular waves simulations in the hybrid model

La méthodologie de couplage est mise en œuvre dans ce chapitre pour simuler la propagation d'une houle régulière non-linéaire en profondeur constante, en deux dimensions. La géométrie du domaine d'étude, ainsi que les caractéristiques de la houle incidente sont issues des expériences menées dans le cadre du projet WAS-XL. La houle retenue présente une période de 15s et une cambrure égale à $\frac{1}{40}$. Comme préalable à la réalisation de calculs couplés, la génération, la propagation et l'absorption de houle sont reproduites séparément dans des simulations n'impliquant qu'un seul code de calcul à la fois. De cette manière, les performances de chacun d'eux sont évaluées, et des combinaisons concluantes de paramètres numériques, portant notamment sur les niveaux de résolution spatiale et temporelle, sont proposées. A la suite de cela, une simulation couplée est conduite dont les résultats sont présentés de manière détaillée. Il est attendu que les choix de paramètres adimensionels retenus pour cette dernière puissent être directement appliqués à d'autres simulations en partageant le même domaine d'étude bidimensionnel, sur toute une gamme de périodes de houle notamment. On suppose également que la succession d'étapes décrite dans ce chapitre a valeur de guide pour de futures simulations couplées portant sur des problèmes d'interactions vagues-structures différents. Il est également espéré que l'essentiel des choix numériques opérés puisse être reproduit à l'identique avec succès dans des simulations en trois dimensions.

4.1 General considerations about 2DV regular waves coupled simulations

When looking for a second test-case for the developed coupled model, the simulation of 2DV nonlinear regular waves naturally comes to mind. Indeed it is a necessary step towards the calculation of 3D wave-structure interaction in periodic waves that is the final aim of this work. The experimental outputs of the WAS-XL (Wave loads and soil support for extra large monopiles) campaign Dadmarzi et al. (2019) are used as reference results for the computation of regular wave forces on a vertical cylinder representing a monopile OWT foundation. To set-up the 2DV study detailed in the current section, we then choose to use WAS-XL incoming waves parameters and domain geometry, in order to validate the generation, propagation, transmission from one coupled domain to the other, and absorption of periodic waves. Such preliminary work therefore enables choices to be made in terms of spatial and temporal discretizations in both models, as well as those related to the coupling parameters $L_{overlap}$ (length of overlapping region) and $N_{\Delta t}$ (time step ratio), with the intention of reusing most of them for later 3D studies. Better knowledge of the coupled model's behavior is also expected. As generation and absorption of regular waves are conducted in potential domains exclusively, correct absorption parameters in *seine3d* should be found prior to further tests. A quick analysis is realized and presented with this aim in mind. The nonlinear wave theory applied to generate waves is the so-called streamfunction method, or more precisely the Fourier series approximation of the streamfunction theory of Dean (1965), already implemented in *seine3d*. A depth-uniform horizontal current is added to the incident wave kinematics so that the net mass flux, averaged over a wave period, is zero, following Grilli and Horrillo (1997). This is equivalent to cancelling the Stokes' drift. Most coupled simulation results presented in this chapter are conducted with the lowest wave steepness $\epsilon = \frac{H}{\lambda} = \frac{1}{40}$ encountered in Dadmarzi et al. (2019), where H and λ are wave height and length respectively. Nevertheless, this 2DV study also serves the goal of determining the hybrid model limits, in particular in terms of wave steepness. Thus, some results with the highest steepness used in Dadmarzi et al. (2019) ($\epsilon = \frac{1}{22}$) are also presented.

4.2 Global simulation setup

4.2.1 Design waves from WAS-XL campaign

The wave steepness, period, and water depth to be tested in the coupled model are selected among WAS-XL experimental values. Contrary to the solitary wave case, here dimensional versions of spatial and temporal variables are used to make the comparison of the simulation outputs with WAS-XL results straightforward. Numerical results are obtained at full scale, while a 1:50 Froude scaling is selected for the models used in wave basin tests. Three wave periods of 9, 12, and 15 s are chosen that cover most of the span

of the experimental wave periods, ranging from 6 to 16.5s in Dadmarzi et al. (2019). To begin with, numerical simulations are set with the lowest depth value of 27 m and the smallest steepness $\epsilon = \frac{H}{\lambda} = \frac{1}{40}$ where H is the wave height.

Such a definition of wave steepness slightly differs from the one used in Dadmarzi et al. (2019). In the WAS-XL campaign indeed, steepness is defined as first order wave height divided by wavelength. It seems that the use of such definition involving the first order wave height and not the total wave height has to do with constraints related to the wave-making device employed in the wave basin. The motion of such piston-type wavemaker appears to be sometimes set according to linear wave theory, whatever the target wave steepness. Hence it calls for the use of the first order wave height in the calculation of the steepness. For strongly nonlinear waves, the wavemaker thus fails in that case at reproducing the target wave height and generates waves whose amplitude is lower than the desired value. In Dadmarzi et al. (2019) however, it is stated that a second-order correction of the piston motion is applied, to better account for the nonlinearity of the generated wave. In the current coupled methodology, fully-nonlinear wave kinematics are imposed at the inlet boundary of the *seine3d* upstream domain to generate waves, therefore steepness is computed as $\epsilon = \frac{H}{\lambda}$ with H the total wave height. Wave height and length are specified following the above-mentioned streamfunction algorithm of Dean (1965), in which no closed-form relation exists to link these two parameters. We then try a few subsequent combinations of wave height and length to roughly converge towards the desired steepness value, following a trial-and-error approach.

Characteristics of the waves with $\epsilon = \frac{1}{40}$ used in this 2DV study are summarized in table 4.1. It appears that the simulated waves all belong to the intermediate depth regime, as

Table 4.1: Characteristics of simulated waves with steepness $\epsilon = \frac{1}{40}$ and $h = 27$ m.

T (s)	λ (m)	H (m)	$\frac{h}{\lambda}$
9	114.446	2.86	0.236
12	171.366	4.28	0.158
15	226.673	5.75	0.119

for all three wave setups the relative water depth satisfies: $\frac{1}{20} < \frac{h}{\lambda} < \frac{1}{2}$.

4.2.2 Numerical domains

The hybrid numerical domain employed for coupled simulation is depicted in figure 4.1. It should be thought of as a projection of the 3D domain featuring the monopile on a vertical plane. In the WAS-XL experimental setup the distance between the monopile, located at $x = 0$ m and the wave generation side is specified as the abscissa of the latter is set to $x = -763$ m. Thus this fixed-length upstream generation and propagation region represents a variable number of wavelengths, depending on the wave period considered.

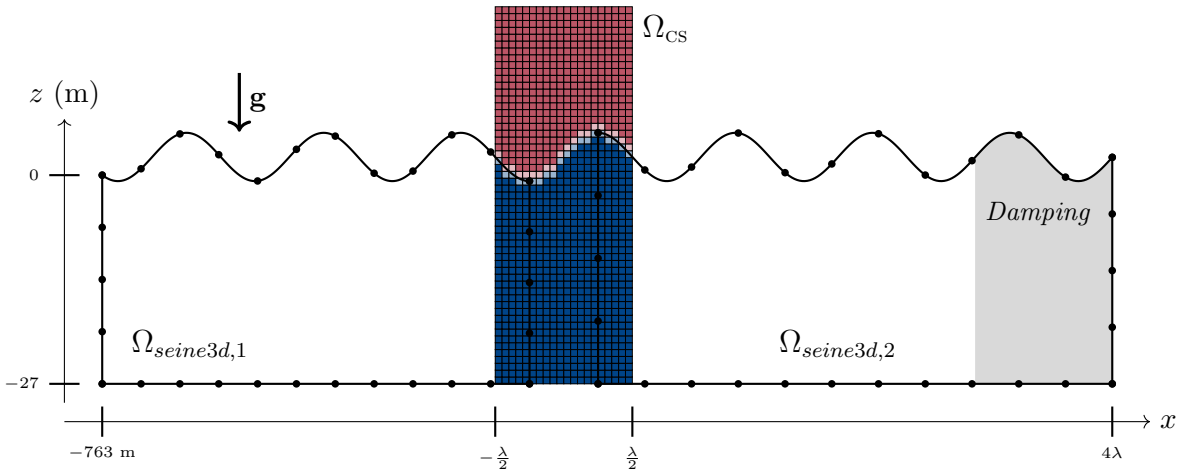

Figure 4.1: Coupled domains for periodic waves simulations. Blue *CS* cells are cells filled with water, while red cells are full of air. Pale blue and pale red cells contain a mix of the two phases. *CS* mesh and *seine3d* boundary elements are drawn for illustrative purposes only. Horizontal proportions are realistic and correspond to the case of $T = 15$ s. The area in shaded grey represents the damping region in $\Omega_{seine3d,2}$, long of one wavelength (reported in table 4.1).

For the largest wave with a period of $T = 15$ s (illustrated in figure 4.1), it still amounts to more than 3 wavelengths. This should be sufficient to accurately generate waves in potential domain *seine3d* 1. As can also be seen in the figure, the upstream region is mainly occupied by *seine3d* 1 domain, *CS* domain being restricted to one wavelength centered on $x = 0$ m.

On the contrary, the distance in the experimental wave basin from the monopile to the beginning of the absorbing beach is not specified. It is therefore arbitrarily set to 3 wavelengths. Again, we make the assumption that such distance will be large enough to propagate and absorb waves - mainly in potential domain *seine3d* 2 - with limited spurious interactions in 3D simulations between wave diffraction by the vertical cylinder and possible wave reflections on the downstream boundary of domain *seine3d* 2. As stated below, a one wavelength-long region at the downstream tip of *seine3d* 2 domain is used to absorb waves going out of the domain. Hence, a distance of 3λ is dedicated to wave propagation downstream of the virtual position of the bottom mounted cylinder.

4.3 Choosing the right parameters and discretization levels in *seine3d*

Prior to applying the coupling methodology to simulate regular waves, it is necessary to ensure that *seine3d* alone is able to generate, propagate, and absorb travelling waves. As already mentioned, generation and damping of waves are realized in potential domains during the hybrid computations, thus we should first make sure that they are mastered in

seine3d. The latter code should also prove capable of providing correct vertical profiles of velocity, thus anticipating their transmission to a *CS* instance.

4.3.1 Wave damping in *seine3d*

The major aspects of the wave damping strategy are described in this section. Calculation of damping region's reflection rate is then explained, and an attempt is made to minimize it.

4.3.1.1 Numerical damping strategy

The damping device made of a parabolic absorbing beach associated with wave dampers in the tank facility is numerically recreated in the downstream potential domain *seine3d* 2 with the help of a damping region. It is based on ad-hoc terms D_η and D_ϕ added to the right hand side of equations 2.9 and 2.10, respectively describing kinematic and dynamic free surface boundary conditions, as presented in section 2.1. As the time-marching strategy selected in *seine3d* is explicit, the damping terms are built from geometrical and kinematic values at current (n) time instant. Damping terms write:

$$\begin{aligned} D_\eta &= -\gamma_{abs}(z-\eta_{ref}(\mathbf{x}))\left(\frac{x-x_{abs}}{L_{abs}}\right)^2 \text{ if } x > x_{abs} \\ D_\phi &= -\gamma_{abs}(w-w_{ref}(\mathbf{x}))\left(\frac{x-x_{abs}}{L_{abs}}\right)^2 \text{ if } x > x_{abs} \end{aligned} \tag{4.1}$$

where x and z are coordinates of any *seine3d* free surface node whose position vector is $\mathbf{x}$ and whose vertical velocity is w. $\eta_{ref}(\mathbf{x})$ and $w_{ref}(\mathbf{x})$ stand for reference values towards which the vertical position and velocity of free surface nodes are forced. In the case of a damping region, these values are those of the hydrostatic solution for the undisturbed free surface:

$$\begin{aligned} \eta_{ref} &= 0 \\ w_{ref} &= 0 \end{aligned} \tag{4.2}$$

x_{abs} and L_{abs} are the starting abscissa and horizontal extent of the damping region respectively. A quadratic progression of D_η and D_ϕ on x is used. γ_{abs} is the damping strength, or damping intensity. If the same numerical value is used for γ_{abs} in both damping terms, physical dimensions differ. Rigorously speaking, two different variables should be employed, namely $\gamma_{abs,\eta}$ and $\gamma_{abs,\phi}$, with s^{-1} and $\mathrm{s}^{-1}\mathrm{m}^{-1}$ as respective units. To simplify the sensitivity analysis presented later, as already mentioned, it was quite arbitrarily decided to test the influence of a unique numerical value attributed to both $\gamma_{abs,\eta}$ and $\gamma_{abs,\phi}$. For this reason, and for the sake of brevity, damping intensity is simply referred to as γ_{abs}, without any specification of units nor distinction between associated free surface boundary equations.

γ_{abs} and L_{abs} should be tuned by the user, as to the author's knowledge, no generic

rule is available to choose their values beforehand. It is also expected that their values are somewhat related, as the damping intensity needed to absorb a given wave may not be independent from the distance over which absorption is realized. As in many wave simulation studies conducted with different physical assumptions and numerical solvers a length of $L_{abs} = \lambda$ is often used, this choice is repeated in the current work, bearing in mind that it is mostly arbitrary. Indeed, although it seems to be a suitable value, no sensitivity analysis related to L_{abs} and assessing the quality of the wave damping was made due to time constraints. For an in-depth description of the wave absorbtion strategy, the reader is referred to Grilli and Horrillo (1997).

The same cannot be said of γ_{abs}, whose value is modified in order to minimize wave reflection on the absorbing region. A quick and non exhaustive study on the influence of γ_{abs} on the reflection coefficient R associated to the damping region is thus realized. The method used to compute this coefficient is that of Goda and Suzuki (1976). It is described in detail in Appendix A.

4.3.1.2 Application to the wave with $T = 15$ s

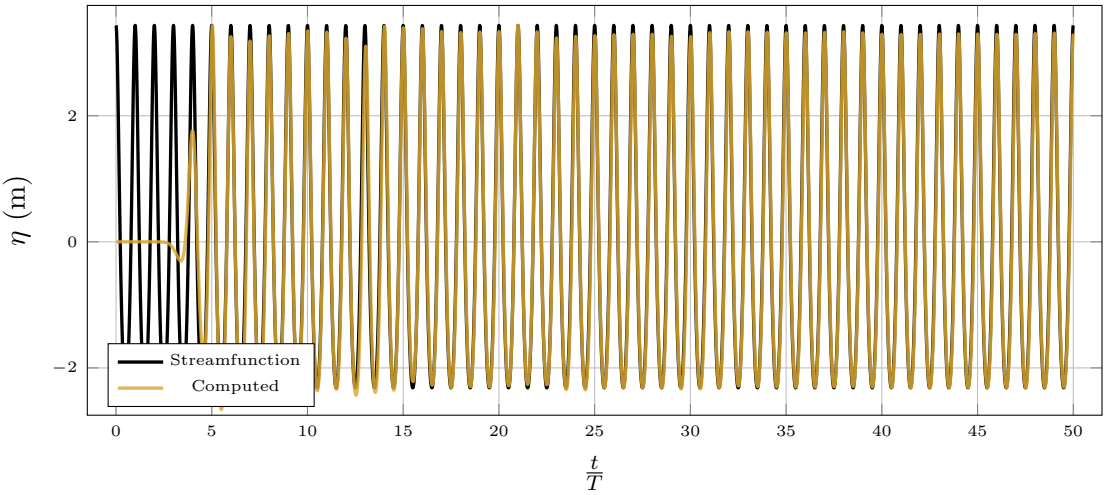

Figure 4.2: Comparison of the streamfunction and computed free surface signals at upstream wave gauge ($x_1 = 3\lambda$) used for the calculation of reflection coefficient.

A *seine3d* domain long of 5 wavelengths is used to find a value of γ_{abs} minimizing the reflection induced by the damping layer, in the case of a wave with $T = 15$ s and $H = 5.75$ m. The depth value of $h = 27$ m is retained. As already stated $L_{abs} = \lambda$. Wave gauges are respectively located at $x_1 = 3\lambda$ and $x_2 = 3.25\lambda$. The selected spatial and temporal discretization parameters are known to be suited to the simulation of wave propagation in *seine3d* alone and will serve as a basis for the coupled simulations to come. *seine3d* boundary elements are given longitudinal and vertical dimensions of $\Delta x = \frac{\lambda}{16}$ and $\Delta z = \frac{h}{4}$.

Time step is set to $\Delta t = \frac{T}{100}$. The CFL is therefore estimated as:

$$\text{CFL} = \sqrt{gh}\frac{\Delta t}{\Delta x} = 0.172 \tag{4.3}$$

The duration of the simulation is set to $50T$. Between 5 and 6 wave periods are computed in an hour with 16 CPU cores on the HPC cluster *Gaia*.

Figure 4.2 shows the streamfunction and simulated free surface position time histories in the most advantageous case with $\gamma_{abs} = 1$ and $R = 1.2\%$. Such a reflection rate is satisfactory and even though lower values may be attainable, they are not sought in this work. It should interestingly be noticed that the simulation takes approximately $20T$ to stabilize, with the occurrence of a few overshoots. Hence making such simulations last for $50T$ seems a reasonable choice, allowing to use $20T$ or $30T$ for the spectral analysis of the signals. Reflection rate R is also assessed for a few other values of γ_{abs}. Results

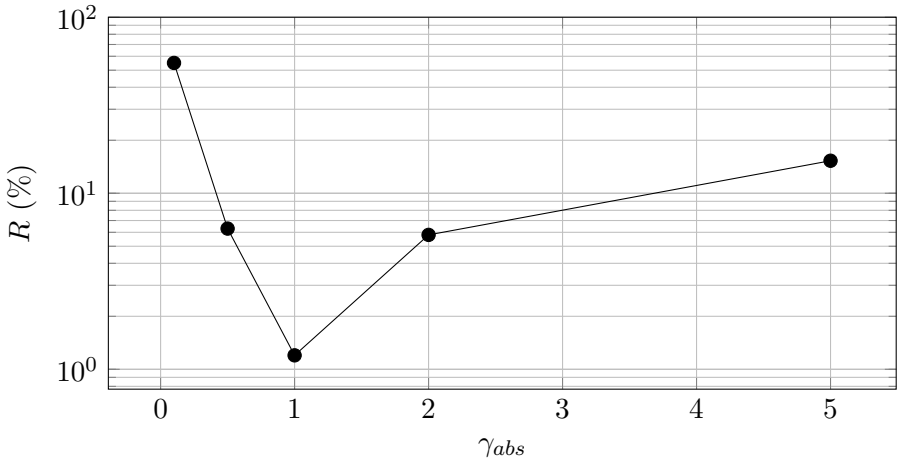

Figure 4.3: Influence of damping intensity on reflection coefficient measured upstream of the damping region.

are depicted in figure 4.3. It can be seen that the influence of damping intensity on wave absorption in *seine3d* conforms with what is intuitively expected. Indeed R reaches a minimum for a given value of γ_{abs}. As γ_{abs} increases, the damping region behaves more and more like a solid vertical wall. Thus if γ_{abs} is too high, strong wave reflection occurs, limited to the upstream part of the damping region. Conversely as γ_{abs} decreases, the absorbing layer tends to full transparency. For too small values of damping intensity, the waves are able to go through it without being sufficiently attenuated. Reflection then occurs on the downstream boundary of the numerical domain, that acts as a vertical wall imposing the nullity of the normal component of the velocity.

Some further tests were conducted on the same setup with different values of Δx and Δt. Very few changes to the previous results were noticed. Even if such sensitivity analyses were not designed to be exhaustive, it might reasonably be assumed that the optimal value of γ_{abs} does not depend on the spatial and temporal discretization levels.

This damping behavior still holds in the case of the other design waves considered in this study. Indeed, the same value of $\gamma_{abs} = 1$ also yields very low reflection rates for waves with $T = 12$ s and $T = 9$ s.

This is very interesting, as it implies that using $L_{abs} = \lambda$ and $\gamma_{abs} = 1$ should suffice to allow for efficient wave absorption in every regular wave coupled simulation of the present test conditions. On the contrary, wave damping in NS computations using damping layers built on source terms added to the momentum conservation equations and/or void fraction transport equation was found heavily dependent on incident waves characteristics as well as spatial and temporal resolutions. This way important time and efforts are saved in the selection of well-suited numerical parameters for the hybrid computations.

4.3.2 Choosing appropriate parameters for *seine3d* simulations

In the previous section, basis values of Δx, Δz and Δt have been introduced and employed in 2DV regular waves simulations with *seine3d* alone. Here, to evaluate more precisely the quality of such simulations, errors on wave height and phase shift are computed and tracked for the whole duration of the calculations.

4.3.2.1 Errors on wave height and phase

Wave height error and phase shift calculations are realized in a post-processing stage. They both rely on automatic detection of local maxima in the simulated free surface signal, thanks to the *Numpy* function already used in section A to establish FFT windows. Once abscissa and ordinate of each local maximum are known, they are compared to those of the nearest (in time) streamfunction local maximum, as predicted by the streamfunction theory. Normalized wave height error ϵ_{H} and phase shift ϵ_ϕ in degree are then defined as:

$$\begin{aligned} \epsilon_{\mathrm{H}} &= \frac{\eta_{sim.}^{max} - \eta_{an.}^{max}}{H} \\ \epsilon_\phi &= \frac{360\,(t_{sim.}^{max} - t_{an.}^{max})}{T} \end{aligned} \tag{4.4}$$

where $\eta_{sim.}^{max}$ and $\eta_{an.}^{max}$ are local free surface maxima of the simulated and streamfunction signal respectively. $t_{sim.}^{max}$ and $t_{an.}^{max}$ are the corresponding time instants.

4.3.2.2 Influence of spatial and temporal resolution levels on wave height and phase errors

To test the values of Δz and Δt used so far, a series of *seine3d* simulations is run with two values of Δt ($\Delta t = \frac{T}{100}$ and $\frac{T}{200}$) as well as two different values of Δz. The latter is replaced with N_z, with the following relation:

$$N_z = \frac{h}{\Delta z} \tag{4.5}$$

It should be noted that the influence of Δx is not treated here, for the sake of brevity. As very few discrepancies were noticed between cases using $\Delta x = \frac{\lambda}{16}$ and $\Delta x = \frac{\lambda}{32}$, only results with the largest value of Δx are displayed. Again as exhaustiveness is not sought, time evolution of ϵ_{H} and ϵ_ϕ are presented in figure 4.4 with three combinations of Δt and N_z. Time values are restricted to $[20T, 50T]$ in accordance with what was observed for the free surface signal. It appears that the wave height error is almost uninfluenced by changes made in the time step size and number of elements in the height of the water column. ϵ_{H} fluctuates between 2% -2.5% approximately, with a sensible peak at $t = 30T$. Normalized wave height error then stabilizes around -2% for the rest of the simulation. This peak is correlated to a phase shift extremum below $5°$. Values of ϵ_ϕ seem slightly

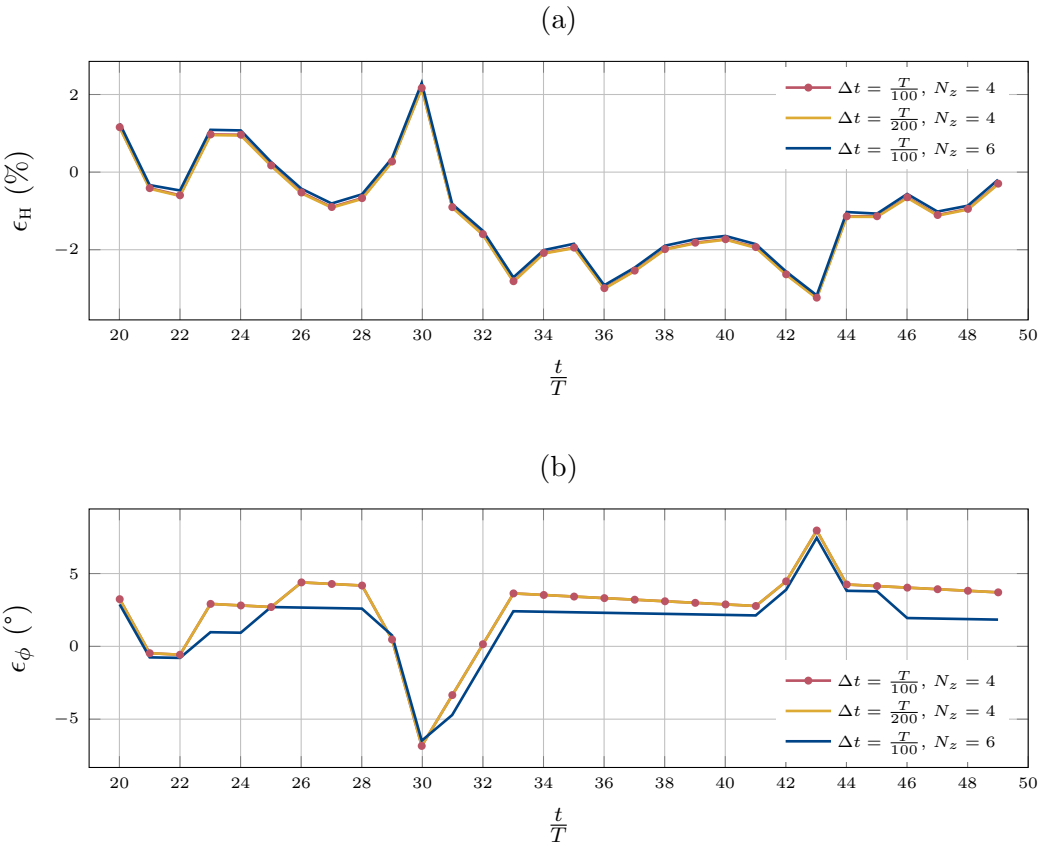

Figure 4.4: Phase shift (b) and relative error on wave height (a) at $x = 0$ m for *seine3d* alone. Longitudinal dimension of *seine3d* boundary elements is set to $\Delta x = \frac{\lambda}{16}$.

more sensitive to N_z, as compared to ϵ_H. Again, influence of Δt is found negligible and the fluctuation of phase shift values diminishes after $t = 30T$.

From these curves and figure 4.2, it also appears that almost 30 wave periods are necessary to reach a relative steadiness of the wave characteristics in this *seine3d* simulation.

Global error levels remain satisfactory, but prior to validating a set of *seine3d* numerical parameters for future coupled simulations, it is useful to check the accuracy of wave kinematics. This way we get a last insight into the capabilities of *seine3d* alone at simulating 2DV regular waves.

4.3.2.3 Checking the vertical profiles of velocity in *seine3d*

It has been established that the simulated and streamfunction free surface time profiles match quite well, even with the default *seine3d* numerical parameters : $\Delta x = \frac{\lambda}{16}$, $N_z = 6$ and $\Delta t = \frac{T}{100}$. We now make sure that vertical profiles of velocity components obtained by *seine3d* comply with the streamfunction ones built from the streamfunction algorithm. It is of central interest, as the coupling methodology relies on the exchange of vertical profiles of velocity between *seine3d* and *CS*. Correct kinematics under the wave are required in

seine3d domains for the hybrid simulations to be accurate. Such a comparison is displayed in figure 4.5 at 10 time instants between $t = 49T$ and $t = 50T$. Simulated velocity profiles are interpolated from the values at mesh nodes thanks to the *Slice* filter of Paraview. N_z points still make up the vertical profile after the filtering operation.

Overall, velocity profiles match quite well, and as in the case of wave height and phase errors, it is difficult to distinguish solutions corresponding to the various combinations of parameters tested. Noticeable discrepancies take place between $t = 49.6T$ and $t = 49.8T$ for horizontal velocity and at $t = 49T$ for vertical velocity, at the very end of the simulation time.

We might therefore conclude that spatial and temporal discretizations employed as default values in *seine3d* calculations, namely $\Delta x = \frac{\lambda}{16}$, $N_z = 4$ and $\Delta t = \frac{T}{100}$, leading to a CFL of 0.172 are adapted for further use in coupled simulations with $\epsilon = \frac{1}{40}$ and $T = 15$ s. It is also assumed that the same normalized parameters are also fitted for *seine3d* computations with wave periods $T = 12$ s and $T = 9$ s and the same wave steepness. Hence the above study is not repeated for these two other setups, for which only results of final 3D hybrid simulations will be presented. These spatial and temporal discretization levels thus serve as a basis to model the propagation of regular waves in coupled potential domains, but are adapted to suit constraints inherent to the couplings with *CS* instances. This is explained in following sections.

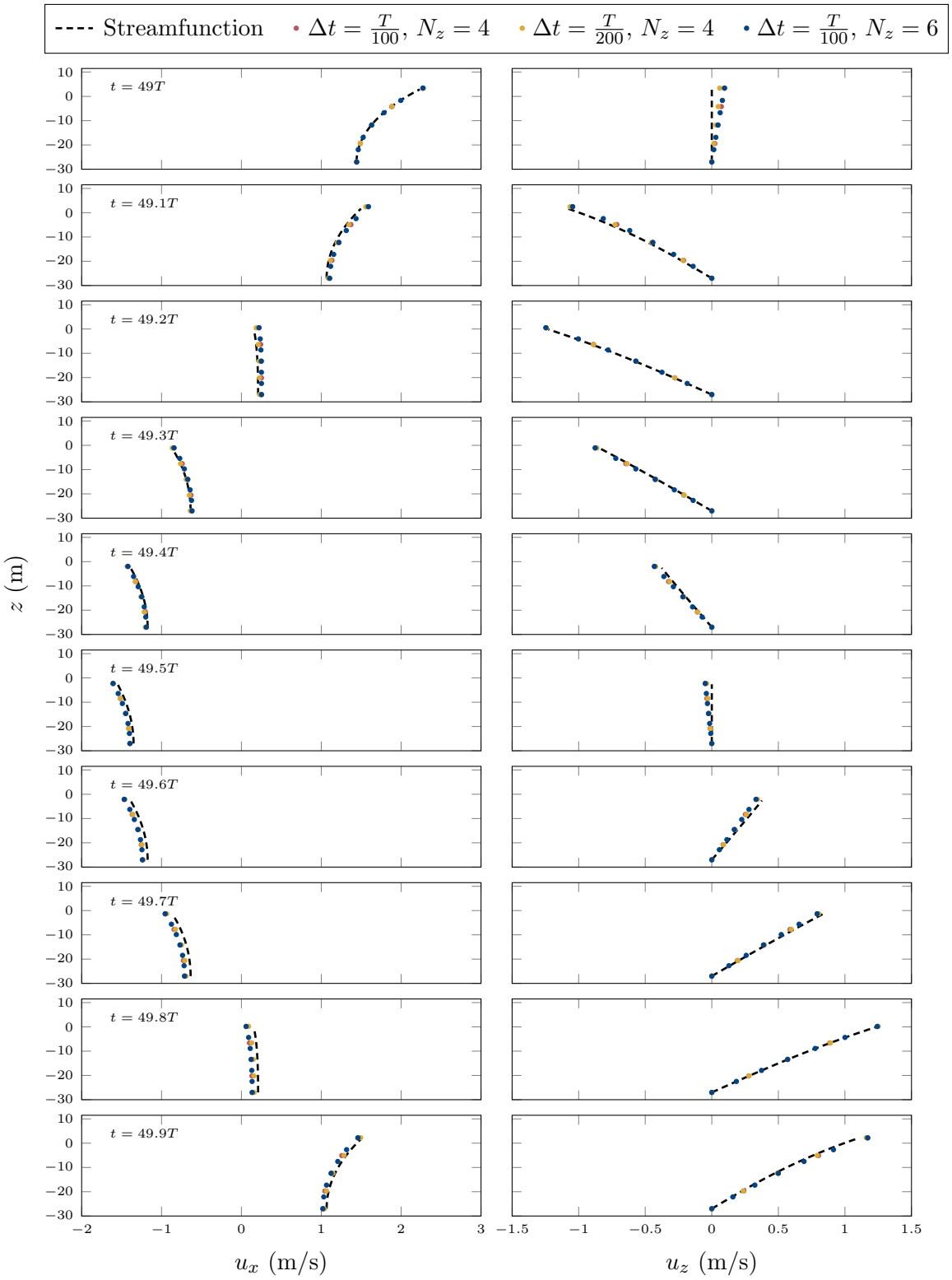

Figure 4.5: Vertical profiles of *seine3d* velocity at the virtual abscissa of the monopile ($x = 0.0$ m) during the 50^{th} wave period for several values of Δt and N_z. Δx is set to $\frac{\lambda}{16}$.

4.4 Improving *CS* simulation results

Similarly to what has been done with simulations involving only *seine3d*, a correct combination of time step and computational cells size is sought for *CS*, for a wave steepness of $\frac{1}{40}$.

4.4.1 Simulation setup for tests in *CS*

A numerical domain long of 4 wavelengths is used. One wavelength is dedicated to wave generation at one end of the domain, whereas a wave damping region of the same length occupies the other end. Appart from the coupled boundaries, the vertical walls and the domain bottom are attributed *Symmetry* boundary conditions in *CS*, equivalent to a slip condition for the velocity, consistent with the fact the wall boundary layers are neglected. Homogeneous Neumann conditions are imposed to void fraction and pressure. A *Imposed Pressure Outlet* boundary condition consisting of a Dirichlet boundary condition on pressure alongside with homogeneous Neumann conditions on the velocity components and void fraction is set at the top of the domain. A detailed description of the different types of boundary conditions in *CS* may be found in the theory guide (Code_Saturne development team, 2019).

To reduce the number of cells in the associated computational mesh, the vertical dimension of the cells is not uniformly distributed. Indeed, and as a default choice, Δz is set to $\frac{H}{20}$ around the free surface, and it gradually increases up to $\frac{H}{4}$ near the floor and ceiling of the *CS* domain. With the same goal in mind, a longitudinal cell aspect ratio of 4 is chosen in the vicinity of the free surface, with $\Delta x = \frac{H}{5}$. A first value for the *CS* time step size was selected based on two previous results, namely the fact that $\Delta t_{seine3d} = \frac{T}{100}$ was found to be a correct value for *seine3d* regular wave simulations, and that time steps ratios in the order of 10 or 15 proved relevant in coupled simulation of solitary wave propagation. Thus the step size verifies $\Delta t = \frac{T}{1500}$. The CFL value becomes:

$$CFL = \sqrt{gh}\frac{\Delta t}{\Delta x} = 0.14 \tag{4.6}$$

Note that some of these choices are somewhat challenged in a coming section 4.4.4. It was also decided to keep using conforming hexahedral meshes in simulations involving *CS* only, at the cost of using rather high cell aspect ratios. Indeed, it should be recalled that only conforming grids are dealt with in the coupling strategy, or at least meshes with conforming parts in the overlapping regions associated to coupling instances.

Wave generation is ensured by a Dirichlet condition on velocity and void fraction at the upstream (inlet) boundary face associated to an additional source term in the void fraction transport equation. Vertical position reached by the free surface at the inlet face, as well as vertical profiles of both velocity components u_x and u_z, needed to set the Dirichlet condition, are provided by a program implementing the semi-analytical streamfunction

wave algorithm of Fenton (1999). A negative homogeneous horizontal current is added to u_x to ensure that Stokes's drift is cancelled. To absorb waves, similar source terms affecting a damping region located at the other end of the tank are added to the same equations.

Here a brief overview of these source terms is given. Generalizing equations 2.12 and 2.13 with modified pressure to the case where a non-zero mass source term S and a user defined momentum source term $S_{\mathbf{u}}$ exist, one gets:

$$\frac{\partial \rho}{\partial t} + \nabla \cdot (\rho \mathbf{u}) = S \tag{4.7}$$

$$\frac{\partial \rho \mathbf{u}}{\partial t} + \nabla \cdot (\rho \mathbf{u} \otimes \mathbf{u}) = -\nabla p + \nabla \cdot \mathbb{T} + (\rho - \rho_{void})\mathbf{g} + S_{\mathbf{u}} \tag{4.8}$$

Making use of the conservation equation to develop the instationary term $\frac{\partial \rho \mathbf{u}}{\partial t}$ in the momentum equation, one obtains:

$$\rho \frac{\partial \mathbf{u}}{\partial t} + \nabla \cdot (\rho \mathbf{u} \otimes \mathbf{u}) - \mathbf{u} \nabla \cdot (\rho \mathbf{u}) = -\nabla p + \nabla \cdot \mathbb{T} + (\rho - \rho_{void})\mathbf{g} + S_{\mathbf{u}} - \mathbf{u} S \tag{4.9}$$

The VOF system of equations under the incompressible flow assumption might then be recalled.

$$\frac{\partial \rho \mathbf{u}}{\partial t} + \nabla \cdot (\rho \mathbf{u} \otimes \mathbf{u}) = -\nabla p + \nabla \cdot (\mathbb{T}) + (\rho - \rho_{void})\mathbf{g} \tag{4.10a}$$

$$\nabla \cdot \mathbf{u} = 0 \tag{4.10b}$$

$$\frac{\partial \alpha}{\partial t} + \nabla \cdot (\alpha \mathbf{u}) = 0 \tag{4.10c}$$

Mass conservation in the VOF model is therefore:

$$\left[\frac{\partial \alpha}{\partial t} + \nabla \cdot (\alpha \mathbf{u})\right] + \frac{\rho_{water}}{\rho_{void} - \rho_{water}} \nabla \cdot \mathbf{u} = 0 \tag{4.11}$$

A forcing source term S_α can be added to the void fraction transport equation 4.10c, following:

$$S_\alpha = \Gamma_\alpha^{frc}(\alpha_{ref} - \alpha) \tag{4.12}$$

with α_{ref} a reference void fraction field towards which the computed field is forced and Γ_α^{frc} a forcing coefficient having the dimension s^{-1}. Hence, a corresponding source term S_α^* has to account for changes in the volume conservation equation 4.10b

$$S_\alpha^* = -\frac{\rho_{void} - \rho_{water}}{\rho_{water}} \Gamma_\alpha^{frc}(\alpha_{ref} - \alpha) \tag{4.13}$$

so that equation 4.11 still holds.

Similarly, considering a momentum source term injected in equation 4.10a with $\mathbf{u}_{ref}$ a

target velocity field, it comes:

$$S_{\mathbf{u}} = \Gamma_{\mathbf{u}}^{frc}\rho(\mathbf{u}_{ref} - \mathbf{u}) \tag{4.14}$$

These source terms have an implicit part, involving the relevant scalar or vector field α or $\mathbf{u}$, and an explicit one to take into account the reference solution. It should also be noted that $S_{\mathbf{u}}$ operates in both phases.

The VOF system of equation then becomes:

$$\frac{\partial \rho \mathbf{u}}{\partial t} + \nabla \cdot (\rho \mathbf{u} \otimes \mathbf{u}) = -\nabla p + \nabla \cdot (\mathbb{T}) + (\rho - \rho_{void})\mathbf{g} + S_{\mathbf{u}} - \mathbf{u}S_{\alpha}^{*} \tag{4.15a}$$

$$\nabla \cdot \mathbf{u} = S_{\alpha}^{*} \tag{4.15b}$$

$$\frac{\partial \alpha}{\partial t} + \nabla \cdot (\alpha \mathbf{u}) = S_{\alpha} \tag{4.15c}$$

In the wave generation region, α_{ref} is based on the free surface profile provided by the streamfunction wave algorithm, *i.e.* it is set to 0 if the vertical coordinate of the considered computational cell's center is lower than the streamfunction value, and to 1 otherwise. Accordingly, $\mathbf{u}_{ref}$ is built using streamfunction velocity field. In the damping region, the same strategy is implemented for α_{ref} on the basis of the resting free surface level, while $\mathbf{u}_{ref}$ is simply set to zero.

Forcing coefficients Γ_f^{frc} where f stands for α or $\mathbf{u}$ are modulated by a spatially varying blending function $\omega(\mathbf{x})$ chosen among those displayed in figure 2.8.

$$\Gamma_f^{frc} = \omega(\mathbf{x})\gamma_f^{frc} \tag{4.16}$$

with γ_f^{frc} the forcing intensity.

As described in section 2.5.3.2, the selected blending function takes the value 1 at the inlet boundary and exponentially decreases down to 0 at the end of the generation region. The opposite is true for the absorbing layer. For wave generation, a suitable value of γ_{frc} is found following a trial-and-error approach in which simulated free surface profiles at the beginning of the simulation - as long as waves have not started to interact with the downstream damping layer - are compared to their streamfunction counterparts. To absorb waves, forcing intensity is selected after a series of tests in which, as in section 4.3.1.2, the smallest possible reflection rate R is sought.

By successive improvements, a working setup was found for the wave case investigated in this section. In the damping layer, γ_{α}^{frc} is identical to $\gamma_{\mathbf{u}}^{frc}$ while $\gamma_{\mathbf{u}}^{frc}$ equals zero in the generation area. Values of γ_{α}^{frc} differ by nearly two orders of magnitude in both regions. Optimal values were found to depend on the wave conditions. As we do not make use of wave generation and absorption capabilities of *CS* in the coupled simulations, a more exhaustive study of the related parameters' influence was not considered relevant and is therefore not shown here.

At last, it should be mentioned that simulating waves propagation during $100T$ takes around 24 hours on 4 cores of the HPC cluster Gaia.

4.4.2 Analysis of free surface elevation signal

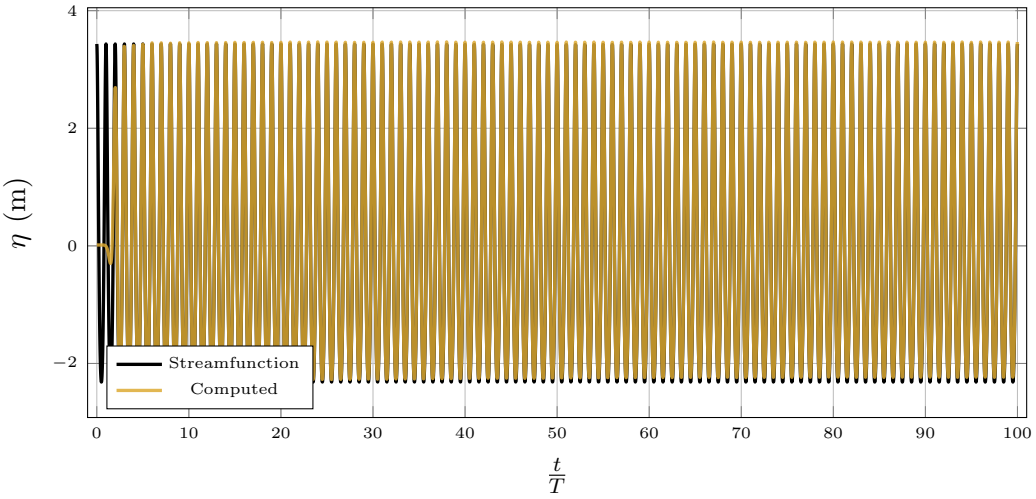

Figure 4.6: Streamfunction and computed free surface time history at $x = 2\lambda$, in a test simulation involving only *CS*.

Indeed it is sufficient to notice that wave generation, propagation, and absorption in this short *CS* domain are very satisfactory. Simulated free surface time history matches the streamfunction solution quite well, as shown in figure 4.6 at $x = 2\lambda$, for the case with $T = 15$ s. A small discrepancy appears at the wave trough in the course of the simulation but remains limited. It should also be noted that all the results displayed in this section were obtained using a design wave with $T = 15$ s and $H = 5.75$ m, see also table 4.1.

Values of wave height error ϵ_{H} and phase shift ϵ_ϕ presented in figure 4.7 are globally lower than those recorded for *seine3d* alone in section 4.3.2, figure 4.4. The first 10 wave periods are not displayed in order to focus on the rather small error values. ϵ_{H} indeed stabilizes between 0.6% and 0.7% after slightly more than $20T$. As a reminder, the wave height error is close to 2% in the *seine3d* simulation with optimal wave absorption. ϵ_ϕ gradually decreases with time, but barely exceeds 2% in absolute value after almost 100 wave periods. It is also to be noticed that in *CS* error curves are globally less chaotic than in *seine3d*, and also that it takes fewer periods to reach low error levels in *CS*, with ϵ_{H} and ϵ_ϕ stabilizing no later than $10T$ after the beginning of the simulation. By contrast, strong error peaks are still seen in *seine3d* after more than $30T$. Still, the drift in time of ϵ_ϕ observed with *CS* is not seen in *seine3d*.

We also consider the free surface spatial profiles in the whole *CS* domain at two different time instants ($t = 5T$ and $50T$) in figure 4.8. $t = 5T$ is deemed a sufficient initialization delay, after which waves are assumed to have fully developed in the domain. Recall that

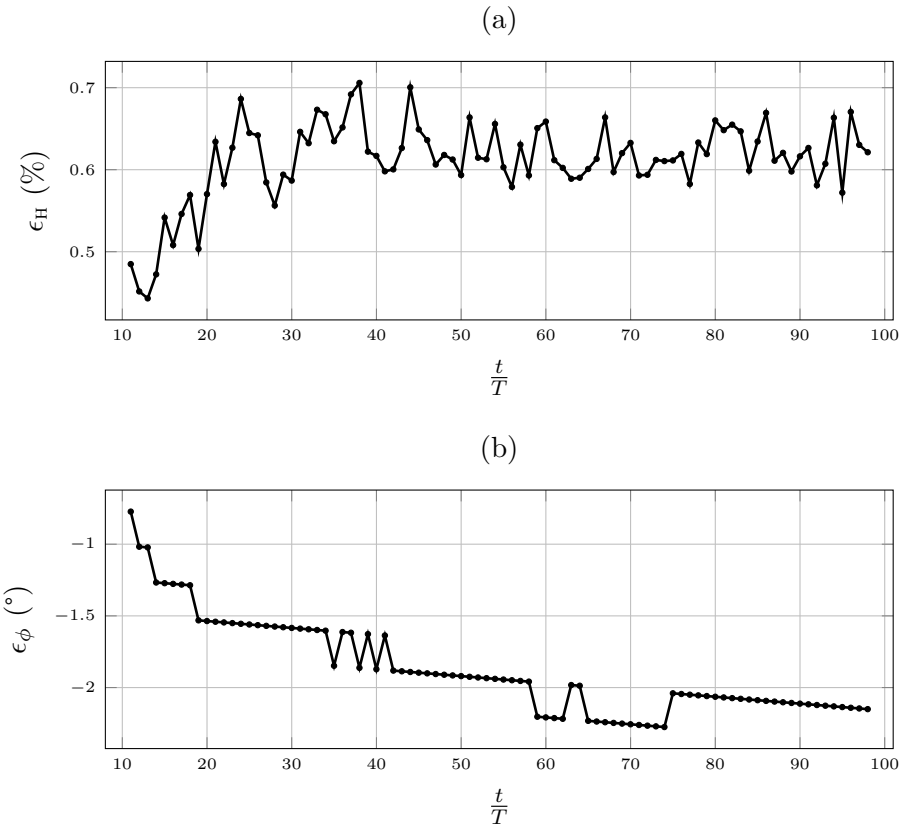

Figure 4.7: Phase shift (b) and relative error on wave height (a) at $x = 2\lambda$. Simulation using only *CS*.

free surface profile is smoothed thanks to the *Contour* filter of Paraview, as the isosurface with $\alpha = 0.5$ is sought. This results in a rather chaotic free surface signal in the damping layer, as well as in a portion of the domain directly upstream of this region at $t = 50T$. It illustrates the important free surface smearing occurring in the absorbing region, due to the forcing brought by the additional source terms. Free surface smearing gradually extends upstream as the computation advances, as can be noticed by comparing both colored curves. Away from the damping zone and its close vicinity, simulated free surface profiles agree well with the streamfunction one. Hence, to avoid disturbances in the free surface profile it seems reasonable not to consider results farther than $x = 2.5\lambda$. Such hypothesis should nevertheless be confirmed or rebutted by means of a study of wave kinematics.

4.4.3 Assessment of wave kinematics

The free surface shape remaining satisfactory on most of the domain through time, we should now assess the quality of the simulated kinematics beneath the wave. Indeed, a correct simulation of the velocity field near the structure of interest is necessary for the accuracy of force calculations in wave-structure interactions.

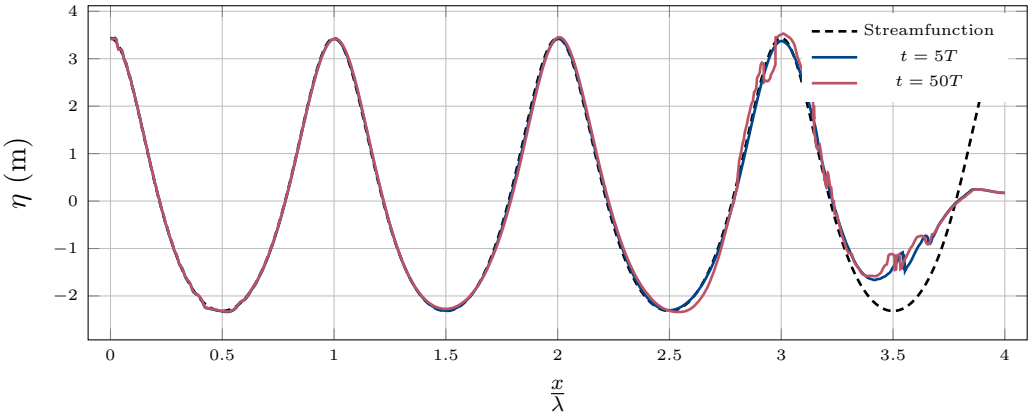

Figure 4.8: Comparison of the streamfunction and computed free surface profiles at time instants $t = 5T$ and $t = 50T$ in a test simulation involving only *CS*.

To that end, the fields of u_x and u_z in the water phase are shown at time instants $t = 5T$ and $t = 50T$, in figures 4.9 and 4.10 respectively. The water domain shape is obtained applying Paraview *Threshold* filter, selecting cells of $\alpha < 0.5$. This was preferred to the alternative method of displaying the fields of αu_i, where u_i is any velocity component with $i \in \{1, 2, 3\}$, to conform with the way air/water interface position has been post-processed so far. Some mesh cells containing a mixture of both phases are thus included in the water domain. This, combined with the free surface smearing inherent to VOF computations, surely has an impact on the nonphysical water velocity values observed close to the free surface, as studied further below. Velocity component fields are the outcome of subsequent Delaunay triangulation and linear interpolation of raw *CS* simulation results. The corresponding streamfunction free surface position is also pictured as a reference, and we may once again notice that the simulated free surface solution looks well for $x < 2.5\lambda$ at least.

The same cannot be said of the velocities in the water phase. If the periodicity of the velocity fields is correctly reproduced for the first 3 wavelengths at the earlier simulations stage, spurious velocity patterns appear slightly upstream of $x = 2.5\lambda$ at $t = 50T$. Their horizontal extent seems correlated to that of the chaotic free surface area, that expands from 3λ to 4λ. Away from this region, however, velocity components seem to agree with what is expected, except close to the wave generation boundary.

Therefore, a quite conservative choice is made to restrict the working length of the *CS* domain to the area enclosed between $x = \lambda$ and $x = 2.25\lambda$, for the whole duration of the simulation. $x = 2\lambda$ is thus chosen to extract and compare the vertical profiles of velocity.

Figure 4.11 depicts vertical profiles of horizontal velocity at different time instants when the theoretical wave crest passes $x = 2\lambda$. A continuous worsening of the horizontal velocity profile is observed through time, as velocity is overestimated close to the free surface and underestimated near the bottom. Vertical profile of vertical velocity is not shown here, as it matched the reference solution a lot better. The phase error that is approximately

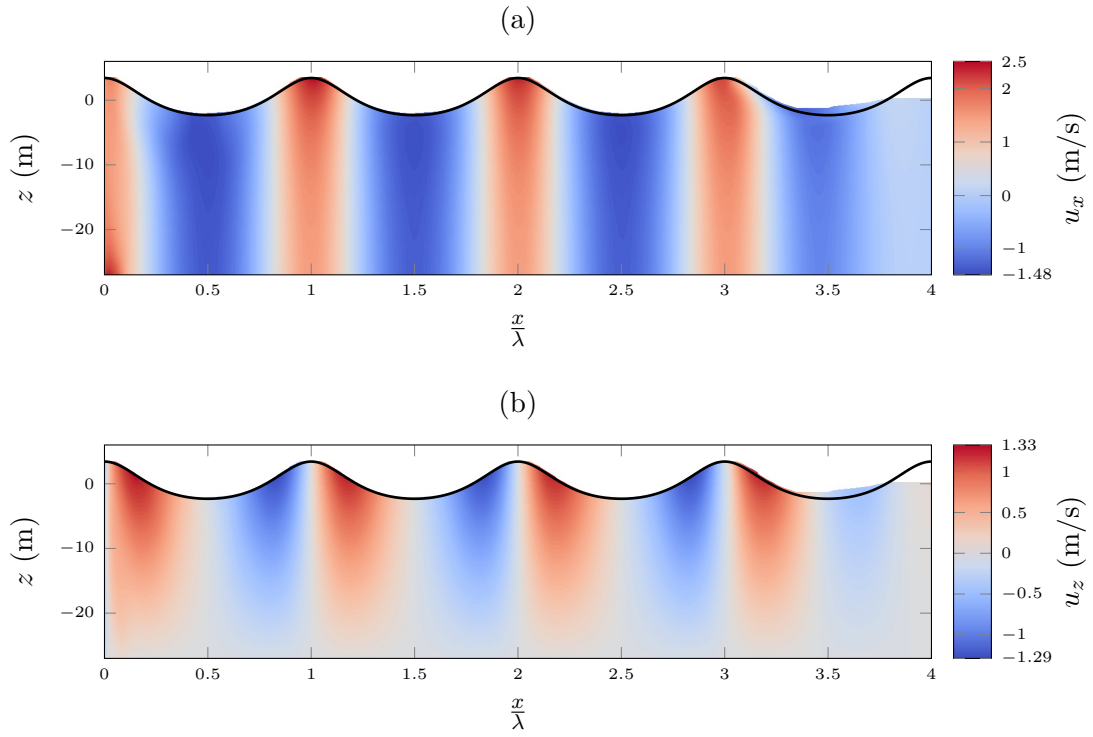

Figure 4.9: Scalar fields of horizontal (a) and vertical (b) velocity components at $t = 5T$. Black line represents the streamfunctionl free surface profile.

kept below 2° in absolute value can not explain these discrepancies alone. Spurious velocity has been extensively reported in VOF simulations including the effects of surface tension forces, but in the present case surface tension is not taken into account. These results rather remind those obtained by Larsen et al. (2019) and references therein with Interfoam, considering the propagation of a streamfunction wave under periodic boundary conditions. The increase in time of the vertical gradient of horizontal velocity observed here is similar to what these authors notice. In Larsen et al. (2019), it is assumed that the existence of nonphysical water velocities close to the free surface is caused by an imbalance in the momentum equation in nearby cells, originating from discretization errors in the force terms of NS equations. Due to the high density ratio between water and air, any spurious transfer of momentum from the dense phase to the light one then leads to large overestimation of air velocity near the free surface. Unrealistic air velocities are then inevitably diffused back to the superficial part of the water phase, as the VOF advection schemes cannot maintain arbitrary high shearing values at the interface between the phases. As Interfoam is comparable to *CS* in its conception, these conclusions should also apply to the current study.

Results in figure 4.11 are complemented by those shown in figure 4.12, where error ϵ_{u_x} between u_x and the reference solutions is computed over one wavelength between $x = 1.25\lambda$ and 2.25λ at $t = 5T$ and $t = 50T$. Normalization is realized with the maximum horizontal

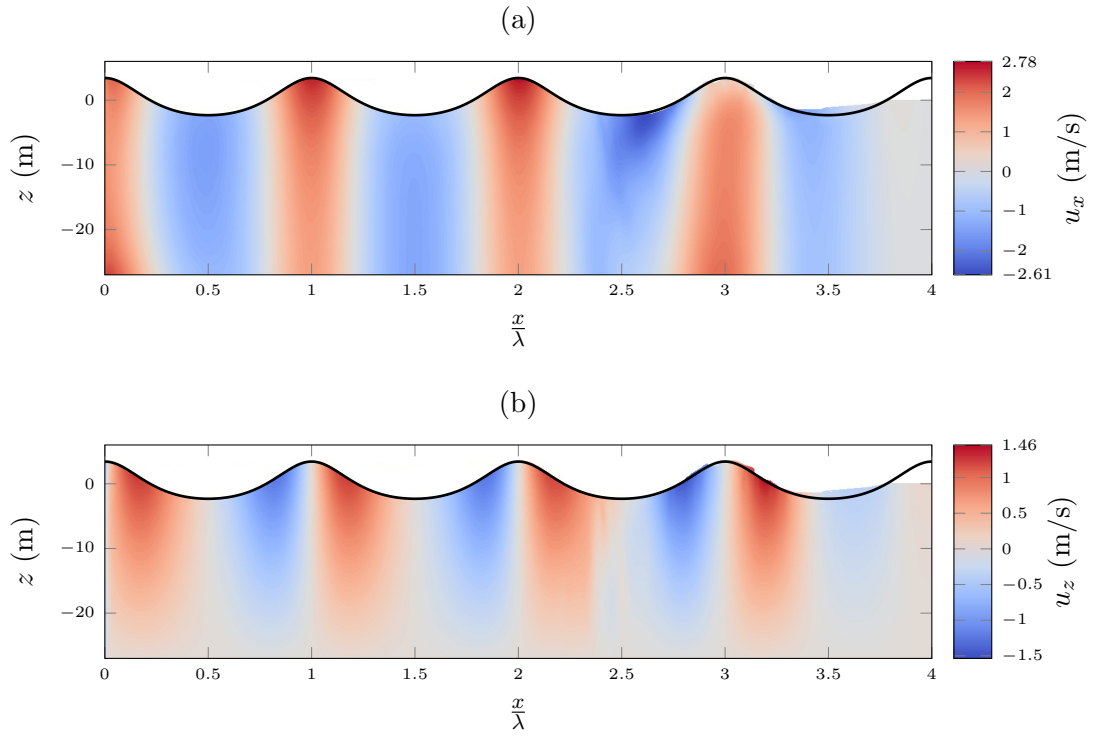

Figure 4.10: Scalar fields of horizontal (a) and vertical (b) velocity components at $t = 50T$. Black line represents the streamfunction free surface profile.

velocity value computed by streamfunction theory:

$$\epsilon_{u_x} = \frac{u_x - u_{x,ref}}{\max(u_{x,ref})} \tag{4.17}$$

Error on the vertical velocity is not shown as it is one order of magnitude lower that its horizontal counterpart. It clearly appears that velocity overestimation close to the free surface not only occurs near the wave crest. It is stronger on the quarter of wavelength extending in front of the wave though. Large values of ϵ_{u_x} concentrate in a layer located just beneath the interface whose thickness increases with time. Velocity underestimation close to the bottom, although smaller, grows by an order of magnitude throughout the simulation.

As a last illustration of the distortion of vertical profiles of horizontal velocity, the time average of u_x along a vertical line located $x = 2\lambda$ is computed. The latter extends from the bottom up to slightly under the wave trough. This maximal ordinate is taken as $z = -\frac{H}{2}$. Results are displayed in figure 4.13. The computed mean profiles indicate that a clockwise circulation builds up in the bulk of the domain. A vertical gradient of mean horizontal velocity appears and grows in time, as opposed to what the streamfunction theory predicts. Mean vertical velocity is negligible as compared to horizontal mean, and is not shown here.

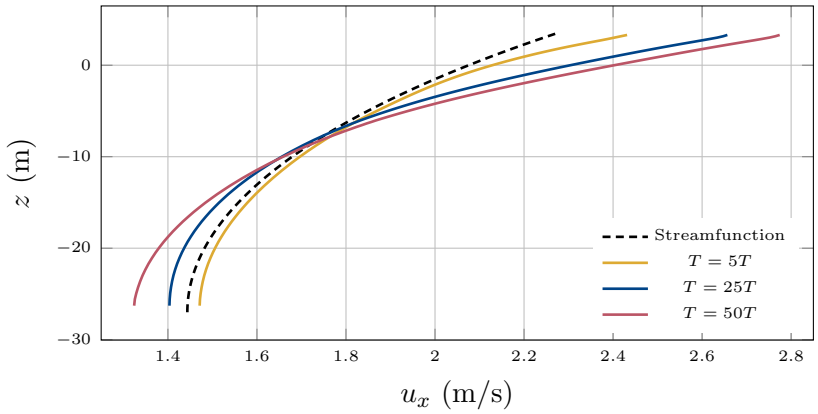

Figure 4.11: Vertical profiles of horizontal velocity beneath the wave crest at $x = 2\lambda$.

So far, the assumption that given the high density ratio between the two fluids, the influence of the light phase on the dense phase is negligible was supposed to hold. Hence velocity field in the air has been of little interest. It might nevertheless cause, for part, the overprediction of horizontal velocities close to free surface. Recent studies conducted with *CS* indeed suggest that the *Imposed Pressure Outlet* condition imposed on the ceiling of the domain yields chaotic velocity fields in the air phase. Such boundary condition consists of an outlet boundary condition with a Dirichlet condition on pressure corresponding to the atmospheric pressure. Other computational variables receive a homogeneous Neumann boundary condition. As indicated in *CS*'s theory manual, if a sign change occurs for the outgoing mass-flux at this boundary, fluxes are clipped. It results in unrealistic behavior of the air phase. A look a the velocity field in the whole *CS* domain at $t = 50T$, as shown in figure 4.14, indicates that velocity in the air is far more chaotic that one can expect. Numerous vortices are observed, and velocity amplitude above free surface reaches important peaks. As already stated, high air velocities may be diffused towards the water phase, generating the above-mentioned overspeeds in water.

The poor quality of the velocity field in the air phase, caused by a top boundary condition that is still to be improved, may well be responsible for the overestimation of horizontal water velocity close to the free surface. Such phenomenon could be associated to the clockwise circulation highlighted in figure 4.13, that the downstream damping region fails to prevent. This would yield a mean return current close to the bottom, growing progressively with time.

At last, the potential influence of the damping region on the generation of this spurious circulation should be addressed. Although the findings of Larsen et al. (2019) with Interfoam involve a periodic domain in which no absorbing layer is implemented, we cannot exclude the possibility that velocity forcing at the downstream end of the *CS* domain has something to do with the worsening of the vertical profile of u_x, observed at least one wavelength upstream from the beginning of the damping region.

Hence, three possible explanations have been provided to describe the occurrence of over-

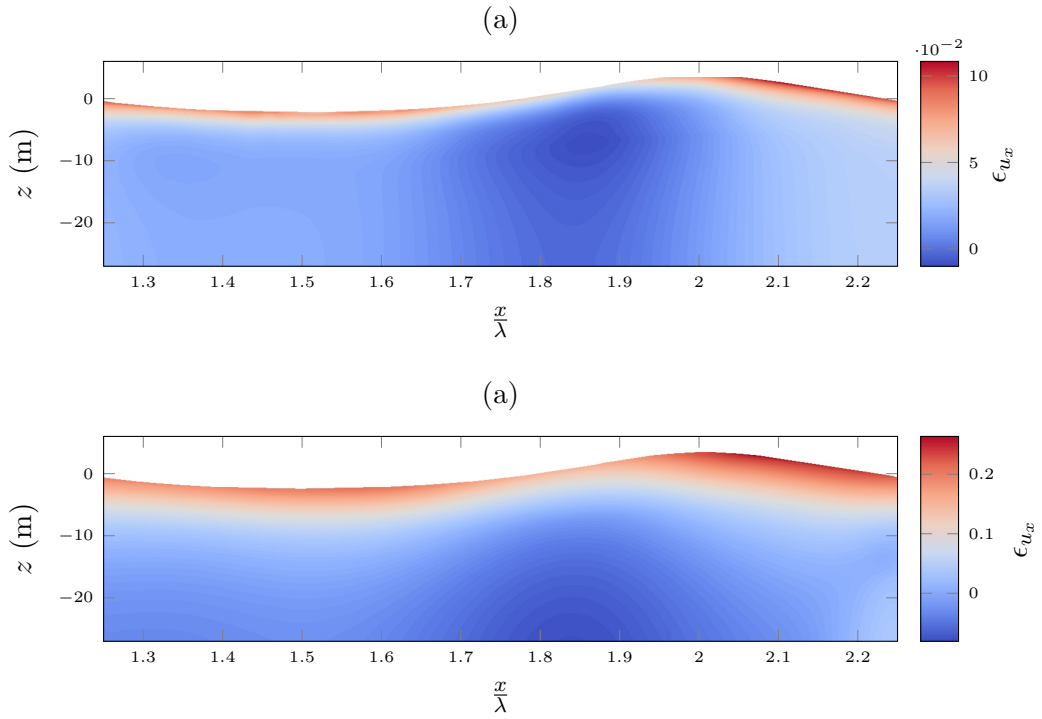

Figure 4.12: Normalized error on vertical velocity over one wavelength, at time instants $t = 5T$ (a) and $t = 50T$ (b). Domain ranges from $x = 1.25\lambda$ to $x = 2.25\lambda$.

speeds just beneath the air/water interface: imbalance in the momentum conservation equations close to the free surface, as described by Larsen et al. (2019), inappropriate velocity boundary condition at the top and upstream influence of the damping region. It should be recalled that this goes along with satisfactory free surface profiles in the major part of the domain. Unfortunately there was not enough time to test these hypotheses and to implement a more appropriate version of the top boundary condition.

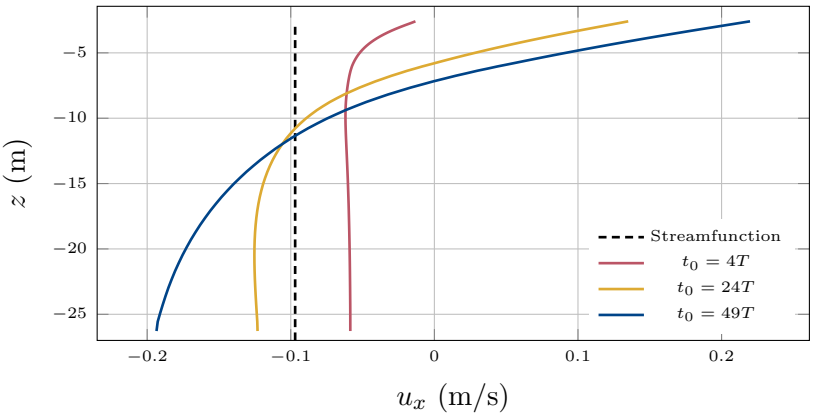

Figure 4.13: Vertical profile of time average of horizontal velocity over one wave period, at $x = 2\lambda$ at various time instants in the *CS* domain. Time average is calculated between t_0 and $t_0 + T$. Mean Eulerian horizontal velocity, as computed by the streamfunction wave algorithm, is shown for comparison.

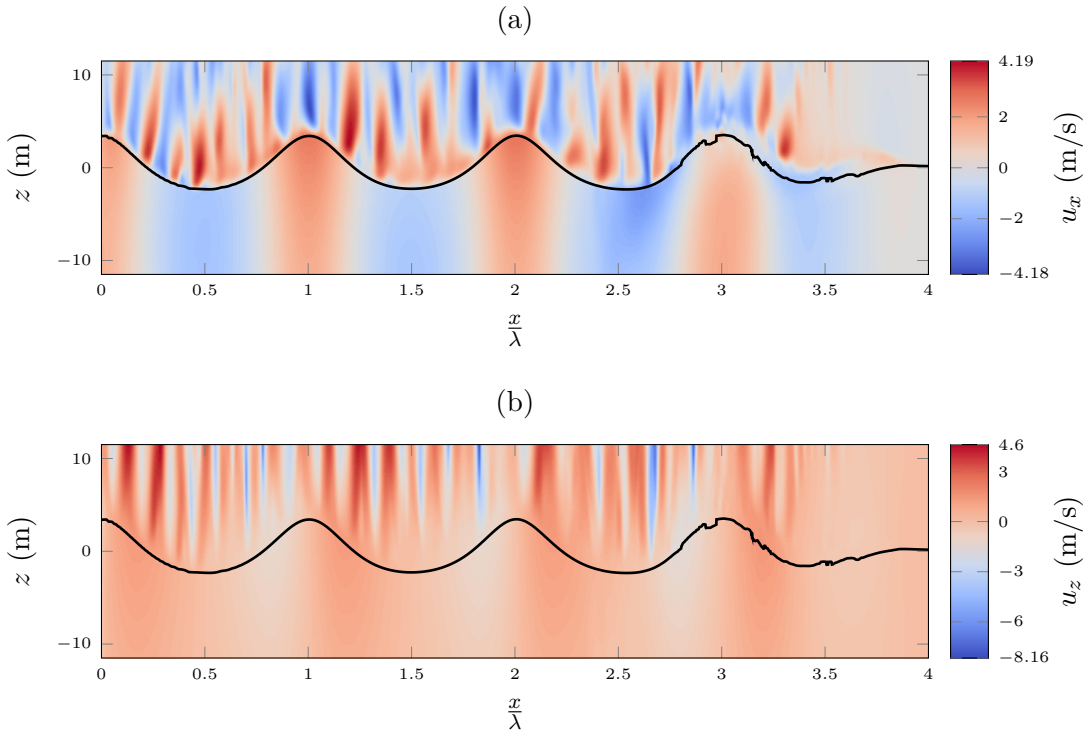

Figure 4.14: Horizontal (a) and vertical (b) velocity fields at $t = 50T$. Close-up view around the interface. Black lines illustrate the position of the free surface.

4.4.4 Influence of certain numerical parameters on the velocity field

Without questioning decisions made while establishing the previous setup for *CS*-only simulations, such as boundary conditions or void fraction advection scheme choices, we describe here some attempts to improve the velocity field beneath the waves. Indeed, issues concerning the agreement of vertical profile of horizontal velocity with the reference solution have been raised in the previous section. At the same time, other wave simulation aspects like free surface spatial profiles and time history where found to live up to our expectations.

A direct way of improving *CS* velocity results is to increase spatial and temporal resolution of the simulations. The wave period and steepness and the domain setup are kept the same. Without exhaustiveness in mind, 3 different values of the cell aspect ratio (AR) close to free surface at rest were tested ($AR \in \{1, 2, 4\}$) while 4 is the default value previously used. The definition given for the aspect ratio is $AR = \frac{\Delta x}{\Delta z}$. Similarly the performances of 3 time step sizes are assessed, namely $\Delta t = \frac{T}{750}$, $\frac{T}{1500}$, and $\frac{T}{3000}$, $\frac{T}{1500}$ being the default setting. So far, cell height close to free surface has been set to $\Delta x = \frac{H}{20}$. It should indeed be recalled that the *CS* mesh is vertically stretched away from the free surface resting position. Simulations were run with additional values of $\frac{H}{10}$, $\frac{H}{15}$, and $\frac{H}{50}$.

To save computational time, results, shown in figure 4.15, are compared with the reference at time $t = 5T$. As the velocity overestimation was already observed at this time instant in previous simulations, it was deemed suitable and it allowed for quick computations.

Analysis of simulation outcomes is quite straightforward: of the 3 parameters of interest, the only one for which noticeable improvements are made as compared to the results with the default value is the time step size. Increasing time resolution from $\frac{T}{1500}$ to $\frac{T}{3000}$ leads to a decrease in the overprediction of horizontal velocity close to free surface. Conversely, the vertical profiles of u_x worsen when a value of $\Delta_t = \frac{T}{750}$ is used.

On the opposite, the influence of the cell aspect ratio, at least in the range considered here, is negligible.

Small spurious wiggles close to free surface are observed in the velocity profiles obtained using cells with a height lower than $\frac{H}{20}$ excluded. Increasing vertical resolution in the free surface region up to $\Delta z = \frac{H}{50}$ proved pointless.

$AR = 4$, $\Delta t = \frac{T}{3000}$ and $\Delta z = \frac{H}{20}$ thus form a set of basis parameters that are used in *CS* in coupled simulations with a wave steepness of $\frac{1}{40}$. This yields a CFL of 0.07, as defined in equation 4.3.

It should also be noted that considering the positive influence of reducing the time step size, computations have been made with even lower values of $\Delta t = \frac{T}{6000}$ and $\Delta t = \frac{T}{12000}$ and the remaining basis parameters, but they proved unstable and/or they failed.

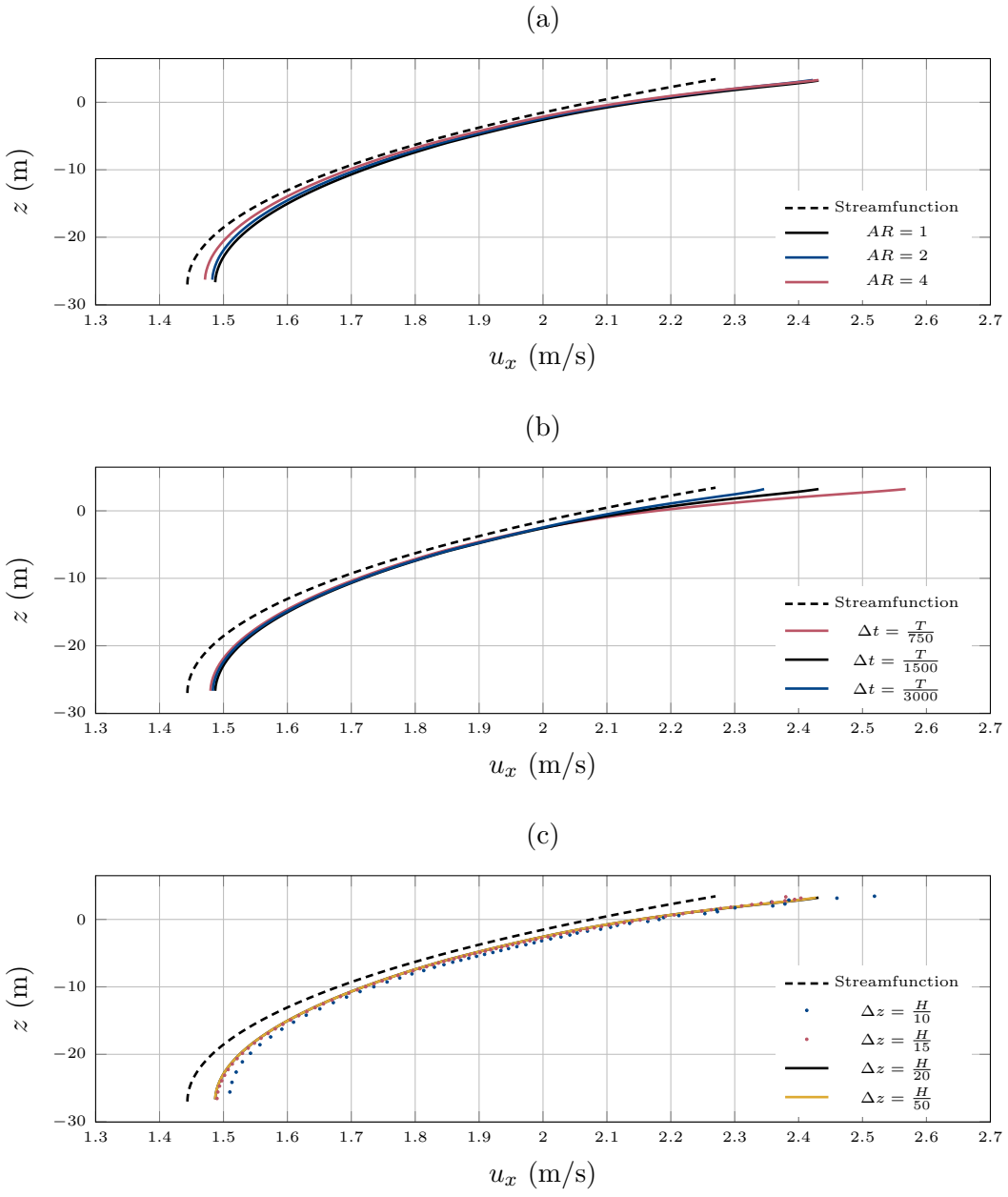

Figure 4.15: Comparison of streamfunction and computed vertical profiles of velocity components at $t = 5T$. Simulations using only *CS* with the same setup as before. (a) simulation with varying cell aspect ratio, other parameters are set to $\Delta z = \frac{H}{20}$ and $\Delta_t = \frac{T}{1500}$. (b) simulation with varying time step, other parameters are set to $AR = 1$ and $\Delta z = \frac{H}{20}$. (c) simulation with varying cell height, other parameters are set to $AR = 1$, $\Delta t = \frac{T}{1500}$.

To get a last insight on the quality of the wave kinematics computed using only *CS*, vertical profiles of velocity over a whole wave period are shown in figure 4.16 at 3 stages of the simulation. This way one visually gets confirmation that vertical velocity matches the reference a lot better than horizontal velocity. u_x vertical profiles exhibit behaviors coherent with what has been previously observed for the horizontal velocity under the crest. Not long after the beginning of the simulation, between $t = 4T$ and $t = 5T$, u_x remains close to the streamfunction solution for the first half of the wave period. During the other half, an almost constant offset affects the horizontal velocity, that disappears later in the simulation. u_x overestimations increase in time, mostly during the first half of the simulation, up to $t = 50T$. In general, it is hard to distinguish between curves with $t_0 = 49T$ and later $t_0 = 99T$. This indicates that the gap between computed velocity and reference does not continuously and monotonically drift with time, but rather seems to reach a steady value. Noticeably, agreement with the reference profile is better beneath the crest than under the trough of the wave.

As we lack time for improvements, no further modification to the wave simulation setup in *CS* is conducted. 3D computations addressed in chapter 6 allow to assess in what extent the accuracy of the horizontal velocity field influences the precision of cylinder inline force calculation.

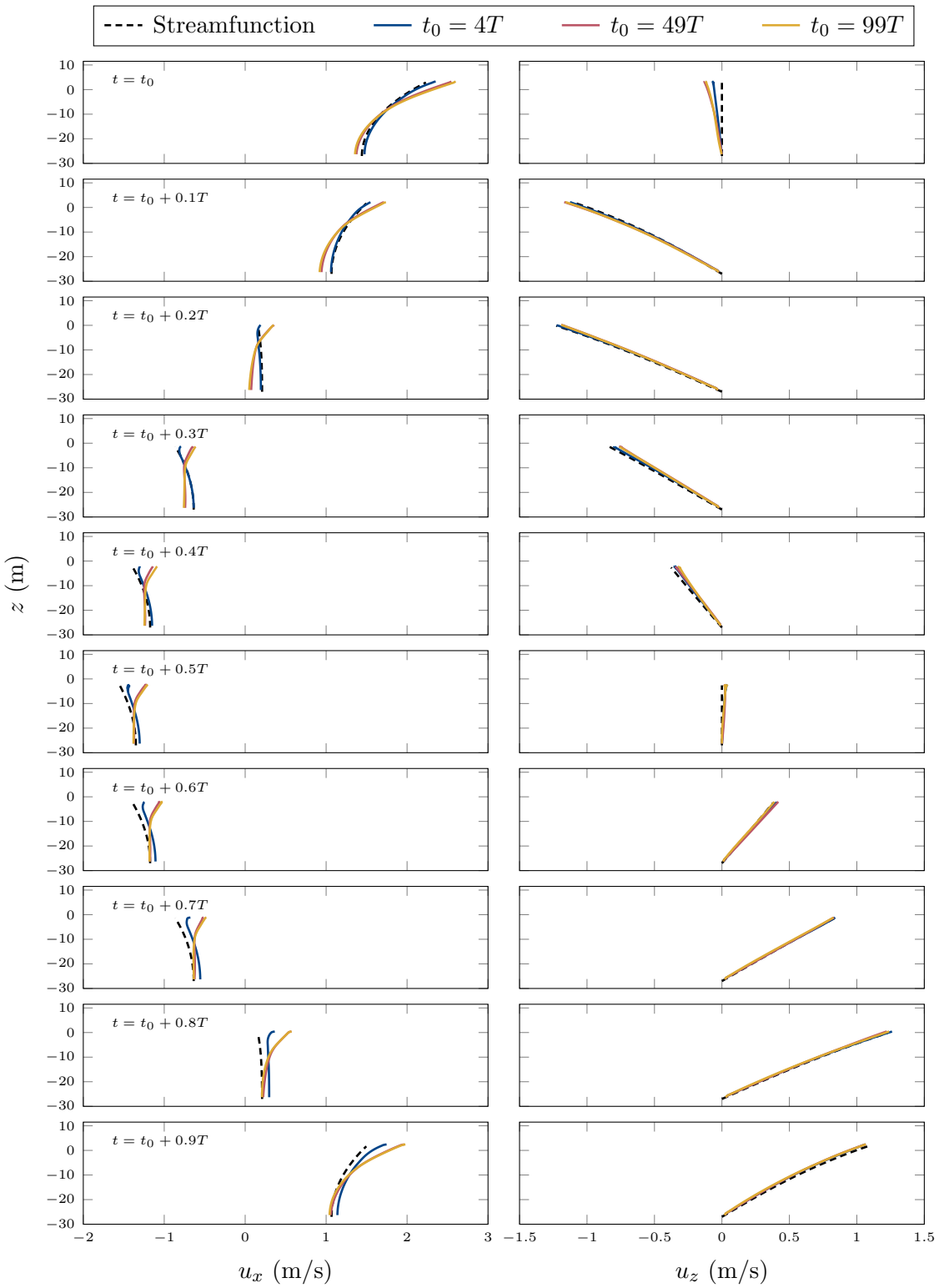

Figure 4.16: Vertical profiles of velocity at $x = 2\lambda$ during one wave period just before $t = 5T$, $t = 50T$ and $t = 100T$. Simulation using *CS* only.

4.5 Coupled simulation of regular wave propagation in 2D

Now that suitable numerical settings have been established to simulate the generation, propagation, and absorption of regular waves with $T = 15$ s and a steepness of $\frac{1}{40}$ in both models separately, we return to the setup presented in figure 4.1 and run a coupled simulation. By the way, the previously used method of trying to optimize wave computations in *seine3d* and in *CS* independently seems justified. It is indeed believed to be the proper way of preparing a novel hybrid simulation case, as the current coupling procedure theoretically enables independent selection of spatial and temporal discretization levels in both programs.

4.5.1 Coupling parameters

As already mentioned, specific numerical strategies and discretization levels used in *seine3d* and *CS* instances, which have been set in previous computations involving only one model, are left unchanged as much as possible. For this 2DV wave case, the only coupling parameter that is yet to be set is the length of the two overlapping regions *seine3d* 1/*CS* and *CS*/*seine3d* 2. Time step ratio $N_{\Delta t}$ is fully constrained by the choices made in model instances *seine3d* 1 and *CS*. Besides, the time step size employed in *seine3d* 1 is enforced in *seine3d* 2. Thus, from the previous section of the current chapter,

$$N_{\Delta t} = \frac{\Delta t_{seine3d}}{\Delta t_{\mathrm{CS}}} = 30 \tag{4.18}$$

as $\Delta t_{seine3d}$ was set to $\frac{T}{100}$ and $\Delta t_{\mathrm{CS}} = \frac{T}{3000}$.

$L_{overlap}$ is the same in both overlapping regions, and it is determined quite arbitrarily. This takes into account the fact that at least 4 *seine3d* boundary elements in the length of the overlapping region seem necessary, as turned out from solitary wave propagation simulations. As $\Delta x_{seine3d}$ was set to $\frac{\lambda}{16}$ beforehand, $L_{overlap}$ is thus set to $\frac{\lambda}{4}$.

Based on preliminary estimations and general guidelines concerning both models behavior, 19 and 15 CPU cores are attributed to *seine3d* 1 and *seine3d* 2 respectively, while *CS* uses 2 cores. This way the computation requests one 36-cores node from the HPC cluster. Such breakdown of computing power is somewhat not intuitive, as *seine3d* is supposed to be less computationally expensive than *CS*, but here requires more cores per wavelength. As its name suggests though, *seine3d* is a 3D code and 4 boundary elements fit the potential domain's width. On the opposite, there is only one the cell in the width of *CS* domain. Therefore computational efficiency is of no interest here, but is addressed while discussing 3D simulations in chapter 6. We might however indicate that it takes about 10 hours to reach a physical time equivalent to $50T$.

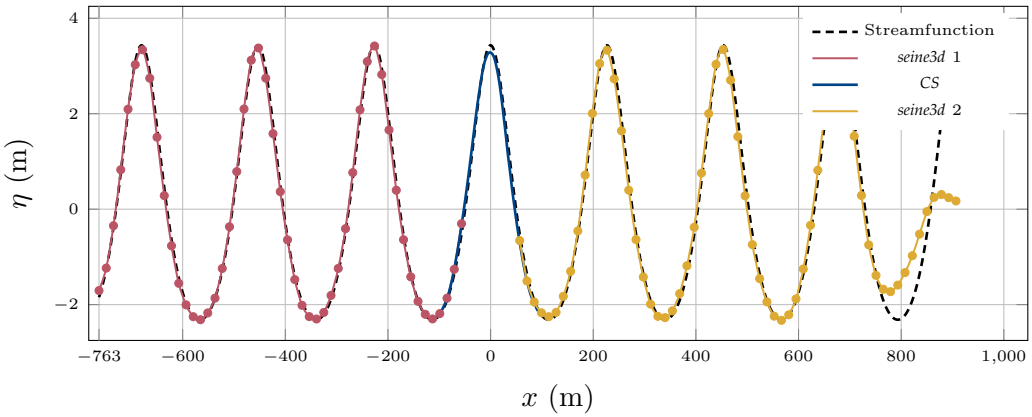

Figure 4.17: Instantaneous free surface profiles from coupled models instances at $t = 50T$. Circles mark the position of *seine3d* free surface nodes.

4.5.2 Simulation results

Figure 4.17 shows the global free surface profile after 50 wave periods. Agreement with the streamfunction reference solution is satisfactory. In particular, free surface matching is ensured in the two overlapping regions. It is interesting to note that at this time instant at least, the wave height is slightly lower in *CS* than in the neighboring potential domains.

To shed light on this aspect of the simulation, time history of the free surface elevation at $x = 0$, corresponding to the abscissa of the monopile in the WAS-XL experiments, is shown in figure 4.19. Again results match the reference reasonably well. Patterns are observed in the transition phase towards fully-developed waves, up to $t = 30T$, that are similar to the ones depicted in figure 4.2 for a simulation involving only *seine3d*. After $t = 30T$, the signal progressively acquires constant characteristics, but a small modulation of the amplitude is however seen, getting stronger in the last wave periods of the simulation.

These remarks may also be made while looking at figure 4.19 displaying the relative errors on amplitude and phase of the simulated waves through time. The amplitude error levels, amounting to around 3%, are closer to the ones reported for *seine3d* only in figure 4.4 than to those recorded in figure 4.7 using only *CS*. The relative phase errors share the same order of magnitude in the three cases, close to 2° on average. The peaks in results occurring at $t = 30T$ remind the ones observed with *seine3d* only. This is in line with what could be expected, as generation and absorption of waves are realized in potential domains. It also indicates that both couplings are quite transparent, as the overall free surface geometry prediction performance of the hybrid simulation does not differ much from *seine3d* standards. In particular, almost no wave reflection is experienced from the presence of overlapping regions.

To further assess the relevance of the coupling methodology applied to regular wave simulation, velocity fields are compared around $t = 50T$ in both overlapping regions in figure 4.20. Good overall agreement is seen. Discrepancies are observed close to the free surface,

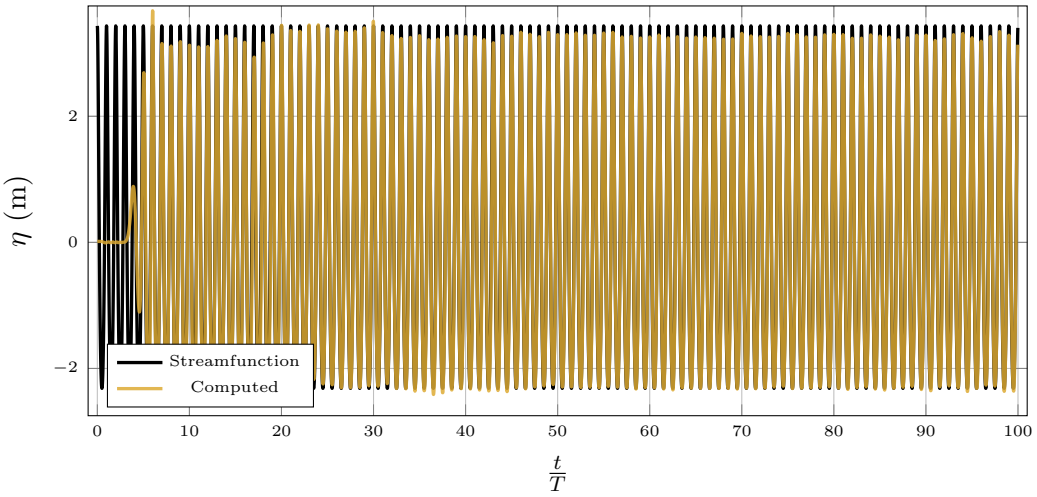

Figure 4.18: Comparison of the streamfunction and computed free surface signals at the virtual position of the monopile ($x = 0$ m).

the largest ones on the upstream boundary of *seine3d* 2 domain. They should be linked to edge/corner singularities in *seine3d* reported and described in more detail while addressing the propagation of a 2D solitary wave. Other discrepancies seem to originate from the viscous domain, as *CS* velocities quite systematically slightly exceed, algebraically speaking, *seine3d* velocity close to the free surface.

At last, vertical profiles of velocity extracted from the central *CS* domain are juxtaposed to the ones predicted by the streamfunction solution. To let enough time for the waves to build, the wave period considered is the 20^{th}. Results resemble those depicted in figure 4.16, thus they are not further described.

The coupling procedure clearly reproduces the behaviors experienced in each model alone.

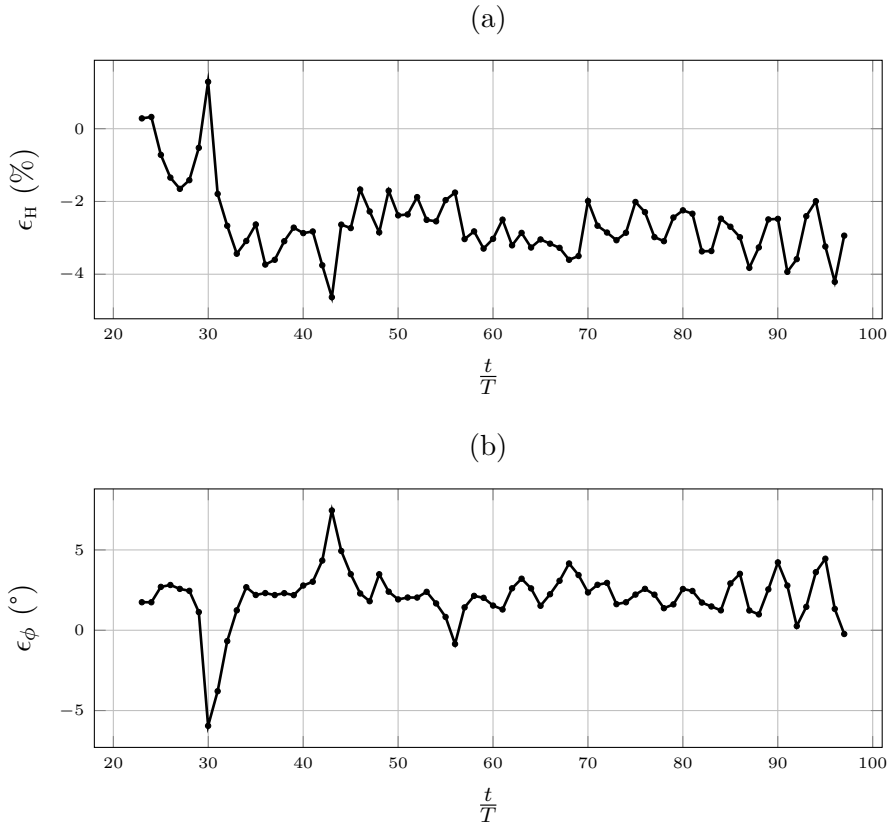

Figure 4.19: Phase shift (b) and relative error on wave height (a) at the virtual location of the monopile in the case of a coupled simulation. The first 20 wave periods are not displayed.

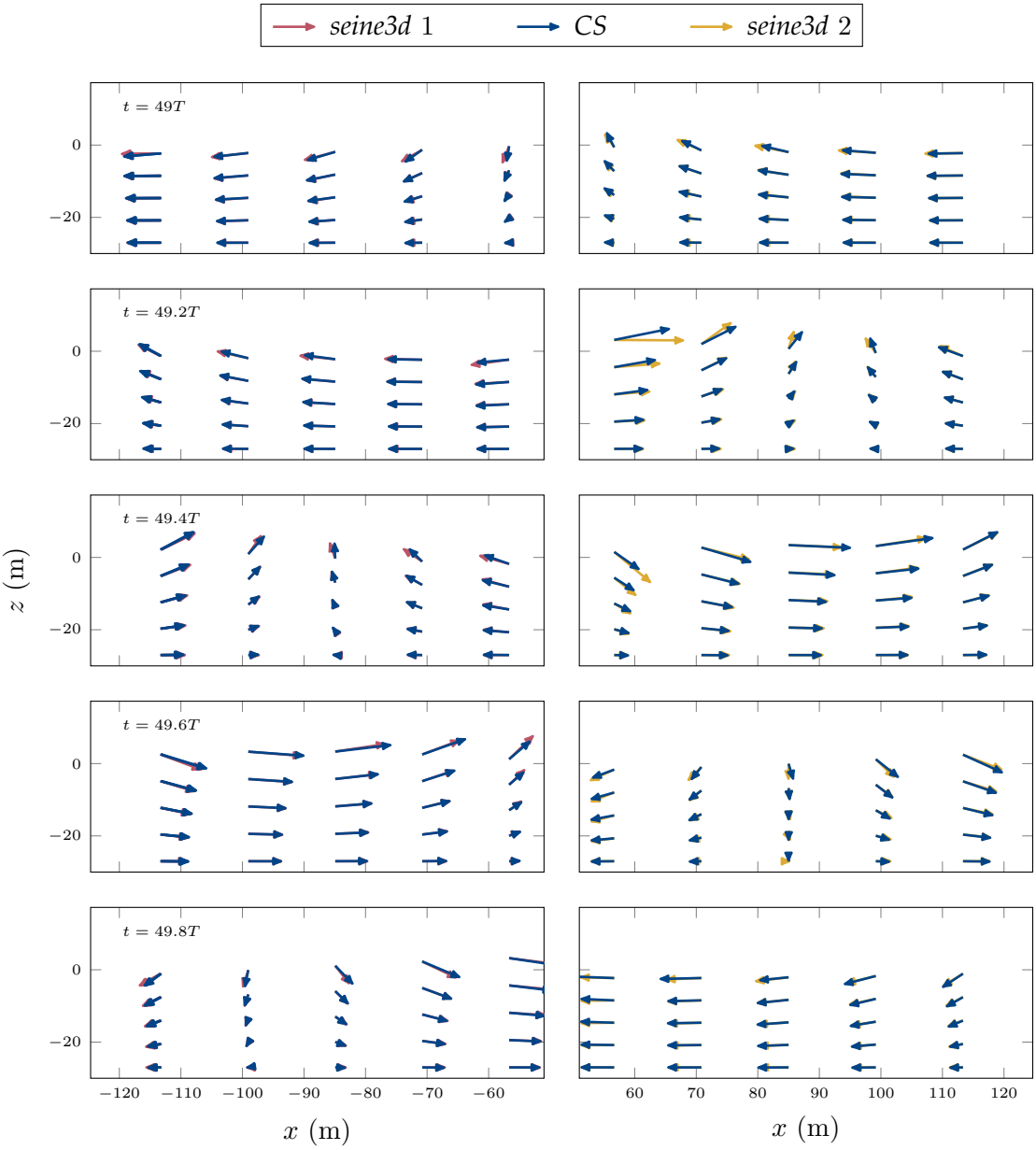

Figure 4.20: *CS* and *seine3d* velocity fields in $\Omega_{overlap}$ and for each coupling during the 50^{th} simulated wave period. Velocity is extracted at the location of *seine3d* boundary nodes.

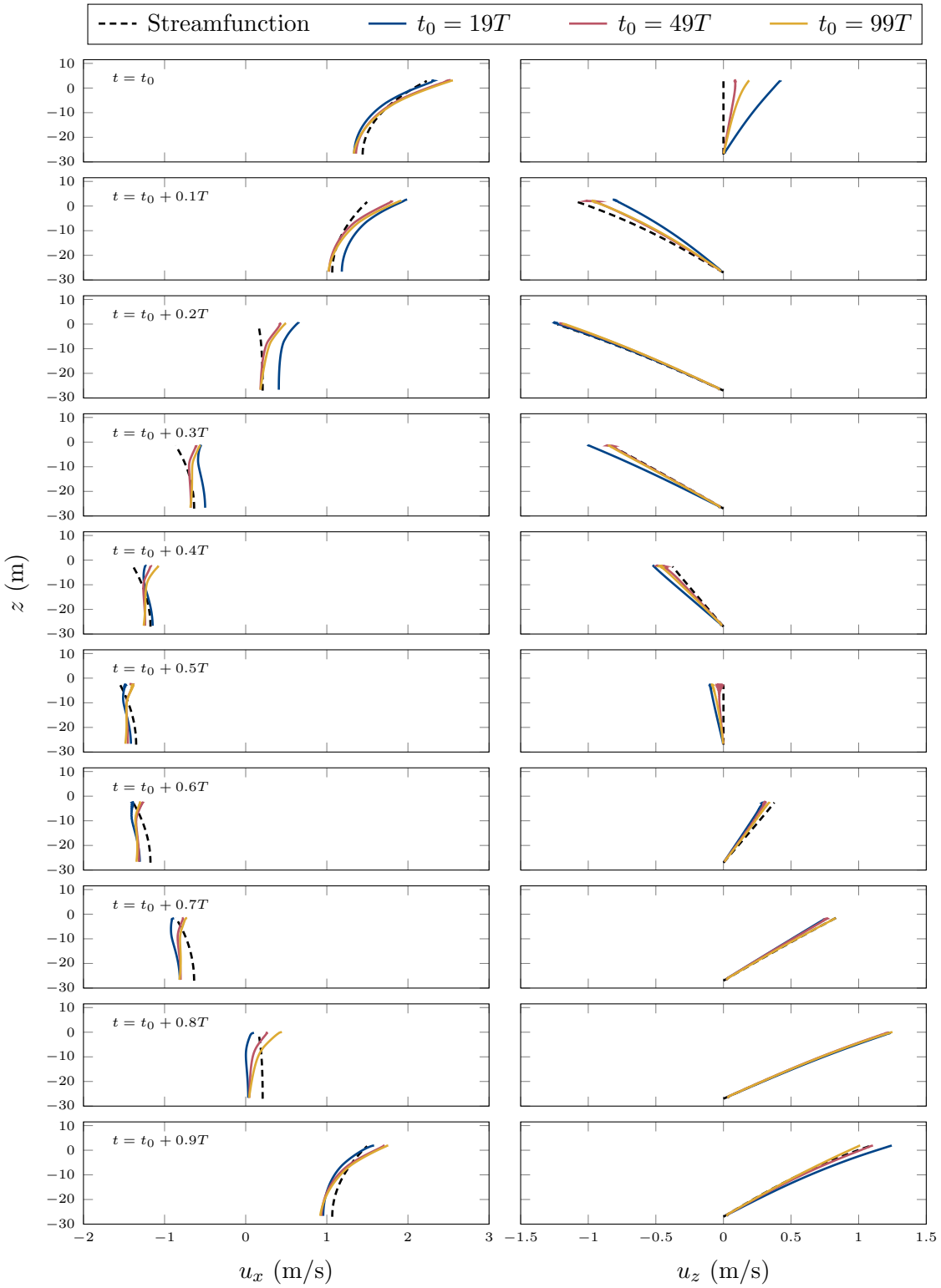

Figure 4.21: Vertical profiles of *CS* velocity in a coupled simulation, compared to the reference streamfunction solution, just before $t = 20T$, $t = 50T$ and $t = 100T$.

4.5.3 Testing coupled model limits in terms of wave steepness

As stated in the current chapter's introduction, a couple of hybrid simulations involving steep non-linear regular waves with a steepness of $\frac{1}{22}$ are run, again with the domain shown in figure 4.1. Such value of ϵ corresponds to the highest non-linear wave considered in the study of Dadmarzi et al. (2019) for which results of force on the monopile are reported. To reach it, a target wave height of $H = 10.5$ m is associated to a wavelength of $\lambda = 231.7$ m using the streamfunction algorithm of Dean (1965) implemented in *seine3d*. This time, and for the sake of time saving, we do not follow the above-mentioned guideline including independent computations with *CS* and *seine3d* to carefully select numerical simulation parameters. Thus, this study is mainly exploratory.

Normalized spatial and temporal resolutions levels used in the case of the mildly nonlinear wave with $\epsilon = \frac{1}{40}$ are retained in a first attempt. In *seine3d* instances, boundary elements dimensions at rest are $\Delta x_{seine3d} = \frac{\lambda}{16}$ and $\Delta z_{seine3d} = \frac{h}{4}$, with $\Delta y_{seine3d} = \Delta x_{seine3d}$. The *CS* mesh is built with the same rules in mind as before, namely $\Delta z_{\text{CS}} = \frac{H}{20}$ close to free surface, progressively stretched to $\frac{H}{4}$ near the floor and ceiling. $\Delta x_{\text{CS}} = \frac{H}{5}$: this corresponds to a longitudinal aspect ratio of 4 near the interface. Time step sizes are set to $\frac{T}{100}$ and $\frac{T}{1500}$ for *seine3d* and *CS* respectively, yielding a time step ratio of 15. Theoretical CFL in potential domains can be established as:

$$CFL_{seine3d} = \sqrt{gh}\frac{\Delta t_{seine3d}}{\Delta_{x,seine3d}} = 0.169 \tag{4.19}$$

In *CS*, it is approximated as:

$$CFL_{\text{CS}} = \sqrt{gh}\frac{\Delta t_{\text{CS}}}{\Delta x_{\text{CS}}} = 0.077 \tag{4.20}$$

A first simulation is launched with these settings but fails after approximately $20T$. The numerical solution indeed diverges in one of the *seine3d* instances. After a few trials, it was found that lowering the $CFL_{seine3d}$ through an increase of the time step size allows to stabilize the computation. Hence, $\Delta t_{seine3d}$ is set to $\frac{T}{30}$, yielding CFL value of 0.562. *CS* parameters are not modified. Therefore, time step ratio verifies $N_{\Delta t} = 50$.

Free surface time history is shown in figure 4.22 at $x = 0$ for comparison with the streamfunction solution. Albeit stable, the free surface signal differs significantly from the reference. This observation is confirmed by the errors levels reached on amplitude and phase, whose time evolution is displayed in figure 4.23. It appears that the simulated wave amplitude is approximately 13% lower than the reference value, while phase error settles at around -10°. Absolute error levels are thus nearly an order of magnitude higher than in the case involving a wave steepness of $\frac{1}{40}$. This does not seem to be related to wave reflection on the coupling or absorbing region. It rather seems to have to do with the intrinsic wave generation and propagation properties of *seine3d*. However, it was reported in a recent work involving *seine3d* in its current state, using the same boundary surface description

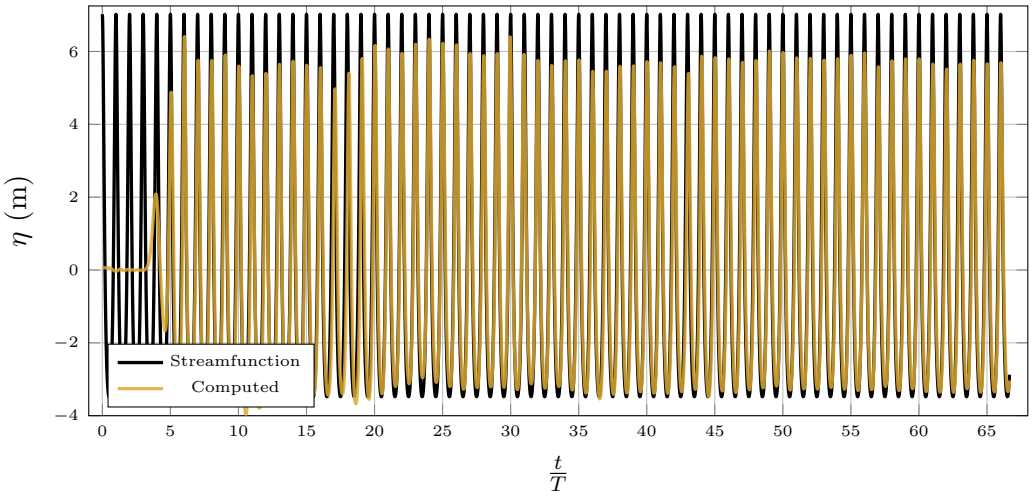

Figure 4.22: Comparison of the streamfunction and computed free surface signals at the virtual position of the monopile ($x = 0$ m) in the case of a wave steepness of $\frac{1}{22}$.

method and time stepping procedure, that generation and propagation of streamfunction waves were ensured in *seine3d* up to a steepness of $\epsilon = 0.092$. As it is equivalent to more than twice the wave steepness used here, it implies that the case of $\epsilon = \frac{1}{22}$ should not raise issues in *seine3d*. However, despite our efforts and due to time constraints, it was not possible to get a better wave field generation within *seine3d* for this wave steepness during this Ph.D work.

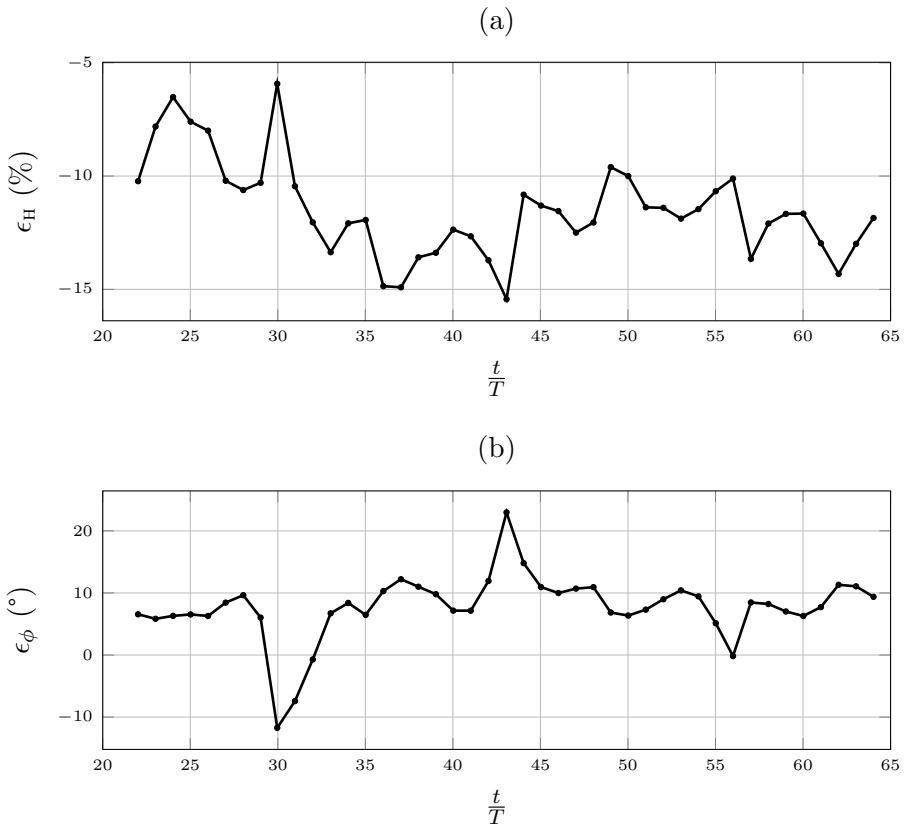

Figure 4.23: Relative error on wave height (a) and phase shift (b) at the virtual location of the monopile in the case of a coupled simulation with $\epsilon = \frac{1}{40}$. The first 20 wave periods are not displayed.

4.6 Conclusions

In this chapter, a test setup aiming at the validation of the generation, propagation, and absorption of 2D regular waves over constant depth withing the frame of the coupled methodology was described. A unique design wave with $T = 15$ and a steepness of $\frac{1}{40}$ is considered. It implies the use of one instance of *CS* sharing parts of its domain with coupled *seine3d* instances. This way it was intended to reproduce in 2D most of the characteristics of the wave basin used in the WAS-XL experiments Dadmarzi et al. (2019), with the idea of reusing most of the numerical parameters for later 3D computations with the same incident wave.

It is also believed that the normalized parameters selected in this study involving one wave case still hold for other wave cases, at least those sharing the same steepness. This assertion is evaluated in chapter 6.

It was therefore necessary beforehand to select appropriate numerical settings for *seine3d* and *CS*. Wave simulations involving each model independently were run and their results were analyzed in detail. Wave generation and absorption techniques, already implemented in *seine3d* were tested, yielding satisfactory results. Fine-tuning of the wave damping routine was required, again with the hope that the choices made for its parameters will prove efficient in future simulations with different incident waves. Free surface time history and profiles, as well as velocity field under waves were displayed and commented.

A similar work was conducted with *CS*. Wave generation and absorption strategies, though not used in coupled simulations, proved efficient. Free surface spatial profiles and time histories agreed very well with the reference solutions in the central working region of the *CS* domain. The occurrence of spurious horizontal velocity close to free surface was highlighted and studied in detail. Hypotheses were proposed to explain this phenomenon, as well as countermeasures. It indeed served as a basis for restricted sensitivity analyses that help choosing optimal time and space discretizations.

Selected *CS* and *seine3d* parameters were then applied to a first coupled regular waves simulation, along with numerical settings inherent to the coupling procedure itself. Results were detailed and found to be satisfactory and coherent with what had been seen of the behavior of each model alone.

The whole work presented in this chapter is thus considered as a guideline to the conception of later hybrid simulations.

Chapter 5

Coupled simulation of the diffraction of a solitary wave on a vertical cylinder

De premières simulations couplées en trois dimensions sont présentées dans ce chapitre. Une onde solitaire plane de hauteur relative modérée ($\frac{H}{h} = 0.3$) est diffractée par un cylindre vertical de diamètre $\frac{D}{h} = 1$. L'agencement des domaines couplés est similaire à celui employé en deux dimensions dans le chapitre 3. Ainsi, deux domaines seine3d *encadrent un domaine* CS*, dans lequel le monopieu est inclus, par le biais d'une approche de maillage adapté. Un problème de stabilité se fait jour au cours de la simulation dans l'un des deux domaines* seine3d*. Un rapprochement est fait avec le comportement du solveur potentiel, tel qu'il a déjà été observé en deux dimensions. Si la réduction de la hauteur relative de l'onde à 0.2 permet certes de limiter le développement de l'instabilité, le déraffinement des maillages* seine3d *dans le plan horizonal parvient au même résultat sans modifier la teneur du problème à résoudre. Un champ de vagues secondaire issu de la diffraction de l'onde solitaire sur le monopieu, puis de réflexions sur les parois du domaine est observé, se propageant en partie vers l'amont. Il est transmis sans modification notable au domaine potentiel amont, ce qui semble indiquer que la résolution horizontale finalement retenue pour* seine3d *est à même de décrire l'évolution d'une surface libre complexe. Cela concourt à valider le caractère bi-directionnel de la procédure de couplage. L'idée n'étant pas, dans ce chapitre, de confronter rigoureusement les résultats obtenus à des références expérimentales ou numériques, nous nous limitons à des considérations générales quant à l'allure de la surface libre. Une comparaison à des résultats expérimentaux est présentée au chapitre 6.*

5.1 General considerations

So far 2DV simulations have been realized based on two distinct setups with constant depth. They respectively aimed at describing the propagation of a solitary wave (chapter 3) and that of regular nonlinear waves (chapter 4). In the context of this PhD work, the constant depth choice is not questioned, but 3D numerical domains involving a fixed surface-piercing vertical cylinder of constant circular cross-section are considered.

As stated above, both solvers involved in the developed coupling methodology require 3D numerical domains. Hence no further extension of the hybrid procedure in the transverse direction is needed, as it already takes three-dimensionality into account, at least for the most simple geometries and configurations of the coupled 3D domains. As a first test case, similarly to the previous 2DV studies, the propagation of an initially plane solitary wave, followed by its diffraction by a monopile, are considered.

The results of such coupled simulations are not intended to be rigorously compared to a reference solution, either experimental, analytical or numerical. The idea is merely to make sure that the coupling procedure enables the reproduction of 3D problems that are not restricted to the propagation of a plane wave through coupled domains. The combination of wave diffraction on the cylinder and reflection on the lateral boundaries of the global domain is indeed expected to yield a complex upstream-propagating secondary wave field. The coupled methodology is deemed transparent enough if such wave field is not noticeably distorted by the presence of the overlapping regions. For the same reason, computational efficiency and cost associated to these exploratory simulations are not addressed in this chapter. The reader is referred to 6 for CPU time comparison.

Note however that the obtained results could be related to the ones of the experimental work of Yates and Wang (1994), the more recent one of Yang et al. (2021), or the numerical studies of Mo (2010) and Chen (2017); Chen et al. (2018).

5.2 Case description

Computations take place in a hybrid numerical domain built from the union of two equally long potential domains (namely *seine3d* 1 and *seine3d* 2) surrounding a *CS* domain containing the vertical cylinder. The global setup is pictured in figure 5.1, with the corresponding axes. The same conventions on normalization of space and time variables as used in chapter 3 are employed here. All variables cited thereafter are thus non-dimensional (*e.g.* physical distances have been normalized by the water depth at rest h, and time variables by $t_0 = \sqrt{\frac{h}{g}}$). A solitary wave with $H = 0.3$ is generated with its crest initially located in *seine3d* 1, as explained in chapter 3 in section 3.1.1. *seine3d* meshes extend from $x = -12$ to $x = 12$, and $x = 28$ to $x = 52$ respectively. Coupled boundaries in *CS* and *seine3d* are vertical and parallel planes, thus overlapping regions are rectangular boxes. Overlapping length $L_{overlap}$ is set to 2, as it was found to be an appropriate and sufficient value in

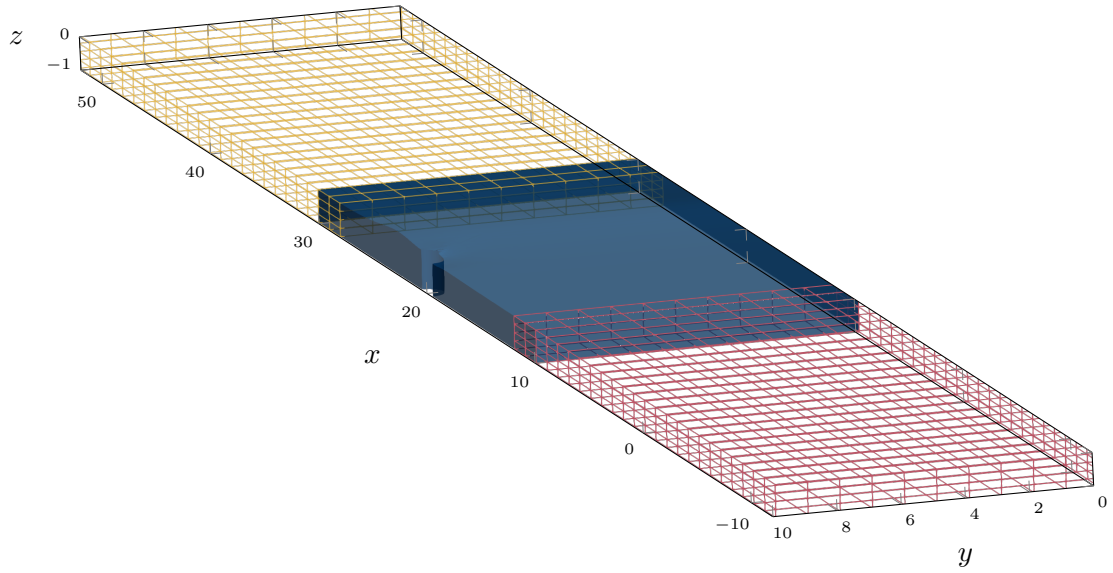

Figure 5.1: Computational domains used in the successful simulation of the diffraction of a solitary wave with $H = 0.3$, see section 5.4.

section 3.1.5. Hence, the *CS* domain corresponds to abscissa in the range $[10, 30]$, and extends from $z = -1$ to $z = 1.5$. All domains share the same width, equal to 10.

More complex shapes could theoretically be given to the overlapping regions in the coupling methodology, such as square or circular rings, as long as their geometry can be described analytically. It requires adapting the routines implemented to compute the distance from a given *CS* cell center to the set of associated coupling *seine3d* nodes, and conversely from a *seine3d* node to the associated *CS* coupling boundary. It is described in detail in chapter 2. However, such generalization is not considered in this work.

The monopile has a diameter D equal to the depth, and is included in the structured *CS* mesh through a body-fitted approach. Its center is located at $x = 0$ and $y = 20$. Figure 5.2 shows a close-up view of the corresponding mesh region. It may be noticed that cells height is uniformly distributed in the *CS* domain. Mesh is cylindrical on the structure, and is forced to a Cartesian grid in a rectangular box enclosing the cylinder. Elsewhere, it reduces to a Cartesian grid. In most of the domain, cells are hexahedra with 2 horizontal square faces, for which $\Delta z_{seine3d}$ is close to $\frac{1}{4}$ of a side of the square. $\Delta z_{seine3d} = \frac{H}{20}$ for the solitary wave with $H = 0.3$. The cylindrical layout of mesh elements allows obtaining almost square-shaped boundary faces on the monopile.

The *seine3d* meshes are built based on the ones used for the corresponding 2DV study, for which a value of 4 elements in the height of a water column was retained, alongside with the restriction that boundary elements should be as close to squares as possible, for computational efficiency purposes. Therefore a first couple of meshes for potential domains *seine3d* 1 and *seine3d* 2 is designed with square elements on their boundaries, with a side length of $\frac{1}{4}$. This amounts to placing 40 elements in the width of both domains, as well

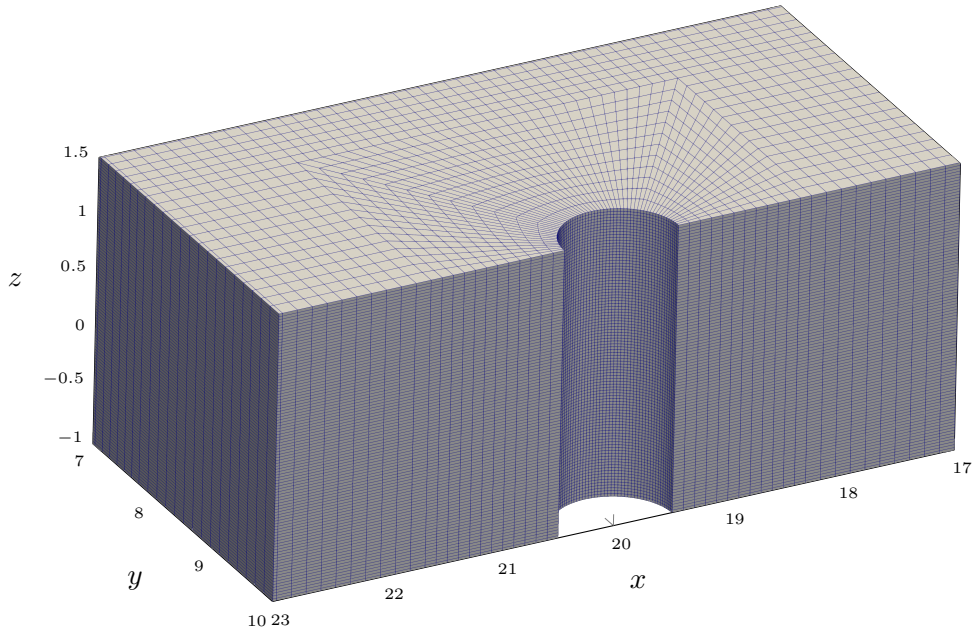

Figure 5.2: Detail of *CS* mesh near the monopile.

as 96 in their length. Boundary elements height is set to $\frac{\eta(\mathbf{x},t)+1}{4}$ where $\eta(\mathbf{x},t)$ is the instantaneous normalized local free surface elevation, measured from the resting level. For the sake of visibility, they are not shown in figure 5.1, where coarser *seine3d* meshes are displayed.

CS and *seine3d* time steps values are identical to the ones used as reference in the 2DV study led in chapter 3, with $\Delta t_{seine3d} = 0.1$ and $\Delta t_{\text{CS}} = 0.01$, thus $N_{\Delta t} = 10$.

5.3 First 3D results and limitations

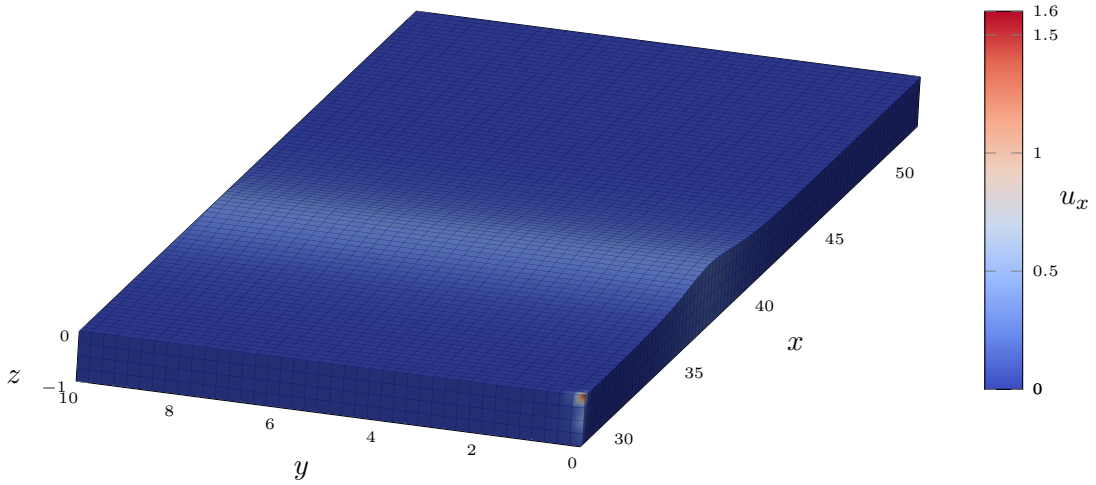

Figure 5.3: Detail corner instability occuring at the downstream boundary of the *seine3d* 2 domain, $t = 32.4$.

The simulation whose numerical parameters are listed in the previous section fails because of a corner instability, occurring on the coupling boundary of the downstream potential domain. This situation is illustrated in figure 5.3 at one of the last simulated time instants. It resembles the stability issues encountered in section 3.1.2.3, as velocity diverges at one corner, albeit fatal this time. Causes for such behavior have already been discussed in the same section, at least in part.

Another simulation is run using the same setup and numerical parameters, except that relative wave height is reduced to 0.2. This time the simulation succeeds, and lasts approximately 50 time units, giving the wave enough time to start interacting and reflecting on the vertical wall closing the *seine3d* 2 domain at $x = 52$. A decrease in initial wave steepness, as expected, enables getting over stability issues in *seine3d*.

Figure 5.4 shows contour plots of free surface elevation at successive time instants in the simulation. Here, the focus should be put less on the fate of the main wave, that keeps on travelling in the incident direction after it has passed the monopile, and more on the diffracted and reflected wave fields propagating upstream, as already mentioned.

As no quantitative comparison is made with reference results, one may only assess the quality of diffracted and reflected fields from an analogy with wave patterns based on experimental or numerical references.

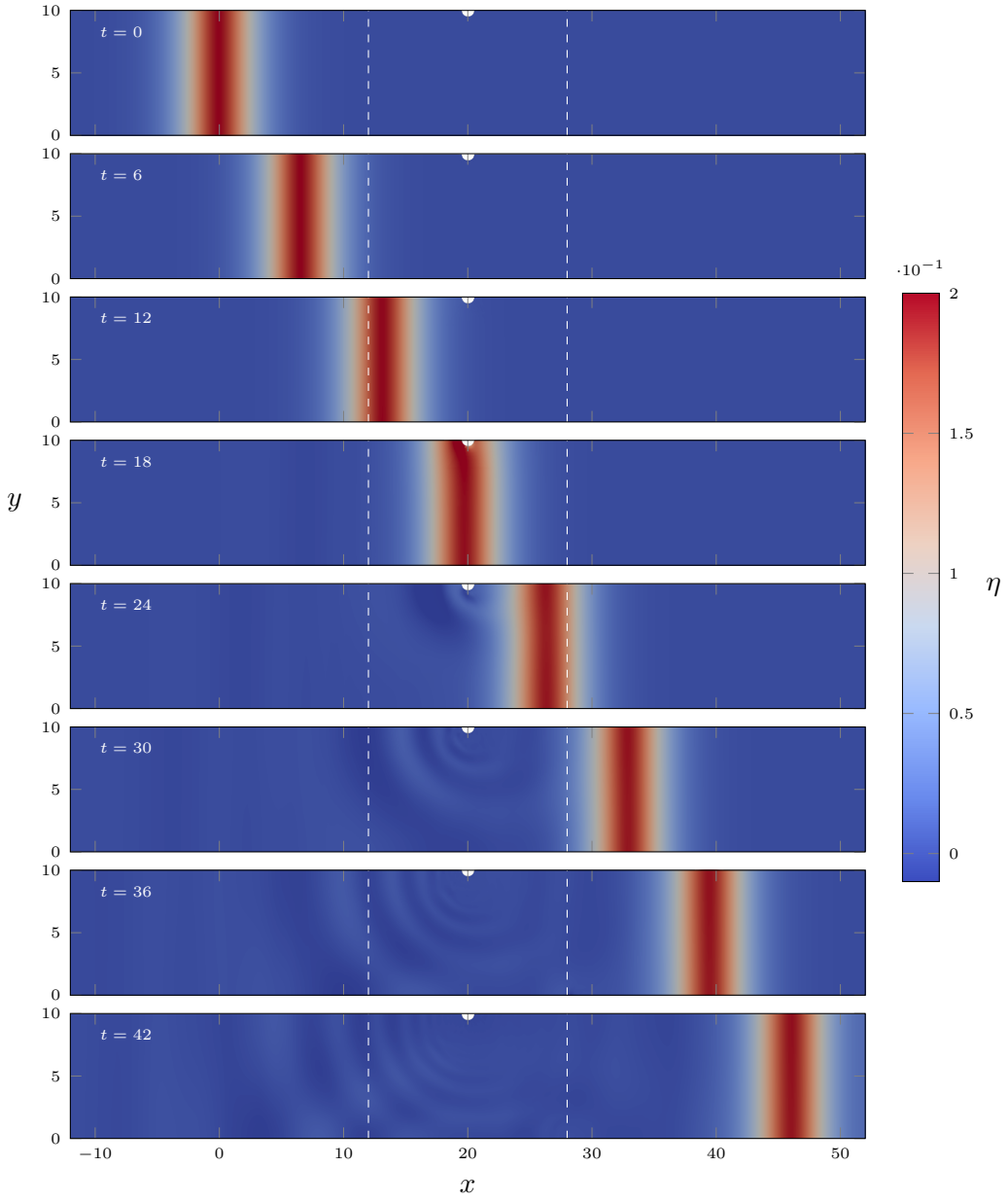

Figure 5.4: Snapshots of free surface elevation contours during the propagation and interaction with a vertical surface piercing cylinder of a solitary wave with $H = 0.2$. Dashed lines indicate limits of potential domains.

5.4 Overcoming stability limitations

Aiming to succeed at simulating the scattering of an initially plane solitary wave with $H = 0.3$ with the monopile, we choose to run a new simulation using coarser meshes to discretize the potential domains. Indeed, it has been experienced in previous *seine3d* simulations that lowering the CFL by increasing horizontal dimensions of boundary elements can help to stabilize the calculations.

Meshes are displayed in figure 5.1 in wireframe representation for these coarser meshes. Boundary elements height is kept the same ($\frac{1+\eta}{4}$). Length and width, at the same time, are doubled. Hence, element aspect ratio is over 1, theoretically leading to a reduced efficiency of the BIE integral problem resolution, due to the need to use adaptive integrals for quasi-singular terms. However, this is more than outbalanced in computational time and cost by the decrease in complexity associated to the use of meshes with fewer elements.

With these changes in horizontal resolution in *seine3d*, simulating the propagation of a solitary wave with $H = 0.3$ and its interaction with the vertical cylinder is possible. As in the previous case with $H = 0.2$, the calculation is stopped when the wave starts reflecting on the far-right vertical boundary of *seine3d* 2, around $t = 42$.

Contour plots of non-dimensional free surface elevation are drawn in figure 5.5. Again a satisfactory behavior of the coupled model is observed, as a small amplitude diffracted field appears soon after the solitary wave hits the structure. This field propagates in accordance with expected diffraction patterns. It then reaches the upstream *seine3d* domain with negligible distortion, between $t = 30$ and $t = 36$. Again coupling transparency seems ensured. The diffracted field then starts reflecting on the horizontal wall located at $y = 0$, yielding a crossing wave field. These steps are pictured in more detail in figure 5.6, with adapted colorbar extrema.

It thus appears that even with rather coarse meshes in potential domains, featuring elements with a width of $\frac{1}{2}$, bi-didirectionally and transparency of the coupling procedure is ensured in 3D simulations. Even small amplitude (*CS* subgrid scale) wave trains can be transmitted from *CS* to *seine3d* without significant modification. It should allow for a reduction of the spatial extent of 3D *CS* domains, hence further confirming the two-way hybrid strategy's relevance, at least in the case of solitary waves.

Figure 5.7 displays the smooth interface geometry at the close vicinity of the vertical cylinder in *CS*. As already mentioned, it is shown mainly for illustrative purposes. We may at least notice that the free surface looks complex enough for the expected highly-nonlinear phenomena to be sufficiently well rendered in future calculations involving similar spatial resolutions. Indeed, an upstream-propagating wave is observed, starting from $t = 21$. Partly owing to the smoothing post-processing stage, no numerical artifact related to cell non-orthogonality is seen at the junction between the cylindrical mesh around the monopile and the Cartesian grid elsewhere in the domain. Thus the *CS* meshing strategy seems relevant.

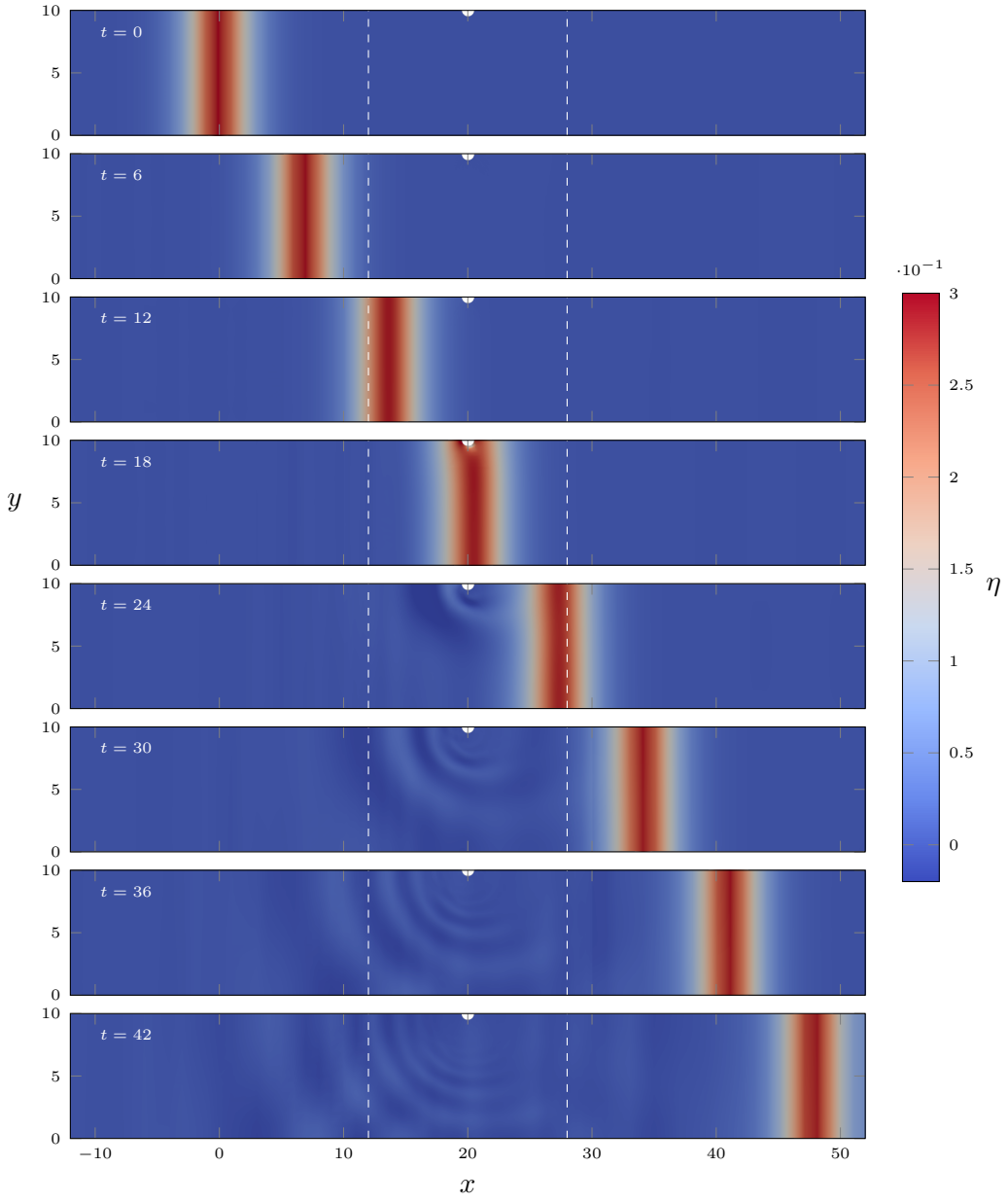

Figure 5.5: Snapshots of free surface elevation contours during the propagation and interaction with a vertical surface piercing cylinder of a solitary wave with $H = 0.3$. Dashed lines indicate limits of potential domains.

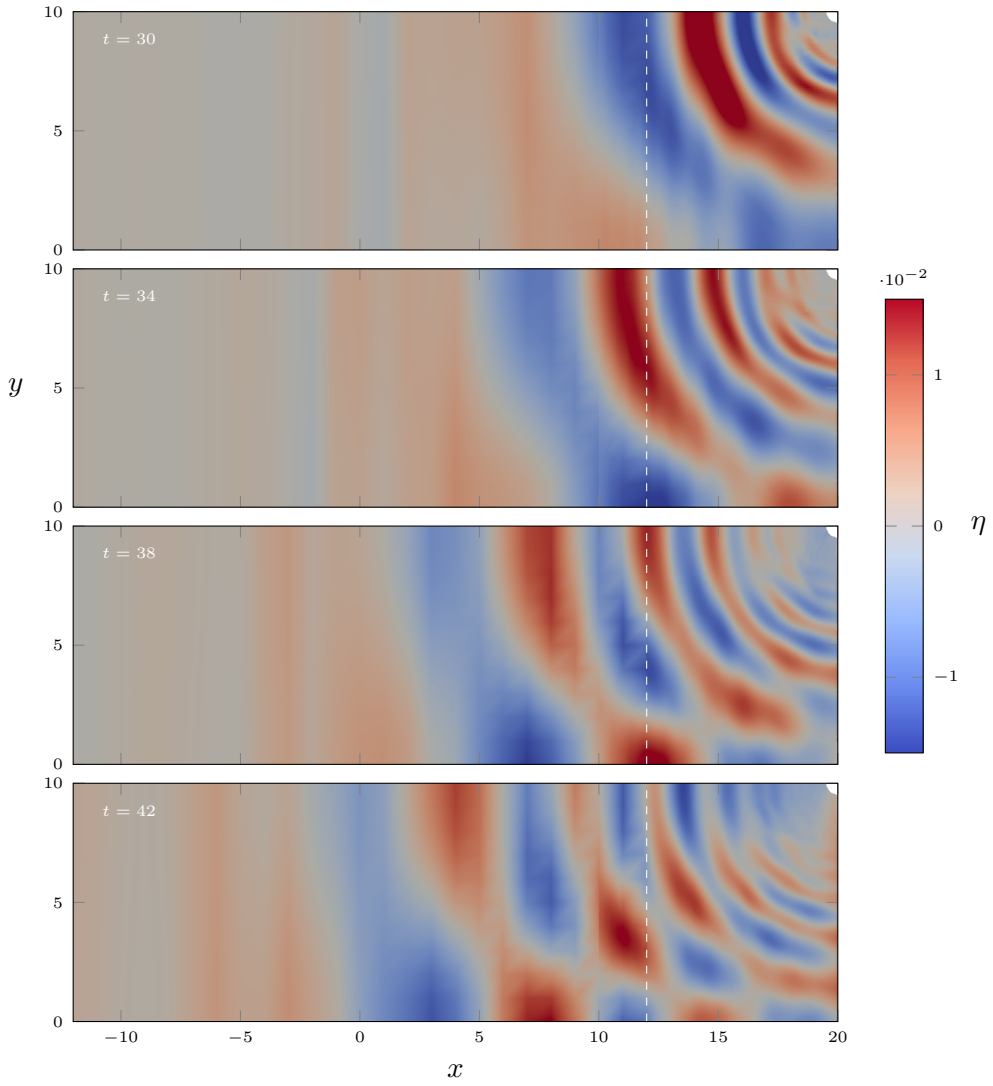

Figure 5.6: Detailed free surface elevation contours at different time instants in the case of $H = 0.3$. Dashed line indicates coupled boundary of *seine3d* 1 instance. Square patterns are visualization artifacts related to the interpolation of values between *seine3d* boundary nodes.

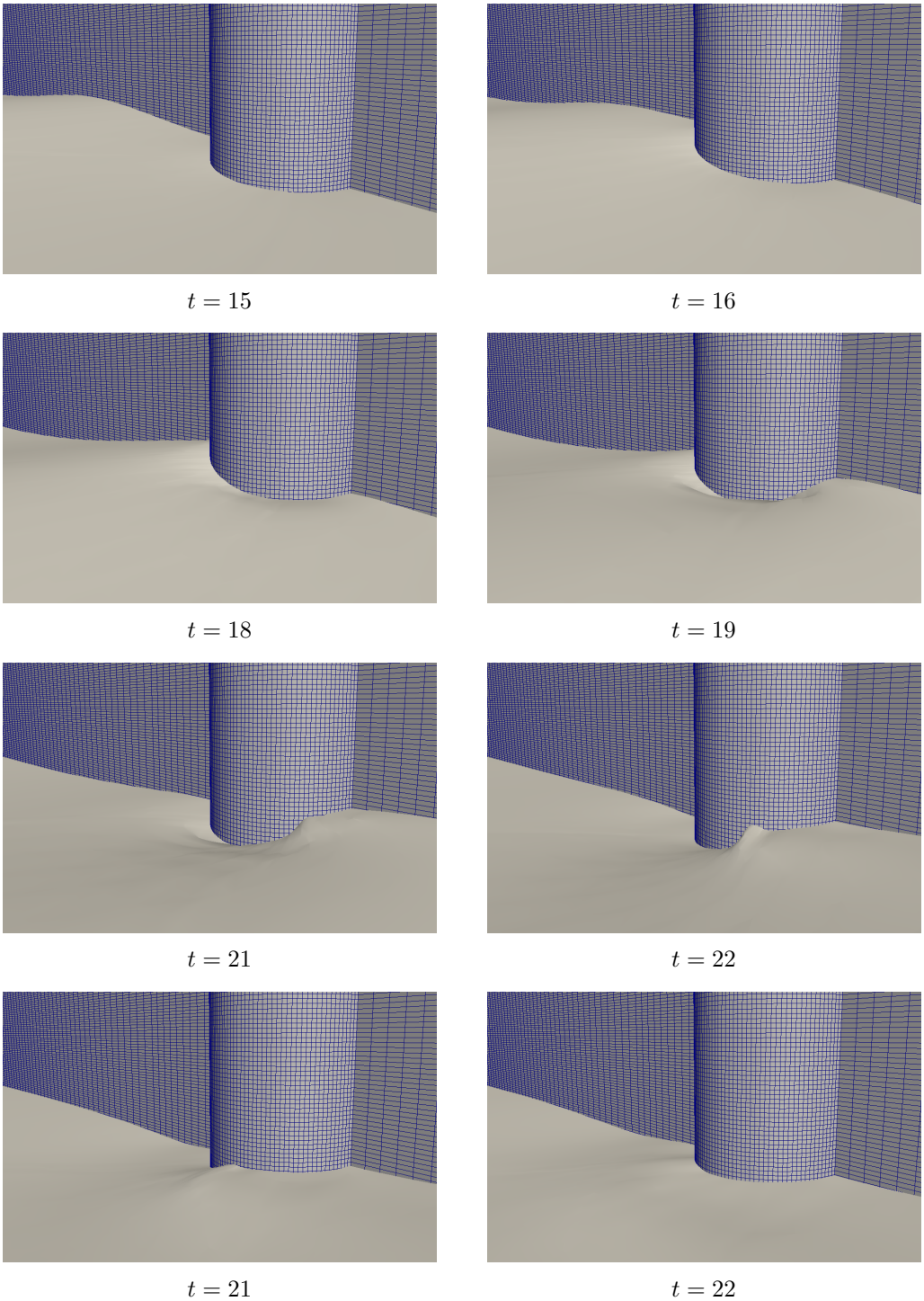

Figure 5.7: Snapshots of free surface shape near the monopile at various time instants. Incident wave comes from the left.

5.5 Conclusions

From the case of a solitary wave of moderate relative height diffracted by a vertical cylinder, it seems that the coupling procedure is suitable for 3D applications, at the cost of a cautious selection of certain numerical parameters. Indeed, the horizontal resolution used in *seine3d* as a default value to compute the propagation of the same plane wave in 2D turned out not to be adapted to the 3D case. Reducing the level of nonlinearity, by selecting a lower wave height value was an option to avoid instabilities appearing at a corner of the downstream potential coupling boundary. However, choosing an appropriate value of $\Delta y_{seine3d}$ has proved necessary and sufficient to enable stable calculations with $H = 0.3$.

No reference solution being sought, the accuracy of the comptuted solution was not rigorously assessed. This could be adressed in the future by considering for instance the experiments done by Yang et al. (2021); Yates and Wang (1994). Simulating the interaction of regular waves with a monopile, as presented in the next chapter, for which experimental reference results are considered, should allow for filling this void.

Chapter 6

Coupled simulations of the diffraction of regular nonlinear waves on a vertical cylinder

Dans ce dernier chapitre, on présente les résultats de simulations en trois dimensions décrivant la diffraction de houles régulières de diverses cambrures sur un cylindre vertical représentant une fondation d'éolienne offshore, en profondeur constante. Trois houles de cambrure $\frac{H}{\lambda} = \frac{1}{40}$ et de périodes différentes (9s, 12s et 15s) sont reproduites numériquement, ainsi qu'un cas de plus forte cambrure ($\frac{H}{\lambda} = \frac{1}{22}$). Des constatations qualitatives sont effectuées, relatives à la géométrie de la surface libre à proximité du monopieu, et des comparaisons sont établies avec des résultats numériques de référence. Les résultats de simulation sont comparés à la solution de vague semi-analytique imposée en entrée du domaine, en terme d'élévation de surface libre à l'abscisse du cylindre, ainsi qu'aux données expérimentales issues de la campagne d'essais WAS-XL, par l'analyse du contenu fréquentiel du signal de force horizontale adimensionnée s'exerçant sur le cylindre. Le coût de calcul de chaque simulation est précisé, estimé par le rapport du nombre d'heures-processeurs au temps physique simulé. L'un des cas de simulation est également reproduit uniquement avec Code_Saturne, ce qui permet de quantifier le gain de performance permis par le recours à des sous-domaines couplés.

6.1 Case presentation and numerical settings

In this chapter, 3D coupled simulations of nonlinear regular waves interacting with a surface-piercing vertical cylinder representing a large offshore wind turbine foundation are presented. Similarly to 3D simulations of the interaction of a solitary wave with a vertical cylinder over constant depth, these 3D cases are based on previous 2DV computations described in chapter 4. The shift to 3D could be pictured as an horizontal extrusion of all 2DV subdomains, with the addition of a semi-circular structure on one side of the central *CS* domain. Hence, global domain geometry matches as much as possible that of the experimental basin used for WAS-XL measurement campaign (Dadmarzi et al., 2019). Intrinsic symmetry of the problem is taken into account to halve the numerical domain size. A *Symmetry* boundary condition is enforced on the cylinder surface, as well as on all vertical walls and bottom, where the velocity vector verifies $\frac{\partial \mathbf{u}}{\partial n} = 0$.

In the experimental study of Dadmarzi et al. (2019), two water depths are considered in the basin, namely 27 m and 33 m at prototype scale, in which two monopile models are placed whose respective diameters are 9 m and 11 m. As already mentioned, only the smallest depth is considered in the current work. Also, $D = 9$ m is selected. It is indeed believed that the coupling procedure will be equally capable of simulating other wave conditions. It should also be noted that, as already discussed in chapter 4, the wave steepness is defined as the first order wave height divided by the wavelength.

6.1.1 Numerical settings

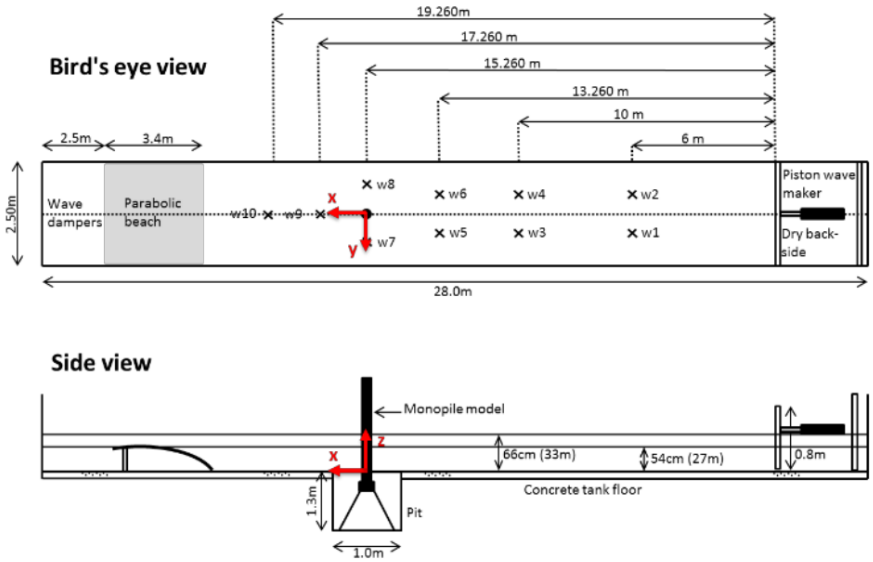

Figure 6.1: Experimental domain layout. Reproduced from Dadmarzi et al. (2019).

Time discretization as well as vertical and longitudinal spatial resolutions, normalized by wave characteristics, are kept the same in code instances *seine3d* 1 and *seine3d* 2, as well

as all other parameters and options, such as solver or time-stepping scheme choices. The reader might refer to figure 4.1 for an overview of the longitudinal layout of domains. Views of the numerically reproduced experimental domain are shown in figure 6.1.

To match the characteristics of the experimental wave basin, the width of the domain is set to 62.5 m. The novelty here resides in the choice of the transverse dimension of boundary elements, which is not trivial, as seen in chapter 5. Thus $\Delta x_{seine3d}$ is kept equal to $\frac{\lambda}{16}$, while $\Delta y_{seine3d}$ is given the value of $\Delta x_{seine3d}$ in both *seine3d* instances. A target value of $\Delta z_{seine3d} = \frac{h}{4}$ where the free surface is at rest is retained. In accordance with the 2DV coupled wave simulations, $\Delta t_{seine3d} = \frac{T}{100}$.

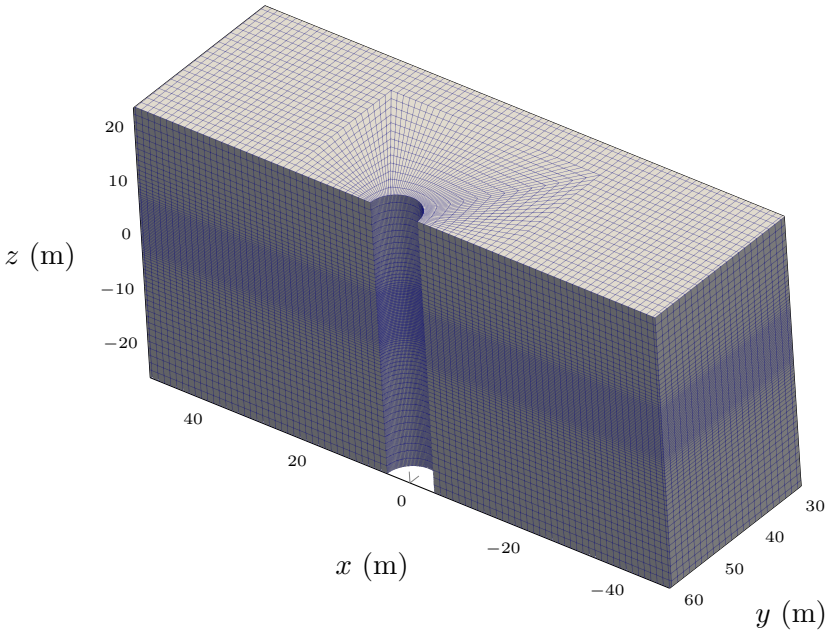

Figure 6.2: Close-up view of the *CS* mesh in the vicinity of the monopile in the case of $T = 15$ s and $\epsilon = \frac{1}{40}$.

Similarly, most *CS* numerical parameters are left unchanged and follow the dimensioning laws established in chapter 4. A computational mesh with a body-fitted description of the monopile surface is built (see figure 6.2), similar to the one employed for chapter 5 simulations. Most meshing specifications elaborated in 2DV cases are met, *i.e.*, Δx_{CS} and Δy_{CS} equal $\frac{H}{5}$ in most of the domain, away from the close vicinity of the monopile. $\Delta z_{\text{CS}} = \frac{H}{20}$ is verified in a layer comprised between $z = -\frac{H}{2}$ and $z = H$. Following the conclusions of the sensitivity analysis conducted in section 4.4.4, Δt_{CS} is set to $\frac{T}{3000}$, thus setting the value of the time step ratio to $N_{\Delta t} = 30$.

The length of the overlapping regions between *CS* and *seine3d* domains equals $\frac{\lambda}{4}$, as established in 2DV studies. The general layout of numerical domains is partly described in figure 6.3.

We aim at assessing the coupling methodology as a tool potentially suited for engineering applications. With this idea in mind, 3D simulations should be straightforwardly conceived

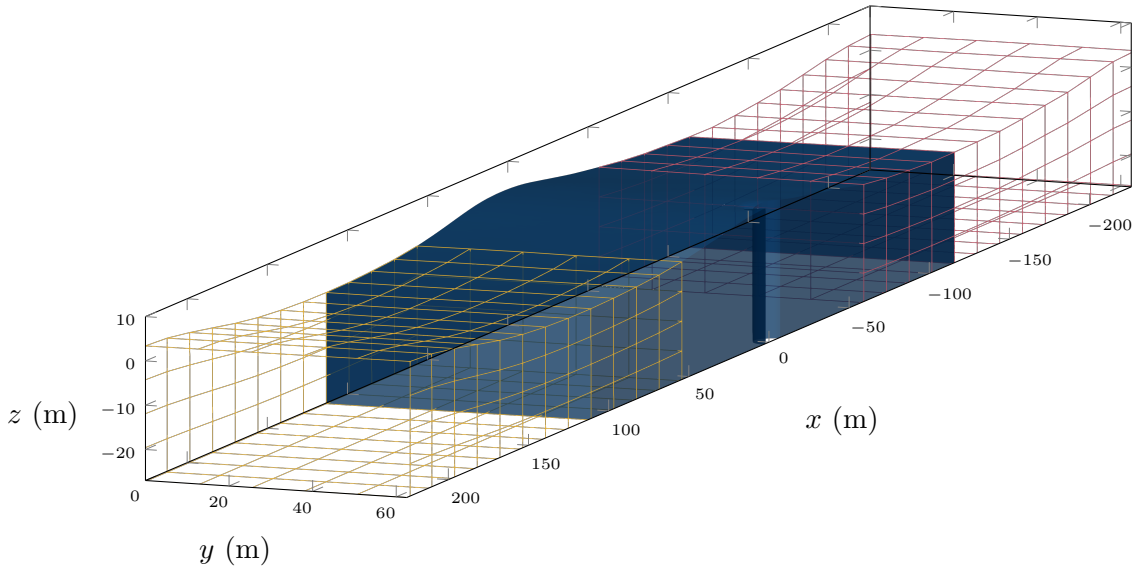

Figure 6.3: View of the computational domains in the case of $T = 15$ s and $\epsilon = \frac{1}{40}$.

from preliminary 2DV computations or general rules based on experience. Therefore only one set of computational results is presented for a given wave condition, the latter being defined by a combination of a wave period and a wave height, or steepness. Four different wave conditions are reproduced from the WAS-XL campaign, with two values of the wave steepness $\frac{H}{\lambda}$: $\frac{1}{40}$ and $\frac{1}{22}$. For the lower wave steepness, wave conditions are summarized in table 4.1. Three wave periods are considered with $h = 27$ m and $D = 9$ m: 9 s, 12 s, and 15 s, the latter corresponding to the case extensively studied in 2D in chapter 4. For the more exploratory case of $\frac{1}{22}$ steepness, only a period of 15 s is investigated, associated to a wave height of $H = 10.5$m.

6.1.2 Spectral analysis of the horizontal force exerted on the monopile

Agreement of coupled simulations with experimental results is assessed through the comparison of the frequency contents of the time signals recorded for the depth-integrated inline force on the cylinder. In Dadmarzi et al. (2019), amplitudes of the first three harmonics of the normalized horizontal load on the monopile are provided for wave periods in the time range [6 s, 16.5 s]. It is also briefly explained that harmonics amplitudes are extracted thanks to a narrow-banded filter based on the Fast Fourier Transform (FFT).

In the current study, and similarly to the linear reflection coefficient calculation described in Appendix A, a short-time Discrete Fourier Transform (DFT) is applied to the wave elevation and inline force time signals, with a one-wave period sliding window. The DFT is computed thanks to the FFT algorithm of the *Numpy* Python library.

The amplitude of the i^{th} harmonic of the depth-integrated inline force is normalized as

follows:

$$F_x^{(i\omega)} = \frac{F_x^{(i\omega),\mathrm{dim}}}{\rho g a^2 A_1} \tag{6.1}$$

where $F_x^{(i\omega),\mathrm{dim}}$ is the horizontal force of the 1^{st} harmonic of the wave frequency $\omega = \frac{2\pi}{T}$, ρ is the water density, g the gravitational acceleration, a the monopile radius, and A_1 the amplitude of the first harmonic of free surface elevation, recorded next to the monopile.

6.2 Coupled results for the smallest wave steepness

In this section, hybrid results are compared with the experimental reference in the case of the $\frac{1}{40}$ wave steepness, with $h = 27$ m and $D = 2a = 9$ m.

6.2.1 15 s wave period

For this wave condition, on which we dwelled in 2DV in chapter 4, it is reminded that the target wave height equals $H = 5.75$ m.

A physical duration of approximately $57T$ is simulated. The *CS* mesh comprises 652 859 numerical cells. *seine3d* 1 mesh has 1181 nodes while *seine3d* 2 has 1401. The computation runs for 3 days on 2 nodes of the HPC cluster, comprising 27 cores each. *CS* instances uses 20 processors, while *seine3d* 1 employs 15 and *seine3d* 2 19. The number of CPU cores assigned to the *CS* instance is calculated based on a recommendation issued for computations involving only *CS*, stating that 30 000 cells should be attributed to each processor. The number of processors used by the different *seine3d* instances was determined based on our small experience of coupled simulations. Therefore, there should be room for improvement, and the computational speed of hybrid computations may well be increased. Scalability analysis of 3D coupled large simulations was nevertheless considered out of the scope of the current work.

It takes around 1.22h of computation with this setup to simulate one wave period. Hence, the ratio of computational time in core-hours (ch) to simulated time expressed in seconds is:

$$N_{cpl.} = \frac{1.22 \times 27 \times 2}{15} = 4.4 \text{ ch.s}^{-1}$$

This quantity might be used for a comparison with a *CS*-only computation of the same wave condition involving a large numerical domain built from the union of *seine3d* 1, *CS* and *seine3d*2 coupled subdomains.

6.2.1.1 Free surface time signals

At first, free surface elevation time history extracted at a wave gauge next to the cylinder, of coordinates $x = 0$ m and $y = 31.25$ m is compared to the streamfunction wave signal. In the description of the experimental setup, no indication is given as to the lateral position, *i.e.* the y-coordinate, of the wave probe of interest. Therefore, in the numerical study it was quite arbitrarily put halfway between the monopile centerline and the opposite lateral wall.

It should be noted that for such comparison to hold, wave interaction with the vertical cylinder should remain negligible at the position of the wave gauge, so that free surface elevation there does not differ much from that of the incident plane wave. This assumption

is tested in Dadmarzi et al. (2019). Indeed, wave calibration tests are conducted with a wave steepness of $\frac{1}{30}$. There, few discrepancies are noticed for the first three harmonics of free surface elevation between the theoretical solution and the basin results, with and without the monopile. Such observation applies for the whole range of wave periods considered. Therefore, it seems reasonable to assume that the output of the selected wave probe can be compared to the streamfunction wave solution evaluated at the same abscissa.

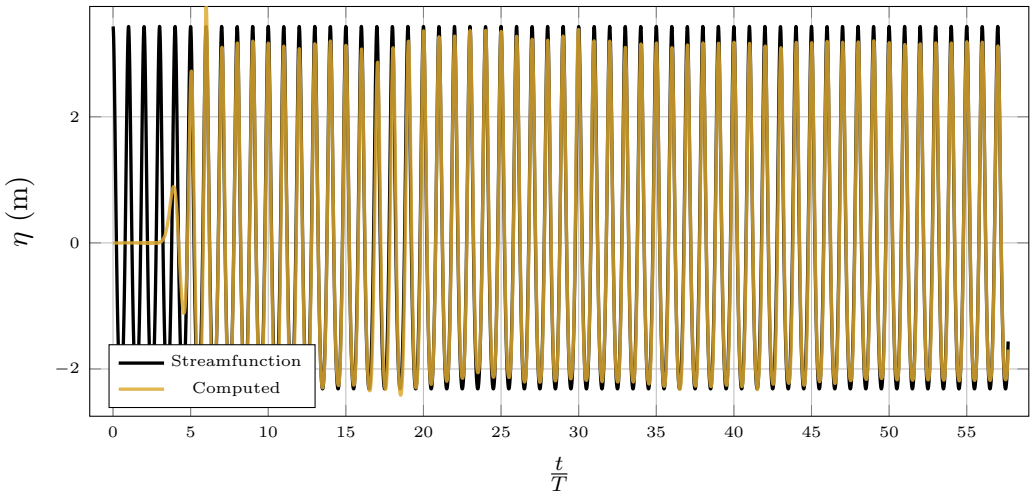

Figure 6.4: Comparison of streamfunction and computed free surface signals at the wave gauge next to the monopile, of coordinates ($x = 0$ m, $y = 31.25$ m).

Simulated free surface elevation time history is displayed in figure 6.4. 3D results are similar to the 2DV ones pictured in figure 4.18, in terms of the time needed for the waves to fully develop (around $20T$).

Wave amplitude and phase errors are shown in figure 6.5. They should be related to results displayed in figure 4.19. Error on amplitude reaches higher levels in the simulation of waves interactions with the monopile (between 4% and 5%), as compared to 2DV (around 3%). Similarly, phase shift slightly increases between 2DV and 3D, amounting to approximately 4° when stabilized, as compared to 3° in the 2DV case.

Hence, we observe discrepancies between 2DV and 3D coupled results when studying time evolution of the free surface elevation at the abscissa of the monopile. These could either originate from wave diffraction by the monopile and subsequent reflections on the lateral walls or unphysical effects introduced by the couplings, that worsen when shifting from 2DV to 3DV. Nonetheless, errors remain limited: accuracy of the hybrid computation in terms of free surface position seems sufficient to justify its use in the simulation of 3D problems. A last insight into wave height error is given below, where the first order wave amplitude is compared to its streamfunction counterpart.

This study serves as a first validation of 3D coupled results. A qualitative assessment of the free surface shape in the *CS* domain, close to the cylinder, is also conducted.

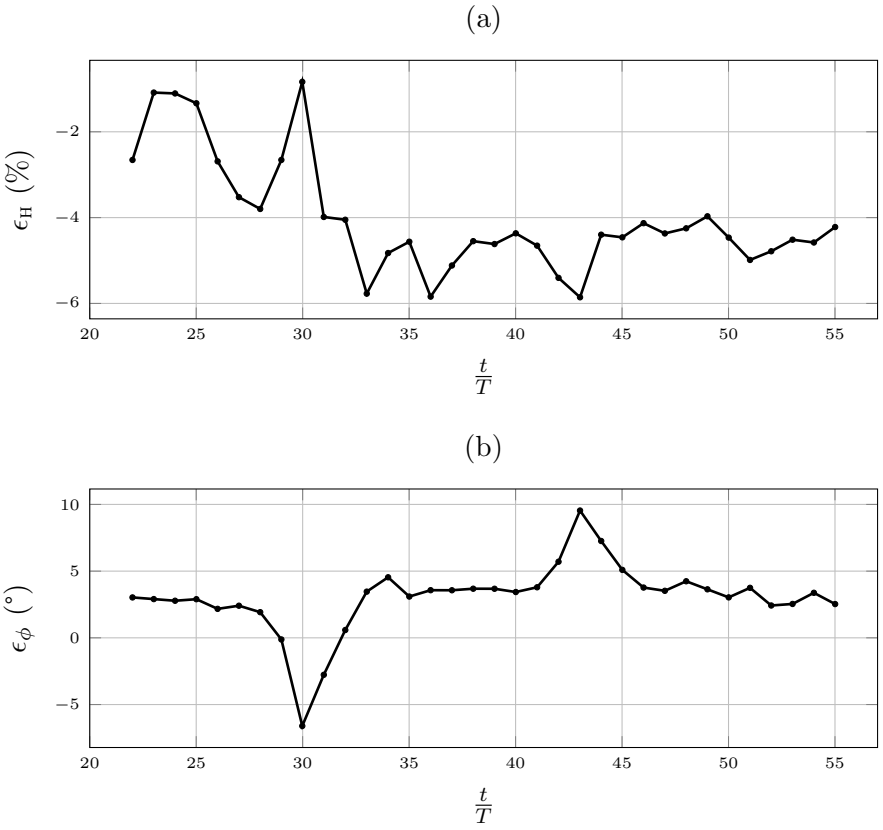

Figure 6.5: Relative error on wave height (a) and Phase shift (b) recorded by a wave gauge located at $x = 0$ m, $y = 31.25$ m. The first $20T$ are excluded from the analysis.

6.2.1.2 Free surface shape close to the cylinder

A series of snapshots of the free surface next to the monopile is presented in figure 6.6, over a time interval of $\frac{T}{5}$ (from $30T$ to $30.2T$), after the wave crest hits the structure. As already mentioned, smooth free surface shape is defined as the void fraction contour surface where $\alpha = 0.5$. A moderate wave run-up is noticed on the upstream side of the cylinder, around $t = 30T$. As the wave is diffracted by the cylinder then reflected on the symmetry plane, an upstream propagating wave appears. This seems to be in line with other numerical results of wave diffraction by a slender circular cylinder, such as those obtained by Paulsen (Paulsen, 2013; Paulsen et al., 2014). The level of accuracy reached in the description of the free surface thus seems sufficient for the considered purposes of the hybrid simulations.

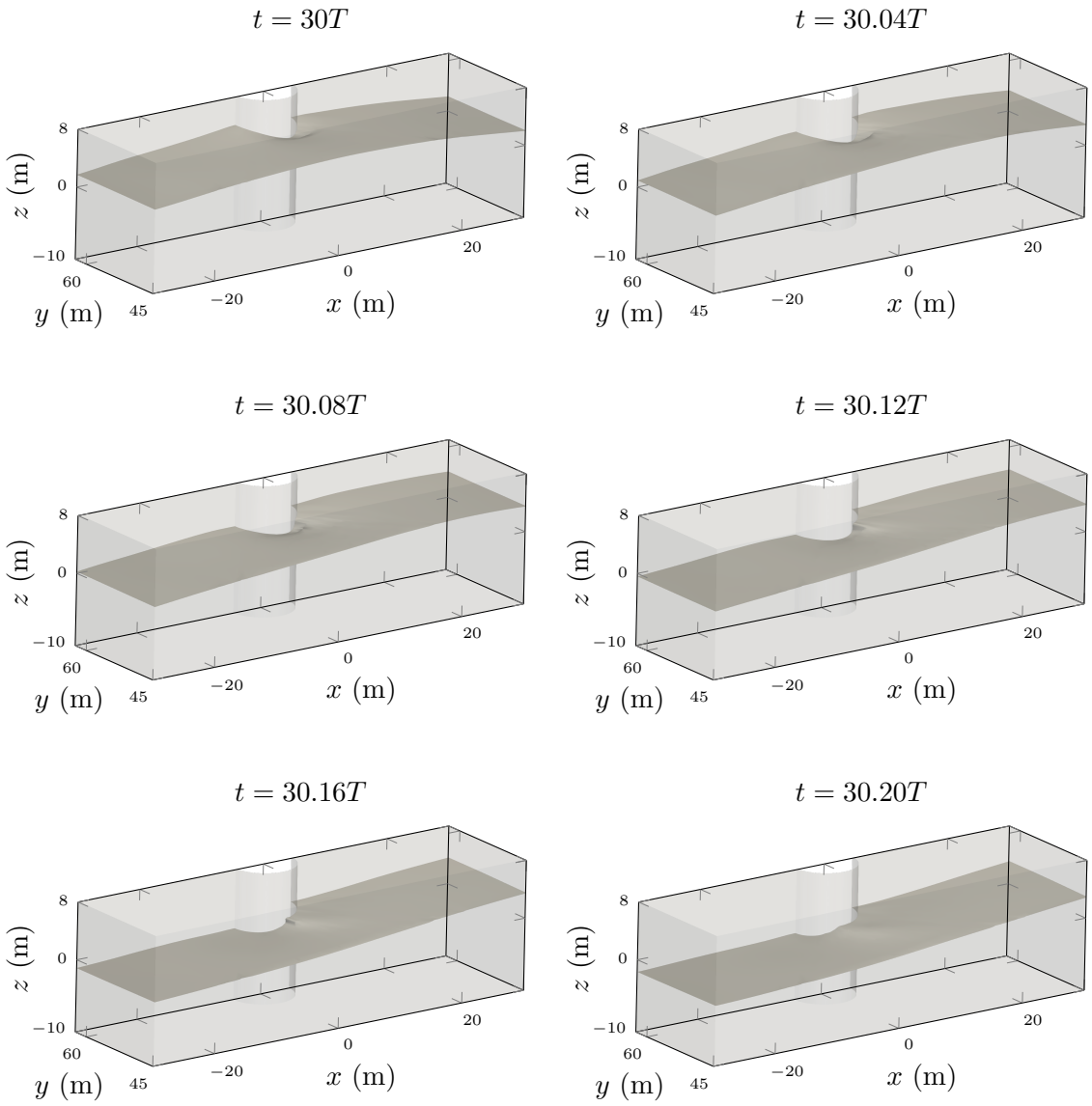

Figure 6.6: Snapshots of the free surface in the *CS* domain near the monopile, as a wave crest passes. Incident waves are coming from the left.

6.2.1.3 First order wave amplitude

Extracting the first order wave amplitude from simulation results is necessary to normalize the horizontal force signal, as described in equation 6.1. It also allows for a measure of the simulated wave steepness, as we have seen that in Dadmarzi et al. (2019) wave steepness is calculated with the first order wave height.

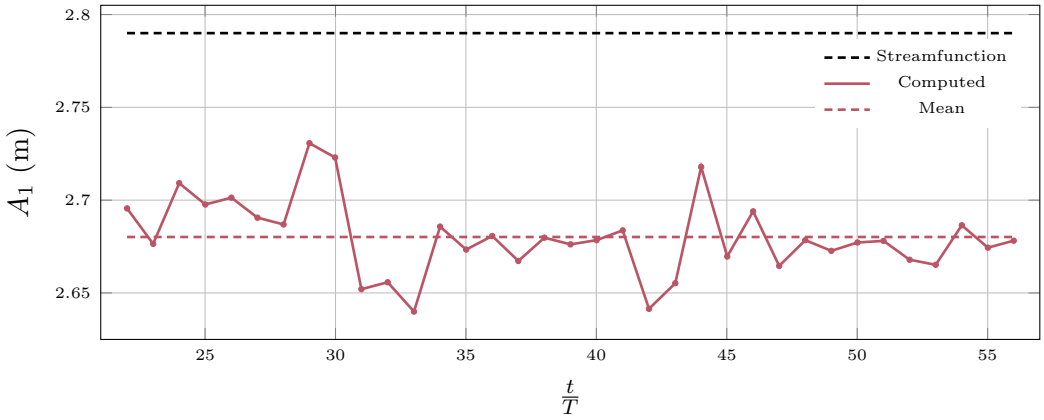

Figure 6.7: First order wave amplitude in the coupled simulation for $T = 15$ s. The spectral analysis of the numerical results is realized over one wave period (red nodes). A dashed red line illustrates the average amplitude over the whole displayed time interval. The free surface signal is recorded by the same wave gauge as in figure 6.4, while the first $20T$ are excluded from the analysis and therefore not shown.

In figure 6.7, the simulation results are compared to the semi-analytical streamfunction solution used for wave generation. As already mentioned, the simulated first order wave amplitude is computed with a FFT applied over successive wave periods, after a sufficient time delay has elapsed. Here this delay is taken as $20T$. The mean value of A_1 in time is also computed, and compared to the streamfunction value. In the current case, it is found that the simulated first order wave amplitude, $A_{1,sim.}$ is 3.9% lower than the streamfunction value, $A_{1,str.}$. This conforms with the findings related to global wave amplitude reported in the previous subsection .

Thus the wave steepness, as defined in the reference experimental work and based on the first order wave height, is 3.9% lower in the coupled simulation as compared to the value used for wave generation. Indeed, the streamfunction and simulated wave steepnesses are:

$$\begin{aligned} \epsilon_{str.} &= \frac{2A_{1,str.}}{\lambda} = 0.0246 \\ \epsilon_{sim.} &= \frac{2A_{1,sim.}}{\lambda} = 0.0236 \end{aligned} \tag{6.2}$$

where it is assumed that the simulated wave length equals the streamfunction value.

It is reminded that $0.025 = \frac{1}{40}$ is the target wave steepness for the current study. Hence, $\epsilon_{sim.}$ is 5.6% lower than the desired value, while $\epsilon_{str.}$ is 1.6% lower. The latter only

originates from divergences in wave steepness definition, as mentioned in chapter 4.

These error levels are deemed acceptable, especially when compared to the results of wave calibration tests reported with $\epsilon = \frac{1}{30}$ in Dadmarzi et al. (2019). Relative errors on A_1 with a magnitude of up to around 5% are indeed recorded between basin measurements including the monopile model and the wave theory used to control the wave-maker.

6.2.1.4 Inline force time signal

The time history of the normalized horizontal force is partly shown in figure 6.8 after 40 wave periods. Even with a moderate wave steepness of $\frac{1}{40}$, nonlinearities are noticeable. As will be further investigated through a spectral analysis, time signal is also not rigorously periodic.

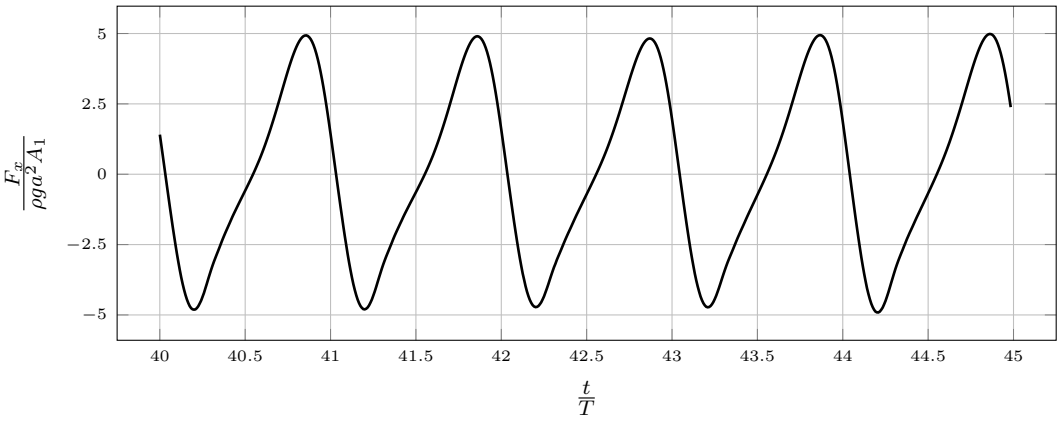

Figure 6.8: Normalized horizontal force time signal between $t = 40T$ and $t = 45T$ for $T = 15$ s and $\epsilon = \frac{1}{40}$.

6.2.2 Amplitude of harmonics of normalized horizontal force

As we now have a time-average simulated value of A_1 available, it is possible to compute the normalized amplitude of the first three harmonics of the horizontal force exerted on the monopile. As before, the fact that the force signal is not perfectly periodic calls for a spectral analysis conducted on a sliding time window. Results are presented in figure 6.9. Again, the first $22T$ are not accounted for in the frequency analysis. The time evolution of the normalized amplitudes of harmonics of F_x is shown, with one point per wave period, as well as their time averages. Experimental results are also drawn for comparison. It can be noticed that amplitudes of harmonics fluctuate with time, therefore the calculated mean values should be taken with some caution.

Comparison with results from wave basin tests is summarized in table 6.1. Relative errors increase approximately by one order of magnitude for each order of the harmonics. Simulated results match the reference quite well for the first and second orders of the inline

Harmonic order	$\frac{F_x^{(i\omega)}}{\rho g a^2 A_1}$ / exp.	$\frac{F_x^{(i\omega)}}{\rho g a^2 A_1}$ / sim.	Relative error (%)
1	4.21	4.22	0.2
2	1.29	1.36	5.4
3	0.19	0.22	15.8

Table 6.1: Normalized amplitude of the first three harmonics of the depth-integrated inline force on the cylinder, in the case of $T = 15$ s and $\epsilon = \frac{1}{40}$.

force. Error on third harmonic's amplitude is larger, but the corresponding absolute value is low. The reader should keep in mind that normalization of F_x involves the simulated value of A_1 and not the streamfunction one.

Hence, the coupling procedure appears to enable quite accurate global horizontal force computations for the largest considered wave period. The following sections address the cases of $T = 12$ s and $T = 9$ s.

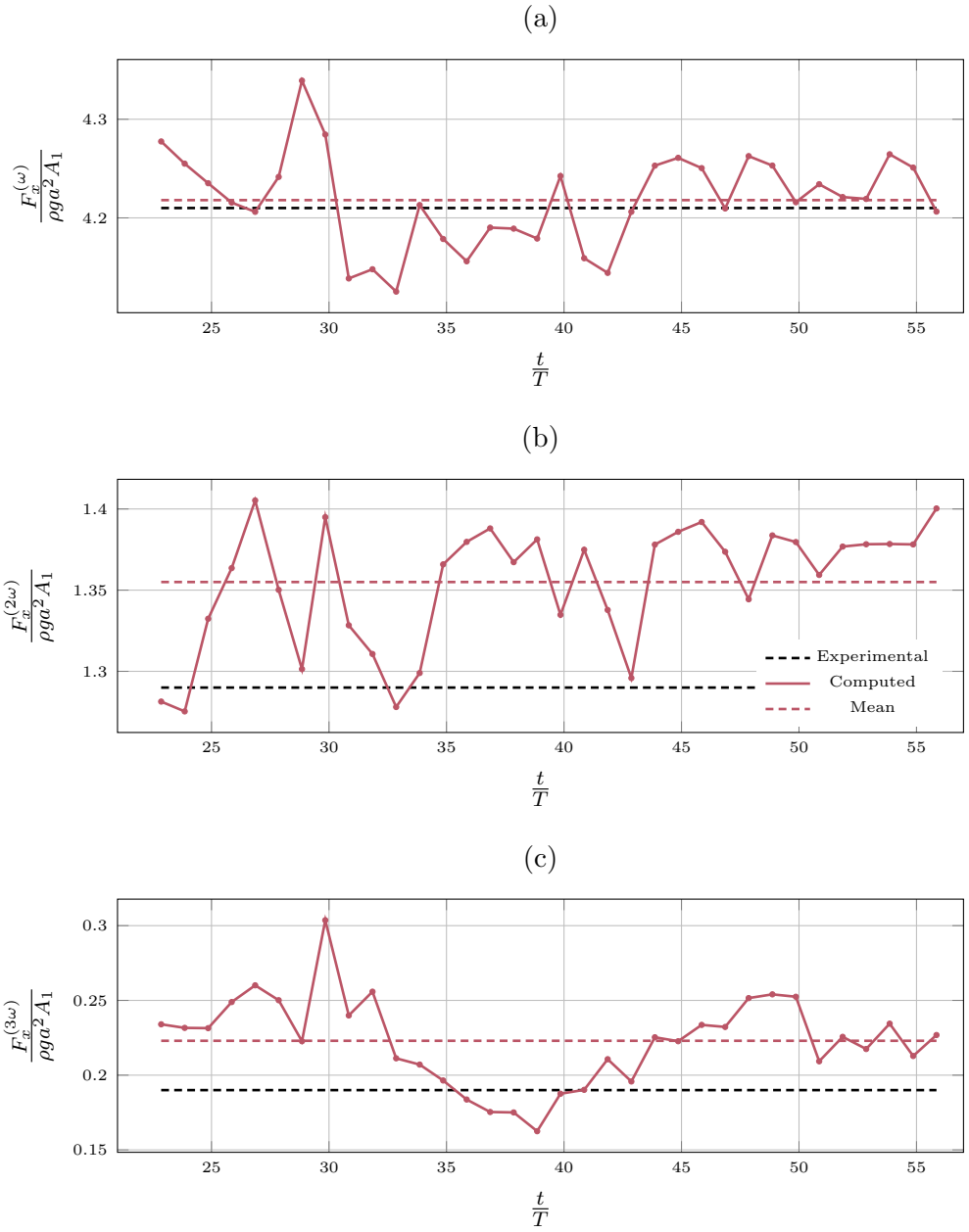

Figure 6.9: Amplitudes of the first three harmonics of horizontal force applying on the monopile, obtained from the WAS-XL experimental campaign and the coupled simulation for $T = 15$ s and wave steepness $\epsilon = \frac{1}{40}$. Spectral analysis of numerical results is realized over one sliding wave period (red nodes). Time-averaged values are illustrated by dashed red lines. The first $22T$ are excluded from the analysis.

6.3 12 s wave period

The previous study is reiterated, this time with $T = 12$ s. Incident streamfunction wave characteristics verify $H = 4.28$ m and $\lambda = 171.366$ m. Global setup of subdomains and meshes follow the same rules as for $T = 15$ s. *CS* computational mesh comprises 1 144 443 cells. *seine3d* 1 mesh has 1701 nodes, while *seine3d* 2 mesh has 1533. The computation runs for 3 days on two 36-cores nodes of the HPC cluster. *CS* instance gets 38 processors, *seine3d* 1 gets 26 and *seine3d* 2 24. Almost $44T$ are simulated. It takes around 1.54h of computation with this setup to simulate one wave period. Hence, the ratio of computational time to simulated time expressed is:

$$N_{cpl.} = \frac{1.54 \times 36 \times 2}{12} = 9.2 \text{ ch.s}^{-1}$$

$N_{cpl.}$ is lower than in the previous case with $T = 15$ s. It indicates that the increase in complexity of the coupled problem, originating from larger computational meshes and subsequent higher extraction and transmission costs of coupled physical fields, is not compensated by the increase in computational power. This would deserve further investigations dealing with hybrid model setup and scalability.

Contrary to the case with $T = 15$ s, no preliminary 2DV study has been conducted with the current wave condition. Therefore, the analysis of 3D coupled results is also less exhaustive.

6.3.1 Free surface time signals

The free surface time histories at the already mentioned wave gauge of abscissa $x = 0$ m and ordinate $y = 31.25$ m are presented in figure 6.10. It is considered that after $12T$, waves have fully developed in the numerical basin. Agreement with the streamfunction results seems to be better than for $T = 15$ s, as is illustrated next with A_1.

6.3.2 First order wave amplitude

Time evolution of the amplitude of the first harmonic of the free surface elevation signal is shown in figure 6.11, alongside with average and streamfunction values. Mean $A_{1,sim.}$ value is closer to $A_{1,str.}$ than for $T = 15$ s, as it amounts to 99% of it. However, it should be noted that the amplitude signal is less stable than with the previous wave condition.

The reason for such improvement of the results is unclear: this could be due to a better performance of the wave generation routine of *seine3d* 1 for this wave condition, or to a better transparency of the couplings.

It should be noted that the cylinder radius to wavelength ratio $\frac{a}{\lambda}$ is greater than in the case with $T = 15$ s, thus first-order diffraction effects are expected to be stronger, but they do not seem to disturb the free signal much in the current case. However, the distance

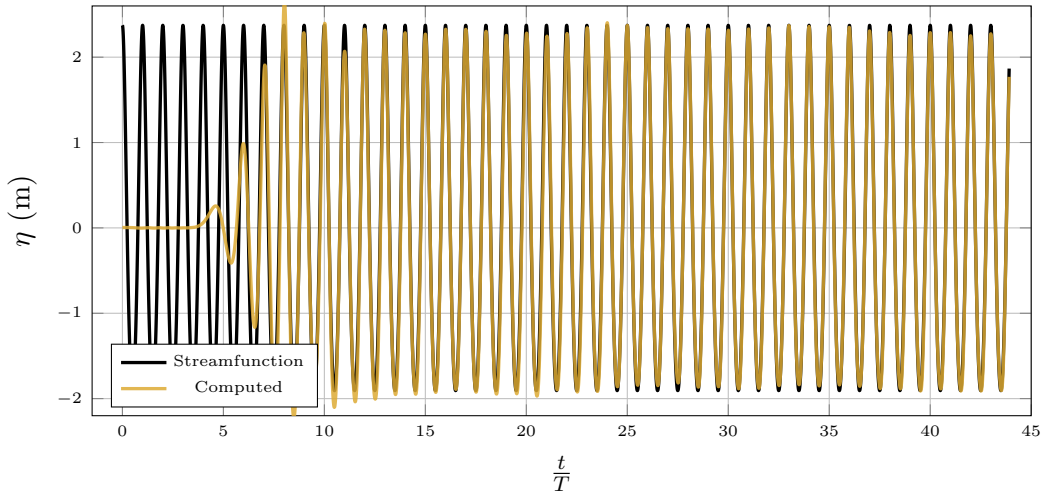

Figure 6.10: Comparison of streamfunction and computed free surface signals at the wave gauge closest to the monopile for $T = 12$ s and $\epsilon = \frac{1}{40}$.

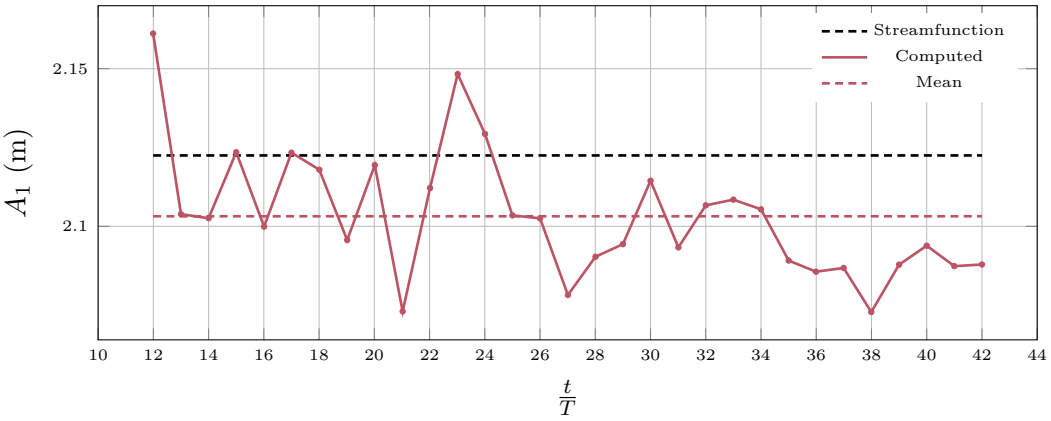

Figure 6.11: First order wave amplitude signal obtained from coupled simulation for $T = 12$ s and $\epsilon = \frac{1}{40}$. The first $12T$ are excluded from the analysis and therefore not shown.

from the monopile's centerline to the wave gauge of interest represents a larger fraction of λ here. Hence, although $y_{gauge} = 31.25$ m seems to be a rather relevant value, it is not sufficient to conclude that wave diffraction does not play any role on the free surface discrepancies illustrated in figure 6.5 for $T = 15$ s.

6.3.3 Amplitude of harmonics of normalized horizontal force

Figure 6.12 displays the amplitudes of the first three harmonics of inline force. It appears that the curves do not fully stabilize with time, in particular that of the second harmonic, which grows steadily and in a unexpected manner, starting from $t = 32T$ approximately. For that reason, it was decided to exclude any results past $t = 33T$ from the computation of mean force harmonics values. Grey areas in figure 6.12 illustrate this choice. Nevertheless, our understanding of this behavior may have benefited from a longer-lasting computation.

Harmonic order	$\frac{F_x^{(i\omega)}}{\rho g a^2 A_1}$ / exp.	$\frac{F_x^{(i\omega)}}{\rho g a^2 A_1}$ / sim.	Relative error (%)
1	4.78	4.832	1.1
2	0.72	0.7357	2.2
3	0.014	0.0779	4.56×10^2

Table 6.2: Normalized amplitude of the first three harmonics of the depth-integrated inline force on the cylinder, in the case of $T = 12$ s and $\epsilon = \frac{1}{40}$. Computation of the mean values is realized over a restricted time window $(12T - 33T)$.

Results are summarized in table 6.2. Again, relative error levels as compared to experimental values increase by an order of magnitude for each order of the harmonic. Under the above-mentioned time restrictions, agreement is found to be good for the first order normalized horizontal force and reasonable for the second. Computed third harmonic strongly differs from its experimental counterpart, but the absolute normalized values are very low.

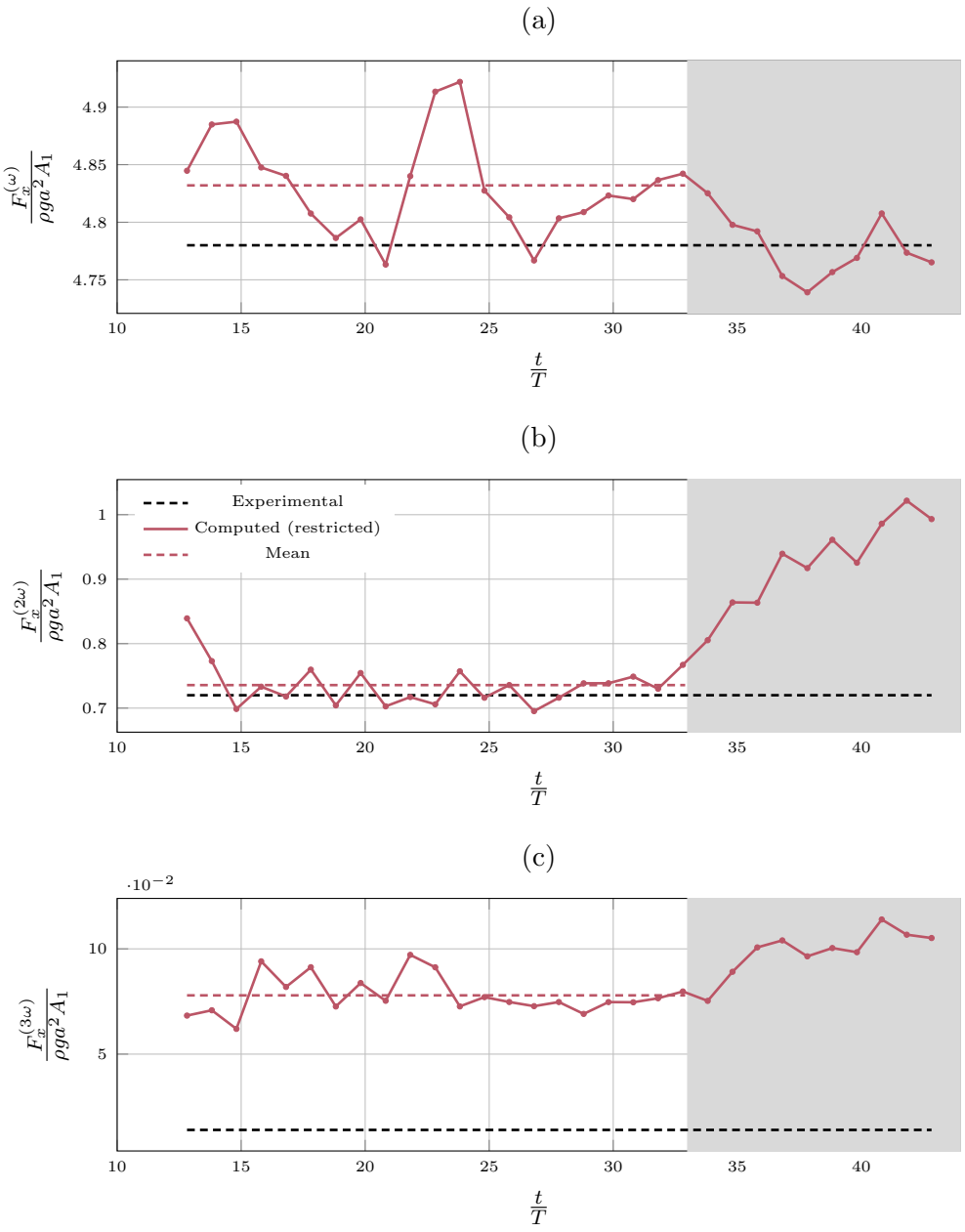

Figure 6.12: Amplitudes of the first three harmonics of horizontal force applying on the monopile, obtained from the WAS-XL experimental campaign and the coupled simulation for $T = 12$ s. Gray areas illustrate the time window excluded from the computation of harmonics mean values starting at $t = 33T$, due to non-convergent behavior of $\frac{F_x^{(2\omega)}}{\rho g a^2 A_1}$, and $\frac{F_x^{(3\omega)}}{\rho g a^2 A_1}$ to a lesser extent. The first $12T$ are excluded from the analysis and therefore not shown.

6.4 9 s wave period

Last in the series of wave conditions with $\epsilon = \frac{1}{40}$ is the case of $T = 9$ s. It corresponds to an incident wave height of $H = 2.86$ m and a wavelength of 114.446 m. The *CS* mesh is the largest used so far in a coupled simulation, with 2 400 293 computational cells.

seine3d 1 has 3219 nodes in its mesh, while *seine3d* 2 has 1929. The computation runs for 3 days on four 36-cores nodes of the HPC cluster, with 80 processors being attributed to the *CS* instance, while 35 are reserved for *seine3d* 1 and *seine3d* 2. Again distribution of computational resources to the different code instances was not questioned, and it is very likely not optimal. A deeper analysis of the influence of processors allocation on the performances of the coupling procedure would be useful here. 338.22 s were computed, corresponding to $37.58T$. With this setup, simulating one wave period takes 1.75h. The ratio of computational time to simulated time expressed becomes:

$$N_{cpl.} = \frac{1.75 \times 36 \times 4}{9} = 28.0 \text{ ch.s}^{-1}$$

For this wave condition, a comparison is made with a computation involving only *CS* on the basis of $N_{cpl.}$, to quantify the savings in computational resources allowed by the coupling methodology. Conclusions are presented below.

6.4.1 Free surface time signals

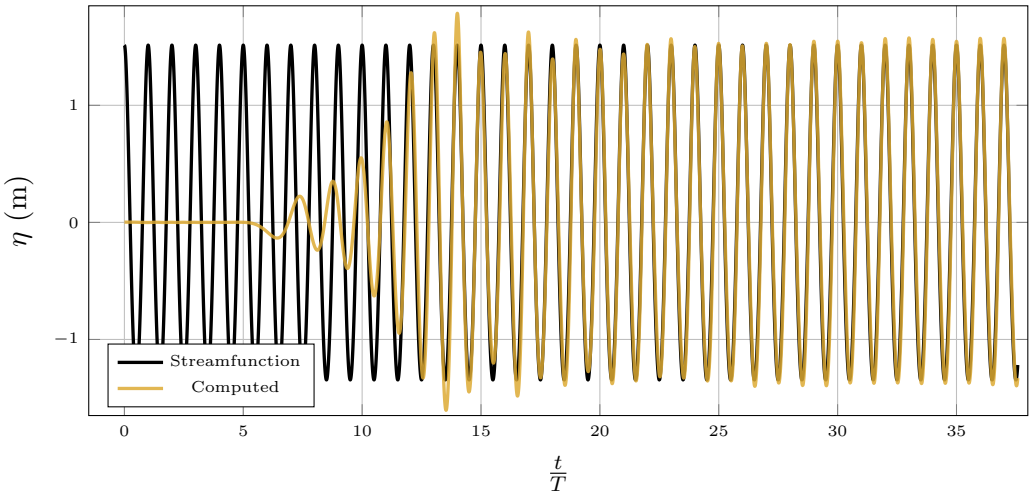

Figure 6.13: Comparison of streamfunction and computed free surface signals at the wave gauge closest to the monopile for $T = 9$ s and $\epsilon = \frac{1}{40}$.

Free surface time signals at the reference wave gauge are shown in figure 6.13. Around $20T$ are needed from the initial stage of the computation to reach a quite stabilized wave regime. Contrary to previous wave conditions, this time the coupled simulation tends to slightly overpredict the free surface elevation. Again, hybrid results would certainly have

benefited from a longer simulated time. Free surface overshoots may be due to spurious wave reflection taking place in the damping region, implemented at the downstream end of the *seine3d* 2 domain.

6.4.2 First order wave amplitude

The study of first order wave amplitude allows one to quantify the free surface elevation error. Results are presented in figure 6.14. Although vertical scale is largely stretched, an increasing trend is observed for $A_{1,sim.}$. This is in line with the previous observations. Nevertheless, overprediction of the time-averaged value of $A_{1,sim.}$ computed over the displayed time domain amounts to less than 1% as compared to the streamfunction solution.

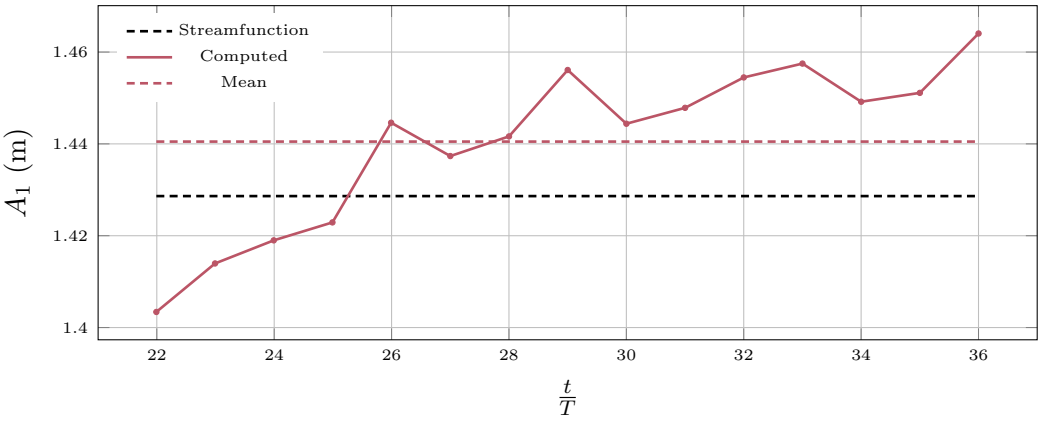

Figure 6.14: First harmonic amplitude of the free surface elevation signal in the coupled simulation for $T = 9$ s and $\epsilon = \frac{1}{40}$. The first $21T$ are excluded from the analysis and therefore not shown.

6.4.3 Amplitude of harmonics of normalized horizontal force

Figure 6.15 gathers results related to the amplitude of the first three harmonics of normalized inline force on the monopile. Second and third order normalized amplitudes amount on average to even lower fractions of $\frac{F_x^{(\omega)}}{\rho g a^2 A_1}$ than observed in previous wave conditions. Due to the limited simulated physical time, the working time domain over which spectral analysis is conducted is not as large as before, but it is sufficient to get a reasonable insight into the coupled model's behavior. Again, a growing trend is seen for first order inline force, that could be related to the increase of $A_{1,sim.}$ with time. Signals for $\frac{F_x^{(2\omega)}}{\rho g a^2 A_1}$ and $\frac{F_x^{(3\omega)}}{\rho g a^2 A_1}$ are more stable.

Table 6.3 presents a summary of the time-averaged results. Agreement between experimental and simulated first order results is satisfactory. Discrepancies are larger for second and third orders, but absolute normalized amplitudes of F_x are 1 to 2 orders of magnitude

Harmonic order	$\frac{F_x^{(i\omega)}}{\rho g a^2 A_1}$ / exp.	$\frac{F_x^{(i\omega)}}{\rho g a^2 A_1}$ / sim.	Relative error (%)
1	5.75	5.835	1.5
2	0.32	0.27	−15.6
3	0.056	0.03	−46.4

Table 6.3: Normalized amplitude of the first three harmonics of the depth-integrated inline force on the cylinder, in the case of $T = 9$ s and $\epsilon = \frac{1}{40}$

lower.

Hence, the implemented coupling procedure allows for simulating wave diffraction by a vertical cylinder for a moderate wave steepness, for various values of relative water depth and relative monopile radius. Assessments have been made of the accuracy and speed of computations. To conclude on the relevance of the BEM-VOF coupling procedure, it is necessary to have at least one comparison point available with a *CS*-only simulation. This is the subject of the next section.

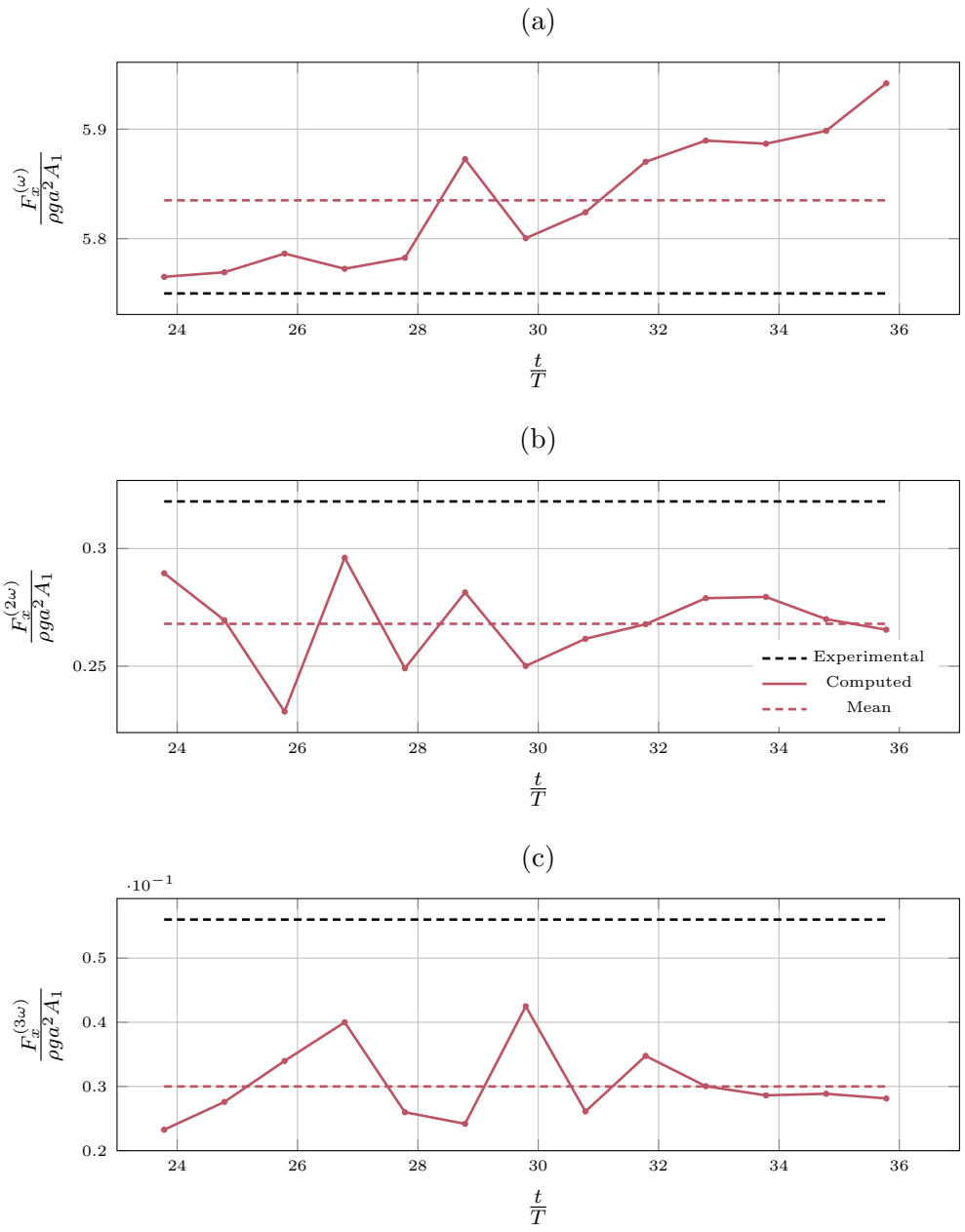

Figure 6.15: Amplitudes of the first three harmonics of horizontal force applying on the monopile, obtained from the WAS-XL experimental campaign and the coupled simulation for $T = 9$ s and $\epsilon = \frac{1}{40}$. The first $23T$ are excluded from the analysis and therefore not shown.

6.4.4 *CS*-only simulation of the same problem with 9 s wave period

As mentioned before, the coupled simulation with $\epsilon = \frac{1}{40}$ featuring the smallest values of T and λ is also the one for which the meshes of the different models instances contain the greatest numbers of elements. It is thus considered a good candidate for a comparison with the computationally expensive results obtained using only *CS*.

A *CS*-only computation is set up with the same numerical parameters as used in the *CS* instance for the coupled simulation with $T = 9$ s. A mesh describing the whole domain is built with 29 181 137 cells. The part of it encompassing the monopile is the same as in the associated coupled simulation. Wave generation and absorption are realized thanks to damping regions involving source terms added to the void fraction and momentum conservation equations, as described in section 4.4. Each region is one wavelength long, thus the *CS*-only numerical domain is one wavelength longer than the global hybrid one, as wave generation is limited to the upstream boundary only in *seine3d* 1 domain, in the hybrid case. Damping intensity, whose optimal value is not independent of the wave conditions, is selected in both regions after a brief sensitivity analysis conducted on 2DV wave simulations.

27 36-cores nodes of the HPC cluster are used for a 3-days-long computation. $79.3T$ are simulated. Simulating one wave period takes 0.76h. Computational time to simulated time ratio is:

$$N_{\text{CS}} = \frac{0.76 \times 36 \times 27}{9} = 82.1 \text{ ch.s}^{-1}$$

N_{CS} is thus 2.93 higher than the previously computed $N_{cpl.}$. This result may be seen as conservative, as we also have specified that computational resources allocation is perfectible in the case of coupled simulations. It is also close to the gain obtained using the SWENSE method for a similar problem reported by Li et al. (2021). Besides, no study of the influence of *CS* numerical domain size has been conducted: it might be even smaller. The same might be said of $L_{overlap}$.

Still, we should ensure that the accuracy of *CS*-only computational results matches or outperforms that of the hybrid method, in terms of free surface elevation and depth-integrated inline force, for the comparison to hold.

6.4.4.1 Free surface time signals

Streamfunction and computed free surface signals at the wave gauge next to the vertical cylinder are compared in figure 6.16. Overall agreement is good, and similar to the one obtained with the hybrid simulation, pictured in figure 6.13. A moderate but growing with time overestimation of free surface elevation is noticed, as well as a slight beating. Perfectible wave damping could be responsible for this.

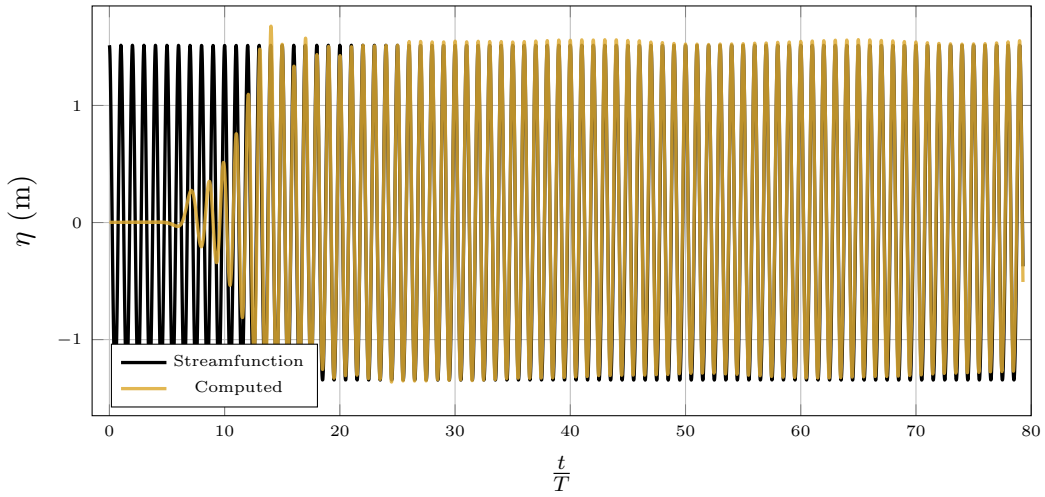

Figure 6.16: Comparison of streamfunction and computed free surface signals at the wave gauge closest to the monopile for a *CS*-only computation with $T = 9$ s.

6.4.4.2 First order wave amplitude

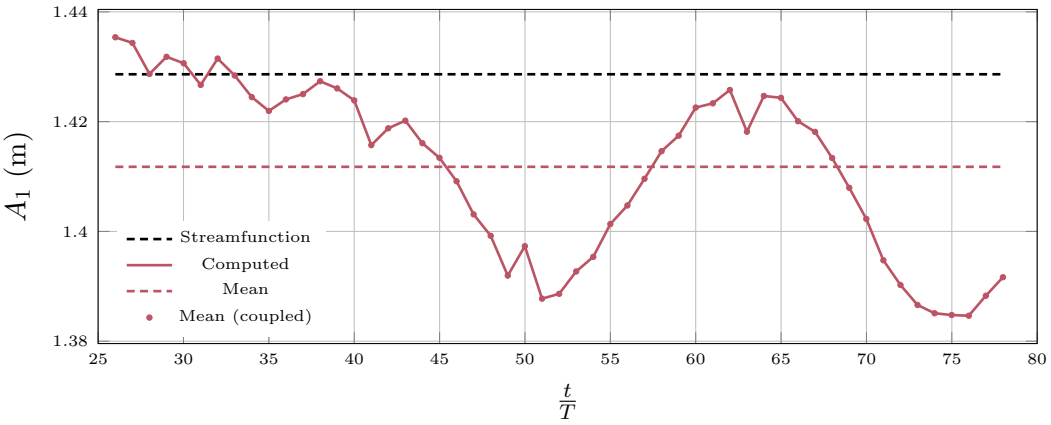

Figure 6.17: First harmonic amplitude of the free surface elevation signal from the *CS*-only simulation for $T = 9$ s and $\epsilon = \frac{1}{40}$. Spectral analysis of numerical results is realized over one sliding wave period (red nodes). The first $24T$ are excluded from the analysis and therefore not shown. Coupled results are drawn in yellow for comparison.

The above-mentioned beating is more easily observed in figure 6.17, picturing the time evolution of the first order wave amplitude. A good level of accuracy is reached, as the time-averaged value of $A_{1,sim.}$ amounts to nearly 99% of $A_{1,th.}$.

6.4.5 Amplitude of harmonics of normalized horizontal force

The spectral analysis of the depth-integrated inline force on the cylinder is presented in figure 6.18. $\frac{F_x^{(2\omega)}}{\rho g a^2 A_1}$ and $\frac{F_x^{(3\omega)}}{\rho g a^2 A_1}$ are quite stable in time, whereas $\frac{F_x^{(\omega)}}{\rho g a^2 A_1}$ features larger fluctuations and is globally underpredicted. At the same time, a value greater than the experimental one was found for the same force harmonic in the coupled simulation.

Harmonic order	$\frac{F_x^{(i\omega)}}{\rho g a^2 A_1}$ / exp.	$\frac{F_x^{(i\omega)}}{\rho g a^2 A_1}$ / sim.	Relative error (%)
1	5.75	5.55	−3.5 (1.5)
2	0.32	0.288	−10.0 (−15.6)
3	0.056	0.034	−39.3 (−46.4)

Table 6.4: Normalized amplitude of the first three harmonics of the depth-integrated inline force on the cylinder, in the case of $T = 9$ s and $\epsilon = \frac{1}{40}$ for a simulation involving only *CS*. Algebraic error levels obtained with the corresponding coupled simulation are recalled in parentheses.

Table 6.4 summarizes the time-averaged results. From a comparison with table 6.3, it appears that global error levels are similar to those found in the coupled simulation, albeit first order agreement is not quite as good. Also, higher order results match the reference better than the hybrid solution.

CS-only and coupled simulation thus reach similar accuracy levels, in terms of free surface elevation and inline force on the cylinder. Comparing their respective computational costs is thus relevant.

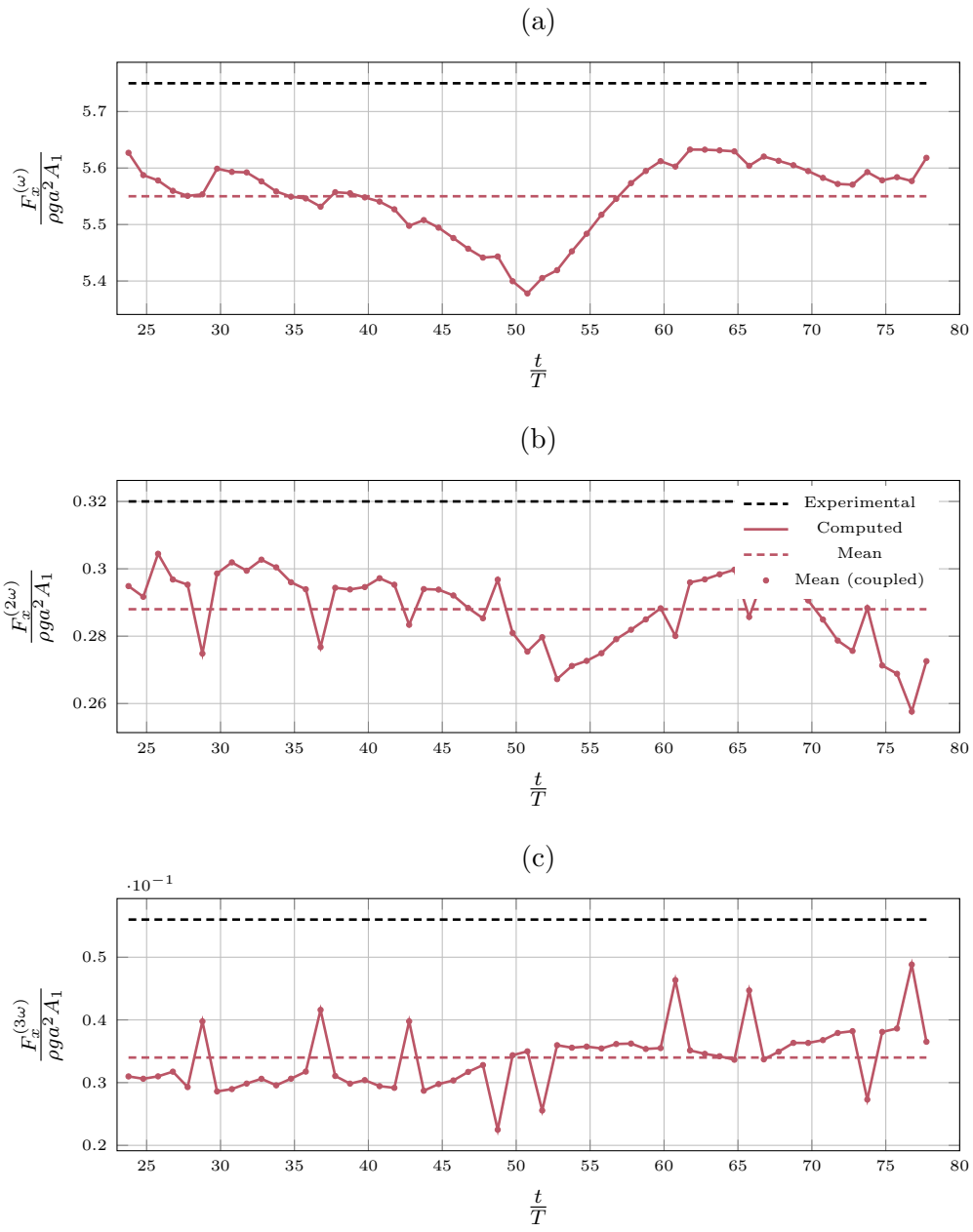

Figure 6.18: Amplitudes of the first three harmonics of horizontal force applying on the monopile, obtained from the WAS-XL experimental campaign and the *CS*-only simulation for $T = 9$ s and $\epsilon = \frac{1}{40}$. The first $23T$ are excluded from the analysis and therefore not shown. Coupled results are drawn in yellow for comparison.

6.5 A coupled simulation featuring waves with higher nonlinearity

In this section, we report on the simulation of interactions of steep regular nonlinear waves with a vertical cylinder, following the coupling methodology. Wave steepness is set to $\frac{1}{22}$, and the case of $T = 15$ s is investigated. Incident streamfunction wave height is $H = 10.5$ m while $\lambda = 231.7$ m. This 3D case refers to the 2DV one described in section 4.5.3, and numerical parameters that enabled a stable 2DV computation are reemployed. In particular, $\Delta t_{seine3d}$ is set to $\frac{T}{30}$ and Δt_{CS} takes the value $\frac{T}{1500}$, yielding $N_{\Delta t} = 50$. Rules governing the geometry of the different 3D subdomains are kept the same, and wave damping parameters are left untouched.

As *CS* mesh cell dimensions are based on fixed fractions of H, the body-fitted mesh used in the current case is the smallest ever built for a 3D coupled simulation, with 121 783 elements. Hence, a single 36-cores HPC node is required to run the simulation, as 4 CPU cores are attributed to *CS*, while *seine3d* 1 and *seine3d* 2 are given 15 and 17 respectively. 100 wave periods are simulated in little more than one day with this setup.

6.5.1 Free surface shape close to the cylinder

Close-up views of the free surface shape are displayed in figure 6.19, at 6 time instants after a wave crest has passed the monopile. An important upstream propagating wave can be seen, as well as strong wave run-ups on the cylinder walls. Results conform rather well, qualitatively speaking, with the free surface snapshots describing the interaction of highly nonlinear non-breaking unidirectional waves with a bottom-mounted circular cylinder reported by Paulsen (2013); Paulsen et al. (2014).

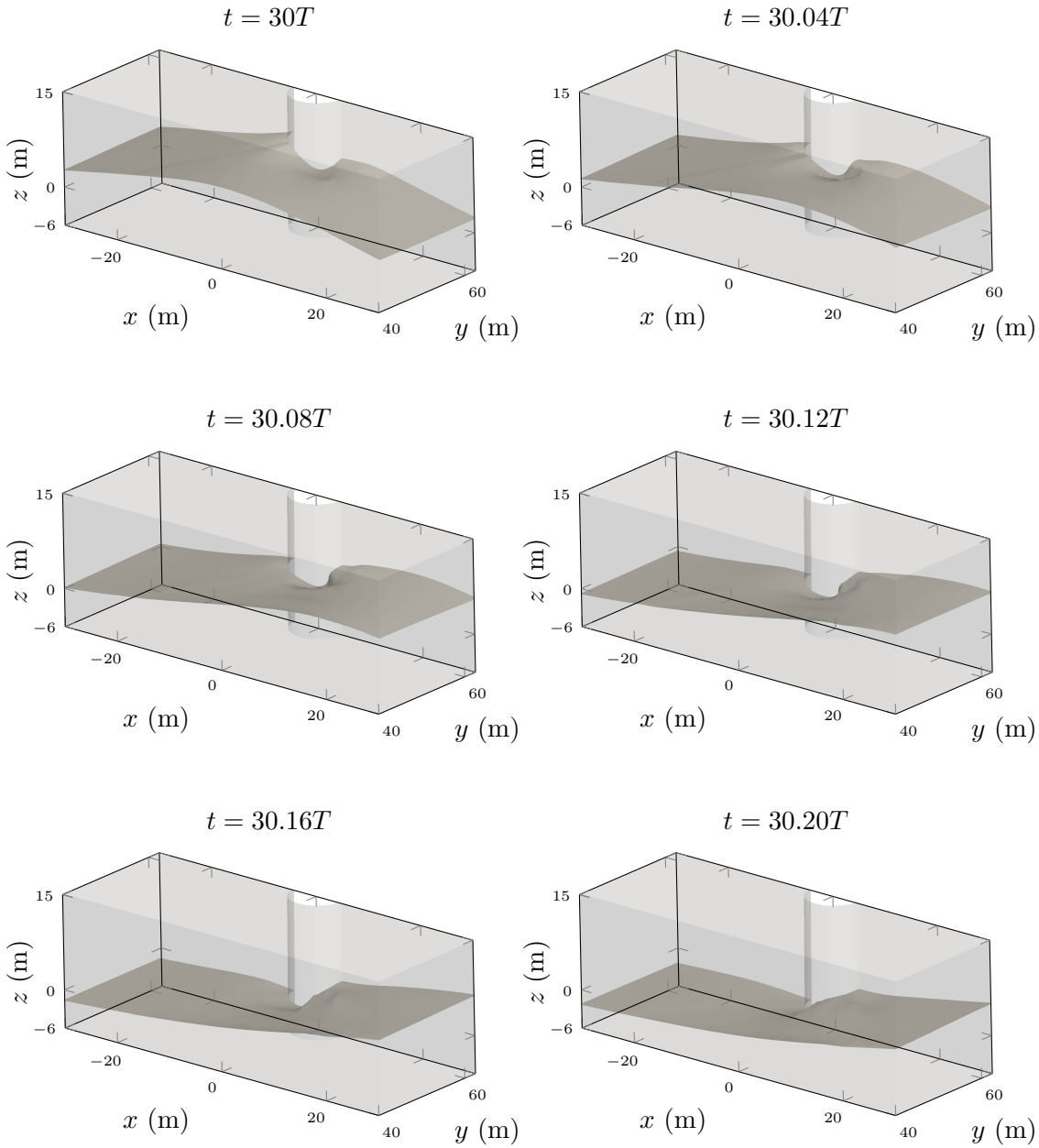

Figure 6.19: Snapshots of the free surface in the *CS* domain near the monopile, as a wave crest passes, with $T = 15$ s and $\epsilon = \frac{1}{22}$. Incident waves come from the left.

6.5.2 Free surface time signals

Free surface time histories recorded by a wave-gauge at the abscissa of the monopile are reported in figure 6.20. Here, it should be reminded that numerical stability was the main concern when 2DV tests with the same wave condition were realized, as stated in section 4.5.3.

The computed free surface elevation signal appears to be quite stable, especially in the second half of the simulation. Again, it calls for longer computational times, in order to yield the most accurate and relevant spectral analysis possible. However, the free surface vertical position is strongly underpredicted at wave crests. Wave troughs are better rendered.

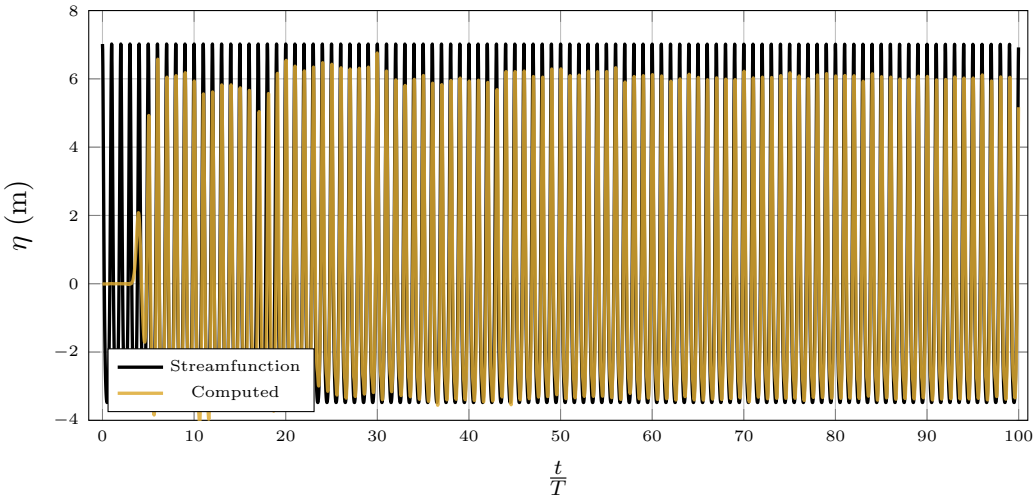

Figure 6.20: Comparison of the streamfunction and computed free surface signals at the wave gauge closest to the monopile for a coupled computation with $T = 15$ s and $\epsilon = \frac{1}{22}$.

6.5.3 First order wave amplitude

First order amplitude analysis enables to quantify inaccuracy in incident wave height, and is shown in figure 6.21. It should be noticed that oscillations of $A_{1,sim.}$ around its time-averaged value decrease with time. This value is also 11% lower than $A_{1,th.}$.

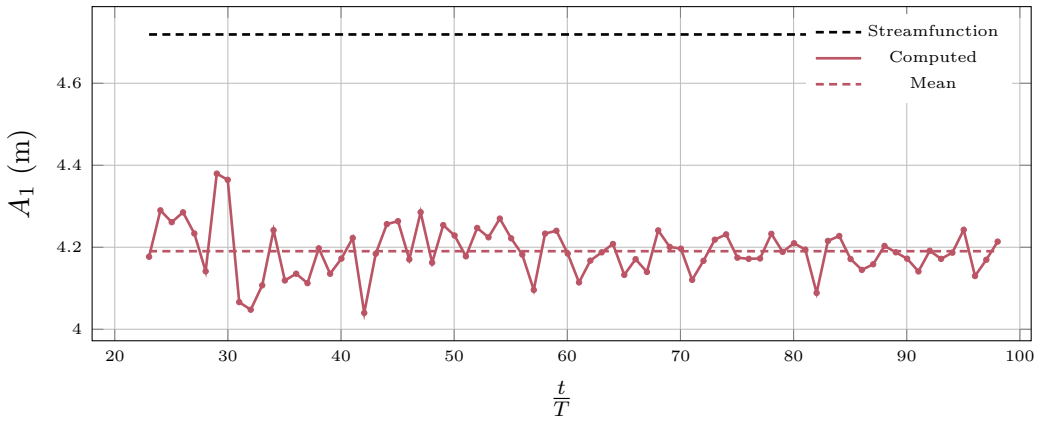

Figure 6.21: First harmonic amplitude of the free surface elevation signal obtained from the coupled simulation for $T = 15$ s for $\epsilon = \frac{1}{22}$. The first $22T$ are excluded from the analysis and therefore not shown.

6.5.4 Inline force time signal

Time history of the normalized horizontal force is partly shown in figure 6.22 after 40 wave periods. As expected, nonlinearities in the signal are higher than for the case with $\epsilon = \frac{1}{40}$, as pictured in figure 6.8.

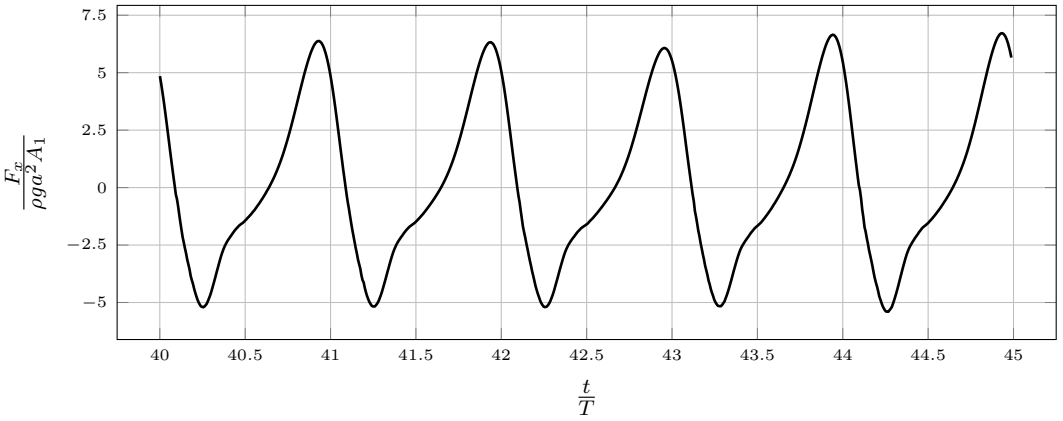

Figure 6.22: Normalized horizontal force time signal between $t = 40T$ and $t = 45T$ for $T = 15$ s and $\epsilon = \frac{1}{22}$.

6.5.5 Amplitude of harmonics of normalized horizontal force

Figure 6.23 shows the time history of the first three harmonics of the normalized horizontal force on the cylinder. As already written, frequency analysis outputs are more trustworthy than in previous 3D cases that lasted shorter. In accordance with discrepancies reported for total wave height and first order wave amplitude, normalized horizontal force is over-predicted by the simulations at first and second orders. The opposite is true for the third force harmonic.

Results are summed up in table 6.5. First order relative error, as expected, is close to being one order of magnitude higher than in previous cases with $\epsilon = \frac{1}{40}$. Second and third order error amplitudes are similar, if not smaller.

Thus, it appears that 3D simulations of highly nonlinear wave diffraction by a vertical cylinder are feasible with the coupling strategy, even at a low computational cost. Limits experienced in 2DV about free surface elevation accuracy explain most of the shortcomings reported in 3D. Therefore, emphasis should be put on 2DV highly nonlinear simulations, in the hope that improvements can later be applied to 3D computations.

Harmonic order	$\frac{F_x^{(i\omega)}}{\rho g a^2 A_1}$ / exp.	$\frac{F_x^{(i\omega)}}{\rho g a^2 A_1}$ / sim.	Relative error (%)
1	4.21	4.57	8.55
2	1.89	2.0	5.82
3	0.4	0.32	−20.0

Table 6.5: Normalized amplitude of the first three harmonics of the depth-integrated inline force on the cylinder, in the case of $T = 15$ s and $\epsilon = \frac{1}{22}$.

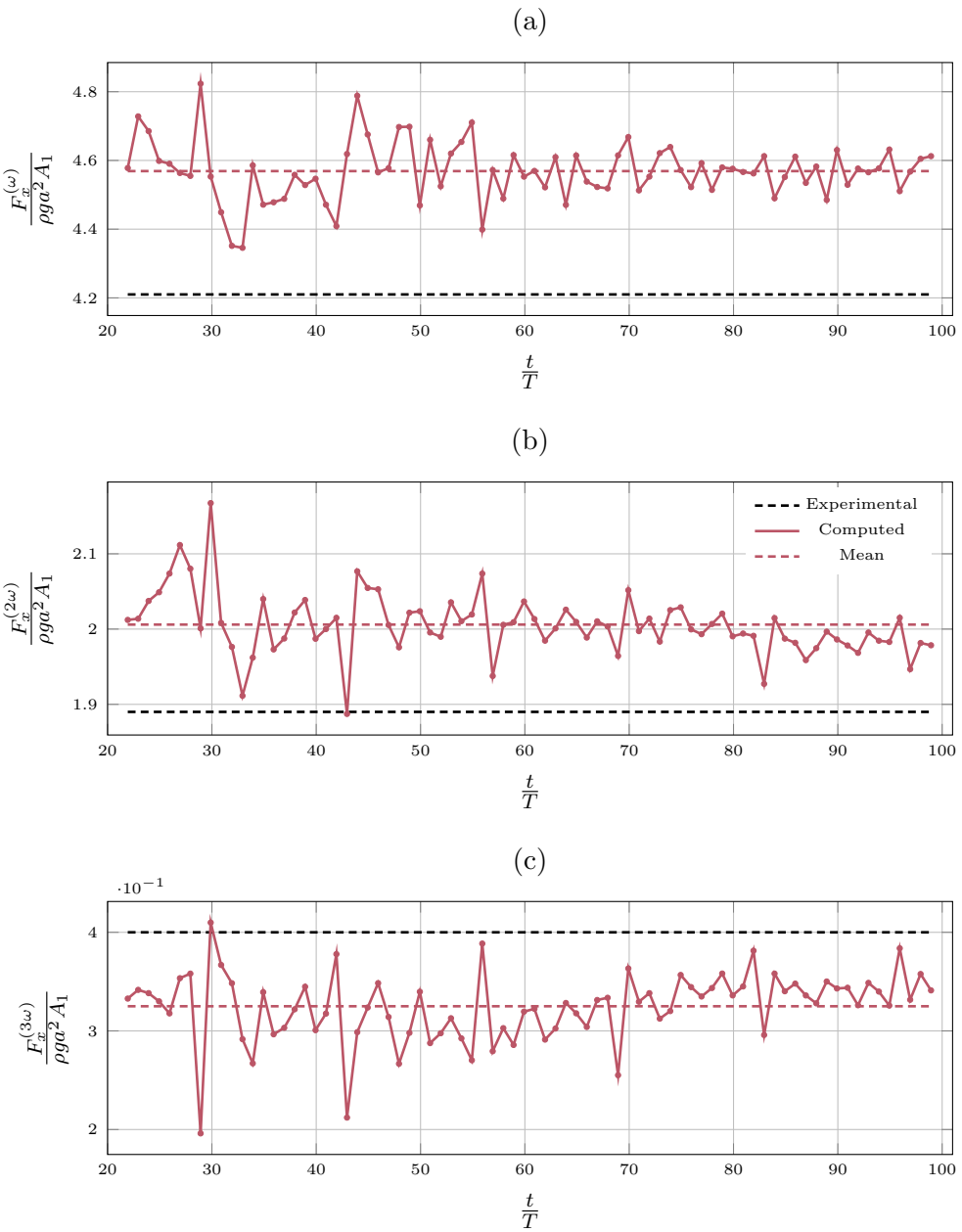

Figure 6.23: Amplitudes of the first three harmonics of horizontal force applying on the monopile, obtained from the WAS-XL experimental campaign and the coupled simulation for $T = 15$ s and $\epsilon = \frac{1}{22}$. The first $20T$ are excluded from the analysis.

6.6 Conclusions

In this chapter, it has been established that the coupling procedure developed in this work is suitable for simulating the interaction nonlinear regular waves with a cylindrical monopile in constant depth. Simulations were realized in realistic full scale numerical domains, built in accordance with the domain-decomposition approach implemented in the coupling strategy. Comparison of total wave height and first order wave amplitude with the incident plane streamfunction solution showed limited discrepancies for mildly nonlinear cases with $\epsilon = \frac{1}{40}$. The extensively studied 2DV case with $T = 15$ s served as a reference for the treatment of free surface elevation results. Wave height error, recorded close to the monopile, appeared to be slightly larger in 3D than in 2D. Which phenomenon is responsible for this remains unclear, as it could be attributed to the wave diffraction caused by the monopile, to the negative influence of the couplings on wave propagation, to shortcomings of the wave generation routine in *seine3d* or to imperfect absorption of waves at the downstream end of the hybrid domain. Errors in the numerical reproduction of the target wave height also lead to discrepancies in depth-integrated inline force exerting on the cylinder. A deeper study of the coupled model's behavior in 3D problems could partly solve this issue.

When comparing simulation results with experimental ones in terms of horizontal effort, another source of error lies in the fact that wave steepness definitions used in Dadmarzi et al. (2019) and in the wave generation routine of *seine3d* used in the current work differ somewhat. Indeed, it is based on the first order wave amplitude in the former study, while in the latter it relies on total wave amplitude. We found that the relative error amounts to around 1.5% in the case of $T = 15$ s with $\epsilon = \frac{1}{40}$. It is also expected to have a smaller impact on computations with $T = 12$ s and $T = 9$ s, in which higher-order components account for a smaller part of total wave amplitude, due to higher relative water depth. On the opposite, discrepancy is even larger for the case of $T = 15$ s and $\epsilon = \frac{1}{22}$. Getting rid of this particular error would not require important developments.

In general, differences between simulated and streamfunction first order wave amplitudes remained below or close to 1%, in absolute value, for the mildly nonlinear waves. They are approximately one order of magnitude higher for the more exploratory case of $\epsilon = \frac{1}{22}$. Besides, in calibration tests conducted in the physical wave basin, error levels of up to 5% for the first order wave amplitude were experienced, for certain wave periods. Therefore, it seems that the hybrid method enables sufficiently accurate reproduction of the target wave height, at least for moderate wave steepness, to be further used for the calculation of hydrodynamic efforts on the monopile.

A spectral analysis of the normalized horizontal force signal was conducted for each simulation result. For moderately steep waves, a very good agreement between simulation and experiments is observed for first order force amplitude, for all wave periods. The agreement worsens as the order increases, but remains correct for the second harmonic, especially in the case of $T = 15$ s, for which experience from 2DV calculations is available.

Very high error levels might be found for the third harmonic, but they are reached when the experimental force coefficient is also very low.

In the unique simulation case featuring a larger wave steepness of $\frac{1}{22}$, a higher error level exists for first order amplitude of the normalized force, but it does not increase for second order. This is fortunate, as in this more non-linear case, greater higher-order amplitudes of the force coefficient are observed.

Hence, it appears that the coupling strategy allows for quite accurate 3D simulations of wave interactions with fixed surface-piercing structures. These computations also come at a reduced cost. Indeed, it was proven, in the case of $T = 9$ s and $\epsilon = \frac{1}{40}$, that a hybrid simulation in which the computational resources breakdown between models instances is not optimized has a computational cost amounting to only one third of that of a *CS*-only simulation, with comparable accuracy. Indeed, the simulation involving only *CS* seems harder to set-up, with wave generation and damping regions that are very sensitive to the design wave characteristics. This all the more bolsters the relevance of a hybrid strategy. It should also be reminded that wave conditions with $T = 9$ s and $T = 12$ s were reproduced in 3D without any preliminary 2DV study, thus the coupled model seems versatile enough to be used as an engineering tool.

Chapter 7

Conclusions and future work

Cette partie conclusive synthétise les avancées obtenues au cours de ce travail de thèse quant au développement et à l'application d'un couplage bidirectionnel entre un code Navier-Stokes et un code de vagues potentiel complètement non-linéaire. Les principaux résultats obtenus y sont résumés, qu'ils portent sur la vérification de la stratégie de couplage implémentée, ou sur sa validation vis-à-vis d'un problème d'interactions vagues-structure d'intérêt pour l'ingénieur. Le gain en coût de calcul permis par le couplage est rappelé. De nombreuses pistes d'amélioration de la méthode sont avancées. Les plus évidentes et immédiates concernent la capacité du couplage à gagner en précision dans la description de certains phénomènes, tels que les interactions d'ordres élevés entre structures et houles régulières non-linéaires. Une meilleure connaissance des performances de l'outil en terme de temps de calcul et de ressources nécessaire est également attendue, afin de mieux répartir les ressources informatiques entre instances des codes couplés et abaisser encore le coût de calcul global. D'autres perspectives plus lointaines sont abordées, qui visent notamment à rendre possible la simulation de l'interaction de vagues avec des structures flottantes.

7.1 Summary of main outcomes and discussion

In this work, the definition, implementation, verification and validation through comparison to analytical solutions and experimental results of a two-way coupling strategy involving fully nonlinear potential BEM and viscous VOF models have been described. This coupling methodology relies on the mutual exchange of fluid velocities between codes, at the boundaries located at both ends of an overlapping region. It enables the simulation of 3D wave-structure interactions on large spatial and temporal scales, making the most of each code's intrinsic performances and ranges of application. Savings in the computational cost of the simulations were obtained (by a factor of about 3 with reference to a CS-only simulation on a domain of the same dimensions). Multiple couplings may be set through the pairing of different instances of *seine3d* and *CS*, thanks to an appropriate division of the global domain of interest into several overlapping subdomains. The designed hybrid procedure is intended to introduce the lowest possible number of additional simulation parameters. After choices have been made in each code about temporal and spatial discretization levels, as well as physical assumptions and solution procedure, theoretically only the length(s) of the overlapping region(s) remains to be set. Stability issues of the hybrid computations with certain values of CFL numbers in the models were however experienced, indicating that respective temporal and spatial resolutions affect the applicability of the coupling strategy. The possibility to run massively parallel computations, available in *seine3d* and *CS*, has also been retained.

The developed computational tool is verified at first by a 2DV study of the propagation of a solitary wave over a constant depth. Conservation of the wave shape and celerity is assessed for moderate ($\frac{H}{h} = 0.3$) as well as high ($\frac{H}{h} = 0.5$) relative wave height. Results are rather satisfactory in the first case, as for example the maximum error recorded on wave height is close to 2%, while the solitary wave travels over more than $40h$. As already mentioned, simulations were not successful with every investigated combination of spatial and temporal discretizations in *seine3d* and *CS* instances. However, sensitivity to these parameters remains reasonable, and little influence on results quality is experienced with moderate variations of time and space resolutions around a reference working setup. This wave case indeed sheds light on stability issues encountered in *seine3d* instances during the hybrid simulations, located on certain edges and corners of the coupled boundaries. Besides this, choices related to the treatment of *seine3d* free surface variables in the coupling regions are tested, and the subsequent conclusions serve as a basis for following computations.

Next, 2DV coupled simulations featuring nonlinear regular waves over constant water depth are presented. The idea is to reproduce most of the characteristics of a reference experimental campaign focusing on wave interactions with a vertical bottom-mounted circular cylinder. In particular, a given wave condition is simulated using each code alone at first, then with the hybrid algorithm. It allows for an assessment of wave generation and absorption techniques in *seine3d* and *CS*. Results are compared with semi-analytical streamfunction wave solutions used for wave generation, in terms of wave elevation time

history, as well as velocity fields underneath the waves. When looking at the vertical structure of fluid velocity, significant differences with the expected streamfunction profiles were observed, increasing with time, calling for a brief sensitivity analysis of various parameters, aiming at reducing error levels. Finally, coupled simulations are run for two values of the wave steepness, namely $\epsilon = \frac{H}{\lambda} = \frac{1}{40} = 2.5\%$ and $\epsilon = \frac{1}{22} = 4.5\%$, with the more nonlinear wave case being more exploratory. It is believed that rules used to set spatial and temporal discretization levels as well as various other numerical parameters in 2DV still hold for more complex 3D cases.

The first 3D simulations are conducted to describe the diffraction of a solitary wave by a vertical circular cylinder. It allows one to check, in a qualitative way, whether the coupling methodology is able to reproduce complex 3D free surface flows, with waves crossing overlapping regions in both directions. Most numerical settings come from previous 2DV solitary wave simulations, therefore transverse resolution of the *seine3d* meshes is the only parameter remaining to be set. It is found to be critical for the stability of computations, but relevant horizontal mesh resolutions do not lead to unreasonable mesh sizes.

At last, hybrid 3D simulations are validated through comparison with experiments (WAS-XL campaign, Dadmarzi et al. (2019)) about regular wave diffraction by a vertical cylinder. Three wave conditions with a moderate wave steepness of $\frac{1}{40}$ are tested, while monopile radius and water depth are constant. For two of them, no preliminary 2DV investigation has been conducted. Satisfactory agreement between simulated and experimental results is found in terms of wave elevation close to the vertical cylinder and depth-integrated inline force on the same cylinder. Computed higher-order force components match the experimental ones reasonably well up to third order. For one wave condition, a *CS*-only simulation is realized that reaches accuracy levels similar to those of its hybrid counterpart, but at a greater computational cost (3 times higher). A more exploratory case featuring highly nonlinear waves is run with $\epsilon = \frac{1}{22}$, showing that coupled simulations of steep regular waves are feasible within the coupled framework, with higher error levels with respect to experimental measurements in comparison with the case $\epsilon = \frac{1}{22}$ however. Thus the relevance of the coupling strategy in the simulation of regular waves forces exerting on the foundation of a fixed offshore wind turbine is established.

7.2 Research and application perspectives

The developed coupling strategy has proven to be quite straightforwardly applicable to problems of interest for the engineer. Reasonable computational costs are achieved even for large computational meshes, made possible by the parallel nature of the hybrid solver. As an example, a 3D wave-structure simulation with $T = 15$ s, $\epsilon = \frac{1}{40}$, where the *CS* mesh has approximately 650 000 elements while *seine3d* instances meshes respectively have 1181 and 1401 nodes requires 1.22 hour to simulate one wave period on 2 HPC nodes featuring 27 CPUs. These costs appear to amount for only a fraction – one third, in the only 3D

case investigated – of that of NS-only similar computations. Thus, this work could enable a more frequent use of CFD tools in the engineering practice. However, additional effort is needed to gain more insight into the behavior and capabilities of the coupling methodology in its current state. Developments could also be expected to further improve efficiency and expand the range of handled problems.

1. **Better knowledge of the performances of the hybrid solver in its current state**

   Additional studies related to the use of *seine3d* in its current state, in this hybrid strategy, are needed. The instabilities reported in coupled *seine3d* instances should be further investigated in order to understand their origin and to possibly avoid them. Deeper convergence studies could be conducted for coupled simulations, to further validate the method and allow for a finer selection of numerical parameters, as well as more accurate results, for example in terms of higher order wave forces. In particular, the respective impacts of the time step ratio and the overlapping length should be better documented. The influence of variations in the characteristics of incident waves, especially their length and period, over the coupled simulations and the choice of the above-mentioned coupled parameters, should be studied. Investigations about the distribution of CPU cores over the different coupled code instances and scalability analysis would be valuable improvements made to the hybrid computations.

2. **Improvements to the viscous model employed in the coupling strategy**

   Investigations related to the performance of the VOF module of *CS* as a tool to model free surface waves, that was conducted in the beginning of this PhD, should be extended. In particular, a better knowledge of the influence of advection schemes available in *CS*, used in the void fraction conservation equation, as well as that of other settings, should be sought. The set of boundary conditions applied in *CS* instances is perfectible: it appears that the currently used top boundary condition can be improved quite straightforwardly. In this work, a slip condition is imposed on the surface of the monopile in *CS*, as well as on all the vertical walls. Even though agreement with experimental results appears to be good, a possible step forward would be to include effects of boundary layer in simulations. As a number of turbulence models are already available in *CS*, this would only require to work on specific boundary conditions for turbulent quantities at the coupled boundaries of *CS* instances. This way, local shear forces applying on partially submerged structures would be accounted for. Increasing the order of the interpolation schemes used in *CS* to extract the values of fluid velocity and free surface elevation needed by a coupled *seine3d* instance is yet another source of improvement. This requires conveniently accessing void fraction and velocity gradient fields in *CS*'s user routines. Another area of improvement is the generalization of the coupling strategy to unstructured *CS* meshes. Currently, it is only possible to use meshes in which overlapping regions are described with Cartesian grids. This would require implementation of a

new method for computing free surface positions in *CS*. This would allow for easier simulation of wave forces on structures of complex shape, with body-fitted meshes. It is also possible to replace *CS* by *Neptune-CFD*, which uses a multi-fluid approach (as opposed to VOF), developed by EDF R&D, that shares most of its components with *CS*. It has been recently successfully applied to solve regular wave diffraction problems investigated in the WAS-XL experimental campaign in engineering studies, similarly to what was done with the coupled solver in chapter 6. It features a porous media approach that allows for a straightforward description of any structure placed in waves, without the need for a complex meshing stage. Note that this feature is also planned for a future release of *CS*.

3. **Improvements to the potential model employed in the coupling strategy**

   For the sake of time saving in the implementation stage of the coupling strategy, not all latest improvements conducted in *seine3d* have been made available for use in the coupled *seine3d* instances. One of these is the use of the Fast Multipole Method that allows for accelerated solution procedure, see Harris et al. (2022) for details. In addition, it might be interesting to evaluate the sensitivity of the coupling procedure to changes made to the time-stepping scheme selected in *seine3d*, as different schemes are already implemented. As discussed above for the viscous CFD code, alternative potential flow solvers could also be considered using the same coupling strategy developed here. This would allow exploring options to overcome stability issues encountered in several cases here with *seine3d*, and/or possibly reducing the total computational cost of the coupled simulations. In this direction, the recently developed FNPF solvers based on the HPC technique (Robaux and Benoit, 2021) or on a spectral approach in the vertical (Zhang and Benoit, 2021) could be considered, among other options.

4. **Using the coupled solver to simulate other applications**

   In this work, only the propagation of unidirectional regular waves over constant depth has been numerically reproduced. Simulation of irregular and/or multidirectional waves, possibly traveling over variable bathymetry could be conducted following the coupling strategy. Phase-focused wave impacts with possible wave breaking could also be investigated. Making the most of the versatile nature of the hybrid solver, one might also use more complex overlapping regions geometry. Indeed, coupling regions having the form of rectangular or circular rings could quite easily be defined, enabling 3D simulations of waves interacting with multiple structures. Last but not least, the potential-CFD coupling procedure could be used alongside with a fluid/structure coupling approach, so that interactions of waves with moving structures could be handled. This is of particular interest for the study of floating offshore wind turbines, that is a promising solution for harvesting wind energy in greater water depths.

Appendix A

Calculation of linear reflection coefficient

To evaluate the amount of reflection attributed to a numerical damping layer submitted to regular monochromatic waves, either in *CS* or in *seine3d*, the method of Goda and Suzuki (1976) is used. It enables the computation a linear reflection coefficient, from the free surface time histories recorded at two wave gauges located upstream of the damping layer. The reflection coefficient is defined as:

$$R = \frac{a_{\mathrm{R}}}{a_{\mathrm{I}}} \tag{A.1}$$

where a_{I} and a_{R} are incident and reflected linear wave amplitudes respectively.

Wave gauges should be far enough from each other so that a sufficient phase difference exists between their respective recorded signals. However, it is also assumed in this method that the frequency content of the incoming wave is kept constant as the waves travel between both locations. Energy transfers between wave components are thus considered negligible, and global wave energy is presumed constant. Therefore, wave gauges should not be placed too far away from each other either. Besides, if both gauges are at a distance of $\frac{\lambda}{2}$, a singularity occurs in the calculation of R. In this work, a value of $\Delta_l = x_2 - x_1 = \frac{\lambda}{4}$ for the distance between gauges 1 and 2 is used. x_1 and x_2 designates the gauges respective longitudinal positions. It is to be noted that in the case of a linear monochromatic wave impinging on a fully-reflective damping region - *i.e* a vertical wall - a standing wave pattern appears in which successive nodes and antinodes are separated by a distance of $\frac{\lambda}{4}$. A short-time Discrete Fourier Transform (DFT) is applied to the wave signals, with a sliding window of one wave period. The DFT is computed with the Fast Fourier Transform (FFT) algorithm implemented in the *Numpy* Python library. Extraction of free surface signals relative maxima is also done thanks to a Python function implemented in the *Scipy* library. This way the DFT window is automatically set, and spectral analysis is repeated for the entire duration of the signals.

Free surface position measured from resting level at time instant t and abscissa x is denoted $\eta(x,t)$. It is split into two terms, one describing the incident wave train η_{I} and the other the reflected wave train η_{R}.

$$\begin{aligned}\eta(x,t) &= \eta_{\mathrm{I}}(x,t) + \eta_{\mathrm{R}}(x,t)\\ &= a_{\mathrm{I}}\cos(kx-\omega t+\epsilon_{\mathrm{I}})\\ &+ a_{\mathrm{R}}\cos(kx+\omega t+\epsilon_{\mathrm{R}}) + HOT\end{aligned} \tag{A.2}$$

where a_{I} and a_{R} are the components amplitudes, assumed to be constant during the wave period over which DFT is applied. k is the wave number and ω is the angular frequency of the simulated regular wave. For the sake of simplicity, their theoretical values are used, without any significant loss in accuracy. ϵ_{I} and ϵ_{R} are the initial phase angles for incident and reflected components and HOT stands for the neglected nonlinear Higher-Order Terms. At any wave gauge i, free surface position becomes:

$$\begin{aligned}\eta(x=x_i,t) &= a_{\mathrm{I}}(\cos\psi_{\mathrm{I}}\cos\omega t + \sin\psi_{\mathrm{I}}\sin\omega t)\\ &+ a_{\mathrm{R}}(\cos\psi_{\mathrm{R}}\cos\omega t - \sin\psi_{\mathrm{R}}\sin\omega t) + HOT\\ &= A_i\cos(\omega t) + B_i\sin(\omega t) + HOT\end{aligned} \tag{A.3}$$

where

$$\begin{aligned}\psi_{\mathrm{I}} &= kx_i + \epsilon_{\mathrm{I}}\\ \psi_{\mathrm{R}} &= kx_i + \epsilon_{\mathrm{R}}\end{aligned} \tag{A.4}$$

Coefficients A_i and B_i are obtained as outcomes of the Fourier decomposition of $\eta(x_i,t)$. As already stated, frequency contents at both wave probes are presumed identical, therefore a_{I} and a_{R} are the the same at x_1 and x_2. The following system thus holds :

$$\begin{aligned}A_1 &= a_{\mathrm{I}}\cos\psi_{\mathrm{I}} + a_{\mathrm{R}}\cos\psi_{\mathrm{R}}\\ B_1 &= a_{\mathrm{I}}\sin\psi_{\mathrm{I}} - a_{\mathrm{R}}\sin\psi_{\mathrm{R}}\\ A_2 &= a_{\mathrm{I}}\cos(\psi_{\mathrm{I}}+k\Delta l) + a_{\mathrm{R}}\cos(\psi_{\mathrm{R}}+k\Delta l)\\ B_2 &= a_{\mathrm{I}}\sin(\psi_{\mathrm{I}}+k\Delta l) - a_{\mathrm{R}}\sin(\psi_{\mathrm{R}}+k\Delta l)\end{aligned} \tag{A.5}$$

It should also be noted that:

$$\begin{aligned}A_2 &= A_1\cos k\Delta l + B_1\sin k\Delta l - 2a_I\sin k\Delta l\sin\psi_I\\ &= A_1\cos k\Delta l - B_1\sin k\Delta l - 2a_R\sin k\Delta l\sin\psi_R\\ B_2 &= -A_1\sin k\Delta l + B_1\cos k\Delta l + 2a_I\sin k\Delta l\cos\psi_I\\ &= A_1\sin k\Delta l + B_1\cos k\Delta l - 2a_R\sin k\Delta l\cos\psi_R\end{aligned} \tag{A.6}$$

a_{I} and a_{R} may then be expressed as:

$$\begin{aligned} a_{\mathrm{I}} &= \frac{1}{2|\sin k\Delta l|}\left((A_2 - A_1\cos k\Delta l - B_1\sin k\Delta l)^2 + (B_2 + A_1\sin k\Delta l - B_1\cos k\Delta l)^2\right)^{1/2} \\ a_{\mathrm{R}} &= \frac{1}{2|\sin k\Delta l|}\left((A_2 - A_1\cos k\Delta l + B_1\sin k\Delta l)^2 + (B_2 - A_1\sin k\Delta l - B_1\cos k\Delta l)^2\right)^{1/2} \end{aligned} \tag{A.7}$$

The reflection coefficient is then defined as a ratio of wave amplitudes:

$$R = \frac{a_{\mathrm{R}}}{a_{\mathrm{I}}} \tag{A.8}$$

Bibliography

S. Abadie, D. Morichon, S. T. Grilli, and S. Glockner. Numerical simulation of waves generated by landslides using a multiple-fluid Navier-Stokes model. *Coastal Engineering*, 57:779–794, 2010.

J. Ahrens, B. Geveci, and C. Law. Paraview: An end-user tool for large data visualization. *The Visualization Handbook*, 717(8), 2005.

C. Altomare, A. Tafuni, J. M. Domínguez, A. J. Crespo, X. Gironella, and J. Sospedra. SPH simulations of real sea waves impacting a large-scale structure. *Journal of Marine Science and Engineering*, 8(10):826, 2020.

F. Archambeau, N. Méchitoua, and M. Sakiz. Code Saturne: A Finite Volume Code for the computation of turbulent incompressible flows - Industrial Applications. *International Journal on Finite Volumes*, 1(1), 2004.

W. Bai and R. Eatock Taylor. Higher-order boundary element simulation of fully nonlinear wave radiation by oscillating vertical cylinders. *Applied Ocean Research*, 28:247–265, 2006.

W. Bai and R. Eatock Taylor. Numerical simulation of fully nonlinear regular and focused wave diffraction around a vertical cylinder using domain decomposition. *Applied Ocean Research*, 29(1-2):55–71, 2007.

K. Belibassakis and G. Athanassoulis. A coupled-mode system with application to nonlinear water waves propagating in finite water depth and in variable bathymetry regions. *Coastal Engineering*, 58(4):337–350, 2011.

K. A. Belibassakis and G. A. Athanassoulis. Extension of second-order stokes theory to variable bathymetry. *Journal of Fluid Mechanics*, 464:35–80, 2002.

H. Bihs, A. Kamath, M. A. Chella, A. Aggarwal, and Ø. A. Arntsen. A new level set numerical wave tank with improved density interpolation for complex wave hydrodynamics. *Computers & Fluids*, 140:191–208, 2016.

E. Campana, A. Di Mascio, P. Esposito, and F. Lalli. Viscous-inviscid coupling in free surface ship flows. *International Journal for Numerical Methods in Fluids*, 21(9):699–722, 1995.

H.-C. Chen and S.-K. Lee. RANS/Laplace calculations of nonlinear waves induced by surface-piercing bodies. *Journal of Engineering Mechanics*, 125(11):1231–1242, 1999.

Q. Chen. *Development of a full particle pic method for simulating nonlinear wave-structure interaction*. PhD thesis, University of Bath, UK, 2017.

Q. Chen, J. Zang, D. M. Kelly, and A. S. Dimakopoulos. A 3D parallel Particle-In-Cell solver for wave interaction with vertical cylinders. *Ocean Engineering*, 147:165–180, 2018.

Y.-M. Choi. *Two-way Coupling between Potential and Viscous Flows for a Marine Application*. PhD thesis, Ecole Centrale de Nantes, France, 2019.

A. J. Chorin. Numerical solution of the navier-stokes equations. *Mathematics of computation*, 22(104):745–762, 1968.

Code_Saturne development team. Code_Saturne 6.0.0 theory guide, 2019. URL https://www.code-saturne.org/documentation/6.0/theory.pdf. Accessed : 2022-02-02.

G. Colicchio, M. Landrini, and J. R. Chaplin. Level-Set Computations of Free Surface Rotational Flows. *Journal of Fluids Engineering*, 127(6):1111–1121, 2005.

G. Colicchio, M. Greco, and O. Faltinsen. A BEM-level set domain-decomposition strategy for non-linear and fragmented interfacial flows. *International Journal for Numerical Methods in Engineering*, 67(10):1385–1419, 2006.

F. H. Dadmarzi, M. Thys, and E. E. Bachynski. Validation of Hydrodynamic Loads on a Large-Diameter Monopile in Regular Waves. volume 7A: Ocean Engineering of *International Conference on Offshore Mechanics and Arctic Engineering*. ASME, 06 2019.

R. A. Dalrymple, A. Herault, G. Bilotta, and R. J. Farahani. GPU-accelerated SPH model for water waves and free surface flows. *Coastal Engineering Proceedings*, 1(32), 2011.

M. Darwish and F. Moukalled. Convective schemes for capturing interfaces of free-surface flows on unstructured grids. *Numerical heat transfer, part B: Fundamentals*, 49(1): 19–42, 2006.

R. G. Dean. Stream function representation of nonlinear ocean waves. *Journal of Geophysical Research*, 70:4561–5472, 1965.

G. Delhommeau. Seakeeping codes AQUADYN and AQUAPLUS. 19th WEGEMT School on Numerical Simulation of Hydrodynamics Ships and Offshore Structures, 09 1993.

A. Di Mascio, R. Broglia, and R. Muscari. On the application of the single-phase level set method to naval hydrodynamic flows. *Computers & Fluids*, 36(5):868–886, 2007.

B. Di Paolo, J. L. Lara, G. Barajas, and Í. J. Losada. Wave and structure interaction using multi-domain couplings for Navier-Stokes solvers in OpenFOAM®. Part I: Implementation and validation. *Coastal Engineering*, 164:103799, 2021.

E. Dombre, M. Benoit, D. Violeau, C. Peyrard, and S. T. Grilli. Simulation of floating structure dynamics in waves by implicit coupling of a fully nonlinear potential flow model and a rigid body motion approach. *Journal of Ocean Engineering and Marine Energy*, 1:55–76, 2015.

D. G. Dommermuth and D. K. P. Yue. A higher-order spectral method for the study of nonlinear gravity waves. *Journal of Fluid Mechanics*, 184:267–288, 1987.

G. Ducrozet, F. Bonnefoy, D. Le Touzé, and P. Ferrant. A modified high-order spectral method for wavemaker modeling in a numerical wave tank. *European Journal of Mechanics-B/Fluids*, 34:19–34, 2012.

G. Ducrozet, A. P. Engsig-Karup, H. B. Bingham, and P. Ferrant. A non-linear wave decomposition model for efficient wave–structure interaction. Part A: Formulation, validations and analysis. *Journal of Computational Physics*, 257:863–883, 2014.

EDF R&D. Neptune solver. URL https://www.code-saturne.org/cms/web/NEPTUNECFD. Accessed : 2022-01-25.

A. Engsig-Karup, H. Bingham, and O. Lindberg. An efficient flexible-order model for 3D nonlinear water waves. *Journal of Computational Physics*, 228:2100–2118, 2009.

European Commission. Resolution on climate change, 2019. URL https://www.europarl.europa.eu/doceo/document/TA-8-2019-0217_EN.html. Accessed : 2022-01-24.

European Commission. Boosting Offshore Renewable Energy for a Climate Neutral Europe, 2020. URL https://ec.europa.eu/commission/presscorner/detail/en/IP_20_2096. Accessed : 2022-01-24.

F. Fàbregas Flavià, C. McNatt, F. Rongère, A. Babarit, and A. H. Clément. Computation of the Diffraction Transfer Matrix and the Radiation Characteristics in the Open-Source BEM Code NEMOH. In *35th International Conference on Ocean, Offshore and Artic Engineering (OMAE2016)*, Jeju, South Korea, 06 2016.

J. D. Fenton. Numerical methods for nonlinear waves. In P. L.-F. Liu, editor, *Advances in Coastal and Ocean Engineering*, pages 241–324. World Scientific Pub. Co. Inc., 1999.

M. Ferrand and J. C. Harris. Finite volume arbitrary Lagrangian-Eulerian schemes using dual meshes for ocean wave applications. *Computers & Fluids*, 219:104860, 2021.

P. Ferrant. Fully Nonlinear Interactions of Long-Crested Wave Packets with a Three-Dimensional Body. In *Proc. 22nd ONR Symposium on Naval Hydrodynamics*, Washington DC., USA, 1998.

C. Fochesato and F. Dias. A fast method for nonlinear three-dimensional free-surface waves. *Proceedings of the Royal Society A*, 462:2715–2735, 2006.

C. Fochesato, S. T. Grilli, and P. Guyenne. Note on non-orthogonality of local curvilinear co-ordinates in a three-dimensional boundary element method. *International Journal for Numerical Methods in Fluids*, 48:305–324, 2005.

Y. Fournier. Massively parallel location and exchange tools for unstructured meshes. *International Journal of Computational Fluid Dynamics*, 34(7-8):549–568, 2020.

L. Gentaz, R. Luquet, B. Alessandrini, and P. Ferrant. Numerical simulation of the 3D viscous flow around a vertical cylinder in non-linear waves using an explicit incident wave model. In *International Conference on Offshore Mechanics and Arctic Engineering*, volume 37432, pages 157–163, 2004.

R. A. Gingold and J. J. Monaghan. Smoothed particle hydrodynamics: theory and application to non-spherical stars. *Monthly Notices of the Royal Astronomical Society*, 181 (3):375–389, 12 1977.

Global Wind Energy Council (GWEC). Global Offshore Wind Report 2020, 2021. URL https://gwec.net/global-offshore-wind-report-2020/.

Y. Goda and T. Suzuki. Estimation of incident and reflected waves in random wave experiments. In *Proc. Int. Conf. on Coastal Engineering (ICCE1976)*, volume 1, pages 828–845, 01 1976.

S. Gottlieb. On high order strong stability preserving Runge-Kutta and multi step time discretizations. *Journal of Scientific Computing*, 25:105–128, 2005.

M. Greco. Water shipping on a vessel in head waves. In *24th Symposium on naval hydrodynamics Fukuoka, Japan, 2002*, pages 40–52, 2002.

M. Greco, O. Faltinsen, and M. Landrini. Numerical simulation of heavy water shipping. In *Proc. 17th Workshop on Water Waves and Floating Bodies, Cambridge UK*, pages 14–16, 2002.

L. Greengard and V. Rokhlin. A fast algorithm for particle simulations. *Journal of Computational Physics*, 73:325–348, 1987.

S. T. Grilli and J. Horrillo. Generation and absoption of fully nonlinear periodic waves. *Journal of Engineering Mechanics*, 123:1060–1069, 1997.

S. T. Grilli and I. A. Svendsen. Corner problems and global accuracy in the boundary element solution of nonlinear wave flows. *Engineering Analysis with Boundary Elements*, 7:178–195, 1990.

S. T. Grilli, P. Guyenne, and F. Dias. A fully nonlinear model for three-dimensional overturning waves over arbitrary bottom. *International Journal for Numerical Methods in Fluids*, 35:829–867, 2001.

S. T. Grilli, S. Vogelmann, and P. Watts. Development of a 3D Numerical Wave Tank for modeling tsunami generation by underwater landslides. *Engineering Analysis with Boundary Elements*, 26:301–313, 2002.

E. Guerber, M. Benoit, S. T. Grilli, and C. Buvat. A fully nonlinear implicit model for wave interactions with submerged structures in forced of free motion. *Engineering Analysis with Boundary Elements*, 36:1151–1163, 2012.

S. Guignard, S. T. Grilli, R. Marcer, and V. Rey. Computation of Shoaling And Breaking Waves In Nearshore Areas By the Coupling of BEM And VOF Methods. International Ocean and Polar Engineering Conference (ISOPE99), Brest, France, 06 1999.

P.-E. Guillerm and B. Alessandrini. 3d free-surface flow computation using a ranse/fourier–kochin coupling. *International Journal for Numerical Methods in Fluids*, 43(3):301–318, 2003.

S. Guillou, N. Barbry, and K. Nguyen. Numerical computation of surface waves by a projection method using an adaptative-Eulerian grid. *Comptes Rendus de l'Académie des Sciences Série II : Fascicule B-Mécanique*, 328(12):875–881, 2000.

L. Guo, D. Sun, and W. Hao. A new numerical wave flume combining the 0–1 type BEM and the VOF method. *Journal of Hydrodynamics, Ser. B*, 24(4):506–517, 2012.

A. N. Hahmann, T. Sīle, B. Witha, N. N. Davis, M. Dörenkämper, Y. Ezber, E. García-Bustamante, J. F. González-Rouco, J. Navarro, B. T. Olsen, and S. Söderberg. The making of the New European Wind Atlas – Part 1: Model sensitivity. *Geoscientific Model Development*, 13(10):5053–5078, 2020.

J. A. Hamilton and R. W. Yeung. Viscous and inviscid matching of three-dimensional free-surface flows utilizing shell functions. *Journal of Engineering Mathematics*, 70(1-3):43–66, 2011.

F.-C. W. Hanssen. *Non-linear wave-body interaction in severe waves*. PhD thesis, Norwegian University of Science and Technology (NTNU), Norway, 2019.

F. H. Harlow and J. E. Welch. Numerical calculation of time-dependent viscous incompressible flow of fluid with free surface. *The Physics of Fluids*, 8(12):2182–2189, 1965.

J. C. Harris and S. T. Grilli. A perturbation approach to large eddy simulation of wave-induced bottom boundary layer flows. *International Journal for Numerical Methods in Fluids*, 68(12):1574–1604, 2012.

J. C. Harris, K. Kuznetsov, C. Peyrard, S. Saviot, A. Mivehchi, S. T. Grilli, and M. Benoit. Simulation of wave forces on a gravity based foundation by a bem based on fully nonlinear potential flow. In *The 27th International Ocean and Polar Engineering Conference*, San Francisco, California, USA, 06 2017.

J. C. Harris, E. Dombre, M. Benoit, S. T. Grilli, and K. I. Kuznetsov. Nonlinear time-domain wave-structure interaction: a parallel fast integral equation approach. *International Journal for Numerical Methods in Fluids*, 94(2):188–222, 2022.

K. Hayami and H. Matsumoto. Improvement of quadrature for nearly singular integrals in 3D-BEM. *WIT Transactions on Modelling and Simulation*, 7, 1994.

P. Higuera, J. L. Lara, and I. J. Losada. Simulating coastal engineering processes with OpenFOAM®. *Coastal Engineering*, 71:119–134, 2013.

A. Hildebrandt and V. Sriram. Pressure distribution and vortex shedding around a cylinder due to a steep wave at the onset of breaking from physical and numerical modeling. In *The Twenty-fourth International Ocean and Polar Engineering Conference*, Busean, Korea, 06 2014.

C. Hirt and B. Nichols. Volume of fluid (vof) method for the dynamics of free boundaries. *Journal of Computational Physics*, 39(1):201–225, 1981.

A. Iafrati and E. Campana. A domain decomposition approach to compute wave breaking (wave-breaking flows). *International Journal for Numerical Methods in Fluids*, 41(4): 419–445, 2003.

J. Kemper, C. Windt, K. Graf, and J. Ringwood. Development towards a nested hydrodynamic model for the numerical analysis of ocean wave energy systems. In *European Tidal and Wave Energy Conference Proceedings*, number 1414, Napoli, Italy, 09 2019. EWTEC.

S.-H. Kim, M. Yamashiro, and A. Yoshida. A simple two-way coupling method of BEM and VOF model for random wave calculations. *Coastal Engineering*, 57(11-12):1018–1028, 2010.

C. Lachaume, B. Biausser, P. Fraunié, S. T. Grilli, and S. Guignard. Modeling of breaking and post-breaking waves on slopes by coupling of BEM and VOF methods. In *The Thirteenth International Offshore and Polar Engineering Conference*, 2003.

E. Laitone. The second approximation to cnoidal and solitary waves. *Journal of Fluid Mechanics*, 9(3):430–444, 1960.

B. E. Larsen, D. R. Fuhrman, and J. Roenby. Performance of interfoam on the simulation of progressive waves. *Coastal Engineering Journal*, 61(3):380–400, 2019.

C. H. Lee. WAMIT Theory Manual. Technical report, MIT, Cambridge, MA, USA, 1995. Report 95-2, Department of Ocean Engineering.

V. Leroy, E. Bachynski-Polić, A. Babarit, P. Ferrant, and J.-C. Gilloteaux. A weak-scatterer potential flow theory-based model for the hydroelastic analysis of offshore wind turbine substructures. *Ocean Engineering*, 238:109702, 2021.

Z. Li, B. Bouscasse, G. Ducrozet, L. Gentaz, D. Le Touzé, and P. Ferrant. Spectral wave explicit navier-stokes equations for wave-structure interactions using two-phase computational fluid dynamics solvers. *Ocean Engineering*, 221:108513, 2021.

H. Lindeboom, H. Kouwenhoven, M. Bergman, S. Bouma, S. Brasseur, R. Daan, R. Fijn, D. De Haan, S. Dirksen, R. Van Hal, et al. Short-term ecological effects of an offshore wind farm in the dutch coastal zone; a compilation. *Environmental Research Letters*, 6 (3):035101, 2011.

M. S. Longuet-Higgins and E. Cokelet. The deformation of steep surface waves on water, I. A numerical method of computation. *Proceedings of the Royal Society A*, 350:1–26, 1976.

X. Lu, D. D. J. Chandar, Y. Chen, and J. Lou. An overlapping domain decomposition based near-far field coupling method for wave structure interaction simulations. *Coastal Engineering*, 126:37–50, 2017.

Q. Ma and S. Yan. Quasi ALE finite element method for nonlinear water waves. *Journal of Computational Physics*, 212(1):52–72, 2006.

J. Maestre, I. Cuesta, and J. Pallares. An unsteady 3D Isogeometrical Boundary Element Analysis applied to nonlinear gravity waves. *Computer Methods in Applied Mechanics and Engineering*, 310:112–133, 2016.

A. Mehmood, D. I. Graham, K. Langfeld, and D. M. Greaves. OpenFOAM Finite Volume Method implementation of a fully nonlinear potential flow model for simulating wave-structure interactions. In *The Twenty-fifth International Ocean and Polar Engineering Conference*, Kona, Hawaii, USA, 06 2015.

F. Mintgen and M. Manhart. A bi-directional coupling of 2D shallow water and 3D Reynolds-averaged Navier–Stokes models. *Journal of Hydraulic Research*, 56(6):771–785, 2018.

A. Mivehchi. *Experimental and Numerical Simulations for Fluid Body Interaction Problems.* PhD thesis, University of Rhode Island, RI, USA, 2018.

W. Mo. *Numerical investigation of solitary wave interaction with group of cylinders.* PhD thesis, Cornell University, NY, USA, 2010.

C. Monroy, G. Ducrozet, F. Bonnefoy, A. Babarit, L. Gentaz, and P. Ferrant. RANS simulations of a CALM buoy in regular and irregular seas using the SWENSE method. In *The Twentieth International Offshore and Polar Engineering Conference*, Beijing, China, 06 2010.

J. Morison, J. Johnson, and S. Schaaf. The force exerted by surface waves on piles. *Journal of Petroleum Technology*, 2(05):149–154, 1950.

W. Musial, S. Butterfield, and A. Boone. *Feasibility of Floating Platform Systems for Wind Turbines*. 2007.

S. Muzaferija. A two-fluid Navier-Stokes solver to simulate water entry. In *Proceedings of 22nd symposium on Naval Architecture, 1999*, pages 638–651. National Academy Press, 1999.

K.-Y. Oh, W. Nam, M. S. Ryu, J.-Y. Kim, and B. I. Epureanu. A review of foundations of offshore wind energy convertors: Current status and future perspectives. *Renewable and Sustainable Energy Reviews*, 88:16–36, 2018.

C. Papoutsellis, A. Charalampopoulos, and G. Athanassoulis. Implementation of a fully nonlinear hamiltonian coupled-mode theory, and application to solitary wave problems over bathymetry. *European Journal of Mechanics - B/Fluids*, 72:199–224, 2018.

B. Paulsen. *Efficient computations of wave loads on offshore structures*. PhD thesis, Technical University of Denmark, Denmark, 2013.

B. T. Paulsen, H. Bredmose, H. B. Bingham, and N. G. Jacobsen. Forcing of a bottom-mounted circular cylinder by steep regular water waves and finite depth. *Journal of Fluid Mechanics*, 755:1–34, 2014.

J. Pawlowski. A nonlinear theory of ship motion in waves. 19th Symposium on Naval Hydrodynamics, Seoul, Korea, 08 1992.

W. J. Pringle, N. Yoneyama, and N. Mori. Two-way coupled long wave-RANS model: Solitary wave transformation and breaking on a plane beach. *Coastal Engineering*, 114: 99–118, 2016.

C. Raoult, M. Benoit, and M. L. Yates. Validation of a fully nonlinear and dispersive wave model with laboratory non-breaking experiments. *Coastal Engineering*, 114:194–207, 2016.

G. Reliquet, A. Drouet, P.-E. Guillerm, E. Jacquin, L. Gentaz, and P. Ferrant. Simulation of wave-body interaction using a single-phase level set function in the swense method. In *International Conference on Offshore Mechanics and Arctic Engineering*, volume 7, Nantes, France, 06 2013. American Society of Mechanical Engineers.

F. Robaux. *Numerical simulation of wave-body interaction: development of a fully non-linear potential flow solver and assessment of two local coupling strategies with a CFD solver*. PhD thesis, Aix Marseille University, Marseille, France, 2020.

F. Robaux and M. Benoit. Development and validation of a numerical wave tank based on the harmonic polynomial cell and immersed boundary methods to model nonlinear wave-structure interaction. *Journal of Computational Physics*, 446:110560, 2021.

F. Robaux and M. Benoit. Assessment of one-way coupling methods from a potential to a viscous flow solver based on domain- and functional-decomposition for fixed submerged bodies in nonlinear waves. *European Journal of Mechanics B/Fluids*, 2022-submitted, in revision.

J. Romate. The numerical simulation of nonlinear gravity waves. *Engineering Analysis with Boundary Elements*, 4:156–166, 1990.

T. Schmitt, D. Schaap, G. Spoelstra, L. Benoit, and P. Cyrille. Emodnet bathymetry a compilation of bathymetric data in the european waters. In *OCEANS 2019, Marseille*, pages 1–7, 06 2019.

Y.-L. Shao and O. M. Faltinsen. A harmonic polynomial cell (HPC) method for 3D Laplace equation with application in marine hydrodynamics. *Journal of Computational Physics*, 274:312–332, 2014.

M. A. Siddiqui, M. Greco, G. Colicchio, and O. M. Faltinsen. Validation of damaged ship hydrodynamics by a domain decomposition approach using the harmonic polynomial cell method and openfoam. In *Proceedings of 33rd International Workshop on Water Waves and Floating Bodies*, Guidel-Plage, France, 04 2018.

K. Sitanggang and P. Lynett. Multi-scale simulation with a hybrid boussinesq-rans hydrodynamic model. *International Journal For Numerical Methods in Fluids*, 62(9): 1013–1046, 2010.

V. Sriram, Q. Ma, and T. Schlurmann. A hybrid method for modelling two dimensional non-breaking and breaking waves. *Journal of Computational Physics*, 272:429–454, 2014.

M. Sueyoshi, H. Kihara, and M. Kashiwagi. A hybrid technique using particle and boundary-element methods for wave-body interaction problems. In *Proceedings of the 9th International Conference on Numerical Ship Hydrodynamics*, volume 1, pages 241–252, Ann Harbor, Michignan, USA, 08 2007.

M. Tanaka. The stability of solitary waves. *Physics of Fluids*, 29:650–655, 1986.

Y. Tian and S. Sato. A numerical model on the interaction between nearshore nonlinear waves and strong currents. *Coastal Engineering Journal*, 50(04):369–395, 2008.

United Nations. The Paris Agreement, 2015. URL https://unfccc.int/process-and-meetings/the-paris-agreement/the-paris-agreement. Accessed : 2022-01-24.

D. Veic and W. Sulisz. Impact pressure distribution on a monopile structure excited by irregular breaking wave. *Polish Maritime Research*, 25(s1):29–35, 2018.

T. Verbrugghe, J. M. Domínguez, A. J. Crespo, C. Altomare, V. Stratigaki, P. Troch, and A. Kortenhaus. Coupling methodology for smoothed particle hydrodynamics modelling of non-linear wave-structure interactions. *Coastal Engineering*, 138:184–198, 2018.

T. Verbrugghe, V. Stratigaki, C. Altomare, J. Domínguez, P. Troch, and A. Kortenhaus. Implementation of open boundaries within a two-way coupled SPH model to simulate nonlinear wave–structure interactions. *Energies*, 12(4):697, 2019.

H. K. Versteeg and W. Malalasekera. *An introduction to computational fluid dynamics: the finite volume method*. Pearson education, 2007.

V. Vukčević. *Numerical modelling of coupled potential and viscous flow for marine applications*. PhD thesis, University of Zagreb. Faculty of Mechanical Engineering and Naval Architecture, 2016.

H.-W. Wang, C.-J. Huang, and J. Wu. Simulation of a 3D numerical viscous wave tank. *Journal of Engineering Mechanics*, 133(7):761–772, 2007.

B. J. West, K. A. Brueckner, R. S. Janda, D. M. Milder, and R. L. Milton. A new numerical method for surface hydrodynamics. *Journal of Geophysical Research: Oceans*, 92(C11): 11803–11824, 1987.

Wind Europe. Wind energy in Europe 2020 Statistics and the outlook for 2021-2025, 2021. URL https://windeurope.org/intelligence-platform/product/wind-energy-in-europe-in-2020-trends-and-statistics/#downloads. Accessed : 2022-01-24.

Z. Xie. Numerical study of breaking waves by a two-phase flow model. *International Journal for Numerical Methods in Fluids*, 70(2):246–268, 2012.

S. Yan and Q. Ma. A Hybrid Approach Coupling MLPG-R With QALE-FEM for Modelling Fully Nonlinear Water Waves. International Ocean and Polar Engineering Conference (ISOPE2017), San Francisco, California, USA, 06 2017.

Z. Yang, B. Huang, A. Kang, B. Zhu, J. Han, R. Yin, and X. Li. Experimental study on the solitary wave-current interaction and the combined forces on a vertical cylinder. *Ocean Engineering*, 236:109569, 2021.

G. Yates and K. Wang. Solitary Wave Scattering By a Vertical Cylinder: Experimental Study. International Ocean and Polar Engineering Conference (ISOPE1994), Osaka, Japan, 04 1994.

M. L. Yates and M. Benoit. Accuracy and efficiency of two numerical methods of solving the potential flow problem for highly nonlinear and dispersive water waves. *International Journal for Numerical Methods in Fluids*, 77(10):616–640, 2015.

W. Yue, C.-L. Lin, and V. C. Patel. Numerical simulation of unsteady multidimensional free surface motions by level set method. *International Journal for Numerical Methods in Fluids*, 42(8):853–884, 2003.

V. E. Zakharov. Stability of periodic waves of finite amplitude on the surface of a deep fluid. *Journal of Applied Mechanics and Technical Physics*, 9(2):190–194, 1968.

D. Zhang, C. Jiang, D. Liang, Z. Chen, Y. Yang, and Y. Shi. A refined volume-of-fluid algorithm for capturing sharp fluid interfaces on arbitrary meshes. *Journal of Computational Physics*, 274:709–736, 2014.

J. Zhang and M. Benoit. Wave–bottom interaction and extreme wave statistics due to shoaling and de-shoaling of irregular long-crested wave trains over steep seabed changes. *Journal of Fluid Mechanics*, 912:A28, 2021.

Y. Zhang and B. Teng. A nonlinear potential flow model for higher-harmonic wave loads and ringing response of a monopile. *Ocean Engineering*, 222:108574, 2021.

Y. Zhang, M. Peszynska, and S. Yim. Coupling of viscous and potential flow models with free surface for near and far field wave propagation. *International Journal of Numerical Analysis and Modeling*, 4(3):256–82, 2013.